# Characterization of Performance-Limiting Flow Mechanisms in a Centrifugal Compressor Stage

by

David W. Erickson

B.S. Aerospace Engineering
Massachusetts Institute of Technology, 2010

Submitted to the Department of Aeronautics and Astronautics
in Partial Fulfillment of the Requirements for the Degree of

Master of Science in Aerospace Engineering

at the

MASSACHUSETTS INSTITUTE OF TECHNOLOGY

February 2017



Author ..... Signature redacted
Department of Aeronautics and Astronautics
February 2, 2016

Certified by ..... Signature redacted .....
Choon S. Tan
Senior Research Engineer of Aeronautics and Astronautics
Thesis Supervisor

Certified by ..... Signature redacted
Michael Macrorie
Consulting Engineer at GE Aviation
Thesis Supervisor

Accepted by ..... Signature redacted .....
Youssef M. Marzouk
Associate Professor of Aeronautics and Astronautics
Chair, Graduate Program Committee

Characterization of Performance-Limiting Flow Mechanisms in a Centrifugal Compressor Stage

by

David W. Erickson

Submitted to the Department of Aeronautics and Astronautics
on February 2, 2017, in Partial Fulfillment of the
Requirements for the Degree of
Master of Science in Aerospace Engineering

# Abstract

This research characterizes the performance of a centrifugal compressor stage with a special focus on the pipe diffuser. Two diffuser configurations are studied, one of which is a truncated version of the other. Experimental data acquired on a research compressor stage is interrogated along with a set of well-designed Reynolds-Averaged Navier Stokes computations, complemented by reduced order flow modeling. The fundamental performance-limiting flow mechanisms in the diffuser are identified and used to physically relate important geometry features and operating conditions to the observed compressor pressure rise, efficiency, and operability characteristics.

Despite large differences in their geometry, the two diffuser configurations exhibit similar pressure recovery characteristics due to differences in exit nonuniformity and flow angle which result in similar effective area ratios. Variations in the diffuser pressure recovery coefficient with operating point are found to be most influenced by the diffuser inlet flow angle, and secondly by the inlet Mach number. The diffuser inlet flow angle has the primary effect of setting the diffuser inlet one-dimensional area ratio, increasing diffusion at high flow angles. In addition, the diffuser incidence angle influences the formation of counter-rotating vortex pairs that persist throughout the diffuser passage. Using a two-dimensional integral boundary layer model that is modified to accommodate three-dimensional effects as source terms, these secondary flows are shown to detrimentally impact the diffuser pressure rise capability by accumulating high loss flow along the diffuser wall near the plane of symmetry between the vortices. This contributes to the extent and location of a large diffuser passage separation, especially for the baseline diffuser. The impact of the vortices on the boundary layer growth rate is shown to scale inversely with diffuser aspect ratio.

The major performance difference between the two diffuser configurations is that the truncated diffuser configuration experiences enhanced stall margin over the baseline diffuser at the design speed. These differences are traced to reduced secondary flows influence and thus reduced separation extent for the higher aspect ratio truncated diffuser. It is hypothesized that the onset of stall for the baseline diffuser configuration is initiated by the transition of the vortex location and corresponding passage separation between diffuser pressure and suction sides with increasing cusp incidence. Conversely, because the extent

of the passage separation in the truncated diffuser is diminished due to the higher aspect ratio, the switch in separation side does not immediately initiate instability.

The fact that secondary flows have a large influence on diffuser pressure rise capability and compressor stability is counter to conventional preliminary diffuser design approaches which neglect such 3D effects. The findings of this research may therefore be considered during preliminary design optimization to produce better-performing diffuser designs.

Thesis Supervisor: Choon S. Tan
Title: Senior Research Engineer of Aeronautics and Astronautics

Thesis Supervisor: Michael Macrorie
Title: Consulting Engineer at GE Aviation

# Acknowledgments

This research was a multi-year endeavor, complete with many ups, downs, and unexpected challenges. However, I had many people beside me, supporting this work and supporting me personally through completion. I would like to thank those people.

I'd like to thank GE Aviation on many levels. First, I am grateful for GE's financial sponsorship of this research through contract 023859-001. Thanks to all who endeavored to work out the associated funding and legal details, including Caitlin Smythe for managing these details throughout the duration of the program. I am also grateful for the expertise and guidance GE provided, especially from Mike Macrorie, Dave Parker, and Steve Donnelly. Lastly, I am grateful for the support and flexibility allowed to me by my manager, Dave Miller, as I struggled to balance work and school.

I also would like to thank both GE and the folks at RWTH Aachen University for all the work that has been done over the past two decades to generate experimental data leveraged by my work. Thanks to you, the most difficult part of this research was completed before I even began.

Thank you to the MIT Gas Turbine Lab (GTL), and particularly to my advisor, Dr. Choon Tan, for your technical expertise and guidance. I am also grateful for the personal relationship that we developed during this period. I feel lucky to have a strong technical advisor who could keep me on track, while also prioritizing casual conversations and oyster feasts.

Thank you to all of my friends. Thank you to my GTL labmates who helped make the oldest offices at MIT feel more like a community. I also appreciated my time leading and competing with my friends in the MIT Sporting Clays Association (SCA). Also, thank you to my mountain biking friends, hiking friends, skiing friends, board game friends, etc., who really made this time enjoyable. Lastly, thank you to my church friends for waking up early with me for Monday motivational coffee, and for conversations that helped me grow personally during this time as much as I grew professionally.

Thank you to my parents for all the work you invested into me in my younger days, only to have me pursue a life hundreds of miles away when I became older. Although you are not here physically, I know that you thought about me often as I worked through this, and that you cared. In the future, I look forward to Christmases at home without the thesis writing distraction. Thank you also to my mother-in-law, who ensures I feel at home here.

Last, but certainly not least, thank you to my wife Julie. I was afraid of marrying you halfway through this intensive degree, but because I did I may never be afraid again. Thank you for always making sacrifices for my sake, but especially these past few months. Thank you for your cheery, carefree personality that helps me to remember the bigger and better picture. I always enjoy coming home to your smiles, hugs, and unconditional love. I am excited for the future because it will be with you. I love you very much.

# Contents

# List of Figures

# List of Tables

# List of Symbols and Abbreviations

## Roman

| | | |
|---|---|---|
| $A$ | | Area of cut plane |
| $A'$ | $A\cos\alpha'$ | 1D area |
| $A_e$ | $A'(1-B_m)$ | Effective area |
| $AR$ | $\frac{h}{c}$ | Vane or blade aspect ratio |
| $c$ | | Chord |
| $C$ | | Circumference or perimeter |
| C | | Choke operating point |
| $C_f$ | | Skin friction coefficient |
| $C_D$ | | Dissipation coefficient |
| CL | | Centerline of diffuser $(y,z)=(0,0)$ |
| $c_p$ | $\frac{\gamma R}{\gamma-1}$ | Specific heat at constant pressure |
| $C_{p(1-2)}$ | $\frac{p_2-p_1}{p_{t1}-p_1}$ | Static pressure recovery coefficient (subscripts denote start and end stations) |
| $C_{pu}$ | | Uniform flow ideal static pressure recovery coefficient (subscripts denote start and end stations) |
| $C_{pu0}$ | | Incompressible uniform flow ideal static pressure recovery coefficient (subscripts denote start and end stations) |
| $d$ | | Diameter |
| $d_e$ | | Effective diameter |
| $E$ | $\frac{C_p}{C_{pu}}$ | Effectiveness |
| E | | Peak efficiency operating point |
| $h$ | | Passage height between endwalls |
| $h$ | | Specific enthalpy |
| $\dot{H}$ | $\int rV_\theta \rho V_n dA$ | Angular momentum flow rate |
| $H$ | $\int h\rho V_n dA$ | Enthalpy flow rate |
| $H$ | $\frac{B_m}{B_P}$ | 1D shape factor |
| $H_x$ | $\frac{\delta_x^*}{\theta_x}$ | Boundary layer shape factor ($x$-flux component) |
| $H_x^*$ | $\frac{\theta_x^*}{\theta_x}$ | Boundary layer kinetic energy shape factor ($x$-flux component) |
| $H_x^{**}$ | $\frac{\delta_x^{**}}{\theta_x}$ | Boundary layer density flux shape factor ($x$-flux component) |

| | | |
|---|---|---|
| $i$ | | Incidence |
| $L$ | | Length (subscripts denote start and end stations) |
| $\dot{m}$ | $\int \rho V_n dA$ | Mass flow rate |
| $M$ | | Mach number |
| $N$ | | Impeller angular velocity |
| $N_v$ | | Number of contributing vortices |
| $p$ | | Pressure |
| $p_{ref}$ | 101,325 Pa | Reference pressure |
| $\vec{P}$ | $\int \vec{V} \rho V_n dA$ | Momentum flow rate (subscript denotes component) |
| $r$ | | Compressor radial coordinate; $r = 0$ at compressor rotation axis |
| $r$ | | Distance from vortex core |
| $R$ | 287 J/(kg-K) | Ideal gas constant |
| $s$ | | Streamline coordinate |
| $s$ | | Specific entropy |
| $s_{ref}$ | 0 J/(kg-K) | Reference specific entropy |
| S | | Stall operating point |
| S' | | Post-stall operating point |
| $SA$ | | Surface area |
| $T$ | | Temperature |
| $T_{ref}$ | 288.15 K | Reference temperature |
| $u$ | | Velocity component along local boundary layer $x$ coordinate |
| $U$ | $r$N | Impeller wheel speed |
| $v$ | | Velocity component along local boundary layer $y$ coordinate |
| $\vec{V}$ | | Velocity (subscripts denote component) |
| $\mathcal{V}$ | | Volume |
| $w$ | | Velocity component along local boundary layer $z$ coordinate |
| $\vec{W}$ | | Velocity in rotating reference frame (subscripts denote component) |
| $\dot{W}$ | | Power |
| $x$ | | Local boundary layer coordinate along primary flow direction |
| $x$ | | Compressor coordinate along diffuser passage throughflow direction; $x = 0$ at diffuser throat |
| $x'$ | | Compressor coordinate along diffuser passage throughflow direction; $x' = 0$ at compressor rotation axis |
| $y$ | | Local boundary layer coordinate normal to wall |
| $y$ | | Compressor coordinate perpendicular to engine axis and diffuser passage throughflow direction; $y = 0$ at diffuser centerline |
| $y'$ | | Compressor coordinate perpendicular to engine axis and diffuser passage throughflow direction; $y' = 0$ at compressor rotation axis |
| $z$ | | Local boundary layer coordinate in transverse direction |

| | | |
|---|---|---|
| $z$ | | Compressor coordinate along compressor rotation axis; $z = 0$ at diffuser mid plane or centerline, increasing from compressor inlet to exit |

# Greek

| | | |
|---|---|---|
| $\alpha$ | $\tan^{-1}\left(\frac{V_\theta}{V_m}\right)$ | Flow angle relative to meridional direction |
| $\alpha'$ | $\cos^{-1}\left(\frac{V_n}{\lvert\vec{V}\rvert}\right)$ | Flow angle relative to cut plane |
| $\beta$ | $\tan^{-1}\left(\frac{W_\theta}{V_m}\right)$ | Flow angle relative to meridional direction in rotating reference frame |
| $\beta$ | | Reduced frequency |
| $\gamma$ | 1.4 | Specific heat ratio |
| $\Gamma$ | $\int \omega_n dA$ | Circulation |
| $\delta_x^*$ | $\int_0^{y_e}\left[1-\frac{\rho u}{(\rho u)_e}\right]dy$ | Boundary layer displacement thickness ($x$-flux component) |
| $\delta_x^{**}$ | $\int_0^{y_e}\left(1-\frac{\rho}{\rho_e}\right)\frac{u}{u_e}dy$ | Boundary layer density flux thickness ($x$-flux component) |
| $\eta_{p(1-2)}$ | $\left(\frac{\gamma-1}{\gamma}\right)\frac{\ln(\pi_{(1-2)})}{\ln(\tau_{(1-2)})}$ | Polytropic efficiency (subscripts denote start and end stations) |
| $\theta$ | | Circumferential position around compressor rotation axis |
| $\theta$ | | Circumferential position around vortex core |
| $\theta_x$ | $\int_0^{y_e}\left(1-\frac{u}{u_e}\right)\left[\frac{\rho u}{(\rho u)_e}\right]dy$ | Boundary layer momentum thickness ($x$-flux component) |
| $\theta_z$ | $\int_0^{y_e}\left(1-\frac{u}{u_e}\right)\left[\frac{\rho w}{(\rho w)_e}\right]dy$ | Boundary layer momentum thickness ($z$-flux component) |
| $\theta_x^*$ | $\int_0^{y_e}\left(1-\frac{u^2}{u_e^2}\right)\left[\frac{\rho u}{(\rho u)_e}\right]dy$ | Boundary layer kinetic energy thickness ($x$-flux component) |
| $\theta_z^*$ | $\int_0^{y_e}\left(1-\frac{u^2}{u_e^2}\right)\left[\frac{\rho w}{(\rho w)_e}\right]dy$ | Boundary layer kinetic energy thickness ($z$-flux component) |
| $\lambda$ | $\frac{h^2}{A'}$ | Aspect ratio of diffuser passage cross-section |
| $\mu$ | | Dynamic viscosity |
| $\pi_{(1-2)}$ | $\frac{p_{t2}}{p_{t1}}$ | Total pressure ratio (subscripts denote start and end stations) |
| $\rho$ | | Density |
| $\sigma$ | | Solidity |
| $\tau$ | | Torque |
| $\tau_{(1-2)}$ | $\frac{T_{t2}}{T_{t1}}$ | Total temperature ratio (subscripts denote start and end stations) |
| $\phi$ | $\frac{V_m}{U}$ | Flow coefficient |
| $\phi$ | $2\tan^{-1}\left(\frac{d_2-d_1}{2L_{(1-2)}}\right)$ | Cone angle for conical diffuser |
| $\phi$ | $\tan^{-1}\left(\frac{V_r}{V_z}\right)$ | Flow angle between meridional and axial directions |
| $\Psi_{(1-2)}$ | $\frac{c_p(T_{t2}-T_{t1})}{U_{27}^2}$ | Work coefficient (subscripts denote start and end stations) |
| $\Psi'_{(1-2)}$ | $\frac{p_{t2}-p_{t1}}{\rho_{t1}U_{27}^2}$ | Pressure rise coefficient (subscripts denote start and end stations) |

| | | |
|---|---|---|
| $\chi$ | | Physical blade angle relative to meridional |
| $\omega$ | | Angular frequency |
| $\bar{\omega}_{(1-2)}$ | $\frac{p_{t1}-p_{t2}}{p_{t1}-p_1}$ | Stagnation pressure loss coefficient (subscripts denote start and end stations) |
| $\bar{\omega}_D$ | | Stagnation pressure loss coefficient estimate based on constant dissipation coefficient (subscripts denote start and end stations) |
| $\bar{\omega}_{D0}$ | | Incompressible stagnation pressure loss coefficient estimate based on constant dissipation coefficient (subscripts denote start and end stations) |
| $\bar{\omega}_{Du0}$ | | Incompressible uniform flow stagnation pressure loss coefficient estimate based on constant dissipation coefficient (subscripts denote start and end stations) |
| $\vec{\omega}$ | | Vorticity (subscripts denote component) |

# Subscripts and Superscripts

| | |
|---|---|
| * | Reference value (average of 100E baseline diffuser experimental measurements) |
| 0 | Incompressible |
| 1D | 1D calculated average |
| 25 | Compressor inlet station |
| 26 | Impeller leading edge station |
| 27 | Impeller trailing edge station |
| 27m | Impeller near trailing edge static pressure measurement station |
| 28 | Diffuser leading edge station |
| 29 | Diffuser exit station (baseline diffuser trailing edge) |
| 31 | Deswirler exit station |
| A | Availability average |
| $D$ | Dissipation |
| D | Dump average |
| $c$ | Corrected to reference conditions |
| $c$ | Compressor, as in $\Delta p_c$ |
| $e$ | Boundary layer edge position |
| $i$ | Idealized calculation, as in $C_{p(1-2i)}$ |
| i | Inlet station (i.e. settling chamber) |
| $L$ | Laminar, as in laminar dynamic viscosity |
| $m$ | Vector component in meridional direction, defined by flow or flowpath direction in $z$-$r$ plane |
| $m$ | Mass, as in mass blockage |
| M | Mixed out average at constant area |
| $n$ | Vector component normal to cut plane or control volume |
| $p$ | Pitchline |

| | |
|---|---|
| $P$ | Momentum, as in momentum blockage |
| P | Potential core average |
| $ref$ | Reference value |
| $t$ | Stagnation or total state |
| $t$ | Blade tip |
| $t$, $t1$, $t2$ | Vector component transverse to cut plane |
| $T$ | Turbulent, as in turbulent dynamic viscosity |
| T | Diffuser throat station |
| Tm | Diffuser near throat total pressure traverse measurement station |
| $u$ | Uniform flow |
| $x, y, z, r, \theta$ | Vector component along respective coordinate |

# Abbreviations

| | |
|---|---|
| 1D | One-dimensional |
| 2D | Two-dimensional |
| 3D | Three-dimensional |
| Aft | Aftward or hub side diffuser endwall |
| AMB | Active magnetic bearing |
| Base | Baseline diffuser configuration |
| CFD | Computational fluid dynamics |
| Exp | Experimental |
| Fwd | Forward or shroud side diffuser endwall |
| HPC | High pressure compressor |
| IGV | Inlet guide vane |
| LE | Leading edge |
| PS | Pressure side of diffuser passage |
| PIV | Particle Image Velocimetry |
| RANS | Reynolds-Averaged Navier Stokes |
| SS | Suction side of diffuser passage |
| Sta | Station |
| TE | Trailing edge |
| Trunc | Truncated diffuser configuration |
| URANS | Unsteady Reynolds-Averaged Navier Stokes |

# Chapter 1 Introduction

## 1.1 Background and Motivation

Centrifugal compressors differ from axial compressors in that they pump a working fluid through a significant radius increase between the inlet and exit of the rotating component. While the relatively large exit radius can sometimes be unmanageable for applications that must be compact or lightweight, the radius change allows the rotating impeller to take advantage of the centrifugal force imparted on the fluid to generate a large static pressure rise for a given blade loading level. This is especially beneficial for situations where large clearance-to-blade height fractions are unavoidable. The radius increase also allows the impeller to utilize its high exit wheel speed to generate a large dynamic pressure rise without experiencing high inlet Mach numbers. Taking all of these considerations into account, centrifugal compressors can be better suited than axial compressors for low airflow applications requiring high pressure rise and low part count or cost. Therefore, it is not surprising that centrifugal compressors are found in many such applications ranging from household vacuum cleaners to vehicle turbochargers to small aircraft engines. It is a high-performance aerospace centrifugal compressor that is the focus of this research.

Downstream of the impeller in a centrifugal compressor is the diffusion system, a non-rotating component which converts the high dynamic pressure exiting the impeller into static pressure rise. There are a few common diffusion system design configurations which range from lower-cost vaneless diffusers with volutes or scrolls to high-efficiency vaned or pipe diffusers, sometimes followed by additional rows of vanes, typically found on aircraft engines. While the increase in flowpath radius throughout a centrifugal compressor inherently benefits the performance of the rotating impeller, the diffusion system does not rotate so it does not experience the same benefit. Conversely, there are a number of factors which actually increase the level of design challenge to the diffuser above that of an axial com-

pressor stator. At the inlet to the diffuser, the meridional direction of the flow is radial, and the Mach number and swirl angle can be high due to the high impeller exit wheel speed. However, in aircraft applications, the centrifugal stage is followed by a combustor requiring that the diffuser exit Mach number and swirl level be low and that the radial velocity component be zero or even slightly inward. This means that aircraft engine centrifugal compressor diffusers must both diffuse and turn the flow substantially.

With high-efficiency aircraft engines trending towards increased overall compressor pressure ratios and decreased core airflow for a given power level, centrifugal compressors have the potential to see even more widespread use in future aircraft engines. However, the physical relationships between centrifugal compressor geometry, the details of the resulting flow behavior, and ultimately the compressor's performance are not as well understood as they are for axial compressors, especially in the diffusion system. This makes the preliminary design of centrifugal compressors a challenging task, with reliance on empirical models of limited applicability or on cumbersome 3D Computational Fluid Dynamics (CFD) simulations not well-suited for preliminary design trade studies.

## 1.2 Experimental Compressor Stage Description

Centrifugal compressors are found in many high-pressure compressors (HPCs) designed and produced by GE Aviation for small turboshaft, turboprop, and turbofan engine applications. Often, the centrifugal compressor is part of an axial-centrifugal HPC, that is, a single-spool compressor consisting of some number of axial stages followed by a single centrifugal stage. Beginning in 2000, GE Aviation supported a centrifugal compressor rig test program at RWTH Aachen University based on the centrifugal stage of a GE axial-centrifugal HPC design. The purpose of this test program was to assess the performance effects of various operating parameters and diffusion system configurations. It is this compressor that is used as the vehicle for the current research. Much of the experimental data and learnings that resulted from the RWTH Aachen test program are leveraged here as well.

The baseline compressor configuration studied for the RWTH Aachen test program is shown in Figure 1.1 and Figure 1.2. The impeller consists of a 46 blades alternating between longer main blades and shorter splitter blades, it features 24.6 deg of backsweep, it has an inlet hub to trailing edge radius ratio of 0.43, and it operates at a design point Reyn-

olds number of $2.5 \times 10^5$ (based on standard day air properties, impeller tip width, and impeller tip speed). The diffusion system for this compressor consists of two main components: the diffuser and the deswirler. The diffuser performs most of the diffusion system's pressure rise while removing some of the swirl from the impeller. It is made up of 30 pipe-type passages oriented radially and tangentially, and its leading edge radius is 3.4% greater than the impeller trailing edge radius. Near the diffuser leading edge, the diffuser passages are wider on the pressure side than they are on the suction side at a constant radial location. As a result, the intersection of adjacent diffuser passages creates leading edge cusps, which project along the endwalls into the vaneless space between the impeller trailing edge and the diffuser leading edge, as seen in Figure 1.4. Downstream of the diffuser, the deswirler contains a flowpath bend followed by a row of 90 vanes, which together turn the flow slightly inward from axial while performing additional diffusion.

During the test program, a number of diffuser and deswirler configurations were studied. This research, however, specifically investigates the details of only two configurations utilizing the same impeller and deswirler but different diffusers—the baseline diffuser and a truncated diffuser, shown in Figure 1.3. As the name suggests, the truncated diffuser is the same as the baseline diffuser except that the diffuser trailing edge has been simply truncated, reducing its radius by 13% from 1.39 to 1.21 times the impeller trailing edge radius. The endwall shapes are identical between the baseline and truncated diffusers.

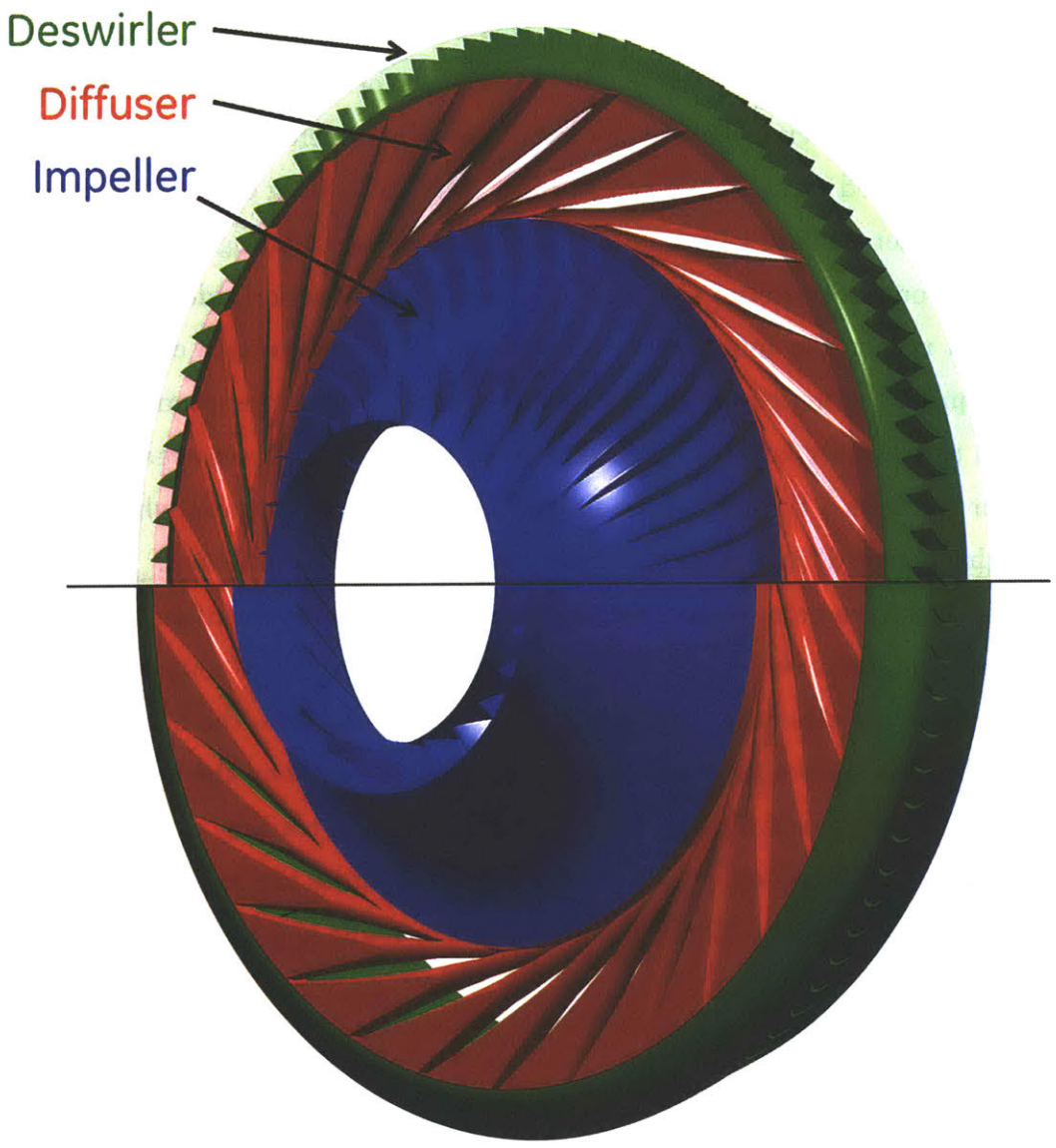


Figure 1.1: 3D cutaway view of experimental centrifugal compressor in baseline configuration.

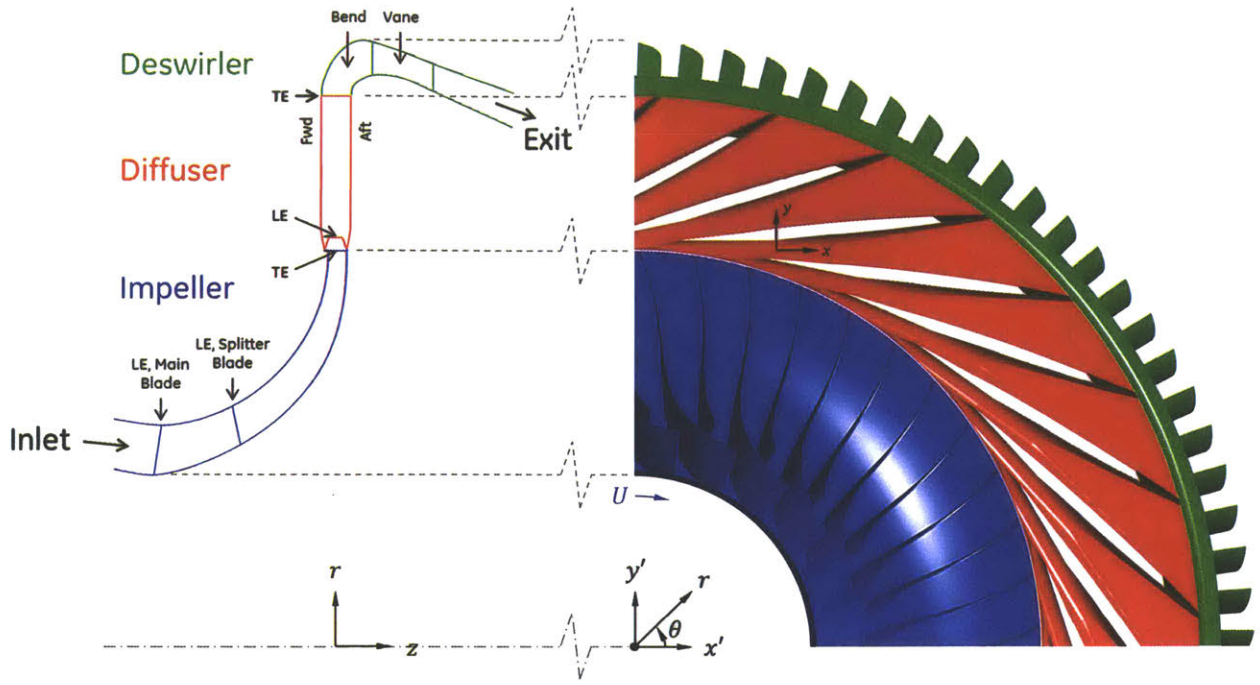


Figure 1.2: Side and front cutaway views of experimental centrifugal compressor with baseline diffuser.

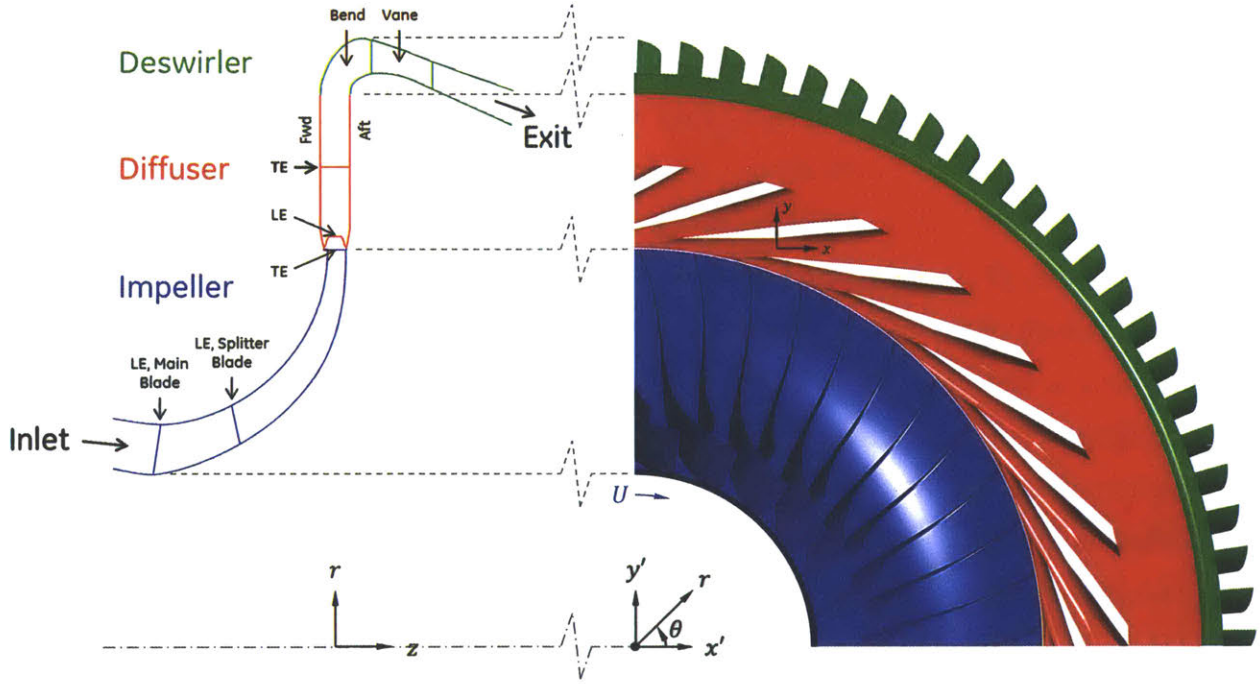


Figure 1.3: Side and front cutaway views of experimental centrifugal compressor with truncated diffuser.

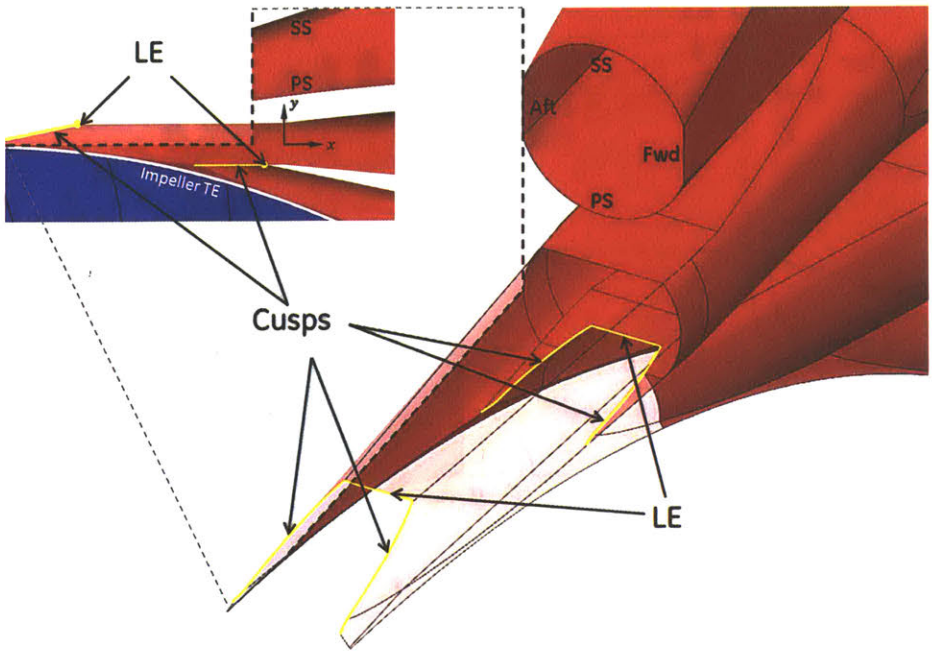


Figure 1.4: Front and 3D cutaway views of diffuser inlet geometry featuring leading edge cusps.

## 1.3 Previous Work

As mentioned, significant work has been performed at RWTH Aachen University to generate the experimental data leveraged in this research, most notably by Zachau et. al. and Kunte et. al. [1] [2] [3] [4]. Furthermore, a number of experimental observations were made in their research that inspired this research. Using high frequency pressure and Particle Image Velocimetry (PIV) measurements, the existence of a large pressure side flow separation in the passage of the baseline diffuser was hypothesized by Zachau et. al. [1] [2]. This was confirmed in additional PIV and stagnation pressure traverse measurements as well as CFD simulations conducted by Kunte et. al. [3]. It was for this reason that a truncated diffuser was tested by Kunte et. al. The truncated diffuser was shown to reduce the extent of this separation and increase the operable range of the compressor at high speed [4]. Additional experimentation and CFD simulations have also been performed on this compressor at RWTH Aachen University, investigating a wide range of diffusion system configurations and operating conditions not directly leveraged here. However, further work is necessary to fundamentally explain the causes of the measured performance characteristics, including how they vary with diffuser geometry and operating point.

Many other attempts have been made to characterize the performance of centrifugal compressors, and diffusers in particular. Experimentally derived diffuser performance maps, relating a diffuser's pressure rise capability to its most basic geometric parameters and operating conditions, were created in the 1960s by Cockrell and Markland [5], Reneau et. al. [6], and Sovran and Klomp [7]. In general, these demonstrated that for a given diffuser area ratio and inlet passage height, an optimal diffuser length exists which maximizes is pressure recovery potential. Attempting too much diffusion in a short length results in a large exit blockage and reduced pressure rise. Conversely, large stagnation pressure losses are incurred due to wall friction if the diffuser is too long. These studies also characterized the effect of inlet mass blockage, which is shown to reduce the pressure recovery potential of a diffuser.

The claim that diffuser throat nonuniformity has a large impact on pressure rise is also made by Cumpsty in his book, where he cites the work of many other authors with the same observation [8]. However, for radial diffusers, there seems to be a disconnect between the diffuser inlet mass blockage and the diffuser throat mass blockage. In the experimental work of Filipenco and Everitt, the spanwise velocity profiles at the inlet to radial pipe and vaned diffusers respectively were varied with little effect on the diffuser pressure rise capability, at least relative to other more important effects. Both hypothesize that the diffuser inlet nonuniformities are rapidly mixed out upstream of the throat, but also caution against the use of inlet mass blockage as a measure of nonuniformity as it lacks important information about the distribution of this nonuniformity [9] [10].

Cumpsty further claims that pipe diffusers can obtain greater pressure recoveries than vaned diffusers for a given level of inlet blockage, hypothesizing that the leading edge cusps play a role by inhibiting inlet secondary flows and thus reducing throat blockage [8]. Zachau et. al., Kunte et. al., and Wilkosz et. al. similarly propose that the leading edge cusps offer an advantage over vaned diffusers in this area, but with a different hypothesis. Their hypothesis is that the cusps actually generate vortices which enhance mixing, thus reducing the throat blockage or disconnecting it from the diffuser inlet blockage [2] [3] [11]. While the work of Kenny does suggest that pipe diffusers operate with lower throat blockage than vaned diffusers, and that greater pressure recoveries can be achieved in pipe diffusers even with the same throat blockage, clear evidence is not provided that link this observation to the leading edge cusps or secondary flows [12] [13]. Furthermore, Wilkosz et.

al. found that the secondary flows in the diffuser passage cause high loss endwall flow to accumulate between them, actually reducing the mixing effectiveness downstream of the throat within the diffuser passage and contributing to the pressure side passage separation identified by Zachau et. al. and Kunte et. al. [11]. What is consistent in each of these hypotheses is that flow nonuniformity is important to the performance of a diffuser, and that it can be affected by secondary flows via changes in mixing effectiveness.

Since the impeller and the diffuser tend to be closely coupled, another form of flow nonuniformity, unsteadiness, has also been a focus of prior research. In summarizing many of these studies, Cumpsty claims that unsteadiness generally has little effect on compressor performance. Again, this may partially be due to the rapid mixing that occurs in the diffuser inlet. However, Cumpsty also posits that this is due to the fact that nonuniformities in impeller exit relative stagnation pressure are translated to flow angle nonuniformities in the absolute reference frame, while the unsteady variations in absolute stagnation pressure at the diffuser inlet are small [8]. In this way, the close coupling of the impeller and diffuser may actually benefit impeller wake recovery. The work by Shum confirms that the unsteadiness plays a small role in the diffuser on a time-averaged basis. The largest role of unsteadiness, Shum claims, is that the pressure field imposed by the diffuser can interfere with the impeller tip clearance flow. This modifies the impeller pressure rise and reduces efficiency through an increase in loss, a reduction in blockage, and a reduction in slip [14]. Everitt investigated the effects of unsteadiness by comparing diffuser performance measurements from a full compressor (high unsteadiness) with those from a swirl rig (low unsteadiness). Everitt saw a little influence of unsteadiness in the middle of the operating range, but he observed impacts close to choke and stall, including a change in the stall line. He hypothesized this is due to unsteady excursions into higher or lower flow angle regimes than experienced in steady operation, which impact the diffuser loss in a nonlinear manner [10]. Wilkosz studied the effects of unsteadiness on the truncated diffuser configuration of interest here, confirming Shum's claim that the largest impact of unsteadiness is on the impeller tip clearance flows. The overall pressure recovery of the diffuser was negligibly affected by unsteadiness, although this was due to an increase in the inlet pressure rise canceling a reduction in the passage pressure rise [15].

Filipenco and Everitt concluded from their research that, while the effects of inlet nonuniformity and unsteadiness are small, the performance of a diffuser correlates strongly

with the inlet flow angle. Filipenco defined his correlation using the impeller exit momentum averaged flow angle, defined based on the mass averaged tangential and meridional velocity components, and a pressure recovery coefficient calculated from an availability average of impeller exit stagnation pressure. The two quantities were positively correlated for his pipe diffuser [9]. Everitt defined the correlation for his vaned diffuser using the mixed out average impeller exit flow angle and the diffuser effectiveness, defined as the ratio of actual and ideal pressure recovery coefficients. Everitt claimed that the effectiveness could correct for operating point variations in Mach number and 1D area ratio. He found the effectiveness to be insensitive to flow angle at high flow angles, but observed that it decreased below a threshold flow angle. He hypothesized that this was due to incidence-related losses [10].

## 1.4 Research Objectives

This research aims to characterize the performance of a centrifugal compressor stage utilizing a pipe diffuser, with a focus on the diffuser. Performance metrics of interest include the compressor's pressure rise capability and efficiency, both of which depend on the diffuser's pressure recovery coefficient, as well as the operable range of the compressor. Specifically, the following questions are addressed:

- What flow mechanisms drive the observed performance trends in the tested centrifugal compressor across a range of speeds and throttle levels? What are the implications for other compressor designs?
- What are the differences in influential flow mechanisms between the baseline and truncated diffuser configurations? Why is the stall line of the centrifugal compressor improved with the truncated diffuser? What are the implications for other compressor designs?
- What impact do diffuser leading edge cusps and secondary flows have on the influential flow mechanisms within the diffuser?
- How do the impacts of the various flow mechanisms scale with different compressor geometries and operating conditions?

The intention is to move beyond simply recognizing performance trends, but to describe and quantify the causal relationships between these trends and the fundamental perfor-

mance limiting flow mechanisms. In this way, the insights gained here may be applied to a wide range of diffuser geometries and operating conditions.

## 1.5 Key Research Findings

This research succeeds in addressing the questions posed. This is accomplished by leveraging the RWTH Aachen University experimental compressor measurements, CFD simulations, and low-order flow models. This includes utilization of the following strategies, which are unique to this research:

- A framework is established for evaluating the diffusion system in terms of interactions between subcomponents: the diffuser inlet, diffuser passage, and deswirler.
- A 2D integral boundary layer growth model is modified to include 3D secondary flows effects as source terms.

Using these approaches, this research yields a number of significant findings. Performance variations between operating points are found to be primarily driven by changes in the impeller exit flow angle and secondarily by changes in impeller exit Mach number. The diffuser incidence angle greatly impacts the formation of secondary flows within the diffuser passage, which are found to have a detrimental effect on the diffuser pressure rise capability. The origin and performance impact of these secondary flows are summarized as follows:

- Secondary flows are made up of a superposition of two types of counter-rotating vortex pairs. "Background vortices" originate in the impeller exit nonuniformity and flow transition from impeller exit to diffuser inlet, while "incidence vortices" result from boundary layer separation off the diffuser leading edge cusps.
- Through accumulation of weak flow on the diffuser wall near the plane of symmetry between the vortices, secondary flows reduce mixing effectiveness in the diffuser passage and contribute to the passage separation extent and location (pressure side near choke, suction side near stall).
- The impact of the secondary flows on boundary layer growth is found to scale inversely with the diffuser aspect ratio.

The baseline and truncated diffuser pressure recovery and loss magnitudes and trends are comparable, though the responsible flow mechanisms differ. This is explained by the following:

- The two diffuser configurations have similar effective area ratios, with the baseline diffuser having a larger exit blockage but lower exit flow angle than the truncated diffuser.
- The truncated diffuser experiences greater loss due to the thicker trailing edge, while the baseline diffuser experiences greater inefficiency due to wall friction and nonuniformity amplification.

The truncated diffuser improves the compressor's high-speed stall line relative to the baseline diffuser. Based on insights gained from the experimental and CFD results, the following hypothesis is developed to explain this observation:

- With the baseline diffuser, the compressor stalls when the diffuser separation switches from the pressure side (stabilizing) to the suction side (destabilizing).
- With the truncated diffuser, the compressor stalls due to a gradual reduction in diffuser stability as suction side loss worsens. Instability is not immediately initiated when separation side switches for the truncated diffuser, since the separation extent is reduced relative to the baseline diffuser. Consequently, compressor stability is also dependent on the impeller pressure rise characteristics.

The fact that secondary flows have a large influence on diffuser pressure rise capability and compressor stability is counter to conventional preliminary diffuser design approaches which neglect such 3D effects. The findings of this research may therefore be considered during preliminary design optimization to produce better-performing diffuser designs.

## 1.6 Organization of Thesis

The process through which the research results and findings are determined from the experimental data and supporting CFD computations are presented as follows. The research approach will be described in Chapter 2, describing the use of experimental measurements, CFD simulations, and reduced-order modeling. A modular perspective is taken to evaluate the compressor and diffusion system, so the remainder of this thesis is organized as such which specific performance-limiting flow mechanisms discussed in the context of each module. The overall compressor performance characteristics are first presented in Chapter 3, and the utility of the CFD results are evaluated. Next, the impeller performance and exit conditions are shown in Chapter 4, and the mechanism contributing to the slope of the impeller pressure rise characteristic is identified. After that, a discussion of diffuser flow fun-

damentals is presented in Chapter 5, and the overall diffusion system performance assessment is given in Chapter 6. Chapter 6 is further broken into a specific analysis of the performance and flow mechanisms in the diffuser inlet (Section 6.5) and the diffuser passage (Section 6.6). Finally, the findings regarding the various flow mechanisms within each component are synthesized in Chapter 7 in a discussion about the overall compressor stability. A summary that highlights the key results of this thesis is provided in Chapter 8. Finally the conclusions are delineated in Chapter 9.

# Chapter 2 Research Approach

To address the research questions posed, experimental data acquired on a research compressor stage is interrogated along with a set of well-designed CFD computations, complemented by reduced order flow modeling. The experimental data is primarily used to determine high-level 1D performance results and trends and to assess where CFD may be used as a tool for detailed investigation. Where CFD and data are determined to follow the same trends, CFD is used to further understand the details of the flow mechanisms present at the 3D level. Additionally, measurements made from CFD results are used to guide another level of data reduction, allowing for a more useful interpretation of the data. Lastly, low-order models are developed and utilized to quantify the importance of specific flow mechanisms observed in the CFD without confounding effects from other mechanisms, and to gain insight into the process by which these mechanisms influence performance.

## 2.1 Compressor Station Designations and Coordinate Systems

Compressor station designations are chosen to be consistent with the industry practice for naming stations in an axial-centrifugal HPC. In this naming convention, the axial compressor is assigned stations 20-25, and the centrifugal compressor is assigned stations 26-31. These numbered stations are surfaces of revolution, which can be defined as lines in the meridional plane. An additional station, T, is defined at the diffuser throat, oriented perpendicular to the diffuser passage. Figure 2.1 shows the locations of the centrifugal compressor test rig stations in more detail. Note that throughout this research, station 29 refers to the radial plane near the trailing edge of the baseline diffuser, such that trailing edge of the truncated diffuser is not at station 29.

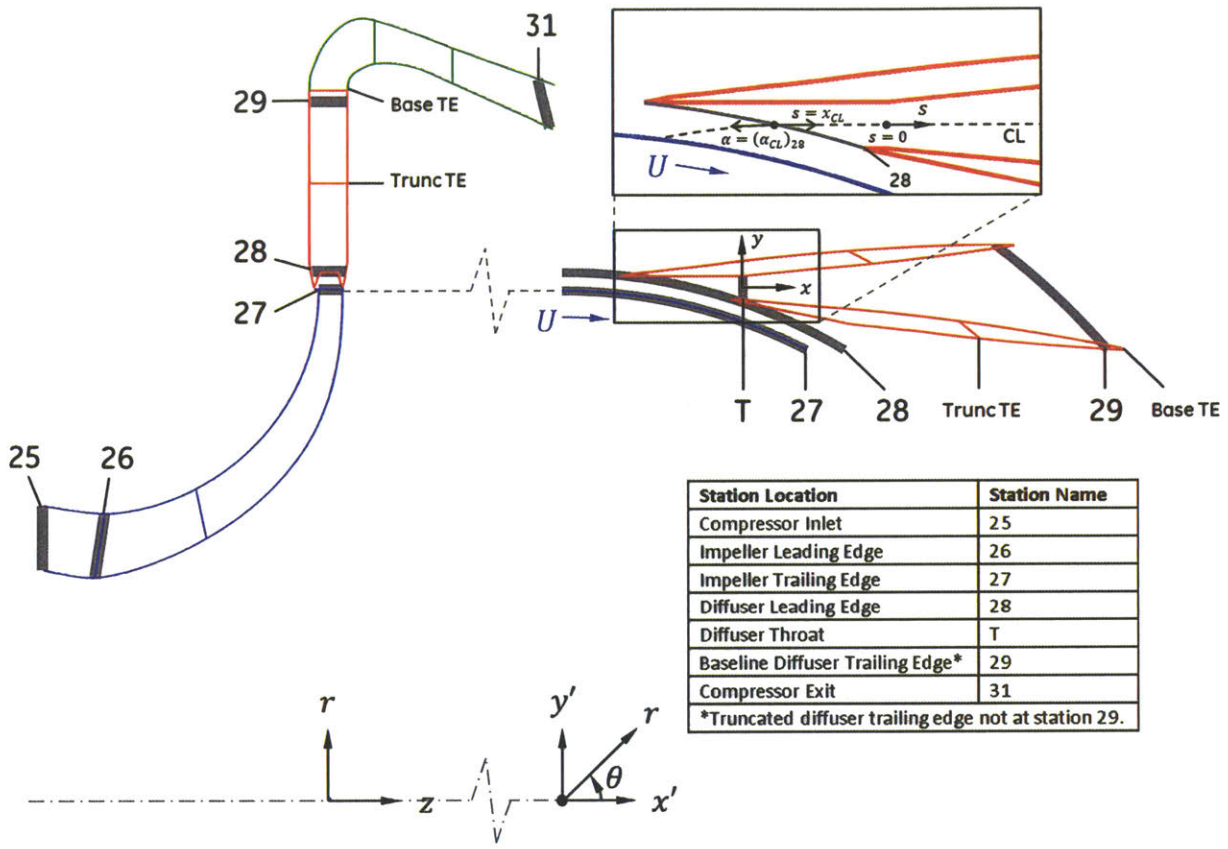


| Station Location | Station Name |
|---|---|
| Compressor Inlet | 25 |
| Impeller Leading Edge | 26 |
| Impeller Trailing Edge | 27 |
| Diffuser Leading Edge | 28 |
| Diffuser Throat | T |
| Baseline Diffuser Trailing Edge* | 29 |
| Compressor Exit | 31 |
| *Truncated diffuser trailing edge not at station 29. | |

Figure 2.1: Centrifugal compressor station designations and coordinate systems.

While all the stations are conceptually located at convenient geometric features in the compressor, only stations 26 and 27 are truly defined by geometric features—the leading and trailing edges of the impeller respectively. Stations 25, 28, 29, 31, and T on the other hand are more accurately defined in this research by the locations of instrumentation in the test rig. Additional stations 27m and Tm are defined at other measurement locations that are near stations 27 and T. Section 2.4.2 describes the instrumentation and their locations in detail.

The present research makes use of several coordinate systems shown in Figure 2.1. First, a global compressor polar coordinate system ($z$, $r$, $\theta$) is aligned with the compressor rotation axis, such that $z = 0$ corresponds to the diffuser mid-plane. This is used to define axial, radial, and circumferential positions throughout the compressor as well as compressor speed. Global compressor Cartesian coordinates ($x'$, $y'$, $z$) are defined using the same origin. In order to more effectively present local diffuser performance results, the local Cartesian coordinate system ($x$, $y$, $z$) is defined relative to each diffuser passage, such that (0, 0,

0) corresponds to the diffuser centerline at the throat station. To present some 1D diffuser performance results, a streamwise position, $s$, is also defined along a hypothetical streamline following the $x$ axis downstream of the diffuser leading edge plane, and following a logarithmic spiral of constant flow angle upstream of the diffuser leading edge. This is given by Equation 2.1. The diffuser throat centerline defines $s = 0$. The engine axial position, $z$, is defined the same way in all of these coordinate systems.

$$s = \begin{cases} \dfrac{(r - r_{28})}{\cos[(\alpha_{CL})_{28}]} + (x_{CL})_{28}, & r \leq r_{28} \\ x_{CL}, & r > r_{28} \end{cases} \qquad \text{Equation 2.1}$$

Note that in the experimental test rig, these coordinate systems are all left-handed. In CFD simulations, the compressor geometry is mirrored such that these become right-handed coordinate systems. For convenience, the same coordinate system is used for both.

## 2.2 1D Flow Analysis

It is sometimes useful to express compressor flow parameters or performance results on a 1D basis. This means a single value for each flow property is assigned at a given station or meridional location even though flow properties may vary widely over space and time. The determination of 1D metrics for flow properties and the associated assumptions are described in the following.

### 2.2.1 Defining a 1D Flow Description

Performing a 1D internal flow analysis is a three step process. First, certain flow properties are measured or estimated. In a test, these measurements occur at discrete points in space, whereas CFD results can be sampled anywhere in space. Second, flow properties which vary over space must be appropriately averaged to a single useful value. Finally, these 1D averaged flow properties can be used to calculate remaining unknown 1D flow properties. This results in a complete set of self-consistent 1D flow properties. All measured quantities referenced here are steady or time-averaged.

This research makes simplifying assumptions that the air is an ideal gas with constant specific heat ratio of 1.4. In reality, the specific heat ratio drops slightly across the compressor due to the temperature rise. However, assuming a constant specific heat allows the 1D flow analysis to be simplified. The effects of the constant specific heat assumption on

data interpretation and CFD results are discussed in Sections 2.4.3.3 and 2.5.1.2 respectively.

With these assumptions, a complete set of the flow properties can be determined from only five known or measured properties. These can include two fluid state variables (e.g. pressure, density, temperature, specific enthalpy, specific entropy, speed of sound, etc.) and three variables that determine the movement of the flow (e.g. stagnation fluid properties, velocity magnitude, velocity components, Mach number, flow angles, mass flow per unit area, momentum flow components per unit area, etc.). While there exists only one possible set of flow properties at a single point and time, due to spatial and temporal nonuniformities it is possible to develop multiple complete self-consistent sets of 1D averaged flow properties. This depends on which flow properties are measured or estimated to begin with, and what averaging schemes are used to convert the measurements to 1D values.

Appropriate averaging of 1D flow properties is explained by Cumpsty and Horlock [16]. Information is lost when spatially and temporally distributed information is reduced to a single value, but an appropriate average preserves the specific information deemed important for the average's use. For example, one might be interested in preserving the entropy flow per unit area of the nonuniform flow for loss evaluation, or preserving the enthalpy flow per unit area for energy conservation. It can sometimes be useful to think of a 1D averaging process as a control volume analysis, where the averaging plane is like a control volume of infinitesimal length. Nonuniform flow properties enter a control volume through the averaging plane, the flow in the control volume undergoes some process, and the flow leaves the control volume with uniform properties which preserve important information about the nonuniform inflow.

Each set of 1D flow properties may be useful for some purposes, and less useful or inaccurate for others. For this reason, it is important to understand the assumptions and limitations behind a set of 1D flow properties, and it is common to use multiple self-consistent sets of 1D flow properties for evaluating different aspects of a flow. Different sets of 1D flow properties may be related to each other using closure parameters. For example, mass blockage is a closure parameter commonly used in 1D internal flow analyses to relate the actual measured mass flow per unit area to some other calculated 1D average mass flow per unit area. Blockage definitions vary widely in the literature because different sets of 1D flow properties are chosen to calculate the mass flow per unit area.

### 2.2.2 1D Flow Property Sets

The present work makes use of four different complete sets of 1D flow properties for different purposes. They are referred to here as the availability average, the potential core average, the dump average, and the mixed out average at constant area. These sets are summarized in Table 2.1.

| Set Name | Base Flow Properties | Applications |
|---|---|---|
| Availability Average (A) | $T_t$: mass averaged<br>$s$: mass averaged<br>$p$: area averaged<br>$\alpha$: momentum averaged<br>$\phi$: momentum averaged or estimated from flowpath geometry | For evaluating performance results (pressure rise and loss). |
| Potential Core Average (P) | $T_t$: mass averaged<br>$p_t$: max value<br>$p$: area averaged<br>$\alpha$: momentum averaged<br>$\phi$: momentum averaged or estimated from flowpath geometry | For determining 1D average boundary layer parameters. |
| Dump Average (D) | $T_t$: mass averaged<br>$p$: area averaged<br>$\lvert\vec{V}\rvert = 0$ | For evaluating flow properties after a hypothetical sudden expansion or dump process. |
| Mixed Out Average at Constant Area (M) | $T_t$: mass averaged<br>$\dot{m}/A$<br>$\dot{P}_n/A + p$: area averaged<br>For meridional cut planes:<br>$\dot{H}/(r_p A)$<br>$\dot{P}_t/A$<br>For planar cut planes:<br>$\dot{P}_{t1}/A$<br>$\dot{P}_{t2}/A$ | • For comparing to other averaging schemes to judge importance of non-uniformity/mixing, and to calculate blockages.<br>• For applying Euler Turbine Equation. |

Table 2.1: Sets of 1D flow properties utilized in this thesis.

The availability averaged set of 1D flow properties is meant to represent a flow that could theoretically be achieved if the actual flow was brought to a uniform state via a reversible process with no external work or heat transfer. In other words, it maintains the stagnation enthalpy and entropy flow per unit area of the true flow via mass averaging of the stagnation temperature and specific entropy as shown in Equation 2.2 and Equation 2.3. This makes the availability average useful for loss evaluation. Together, the 1D aver-

aged stagnation temperature and entropy can be used to calculate a stagnation pressure, given by Equation 2.4 [16] [9].

$$T_t{}^A = \frac{\int T_t d\dot{m}}{\dot{m}} \qquad \text{Equation 2.2}$$

$$s^A = \frac{\int s d\dot{m}}{\dot{m}} \qquad \text{Equation 2.3}$$

$$p_t{}^A = p_{ref}\left(\frac{T_t{}^A}{T_{ref}}\right)^{\frac{\gamma}{\gamma-1}} exp\left[\frac{-(s^A - s_{ref})}{R}\right] \qquad \text{Equation 2.4}$$

In the literature, the term "availability average" is typically only used to describe this derived stagnation pressure quantity, but in this thesis the term will be used to refer to a complete set of derived and base 1D flow properties, which also includes an average static pressure and flow angle. The static pressure does not vary as much as stagnation pressure over the surface of a cut plane, so the average is not as sensitive to the choice of averaging scheme. However, the area averaged static pressure, given by Equation 2.5, is commonly used to average static pressure as it preserves the pressure force, $F = \int p dA$, acting over the averaging plane [16]. The 1D flow angle comes from a momentum average, introduced by Filipenco and given by Equation 2.6 [9]. It is calculated from the mass averaged tangential and meridional velocity components. In other words, for a purely radial-tangential flow as in the diffuser, the averaged flow preserves the momentum flow unit vector of the true flow. Filipenco found that this 1D averaged impeller exit flow angle correlates well with important diffuser performance criteria.

$$p^A = \frac{\int p dA}{A} \qquad \text{Equation 2.5}$$

$$\alpha^A = \tan^{-1}\left(\frac{\int V_\theta d\dot{m}}{\int V_m d\dot{m}}\right) \qquad \text{Equation 2.6}$$

The second set of 1D flow properties is referred to as the potential core average. This is meant to represent the uniform flow that could exist in place of the nonuniform flow if shear forces did not weaken the flow near the wall. The properties of this potential core can then be compared to the nonuniform flow for determining mass and momentum blockage parameters that are analogous to displacement and momentum thickness integral boundary layer parameters. Like the availability average, the potential core average also utilizes the mass averaged stagnation temperature, area averaged static pressure, and momentum averaged flow angle. However, instead of preserving the entropy flow per unit area of the

true flow, it preserves the peak stagnation pressure of the true flow at the averaging plane, given by Equation 2.7. This results in lower entropy flow per unit area than the true flow.

$$p_t{}^P = \max_A(p_t) \qquad \text{Equation 2.7}$$

The third set of 1D flow properties is named the dump average. This is meant to capture the hypothetical fluid state that would result if the flow were dumped into a plenum, undergoing a sudden expansion and mixing with the stagnant plenum flow. In this process, the fluid loses its velocity and dynamic pressure by incurring losses through mixing, but energy is conserved. Stagnation and static flow properties become equivalent, with temperature being equal to the initial mass average stagnation temperature (Equation 2.8), and pressure being equal to the initial area average static pressure (Equation 2.9). The dump average is especially useful to consider at the deswirler exit since it is followed by the combustor plenum, the Mach number is low, and the static pressure is more uniform and thus easier to measure than the stagnation pressure.

$$T_t{}^D = T^D = \frac{\int T_t d\dot{m}}{\dot{m}} \qquad \text{Equation 2.8}$$

$$p_t{}^D = p^D = \frac{\int p dA}{A} \qquad \text{Equation 2.9}$$

The final set of 1D flow properties used is the constant area mixed out average. As the name suggests, this 1D averaging scheme simulates an instantaneous mixing process, where the flow is brought to a uniform state at constant area via mass, momentum, and energy conservation [16] [10] [17]. Like the availability and potential core averages, this means the mass averaged stagnation temperature is utilized, but the mass and momentum conservation equations given by Equation 2.10, Equation 2.11, Equation 2.12, and Equation 2.13 are also used.

$$(\rho V_n)^M = \frac{\dot{m}}{A} \qquad \text{Equation 2.10}$$

$$\left(\rho V_n{}^2 + p\right)^M = \frac{\dot{P}_n + \int p dA}{A} \qquad \text{Equation 2.11}$$

$$(\rho V_n V_t)^M = \frac{\dot{P}_t}{A} \qquad \text{Equation 2.12}$$

$$(\rho V_n V_\theta)^M = \frac{\dot{H}}{r_p A} \qquad \text{Equation 2.13}$$

Notice that momentum conservation is applied to all three components of momentum. For the component that is normal to the cut plane, a static pressure term is included to ac-

count for the force imparted by the difference in area averaged and mixed out average static pressures (Equation 2.11). During a constant area mixing process, static pressure increases so there must be a decrease in the normal component of momentum flow. For planar averaging planes, such as the diffuser throat station, the other two momentum components are parallel to the averaging plane (Equation 2.12). Conversely, for meridional averaging planes, such as the impeller exit station, only one momentum component parallel to the averaging plane is used (Equation 2.12) along with the angular momentum about the engine axis (Equation 2.13). There is no difference between these two momentum averaging procedures for the constant radius meridional averaging planes used throughout the diffuser. However, for conical meridional averaging planes such as at the impeller inlet, the 1D mixed out average does not represent a physical mixing process, since a swirling flow can only exist with a static pressure gradient in the radial direction. To get around this, a single 1D value of radius must be used, and the pitchline radius is chosen. The redistribution of hub and tip flow in the actual 3D compressor to the pitchline radius in the 1D average requires that angular momentum conservation be distinguished from linear momentum conservation.

The constant area mixed out average has several applications in the present work. First, it can be compared with the results of the other averaging schemes to get a sense of the level of nonuniformity present in the flow. Because the mixed out average utilizes the actual mass and momentum flows per unit area, one can think of blockage as a closure parameter that quantifies non-uniformity by relating the availability or potential core average mass and momentum flows per unit area to those of the mixed out average. Also, because flow nonuniformity can be viewed as static pressure rise and loss which has not yet been incurred, using a mixed out result book-keeps nonuniformity as pressure rise and loss at the station where the nonuniformity is present. Note that one has to be careful about this interpretation, since the mixed out loss represents a constant area process and diffusers are certainly not constant area (non-uniformity in a diffusing process results in greater loss and lower pressure rise than a constant area process). The last benefit of the mixed out average is that the Euler Turbine Equation, relating the impeller work input to the change in angular momentum of the flow, can be appropriately applied to 1D mixed out flow properties to estimate impeller exit conditions not measured during testing. This is because the mixed

out average conserves both energy and angular momentum of the true flow. This process will be discussed more in Section 2.4.3.3.

Everitt proposed that the mixed out average was a better choice of averaging schemes for interpreting diffuser performance results than the availability average used by Filipenco [10], finding that the mixed out average diffuser inlet flow angle could be used to fully characterize the mixed out average effectiveness of his diffusers [10]. However, while both availability and mixed out averaged 1D flow properties are useful, more weight is placed on the availability average here for reasons discussed in Appendix A. Throughout this report, availability average 1D flow properties are used for most calculations and figures, except where a different averaging scheme is specifically noted either in the text or through a modification to the station name (e.g. station 31D refers to the deswirler exit dump average flow properties).

### 2.2.3 1D Closure Parameters

Closure parameters are used to compare 1D flow parameters from one set of properties to another set. One such closure parameter is mass flow blockage, given generally in Equation 2.14. Mass blockage, relating the flow's true mass flow per unit area to a 1D calculated value, can be used to quantify the level of non-uniformity of the true flow. It can be interpreted as the fraction by which nonuniformity reduces the mass flow at constant area, or it can be interpreted as the fraction of passage area that would have to be blocked for a uniform flow to pass the same mass flow as the nonuniform flow. Two mass blockage parameters utilizing different definitions of the theoretical uniform flow are used here: one that utilizes the mass flow per unit area calculated from the availability average (Equation 2.15), and the other one calculated from the potential core average (Equation 2.16). The magnitudes of these two different blockage terms can differ substantially. Because the availability average effectively utilizes an average mass flow per unit area, its blockage is insensitive to the exact distribution of the mass flux. Conversely, the potential core average effectively utilizes the peak mass flux of the true flow, which can vary widely between operating points even if the average does not. The usefulness of the potential core average blockage is that it is analogous to the 2D integral boundary layer parameter, displacement thickness, given by Equation 2.17.

$$B_m = 1 - \frac{\dot{m}/A}{(\rho V_n)^{1D}} = \int \left[1 - \frac{\rho V_n}{(\rho V_n)^{1D}}\right] \frac{dA}{A} \quad \text{Equation 2.14}$$

$$B_m{}^A = 1 - \frac{\dot{m}/A}{(\rho V_n)^A} \quad \text{Equation 2.15}$$

$$B_m{}^P = 1 - \frac{\dot{m}/A}{(\rho V_n)^P} \quad \text{Equation 2.16}$$

$$\frac{\delta_x^*}{h} = \int \left[1 - \frac{\rho u}{(\rho u)_e}\right] \frac{dy}{h} \quad \text{Equation 2.17}$$

Another closure parameter that can be used as a measure of flow non-uniformity is the momentum blockage, given generally by Equation 2.18, relating the flow's true momentum flow per unit area to a 1D calculated value. At constant area it can be interpreted as the fraction by which nonuniformity reduces the momentum flow beyond the reduction attributed to lower mass flow, or at constant momentum flow it can be interpreted as the fraction of passage area that would have to be blocked above and beyond the constant mass flow area blockage. The momentum blockage is only calculated for the potential core average 1D properties given by Equation 2.19, making it analogous to the 2D integral boundary layer parameter, momentum thickness, given by Equation 2.20. This enables the calculation of another closure parameter, a 1D average shape factor given by Equation 2.21.

$$B_P = 1 - \frac{\left|\vec{P}/A\right|}{\left|\rho V_n \vec{V}\right|^{1D}} - B_m = 1 - \left| \int \frac{\rho V_n \vec{V}}{\left(\rho V_n \left|\vec{V}\right|\right)^{1D}} \frac{dA}{A} \right| - B_m \quad \text{Equation 2.18}$$

$$B_P{}^P = 1 - \frac{\left|\vec{P}/A\right|}{\left|\rho V_n \vec{V}\right|^P} - B_m{}^P \quad \text{Equation 2.19}$$

$$\frac{\theta_x}{h} = \int \left(1 - \frac{u}{u_e}\right) \left[\frac{\rho u}{(\rho u)_e}\right] \frac{dy}{h} = 1 - \int \left(1 - \frac{\rho u^2}{(\rho u^2)_e}\right) \frac{dy}{h} - \frac{\delta_x^*}{h} \quad \text{Equation 2.20}$$

$$H^P = \frac{B_m{}^P}{B_P{}^P} \quad \text{Equation 2.21}$$

The momentum blockage calculation is similar to one proposed by Filipenco and used by Everitt [9] [10]. However, two major differences make this calculation analogous to the momentum thickness 2D integral boundary layer parameter where Filipenco's proposal is not. First, as described above, the momentum blockage parameter is corrected for the impact that mass flow blockage has on momentum reduction. This is illustrated by rearranging the equation for momentum thickness, shown in Equation 2.20. Second, careful consideration is taken to use the magnitude of the overall momentum flow vector, $\left|\int \rho V_n \vec{V} dA\right|$, in-

stead of simply using the magnitude of the velocity to calculate momentum flow, $\int \rho V_n |\vec{V}| dA$. The importance of this is illustrated by considering that ${V_n}^2$ is always greater than zero, while $V_n|\vec{V}|$ can be less than zero. In addition, the proposed formulation always penalizes secondary flows as a source of momentum blockage or nonuniformity, which is not true if high velocity is always considered to contribute positively to momentum flow without considering velocity direction.

The final closure parameter used here is an angular momentum blockage, calculated generally by Equation 2.22. Its meaning is the same as the momentum blockage, except the angular momentum about the engine axis is the only momentum component considered. The angular momentum blockage is calculated for the availability average 1D properties, given in Equation 2.23, and used for estimating availability average impeller exit properties by utilizing the Euler Turbine Equation across the impeller. This procedure is discussed in more detail in Section 2.4.3.3.

$$B_H = 1 - \frac{\dot{H}/A}{\left(\rho V_n r_p V_\theta\right)^{1D}} - B_m = \int \left(1 - \frac{r V_\theta}{\left(r_p V_\theta\right)^{1D}}\right)\left[\frac{\rho V_n}{(\rho V_n)^{1D}}\right]\frac{dA}{A} \qquad \text{Equation 2.22}$$

$${B_H}^A = 1 - \frac{\dot{H}/A}{\left(\rho V_n r_p V_\theta\right)^A} - {B_m}^A \qquad \text{Equation 2.23}$$

It is important to define and distinguish total blockage, flow or aerodynamic blockage, and solid blockage. If an averaging plane cuts through a solid body, such as the diffuser passage wall, the region consumed by the solid body may or may not be included in the area integral calculations. The ratio of the solid body area to the entire averaging plane area is called the solid blockage. Aerodynamic blockage on the other hand is purely an attribute of the flow and is used as a measure of nonuniformity, so the solid body area is not included in the area integral calculations. However, it is sometimes useful to determine a total blockage given by Equation 2.24 (Equation 2.25 for small blockages), including both sources of blockage as an estimate of what the aerodynamic blockage would be if the body was suddenly removed. This is useful for evaluating blockage near the trailing edge of an airfoil, where the flow will experience the body ending suddenly. It is also useful to use total blockage when making back-to-back comparisons of the baseline and truncated diffuser near the trailing edge, since the averaging plane intersects a solid body for the baseline diffuser but not for the truncated diffuser.

$$B_{Total} = 1 - (1 - B_{Aero})(1 - B_{Solid})$$ Equation 2.24

$$B_{Total} \approx B_{Aero} + B_{Solid}$$ Equation 2.25

Throughout this report, all blockages are most often calculated from availability average 1D flow properties except where noted, while the 1D shape factor is calculated from the potential core average 1D flow properties. In addition, both aero and total blockages are utilized as noted.

## 2.3 Performance Assessment Criteria

There are three primary compressor performance criteria of interest: the pressure rise, the efficiency or loss, and the operable range. For the overall compressor, the first two of these performance metrics are captured using the pressure ratio, temperature ratio, and polytropic efficiency. These are conventionally characterized as functions of the inlet corrected flow and corrected speed. All of these quantities are defined according to Equation 2.26, Equation 2.27, Equation 2.28, Equation 2.29, and Equation 2.30 respectively, assuming a constant specific heat ratio for the efficiency calculation. The pressure ratio, temperature ratio, and polytropic efficiency can also be defined for the impeller alone by replacing station 31 properties with station 27 properties.

$$\pi_{(25-31)} = \frac{p_{t31}}{p_{t25}}$$ Equation 2.26

$$\tau_{(25-31)} = \frac{T_{t31}}{T_{t25}}$$ Equation 2.27

$$\eta_{p(25-31)} = \left(\frac{\gamma - 1}{\gamma}\right)\frac{\ln\left(\pi_{(25-31)}\right)}{\ln\left(\tau_{(25-31)}\right)}$$ Equation 2.28

$$\dot{m}_{c25} = \frac{\dot{m}_{25}\sqrt{T_{t25}/T_{ref}}}{p_{t25}/p_{ref}}$$ Equation 2.29

$$N_{c25} = \frac{N}{\sqrt{T_{t25}/T_{ref}}}$$ Equation 2.30

In evaluating the compressor and impeller performance over a range of corrected speeds, it can be useful to correct the performance trends for these speed differences. This is done by leveraging the flow coefficient, work coefficient, and pressure rise coefficient in place of the corrected flow, temperature ratio, and pressure ratio. These quantities are defined for the overall compressor according to Equation 2.31, Equation 2.32, and Equation

2.33 respectively, and they can be evaluated for the impeller alone by replacing station 31 properties with station 27 properties. Again, the assumption of constant specific heat is made for the work coefficient calculation.

$$\phi_{27} = \frac{V_{m27}}{U_{27}} \qquad \text{Equation 2.31}$$

$$\Psi_{(25-31)} = \frac{c_p(T_{t31} - T_{t25})}{U_{27}^2} \qquad \text{Equation 2.32}$$

$$\Psi'_{(25-31)} = \frac{p_{t31} - p_{t25}}{\rho_{t25} U_{27}^2} \qquad \text{Equation 2.33}$$

The impeller exit flow coefficient is primarily used rather than the inlet flow coefficient. This is because the impeller exit wheel speed, U27, is more influential than the inlet wheel speed, U25, in determining the work input of the impeller. In fact, employing the 1D Euler Turbine Equation on an impeller with U27<<U25 yields the insightful relation given by Equation 2.34, indicating that a backswept impeller should exhibit a negative relationship between the flow and work coefficients which is independent of speed. Another insightful relationship is that which exists for small pressure rise compressors between the pressure rise coefficient, work coefficient, and polytropic efficiency. This is given by Equation 2.35.

$$\Psi_{(25-31)} \approx 1 - \phi_{27} \tan \beta_{27} \qquad \text{Equation 2.34}$$

$$\Psi'_{(25-31)} \approx \eta_{p(25-31)} \Psi_{(25-31)} \qquad \text{Equation 2.35}$$

The diffusion system can be thought of simply as a device which converts a large dynamic pressure into static pressure rise while minimizing the stagnation pressure loss. With this in mind, the diffusion system's pressure recovery coefficient and stagnation pressure loss coefficient, defined by Equation 2.36 and Equation 2.37 respectively, are conventionally used to characterize its performance. If the dynamic pressure is entirely converted to static pressure, the pressure recovery coefficient will be equal to 1 and the stagnation pressure loss coefficient will be equal to zero. The converse is true if the diffuser converts all of its dynamic pressure to loss, as is the case in a dump process. These quantities can also be calculated for a sub-portion of the diffusion system by replacing the impeller and diffuser exit properties with other appropriate inlet and exit flow properties. This research will focus on characterizing these performance quantities in terms of other flow properties including flow angles, Mach numbers, blockages, secondary flows, etc.

$$C_{p(27-31)} = \frac{p_{31} - p_{27}}{p_{t27} - p_{27}} \qquad \text{Equation 2.36}$$

$$\bar{\omega}_{(27-31)} = \frac{p_{t27} - p_{t31}}{p_{t27} - p_{27}}$$ Equation 2.37

The diffuser effectiveness, defined as the ratio of actual to ideal uniform pressure recovery coefficients, is also commonly used as a measure of diffusion system efficiency. Relative to the pressure recovery coefficient, the effectiveness metric reduces the penalty attributed to the dynamic pressure that remains at the diffuser exit, thus allowing diffusers of different 1D area ratios to be compared on a more equal basis. However, for the diffusers of interest, which have large 1D area ratios, the ideal pressure recovery coefficient approaches unity. As a result, the diffuser effectiveness is not quantified.

To gain insight into where and how the inefficiencies arise within the diffusion system, specifically in post-processing CFD solutions, the entropy generation rate is also utilized. Wilkosz provides a good description and derivation for this quantity [18]. Entropy can be generated as a result of heat transfer between streamlines of differing static temperature, or viscous shear between streamlines of differing velocity. For the applications of interest in this research, the heat transfer portion of the entropy generation rate is found to be negligible in comparison to the viscous portion. Therefore, only the viscous portion is calculated. This is defined according to Equation 2.38 on a per-unit-volume basis, where $\mu_L$ and $\mu_T$ are the laminar and turbulent dynamic viscosities respectively. Integrating this quantity over a control volume yields the total entropy generation rate within that control volume. As such, when assessing the CFD calculated spatial distribution of this quantity within some fluid domain, it is easy to see where loss is incurred.

$$\rho\frac{Ds}{Dt} = \left(\frac{\mu_L + \mu_T}{T}\right)\left[2\left(\frac{\partial V_x}{\partial x}\right)^2 + 2\left(\frac{\partial V_y}{\partial y}\right)^2 + 2\left(\frac{\partial V_z}{\partial z}\right)^2 + \left(\frac{\partial V_x}{\partial y} + \frac{\partial V_y}{\partial x}\right)^2 + \left(\frac{\partial V_x}{\partial z} + \frac{\partial V_z}{\partial x}\right)^2 + \left(\frac{\partial V_y}{\partial z} + \frac{\partial V_z}{\partial y}\right)^2 - \frac{2}{3}\left(\frac{\partial V_x}{\partial x} + \frac{\partial V_y}{\partial y} + \frac{\partial V_z}{\partial z}\right)^2\right]$$ Equation 2.38

All flow and performance quantities presented in this thesis are normalized by reference quantities. Most quantities are normalized by the experimentally measured value on the baseline diffuser configuration at 100% $N_{c25}$ near peak efficiency (100E operating point defined in Section 2.4.2). Because many measurements are performed at 100E, the average values are used as the reference values. These reference quantities are denoted by an asterisk (*) superscript. For some flow properties or performance metrics, the 100E baseline diffuser experimental quantity is not known. In these cases, the 100E baseline diffuser

CFD calculated quantity is utilized as the normalization quantity. All length quantities are normalized by a reference length, $L^*$, which is the diffuser throat hydraulic diameter defined as the throat area divided by one quarter of its perimeter.

Some quantities are presented using normalizations that depend on the operating point. The entropy generation rate is normalized according to Equation 2.39, where $\mathcal{V}^*$ is the volume of the baseline diffuser CFD domain. This normalization is chosen because, when integrated over some fraction of the diffuser volume $\mathcal{V}/\mathcal{V}^*$, it represents the lost specific work potential of the flow within that volume if the process were incorporated into a Carnot cycle with temperature sink $T_{t25}$. This is further normalized by an estimate for the specific work of the impeller, $U_{27}^2$.

$$\frac{\rho(Ds/Dt)}{[\rho(Ds/Dt)]_{ref}} = \rho\frac{Ds}{Dt}\left(\frac{T_{t25}\mathcal{V}^*}{\dot{m}_{25}U_{27}^2}\right) \qquad \text{Equation 2.39}$$

A number of quantities are also used to measure the strength and impact of secondary flows. All velocity gradients, including vorticity (defined as the curl of the velocity), are normalized according to Equation 2.40 and Equation 2.41 respectively using the same reference quantity. This reference quantity represents the hypothetical uniform velocity gradient associated with accelerating a flow from zero velocity to the throat velocity over a length of $L^*/2$. The reference circulation is then derived by integrating the reference vorticity over half of the diffuser throat area. Thus, the normalization for circulation quantities is given by Equation 2.42.

$$\frac{\partial w/\partial z}{(\partial w/\partial z)_{ref}} = \frac{\partial w/\partial z}{2\,V_T/L^*} \qquad \text{Equation 2.40}$$

$$\frac{\vec{\omega}}{\vec{\omega}_{ref}} = \frac{\vec{\omega}}{2\,V_T/L^*} \qquad \text{Equation 2.41}$$

$$\frac{\Gamma}{\Gamma_{ref}} = \frac{\Gamma}{V_T A_T/L^*} \qquad \text{Equation 2.42}$$

Flow range is one measure of compressor operability, defined as the difference in corrected mass flow of the compressor between stall and choke at constant speed. Increases in the stalling pressure ratio at constant mass flow and speed also signifies improved operability. These quantities are worth maximizing, as they allow a compressor to operate over a wider range of conditions without the use of variable geometry or bleed, which add complexity and weight and reduce cycle efficiency in the case of bleed. Operability parameters are not explicitly quantified in this work. However, differences in stall line between the base-

line and truncated diffusers can be seen qualitatively in various figures showing pressure ratio (or pressure rise coefficient) with respect to flow (or flow coefficient).

Most often throughout this thesis, the quantities presented here are calculated using availability averaged flow properties. However, other averages are used in some cases where noted.

## 2.4 Experimental Data

Experimental data was generated through years of experimentation on the compressor rig at RWTH Aachen University. It is primarily used to assess the CFD results, which are then used to interrogate the flow field in more detail. Testing was performed on both diffuser configurations of interest over a wide range of speeds and operating lines from choke to stall. Additional detailed measurements were performed at select operating points, giving insight into the spatial and temporal dependencies in the flow field. This section describes the details of the experimental rig, tested operating points and compressor configurations, and data post-processing procedures.

### 2.4.1 Description of Test Rig

A schematic of the compressor test rig is shown in Figure 2.2, and a more detailed cross-section of the centrifugal compressor itself is shown in Figure 2.3. The impeller is driven by an electric motor and gearbox. It is fed from the settling chamber by an inlet pipe containing a honeycomb flow straightener, followed by a tailored inlet flowpath with rotating hub and fixed inlet guide vanes (IGVs). This hardware is intended to supply impeller inlet pressure, temperature, and swirl profiles similar to those seen in an aircraft engine. The compressor exhausts into a plenum followed by a discharge valve and mass flow orifice. The entire system is closed-loop, so the flow also passes through a heat exchanger for cooling, removing the energy added to the flow by the impeller.

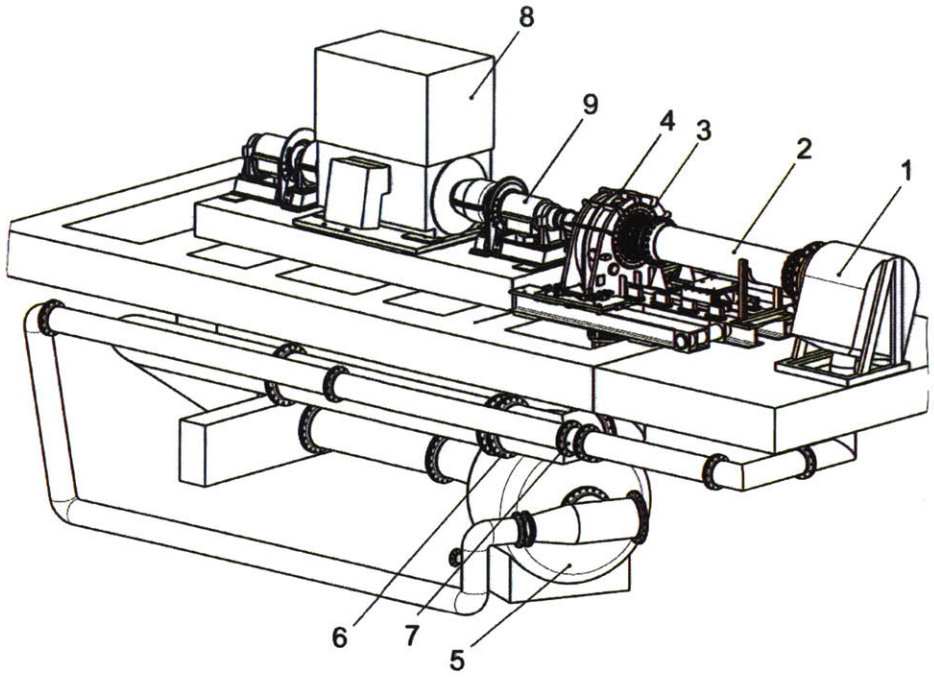


Figure 2.2: RWTH Aachen University compressor rig schematic [18]: (1) settling chamber, (2) inlet pipe, (3) centrifugal compressor, (4) exit plenum, (5) heat exchanger, (6) throttling valve, (7) mass flow orifice, (8) electric motor, (9) gearbox.

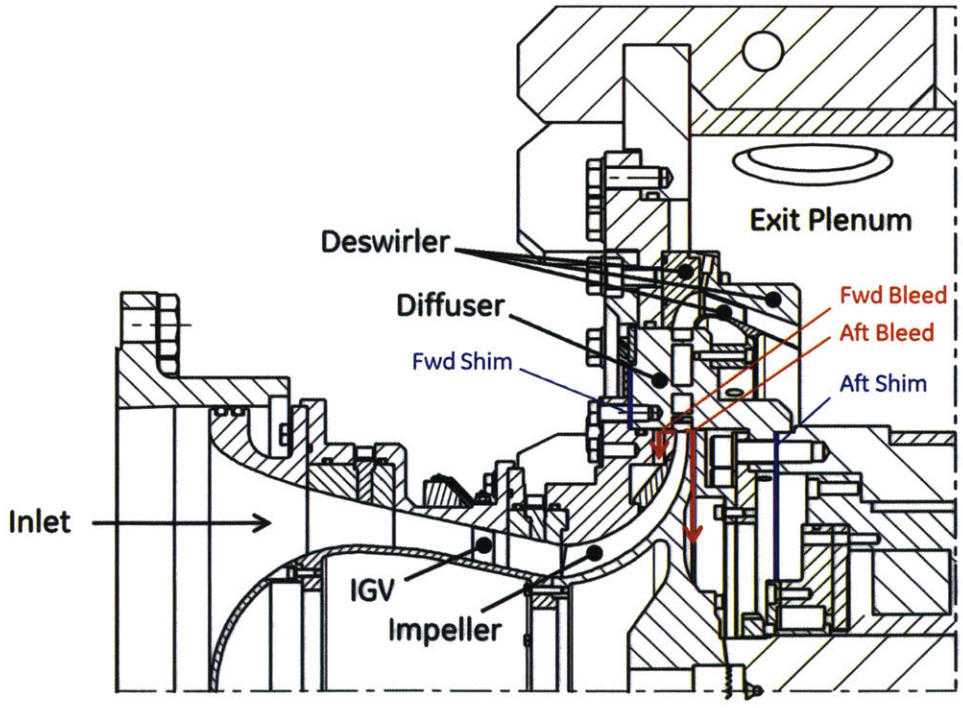


Figure 2.3: RWTH Aachen University centrifugal compressor cross-section [1].

The rig is designed such that various diffuser and deswirler configurations can be interchanged, and the clocking or relative circumferential positions of the diffuser and deswirler can be adjusted. In addition, for a given diffuser/deswirler configuration the rig can be varied in a number of ways to set different compressor operating conditions:

- Compressor inlet pressure—set by pressurizing closed-loop test system using external compression and regulation system.
- Compressor rotation speed—set by speed of electric drive motor.
- Compressor operating line—set by compressor orifice and discharge valve position.
- Impeller tip forward bleed fraction—set by forward bleed orifice and discharge valve position.
- Impeller tip aft bleed fraction—set by aft bleed orifice and discharge valve position.
- Impeller tip clearance—set by combination of active magnetic bearing (AMB) that can adjust axial position of impeller and by forward shim that determines axial position of impeller shroud.
- Impeller-diffuser alignment—set by combination of AMB that can adjust axial position of impeller and by aft shim that determines axial position of diffusion system.

Aside from the diffuser geometry, the only operating variables assessed in the present research are compressor speed and operating line. Using the baseline impeller, diffuser, and deswirler configuration, a range of forward and aft bleed levels and shims were experimentally studied early in the test program, and nominal levels were selected near their optimal values. A nominal clearance level was also defined [1]. The present research only utilizes data measured with these nominal bleed, shim, and clearance levels with the exception of stall data where the impeller is shifted aft via AMB adjustment, doubling the clearance for rub avoidance and impacting the impeller-diffuser alignment slightly. The impeller inlet conditions are also held at the same level in all data utilized here. That is, impeller inlet pressure is ambient, and the IGV stagger position is constant. It should be noted that nominal bleed fractions and clearance levels are defined at the compressor's design speed and peak efficiency operating line, so bleed valve and AMB positions are set and fixed at this operating point. However, bleed fractions, clearances, and impeller-diffuser alignment vary off-design in a manner similar to how they would vary in an engine.

More detailed descriptions of the test rig can be found in the thesis by Zachau [1].

## 2.4.2 Summary of Experimental Data

Testing was performed on both diffuser configurations of interest over a wide range of speeds and operating lines. Stall (S) testing was performed over the full range of speeds for the baseline diffuser, but the 100% $N_{c25}$ stall point was not measured for the truncated diffuser due to concerns about the structural integrity of the test vehicle. More detailed measurements from traverses, Kulites, and Particle Image Velocimetry (PIV) were performed at 80%, 90%, and 100% $N_{c25}$ near choke (C) and peak efficiency (E), giving insight into the spatial and time dependence of the flow field. These six detailed operating points are given the names 80C, 80E, 90C, 90E, 100C, and 100E, while the stall points at the same speeds are denoted 80S, 90S, and 100S. These points are shown on a compressor map in Figure 2.4.

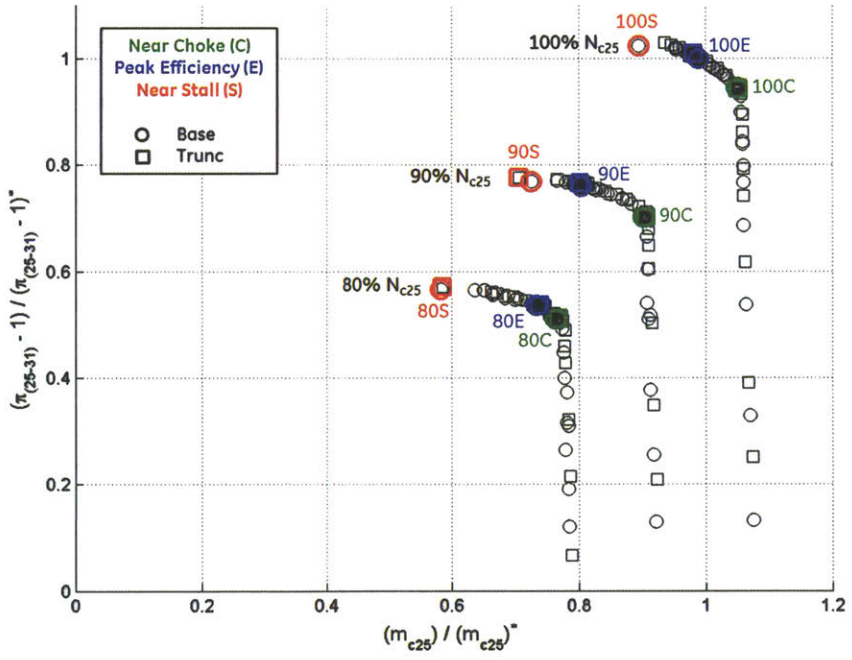


Figure 2.4: Overall compressor pressure ratio versus inlet corrected mass flow based on experimental measurements, highlighting key operating points. Symbols denote diffuser configuration, while colors denote operating point (note: colored experimental points averaged from multiple tests). Note that 90S and 100E points differ between baseline and truncated diffusers, and no 100S experiment is performed for truncated diffuser configuration.

Note that the operating lines for each of the C and E points are held approximately the same between the baseline and truncated diffusers with the exception of the 100E point, for which the baseline diffuser operating line is set slightly lower. The higher 100E throttle

point of the truncated diffuser is actually closer to the true peak efficiency point for both the baseline and truncated diffusers, but the baseline diffuser stalls on a lower operating line than the truncated diffuser, so its 100E point was set accordingly so as to not risk accidental stall caused by instrumentation blockage.

Detailed descriptions of the test instrumentation, measurements, and measurement error analysis can be found in the thesis by Zachau [1].

#### 2.4.2.1 Permanent Instrumentation

Permanent instrumentation on the test rig includes the mass flow orifice, calibrated to accurately measure compressor flow rate, and the torque meter, which measures compressor rotational speed. These are seen in Figure 2.2. In addition, a series of steady static pressure, stagnation pressure, and stagnation temperature sensors are located throughout the compressor. The reason this instrumentation may be permanently installed is that it does not significantly disrupt the flow field. These sensors are therefore used to record data for every test point, and in fact they provide the only measurements taken during the detailed compressor mapping and stall testing phases of the test program [1].

The locations and numbers of the permanent pressure and temperature sensors utilized in the present research are shown in Figure 2.5. Although the sensors are displayed on a single axial-radial plane or relative to only a single diffuser passage, in reality these sensors were distributed around the entire circumference of the compressor rig on multiple diffuser passages. Stagnation pressures and stagnation temperatures are measured at three radial positions along three circumferential distributed rakes at the deswirler exit. Even though these measurements are not taken exactly on the station 31 meridional plane, which is technically defined by the static pressure measurement locations, this research still reports all deswirler exit measurements as at "station 31".

The impeller shroud includes a total of 17 static pressure transducers distributed between eight radial positions, with the six transducers located at the highest radius distributed between four unique circumferential positions relative to the diffuser passage. A total of 28 static pressure transducers located along the diffuser forward wall are utilized in this research. These are located at 14 unique positions along the diffuser centerline including one at the throat (station T), three unique circumferential positions relative to the diffuser leading edge (station 28), and four unique circumferential positions relative to the baseline

diffuser trailing edge (station 29). Finally, 16 static pressure transducers are distributed between the inner and outer walls near the deswirler exit (station 31). Static pressures and temperatures are also measured in the settling chamber, not shown in Figure 2.5 [1].

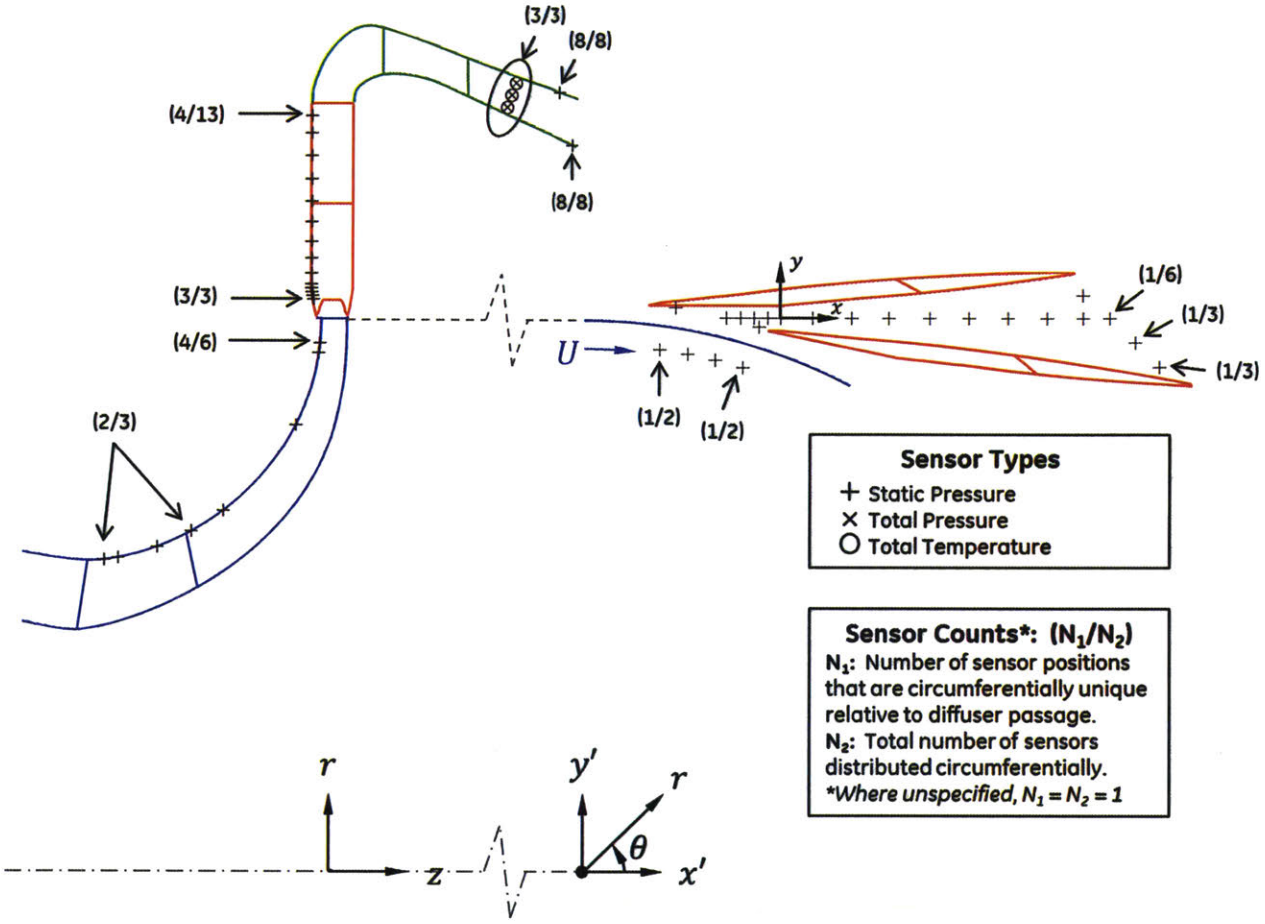


Figure 2.5: Types and locations of permanent instrumentation utilized in current research.

### 2.4.2.2 Traverse Measurements

Additional measurement traverses are performed at select operating points near the impeller inlet (station 25), diffuser throat, and baseline diffuser trailing edge (station 29) as shown in Figure 2.6. The impeller inlet measurements are used to inform the inlet boundary conditions for CFD simulations, as described in Section 2.5.1.2. They are also used to develop flowrate-based correlations for temperature rise and pressure loss between the settling chamber and impeller inlet, as described in Section 2.4.3.2. The impeller inlet measurements include traverses of a 5-hole pressure probe, a stagnation temperature probe, and a triple hotwire. These are performed at a wide range of compressor flowrates, but only along a choked operating line to ensure the instrumentation blockage does not stall the

compressor. The 5-hole probe is used to determine profiles of stagnation pressure and flow angle in two planes. The triple hotwire is primarily used to measure time-varying velocity fluctuations so that the turbulence intensity can be determined, but it is also used to validate the flow angle measurements of the 5-hole probe. As discussed by Zachau, the 5-hole probe and triple hot wire measurements of flow angle agree in the meridional-circumferential plane, but differ in the axial-radial plane [1]. Furthermore, neither the 5-hole probe nor the triple hot wire measurements of flow angle in the axial-radial plane are equal to the flowpath slopes near the outer and inner endwalls.

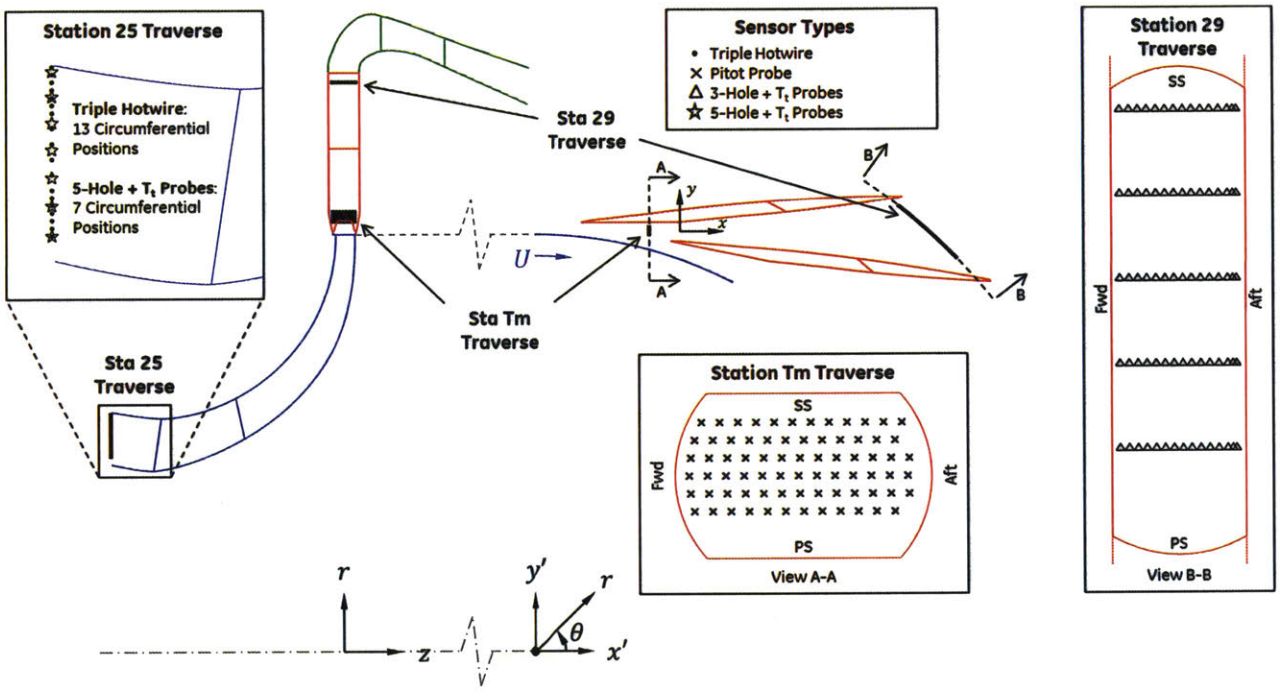


Figure 2.6: Types and locations of traverse measurements utilized in current research.

Just upstream of the diffuser throat at a location denoted station Tm, a pitot probe traverse is used to map out stagnation pressures. These measurements are used to guide the data reduction procedure so that losses are appropriately split between the impeller and the diffusion system, and the stagnation pressure distribution is used to validate CFD simulations. The pitot probe traverses are performed at the 80C, 80E, 90C, 90E, 100C, and 100E operating points [1].

Near the trailing edge of the baseline diffuser (station 29), 3-hole pressure probe traverses are performed. These are again conducted at the 80C, 80E, 90C, 90E, 100C, and 100E operating points, and are used to measure stagnation pressure as well as flow angle

in the radial-circumferential plane [1]. This allows for estimation of all the flow conditions between the diffuser and deswirler.

#### 2.4.2.3 Unsteady Pressure and PIV Measurements

Unsteady pressure and PIV measurements were also taken in the diffuser to capture even more detail about the flow at the 80C, 80E, 90C, 90E, 100C, and 100E operating points. The present research does not utilize the unsteady Kulite pressure data, and the PIV measurements are only used at a high-level to assess the CFD, but Zachau provides more information about these measurements [1].

### 2.4.3 Data Post-processing

In post-processing and presenting the measurement data, a number of assumptions and simplifications are made. These include averaging measurements taken at the same station or meridional location for 1D evaluation, using correlations to estimate the compressor inlet (station 25) conditions, and estimating impeller trailing edge (station 27) flow properties from available measurements and first-principle approximations.

#### 2.4.3.1 1D Averaging

To express compressor flow parameters or performance results on a 1D basis, measurements from multiple sensors at different locations must be averaged. This can be done for all the permanent static pressure, stagnation pressure, and stagnation temperature sensors located at the same station or meridional location (includes station 28, 29, 31, and three meridional locations through the impeller). The averaging is performed in two steps. First, if multiple sensors distributed near different diffuser passages share the same positions relative to their respective diffuser passage, then those measurement values are arithmetically averaged. This conceptually results in a set of measurement averages at unique positions relative to a single diffuser passage. Next, those average values corresponding to the same station or meridional location but different circumferential or spanwise locations relative to the diffuser passage are averaged one step further. With the exception of the deswirler exit measurements where this second averaging step is done arithmetically, the averaging is performed on an area weighted basis assuming circumferential periodicity and approximating integrals numerically using trapezoidal integration. As a reminder, even

though the deswirler exit stagnation temperature and stagnation pressure measurements are not taken exactly on the station 31 meridional plane, this research still reports all deswirler exit measurement averages as at "station 31". These averages are used to approximate the availability average set of 1D flow properties even though errors to this approximation are knowingly introduced by the arithmetic averaging at the deswirler exit and the general measurement sparsity (at some stations only one sensor may be present). These errors are mitigated by the fact that static pressure is a fairly uniform quantity at a given averaging station, and stagnation pressures and temperatures are more uniform at the deswirler exit than they are anywhere else in the diffusion system.

The traverse measurements taken near the throat and at plane 29 can also be averaged for 1D interpretation. Because the traverses provide information with higher spatial resolution than the permanent instrumentation, the availability average can be more accurately calculated with some approximations. The first approximation is that the stagnation temperature at each point in the traverse is equal to the station 31 1D average value. Second, the static pressure at each point in the traverse is approximated to be equal to the 1D average value at the traverse location (the near throat traverse averaging only utilizes a single static pressure measurement taken at the diffuser centerline). The stagnation temperature and static pressure are then combined with the measured stagnation pressure at each point to calculate all remaining flow states including entropy. Finally, the mass flux distribution is calculated with the use of the flow angle distribution, which is measured in the station 29 traverse and assumed to align with the diffuser passage centerline for the near throat traverse. Mass averages of stagnation temperature and entropy can then be calculated at the traverse locations, approximating integrals numerically using trapezoidal integration.

The approximations made in this process can be rationalized as follows. First of all, using station 31 stagnation temperatures at the traverse planes is adequate because there is no work input and negligible heat transfer between the traverse planes and exit station, so the mass averaged stagnation temperature should not change downstream of the impeller. Second, assuming uniform stagnation temperatures and static pressures at the traverse planes makes sense because the nonuniformities in stagnation pressure and flow angle, which are measured and accounted for, are the dominant cause of nonuniformities in the entropy and mass flux.

In addition to averaging stagnation pressure, the station 29 flow angle measurements can also be averaged. Averaging of the flow angle is achieved using the momentum average described in Section 2.2.2. Velocities are calculated at each traverse point as previously discussed, and the measured flow angle at each point is then used to decompose the velocity into its components. Mass averaged velocity components are calculated utilizing the mass flux at each point, approximating integrals numerically using trapezoidal integration.

Though it is possible, the potential core and mixed out averages are not calculated from the traverse data. These averages are only applied to the CFD results.

#### 2.4.3.2 Estimation of Compressor Inlet Conditions

As mentioned, the compressor inlet (station 25) stagnation temperature and pressure are not measured for each test. Instead, station 25 conditions are estimated by measuring stagnation temperature and pressure in the inlet settling chamber (i) and using correlations for inlet temperature rise and pressure loss that were developed by researchers at RWTH Aachen based on the station 25 traverse measurements. These correlations are intended to account for the frictional losses due to all the non-rotating surfaces, frictional work done on the flow by the rotating inlet hub, and any heat transfer that occurs in the inlet. The forms of these correlations are shown in Equation 2.43 and Equation 2.44.

$$T_{t25} = T_{ti} + \Delta T_t, \text{ where } \Delta T_t = f(\dot{m}_{ci}) \geq 0 \qquad \text{Equation 2.43}$$

$$p_{t25} = p_{ti}\left(1 + \frac{\Delta p_t}{p_{ti}}\right), \text{ where } \frac{\Delta p_t}{p_{ti}} = f(\dot{m}_{ci}) \leq 0 \qquad \text{Equation 2.44}$$

Note that the correlations for stagnation temperature and pressure change are functions of the inlet corrected flow only. One would expect that because the rotating inlet hub affects the inlet stagnation temperature and pressure, the true temperature and pressure changes through the inlet might depend on compressor speed as well as flow. This means that as the compressor is throttled out of choke at constant speed, correlations based purely on inlet flow could introduce some error. Because station 25 measurements were only taken in choke this error cannot be determined exactly. Fortunately, the error is mitigated by the facts that these correlations only modify the compressor stagnation temperature and pressure by a small fraction of the overall compressor temperature and pressure rise, and that the flow only varies by ~20% from choke to stall at the compressor design speed. If the correlations are based purely on speed, the calculated compressor stagnation temperature and pressure ratios at compressor stall are found to differ from the flow-based correlation

by +0.07% and -0.04% respectively. Of course this is a limiting-case estimate of the error source, but for comparison it is on the same order as the sensor measurement error reported by Zachau for temperature, and about one order of magnitude greater than the sensor measurement error reported by Zachau for pressure [1].

#### 2.4.3.3 Estimation of Impeller Exit Conditions

In order to distinguish between the impeller and diffusion system performance, the availability average 1D impeller exit (station 27) conditions must be known. Because there are no measurements taken immediately at the impeller exit, all of the flow states must be estimated. This is accomplished using the impeller inlet conditions, the compressor exit stagnation temperature, static pressure measurements near the impeller tip, and CFD calculated blockages and corrections factors based on availability averages.

To start, a number of simplifying assumptions are made. The 1D average impeller exit axial velocity is assumed equal to zero. This is reasonable since the flowpath is oriented radially at the impeller exit. Next, the impeller exit stagnation temperature is assumed equal to the 1D average deswirler exit stagnation temperature. The rational for this assumption is that there is no work input and negligible heat transfer between the impeller exit and the deswirler exit. Lastly, the availability averaged mass flow per unit area is estimated according to Equation 2.45, which uses the experimentally measured mass flow per unit area along with the availability averaged mass blockage determined from the 100E CFD results.

$$(\rho V_m)_{27}^{A} = \frac{\dot{m}}{A_{27}}\left(1 - {B_{m27}}^{A}\right) \qquad \text{Equation 2.45}$$

Next, the Euler Turbine Equation is employed to relate the work done by the impeller to the change in angular momentum of the flow, thus enabling the determination of the impeller exit tangential velocity. The general equation, given by Equation 2.49, is derived by applying energy conservation (Equation 2.46) and angular momentum conservation (Equation 2.47) to a control volume enclosing the impeller, and finally relating the two by the impeller's angular velocity (Equation 2.48). Regarding angular momentum conservation, one must consider the torque applied to the flow by the impeller pressure forces and hub friction, as well as the opposing shroud friction torque. The shroud torque must be accounted

for separately from the rotor torque, as it does resist the change in angular momentum of the flow, but it does not do work on the flow.

$$\dot{W} = H_{t27} - H_{t25} \qquad \text{Equation 2.46}$$

$$\tau_{rotor} + \tau_{shroud} = \dot{H}_{27} - \dot{H}_{25} \qquad \text{Equation 2.47}$$

$$\dot{W} = N\tau_{rotor} \qquad \text{Equation 2.48}$$

$$H_{t27} - H_{t25} = N\left(\dot{H}_{27} - \dot{H}_{25} - \tau_{shroud}\right) \qquad \text{Equation 2.49}$$

The magnitude of the shroud torque as a fraction of rotor torque is determined from the 100E CFD results, but its value is doubled for the data reduction. It is possible that the shroud torque imposed on the flow in the experiment is in fact greater than in the CFD simulation due to the presence of shroud static pressure and clearance probes in the experiment. However, the primary reason for doubling the CFD calculated shroud torque for experimental data reduction is to obtain a better match between the experimental and CFD calculated diffuser performance levels. The justification for this decision will be explained more in Sections 4.1 and 6.1. It should be noted that while this empiricism impacts the measured performance split between the impeller and diffuser, it does not impact trends or the major conclusions of this work.

The Euler Turbine Equation is applied to availability averaged quantities. This means the enthalpy rise can be written as the availability or mass averaged temperature rise, as in Equation 2.50.

$$\frac{H_{t27} - H_{t25}}{\dot{m}} = c_p\left({T_{t27}}^A - {T_{t25}}^A\right) \qquad \text{Equation 2.50}$$

Similarly, the change in angular momentum can be written as a change in availability average tangential velocity. However, because the availability average does not conserve angular momentum, a conversion between the true and availability average angular momentum values is performed using assumed values of mass and angular momentum blockages as in Equation 2.51.

$$\frac{\dot{H}_{27} - \dot{H}_{25}}{\dot{m}} = \left[r_p V_\theta \left(\frac{1 - B_H - B_m}{1 - B_m}\right)\right]_{27}^{A} - \left[r_p V_\theta \left(\frac{1 - B_H - B_m}{1 - B_m}\right)\right]_{25}^{A} \qquad \text{Equation 2.51}$$

These blockages are the availability averaged values calculated from the 100E CFD results. Upon manipulation of these equations, the impeller exit availability averaged tangential velocity calculation is given by Equation 2.52.

$$\left[r_p V_\theta \left(\frac{1-B_H-B_m}{1-B_m}\right)\right]_{27}^{A}$$

$$= \left[r_p V_\theta \left(\frac{1-B_H-B_m}{1-B_m}\right)\right]_{25}^{A} \qquad \text{Equation 2.52}$$

$$+ \left[\frac{c_p\left({T_{t27}}^A - {T_{t25}}^A\right)}{N}\right]\left[1 + \frac{N\tau_{shroud}}{\dot{m}c_p\left({T_{t27}}^A - {T_{t25}}^A\right)}\right]$$

With the 1D estimates for the impeller exit total temperature, axial velocity, tangential velocity, and mass flow per unit area, one more flow quantity is needed to calculate all of the remaining 1D flow properties. The impeller exit static pressure is estimated for this purpose. This estimate utilizes the measured shroud static pressures near the impeller exit, but it corrects for the difference in radial and axial position using a radial and axial momentum balance. Figure 2.7 illustrates the location of the measured static pressures, denoted station 27m, relative to the impeller exit station 27. Upon linearizing the static pressure distribution in the vicinity of the impeller tip, the static pressure distribution is given by Equation 2.53. Applying this at the impeller exit radius and area averaging in the axial direction gives Equation 2.54 for the availability average impeller exit static pressure.

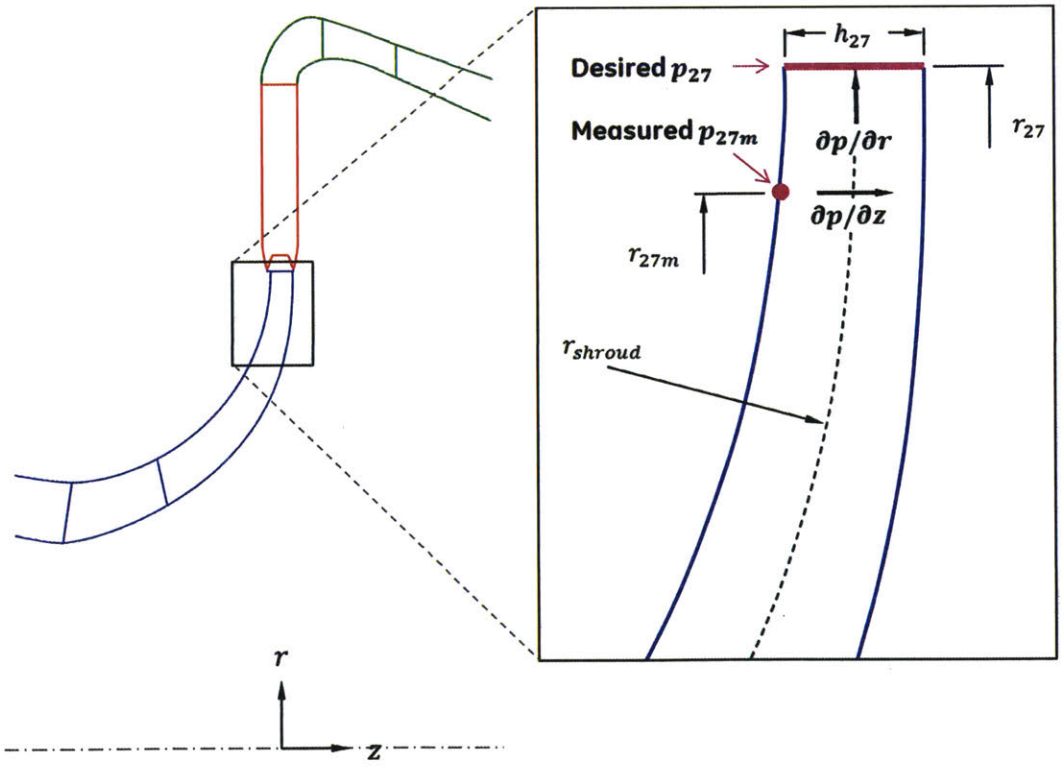


Figure 2.7: Considerations for estimating 1D average impeller exit static pressure.

$$p(z,r) \approx p_{27m}{}^{A} + (r - r_{27m})\left(\frac{\partial p}{\partial r}\right)_{27} + (z - z_{27m})\left(\frac{\partial p}{\partial z}\right)_{27} \quad \text{Equation 2.53}$$

$$p_{27}{}^{A} = p_{27m}{}^{A} + (r_{27} - r_{27m})\left(\frac{\partial p}{\partial r}\right)_{27} + \frac{h_{27}}{2}\left(\frac{\partial p}{\partial z}\right)_{27} \quad \text{Equation 2.54}$$

Local to the impeller exit, one can infer from the high Reynolds number that viscous forces have a negligible impact on the static pressure gradients relative to inertial forces. Therefore, the radial and axial pressure gradients can be calculated from the Euler Equations for momentum conservation, Equation 2.55 and Equation 2.56.

$$\frac{\partial p}{\partial r} = -\rho\left(\frac{\partial V_r}{\partial t} + V_r\frac{\partial V_r}{\partial r} + \frac{V_\theta}{r}\frac{\partial V_r}{\partial \theta} - \frac{V_\theta^2}{r} + V_z\frac{\partial V_r}{\partial z}\right) \quad \text{Equation 2.55}$$

$$\frac{\partial p}{\partial z} = -\rho\left(\frac{\partial V_z}{\partial t} + V_r\frac{\partial V_z}{\partial r} + \frac{V_\theta}{r}\frac{\partial V_z}{\partial \theta} + V_z\frac{\partial V_z}{\partial z}\right) \quad \text{Equation 2.56}$$

Reducing these equations to their dominant terms, the impeller exit flow is approximated as axisymmetric and steady in the stationary frame, and additional local approximations are made that axial velocity is small and radial velocity is nearly constant with increased radius. This leaves the simplified radial and axial momentum equations near the impeller exit, Equation 2.57 and Equation 2.58.

$$\frac{\partial p}{\partial r} \approx \frac{\rho V_\theta^2}{r} \quad \text{Equation 2.57}$$

$$\frac{\partial p}{\partial z} \approx -\rho V_r\frac{\partial V_z}{\partial r} \quad \text{Equation 2.58}$$

The impeller exit density and radial velocity are determined in conjunction with the static pressure through an iterative procedure. Also, the approximation $\partial V_z/\partial r \approx -V_r/r_{shroud}$ is derived based on geometry, and the shroud radius is estimated to be equal to the impeller pitchline length. Finally, to compensate for many of the simplifying assumptions that have been made, empirical factors are derived from the 100E CFD results and applied to the pressure gradient calculations. The final impeller exit pressure gradient calculations given by Equation 2.59 and Equation 2.60 are used in Equation 2.54 to obtain the goal value of impeller exit static pressure. Note that at the 100E operating point, the radial pressure gradient is found to be almost four times larger than the axial pressure gradient.

$$\left(\frac{\partial p}{\partial r}\right)_{27} \approx 0.920\left(\frac{\rho V_\theta^2}{r}\right)_{27} \quad \text{Equation 2.59}$$

$$\left(\frac{\partial p}{\partial z}\right)_{27} \approx 1.033\left(\frac{\rho V_r^2}{r_{shroud}}\right)_{27} \quad \text{Equation 2.60}$$

This impeller exit condition estimation procedure is found to introduce the least amount of error to the calculated impeller exit conditions relative to other procedures considered. While some empirical factors derived from CFD are used in the process, the equations are primarily based on physics so trends are physically driven. Table 2.2 shows the sensitivities of some important impeller exit conditions to changes in the measured or assumed variables used in this process. It is clear that the estimated impeller performance parameters are far more sensitive to the experimentally measured variables than the CFD-guided empirical variables, indicating that this procedure is robust to the assumptions. Note that the constant specific heat assumption may result in an underestimate in impeller pressure ratio and an overestimate in impeller efficiency if specific heat actually reduces noticeably through the impeller.

| Change in Measurement or Assumption | $\Delta M_{27}$ | $\Delta\alpha_{27}$ [deg] | $\%\Delta\pi$ (25 – 27) | $\%\Delta\eta_p$ (25 – 27) |
|---|---|---|---|---|
| $\%\Delta N = +1\%$ | -0.009 | -0.22 | -1.10% | -0.90% |
| $\%\Delta\dot{m} = +1\%$ | 0.002 | -0.14 | 0.23% | 0.19% |
| $\%\Delta\alpha_{25} = +1\ deg$ | 0.004 | 0.09 | 0.47% | 0.38% |
| $\%\Delta p_{t25} = +1\%$ | -0.001 | -0.02 | -1.09% | -0.89% |
| $\%\Delta p_{27m} = +1\%$ | -0.001 | 0.16 | 0.87% | 0.70% |
| $\%\Delta T_{t25} = +1\%$ | -0.019 | -0.47 | -2.29% | 0.77% |
| $\%\Delta T_{t27} = +1\%$ | 0.024 | 0.49 | 3.11% | -0.14% |
| $\%\Delta\gamma = -1\%$ | 0.027 | 0.49 | 2.90% | -0.29% |
| $\%\Delta B_{m25} = +10\%$ | 0.000 | 0.01 | 0.03% | 0.03% |
| $\%\Delta B_{H25} = +10\%$ | 0.000 | 0.00 | -0.01% | -0.01% |
| $\%\Delta B_{m27} = +10\%$ | 0.001 | -0.13 | 0.13% | 0.11% |
| $\%\Delta B_{H27} = +10\%$ | 0.002 | 0.05 | 0.27% | 0.22% |
| $\%\Delta\tau_{shroud} = +10\%$ | -0.005 | -0.12 | -0.58% | -0.47% |
| $\%\Delta(\partial p/\partial r)_{27} = +10\%$ | 0.000 | 0.08 | 0.42% | 0.34% |
| $\%\Delta(\partial p/\partial z)_{27} = +10\%$ | 0.000 | 0.01 | 0.06% | 0.05% |

Table 2.2: Average sensitivities of calculated impeller exit conditions to measurements and assumptions for baseline diffuser at 100E operating point.

The results of the availability average impeller exit condition estimation procedure are assessed in two ways. First, the calculated impeller exit stagnation pressure is compared to the availability average stagnation pressure measured at the near throat traverse, denoted station Tm, for the 80E, 80C, 100E, and 100C operating points. Because the compressor operating point moves around slightly during the traversing, and because each point in the

traverse has a corresponding impeller exit condition calculation, the averages and standard deviations of the losses are provided. As shown in Table 2.3, the average losses are found to be consistent with the CFD results within the realm of variation. Note that the steady CFD simulation utilized a mixing plane downstream of the impeller exit, actually introducing some additional uncertainty into the reliability of the CFD-predicted loss across this region.

| Operating Point | Average $\bar{\omega}_{Exp} - \bar{\omega}_{CFD}$ $(27 - T_m)$ | Std Dev $\bar{\omega}_{Exp}$ $(27 - T_m)$ |
|---|---|---|
| 100E | 0.0107 | 0.0102 |
| 100C | 0.0125 | 0.0092 |
| 80E | 0.0002 | 0.0105 |
| 80C | 0.0047 | 0.0074 |

Table 2.3: Differences in experimental and CFD calculated stagnation pressure loss between impeller exit and near throat traverse for baseline diffuser.

To assess the impeller exit calculation a second way, the calculated impeller exit shroud static pressure rise coefficient is plotted along with the measured impeller shroud static pressure rise coefficient in Figure 2.8 for six major operating points. It is observed that the static pressure rises approximately linearly with increased radius, and the calculated value at the impeller exit reasonably continues this trend. It is clear that the shapes of these curves near the impeller exit differ between operating points. This is a result of a circumferential static pressure nonuniformity imposed upstream by the diffuser, which also varies with operating point. However, the station 27m measurements used to estimate the impeller exit pressure are less affected by this since multiple circumferentially distributed measurements are able to be averaged. Note that Figure 2.8 shows the averages of multiple tests performed at the 80C, 80E, 100C, and 100E operating points. Also note that the plotted impeller exit pressure excludes the axial pressure gradient term in Equation 2.54, as it is only the shroud value that is of concern.

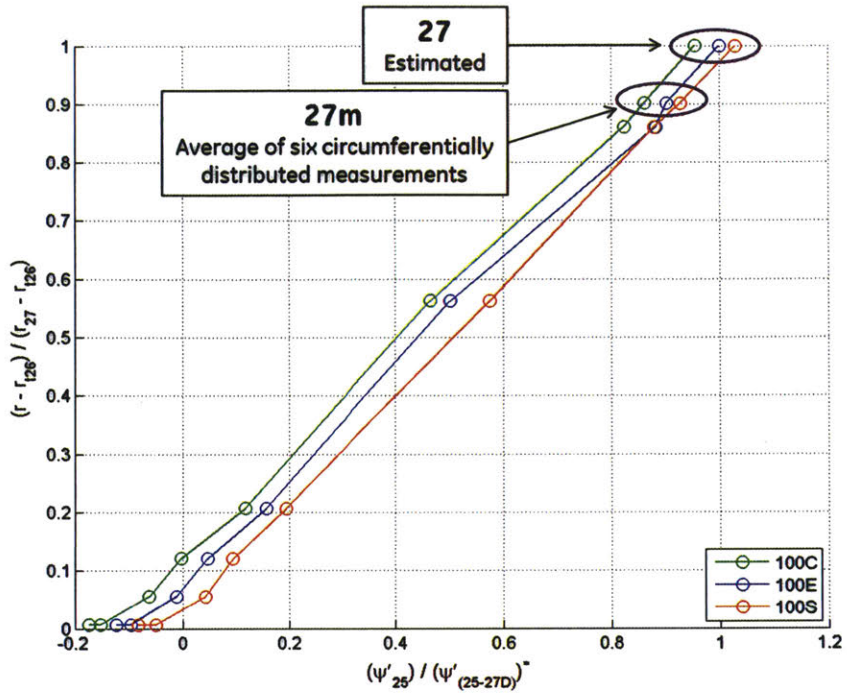


(a) 100% $N_{c25}$.

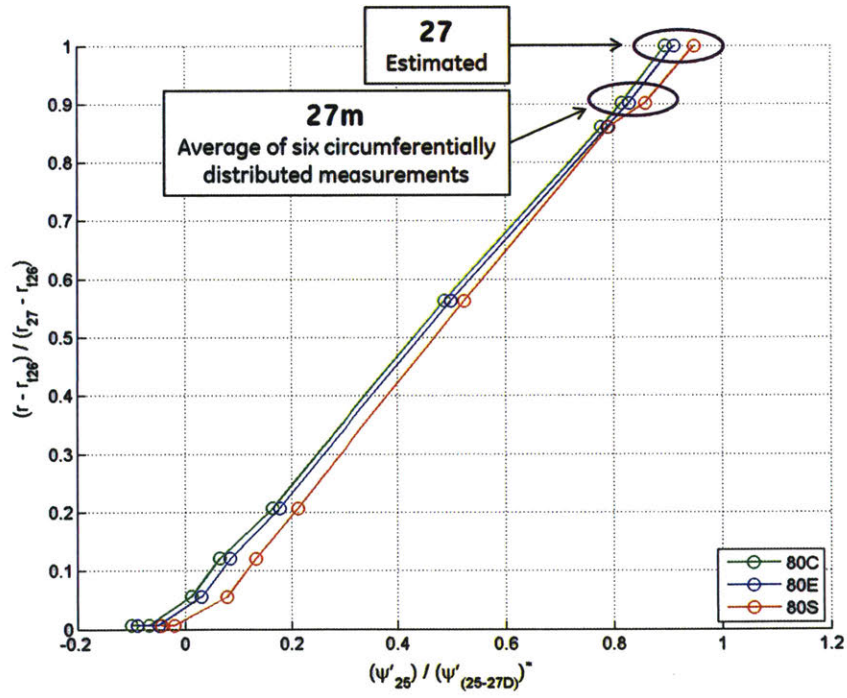


(b) 80% $N_{c25}$.

Figure 2.8: Measured and estimated impeller shroud static pressure rise coefficient, $\Psi_{25} = (p_{shroud} - p_{t25})/(\rho_{t25}U_{27}^2)$, versus radius for baseline diffuser. Impeller tip static pressure estimate reasonable given linear trend of measured pressure versus radius throughout impeller.

#### 2.4.3.4 Estimation of Diffuser Throat Stagnation Pressure

It is useful to know the stagnation pressure at the diffuser throat in order to calculate other flow conditions there which are hypothesized to influence the performance of the downstream diffuser passage, such as Mach number and mass blockage. The throat stagnation pressure is also used to estimate the dynamic pressure at the throat, which is furthermore used to calculate pressure recovery coefficients that are referenced to the throat. This estimation procedure is not used to determine stagnation pressure losses referenced to the throat.

Although a stagnation pressure traverse is performed just upstream of the diffuser throat, it is deemed insufficient for this purpose primarily because it does not capture the weak flow near the endwalls. Instead, a constant stagnation pressure loss coefficient is assumed between the impeller exit and diffuser throat. This is taken from the CFD solutions. The impeller exit static and stagnation pressures, which are already themselves estimates, are then used to calculate the throat stagnation pressure.

## 2.5 Computational Fluid Dynamics (CFD)

CFD simulations are utilized to obtain flow fields corresponding to the Aachen experiments, where computed flow variables are available at discrete grid points distributed throughout the entire compressor. The CFD solutions complement the experimental data in obtaining a quantitative understanding of the underlying flow processes driving the observed trends. CFD simulations are performed for both the baseline and truncated diffusers at 80% $N_{c25}$ and 100% $N_{c25}$ from choke to stall. This section describes the details of the CFD modeling assumptions and simplifications, simulated cases, and post-processing procedures.

### 2.5.1 Description of CFD Modeling

Steady Reynolds-Averaged Navier Stokes (RANS) CFD simulations are performed using ANSYS CFX 16.1 software on the full compressor stage, consisting of the impeller, diffuser, and deswirler components together in one model.

#### 2.5.1.1 Geometry

The full stage model includes a single impeller sector consisting of a full and splitter blade (1/23 wheel), a single diffuser passage (1/30 wheel), and three deswirler vanes (1/30 wheel)

as shown in Figure 2.9. These components are simulated together assuming circumferential solution periodicity, using a mixing plane to pass flow properties in a steady conservative manner from the impeller to the diffuser, and using a general connection to pass spatially accurate flow properties between the diffuser and deswirler. Notice that the CFD model is mirrored relative to the actual compressor rig, with the impeller rotating in the opposite direction.

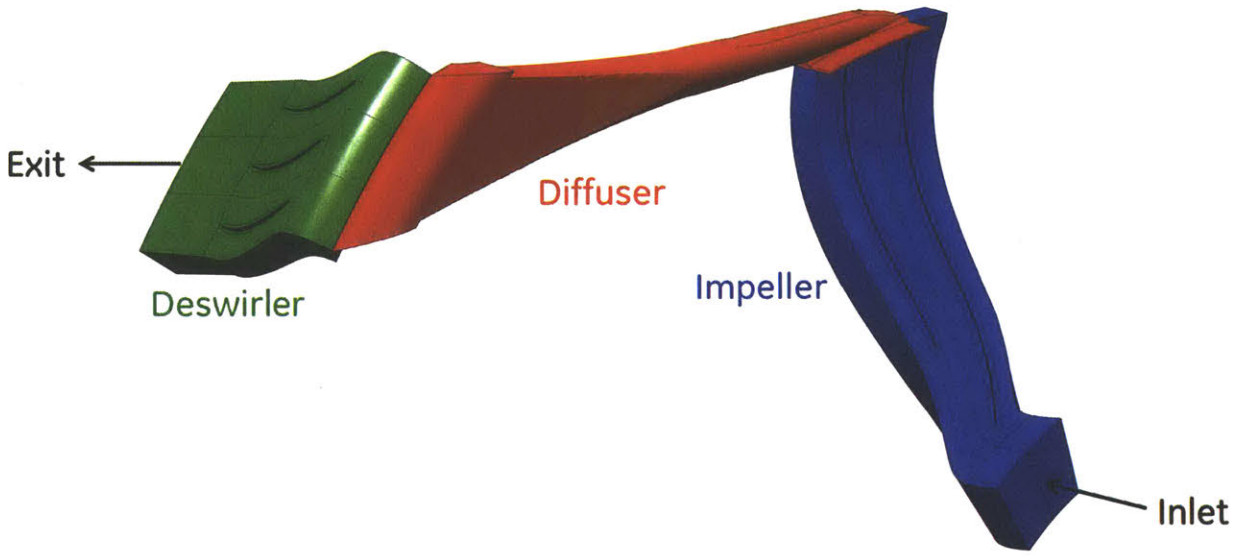


Figure 2.9: CFD model of compressor stage featuring baseline diffuser.

The impeller CFD domain begins at station 25, and the deswirler domain exit is placed slightly downstream of station 31. The diffuser domain begins at a radius just 0.13% greater than the impeller trailing edge radius, and it ends downstream of station 29 midway through the bend. Placing the impeller-diffuser interface so close to the impeller trailing edge is not ideal, as the high level of impeller exit flow nonuniformity can introduce error to the mixing plane solution approximation. However, the close proximity of the impeller and diffuser make this unavoidable, with the axisymmetric portion of the diffuser inlet geometry ending immediately downstream of the bleed slots. Another option is to place the impeller exit after bleed slots, but this would not be consistent with the geometry used by Wilkosz to characterize the mixing plane approximation by performing back-to-back steady and unsteady simulations [18].

The impeller tip bleeds are modeled as axial-circumferential slots that extend approximately one passage width forward and aft from the walls of the diffuser inlet region, as

shown in Figure 2.10. Figure 2.3 shows the more complicated bleed slot geometry present in the actual rig, which consists of shorter slots, corners, plenums, and both rotating and nonrotating boundaries.

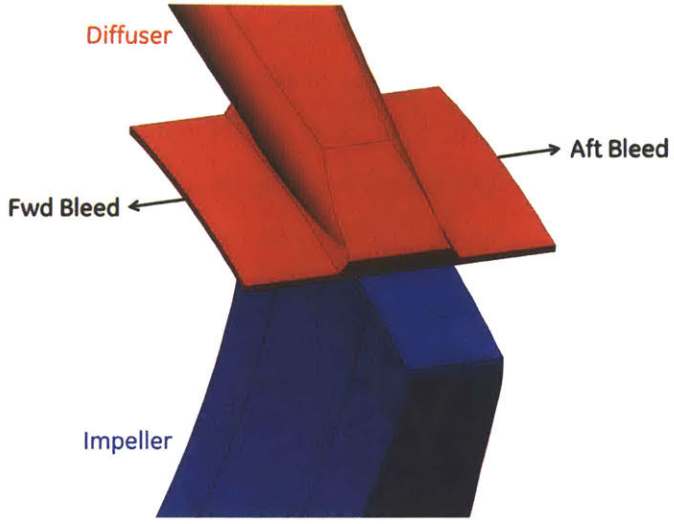


Figure 2.10: CFD model of impeller-diffuser interface featuring forward and aftward bleed slots.

There are some differences in the tested and CFD modeled impeller tip clearances. As reported by Zachau, the impeller clearances measured experimentally using clearance probes vary from inducer to exducer, between main and splitter blades, and circumferentially around the impeller (variation circumferentially around the shroud is not measured). However, the clearances in the CFD model are set uniformly and equal to the test rig's nominally-defined 100% $N_{c25}$ clearance level, which is actually 20% lower than the circumferential average clearance at the exducer. Experimentally derived performance derivatives reported by Zachau indicate that increasing the exducer clearance by 20% could be expected to reduce the compressor polytropic efficiency by only 0.14% at the 100E operating point [1].

There are also differences in the tested and CFD modeled impeller-diffuser alignment. It was initially thought that the nominal forward shim used in the experiment produced a slight misalignment of the impeller and diffuser during operation, with the diffuser centerline being slightly forward of the impeller centerline. This misalignment was incorporated into the CFD model. However, it now appears that the impeller and diffuser centerlines are more nearly aligned at 100% $N_{c25}$ than originally thought. There is still some uncertainty about this. Fortunately, near the optimal alignment setting, the compressor performance is

experimentally found to be insensitive to misalignments of the level implemented in the CFD model, with 100E compressor polytropic efficiency being unaffected [1].

Another CFD modeling simplification is that the geometry is assumed constant for all operating points. In reality, the compressor components deform slightly under centrifugal, thermal, and pressure loads in a manner that varies with operating point. This can primarily impact compressor performance through changes in both impeller tip clearance and impeller-diffuser alignment. The CFD model incorporates the impeller tip clearance measured at 100% $N_{c25}$, but the true impeller tip clearance is likely increased at lower speed with a corresponding change in alignment due to reduced outward and forward deflection of the impeller tip. Furthermore, experimental stall testing was performed at twice the nominal 100% $N_{c25}$ clearance setting, but the CFD model clearance or alignment are not changed for stall simulations.

Fillets are not incorporated into the CFD geometry for the impeller, diffuser, or deswirler. This is because the fillets are so small, contributing only a small fraction of the total blockage throughout these components (e.g. 0.06% of throat area nominally). Furthermore, none of the influential flow mechanisms observed are believed to be influenced by the presence of small fillets (e.g. there are no corner separations). Excluding the fillets from the CFD geometry also makes for simpler grid generation.

In summary, there are small differences between the CFD model and the experimental compressor geometry. These include differences in impeller tip forward and aft bleed slot geometry, impeller tip clearance levels, impeller-diffuser alignment levels, and fillet geometry. However, the impacts of these differences on the CFD solutions, trends, and responsible flow mechanisms are determined to be small based on experimental measurements or rational arguments.

#### 2.5.1.2 Modeling Assumptions and Numerics

ANSYS CFX 16.1 is used to perform steady RANS simulations on the compressor stage. The air is assumed to be an ideal gas, and a constant specific heat ratio of 1.4 is used to keep post-processing simple and intuitive. The constant specific heat assumption is known to cause a slight overestimation of the calculated impeller stagnation pressure and temperature ratios, altering efficiency, but performance trends should not be significantly affected. The flow is assumed turbulent, and a $k$-$\omega$ turbulence model is selected incorporating CFX

automatic wall functions. The solution is obtained using CFX's high resolution advection scheme, which uses a combination of upwind and 2nd order calculations to maximize accuracy while maintaining solution stability. The turbulence numerics are solved to first order. CFX's double precision solver is used.

The simulations are run for as long as necessary in order for residuals and flow properties to stabilize. All cases are converged to yield mass, momentum, and enthalpy RMS residuals less than $1x10^{-4}$. In addition, each component's mass flow, momentum flow, and enthalpy flow between the inlet and exit are found to be within 0.1% of each other or less. Temperatures, pressures, and Mach numbers are also monitored at various points throughout the diffuser and deswirler to ensure they are stabilized.

Some unconverged simulations are still deemed useful. These include some solutions near stall or near a transition point in the diffuser operation, which do not reach steady state, but oscillate periodically in pseudo-time. These solutions still have RMS residuals less than $1x10^{-4}$. However, overall component mass, momentum, and/or enthalpy imbalances may oscillate up to 1%, and monitored values of temperatures, pressures, and Mach numbers are oscillatory. These oscillatory solutions will be pointed out when referenced.

Unsteady RANS (URANS) simulations are not performed in the present work. One measure of the importance of unsteady effects on local variations in flow quantities is the reduced frequency, given by Equation 2.61 [17]. It is the ratio of the steady time scale of interest, $L_{ref}/V_{ref}$, to the unsteady time scale of interest, $1/\omega_{ref}$. For reduced frequencies much less than 1, unsteady effects have a negligible influence on local changes in flow quantities such that the flow is quasi-steady. Conversely, for reduced frequencies much greater than 1, unsteady effects dominate local time-accurate changes in flow quantities. Equation 2.62 shows that for length scales above 2% of the impeller exit radius, unsteadiness due to impeller blade passing results in a reduced frequency greater than 1 for the diffuser (reference velocity is estimated as the impeller tip speed). The diffuser passage length is certainly greater than this, and the RANS results discussed in Section 6.5.4 show that the level of impeller exit non-uniformity is not small. For self-excited unsteadiness, such as unsteadiness due to separated flow which is known to exist in the diffuser passage being studied, the reduced frequency is also close to 1. This suggests that unsteadiness has an important influence on the time-accurate flow field throughout the diffuser.

$$\beta = \frac{\omega_{ref} L_{ref}}{V_{ref}} \qquad \text{Equation 2.61}$$

$$\left(\frac{L_{ref}}{r_{27}}\right)_{\beta=1} = \frac{1}{Number\ of\ Blades} = 2.17\% \qquad \text{Equation 2.62}$$

As the reduced frequency suggests, previous work performed by Wilkosz on this topic has in fact demonstrated that unsteady effects do impact the time-accurate flow field in centrifugal compressors [15] [18]. However, this time-accurate behavior is shown to have a small effect on global time-averaged performance metrics of interest. Everitt showed that RANS simulations successfully captured the overarching effects of diffuser inlet flow angle and Mach number on the performance of a vaned diffuser [10]. RANS simulations performed by Wilkosz on the baseline and truncated diffusers of interest were able to successfully capture the extent of the flow separations measured experimentally by Zachau and Kunte using PIV [2] [4] [18]. This included differences in separation behavior between the two diffusers. Wilkosz also found that the same flow weakness was present in the results of URANS simulations of the truncated diffuser on a time-averaged basis [15] [18]. Other examples of previous work noted in Section 1.3 also support the claim that unsteadiness has little effect on the time-averaged performance criteria of interest for centrifugal compressor diffusers. Therefore, it is argued that for the purposes of this research, RANS can be used to sufficiently characterize the most important flow mechanisms driving the compressor performance trends.

#### 2.5.1.3 Boundary Conditions

The compressor inlet boundary conditions used for the CFD simulations are plotted in Figure 2.11. They are based on the station 25 traverse measurements taken at 100% $N_{c25}$ in compressor choke, as described in Section 2.4.2.2. This includes 5-hole probe measurements of stagnation pressure and flow angle in two planes, stagnation temperature probe measurements, and turbulence intensity derived from triple hot wire measurements. Since the measurements taken in the stationary reference frame are applied to the rotating impeller boundary, they are averaged circumferentially and arithmetically at each spanwise location. To capture the inlet boundary layers and the effect of the rotating inlet hub near the endwalls where measurements cannot be obtained, these radial profiles are extrapolated with the guidance of a CFD simulation of the compressor inlet and IGVs performed at RWTH Aachen. To completely define the initial conditions for the two-equation turbulence

model, an inlet turbulence length scale is also chosen to be uniformly equal to 0.7% of the annulus height, consistent with the results of the same RWTH Aachen inlet CFD simulation.

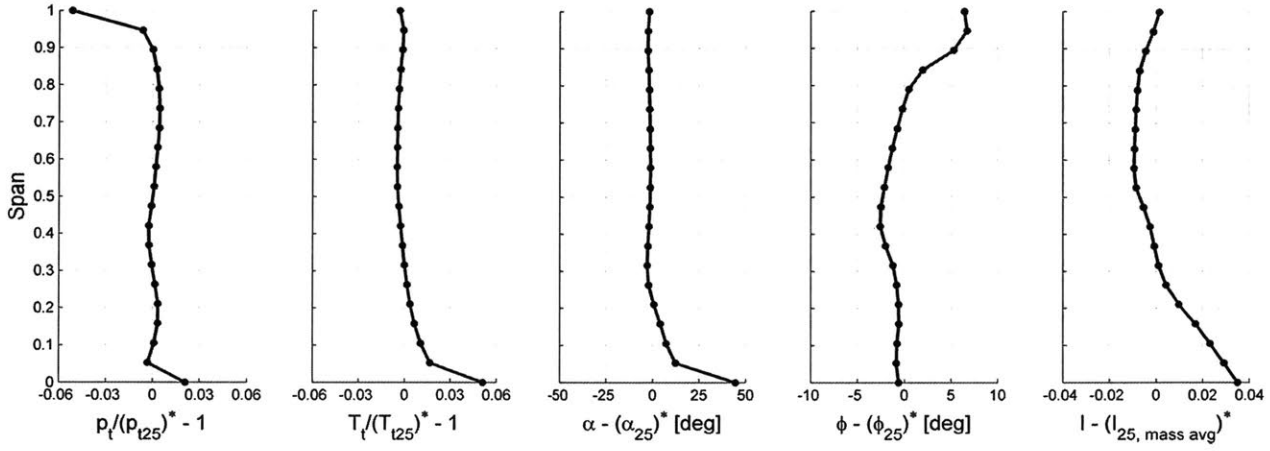


Figure 2.11: Compressor inlet conditions versus span used for CFD simulations.

As discussed in Section 2.4.2.2, the 5-hole probe measurements of flow angle in the axial-radial plane may contain errors, but they are applied as CFD boundary conditions regardless. Another potential source of error is that the same compressor inlet conditions are applied to CFD simulations for all selected operating points. This is not an issue for the average levels and spatial distributions of flow angle and turbulence intensity, as Zachau showed these changed negligibly between the different measurement conditions (+/-0.20 deg for flow angle, +/-0.035% for turbulence intensity) [1]. Differences observed in the average levels of inlet stagnation pressure and temperature between operating conditions also do not need to be incorporated into the CFD boundary conditions, since performance metrics are corrected for these differences. On the other hand, some CFD boundary condition error is expected from neglecting to incorporate operating point variation in the spatial distributions of inlet stagnation pressure and stagnation temperature, especially near the endwalls where the boundary layers may differ.

The diffuser exit boundary condition is modeled as an outlet with a specified average static pressure. The CFX "outlet" boundary designation forbids reversed flow at the boundary, instead locally placing imaginary walls to block the reversed flow wherever it would otherwise appear. The static pressure distribution at the diffuser exit may vary so long as circumferentially averaged values meet the requirement. Along with the impeller angular

velocity, the diffuser exit static pressure is varied for different CFD simulations to set the compressor operating point.

The forward and aft bleed slots are also modeled as outlets. Mass flow rate is specified, and CFX iterates on the static pressure level and distribution to meet this requirement. The bleed mass flow rates are set to one level for all 100% $N_{c25}$ operating points, and another level for all 80% $N_{c25}$ operating points. These levels are chosen such that the 100E and 80E bleed mass flow fractions are equal to the nominal experimental levels.

The mixing plane between the impeller and diffuser passes circumferentially averaged flow properties in a steady, conservative manner between the two components while still allowing for different spatial distributions of these properties on each side of the mixing plane. The mixing plane attempts to maintain circumferentially averaged static pressures in spanwise discretized bands on each side of the impeller-diffuser interface. To constrain the velocity on the diffuser side of the mixing plane, the choice is made to use CFX's option to calculate velocities from average band stagnation pressures and flow angles in the impeller reference frame, as this option allows for downstream circumferential velocity variations necessary to accommodate the pressure field induced by the diffuser.

Circumferential-facing surfaces formed by "cutting" component sectors from the full wheel are modeled as rotationally periodic boundaries. Endwalls and airfoil surfaces are modeled as smooth, no-slip, adiabatic walls.

#### 2.5.1.4 Grids

Autogrid is used to generate the impeller and deswirler meshes, and ICEM is used to generate the baseline and truncated diffuser meshes, all of which are structured hex grids. In an attempt to study mesh sensitivity in the diffuser, an unstructured baseline diffuser grid is also generated using the ANSYS Meshing tool. The unstructured grid is more refined than the structured grid in the streamwise direction around the sharp diffuser cusps and leading edge, as shown in Figure 2.12. Simulations using the unstructured grids were qualitatively found to reproduce the same performance-limiting flow mechanisms as the structured grids, with only small differences in the quantitative performance levels. A comparison of the baseline diffuser structured and unstructured grid results are presented in Section 3.3.2.

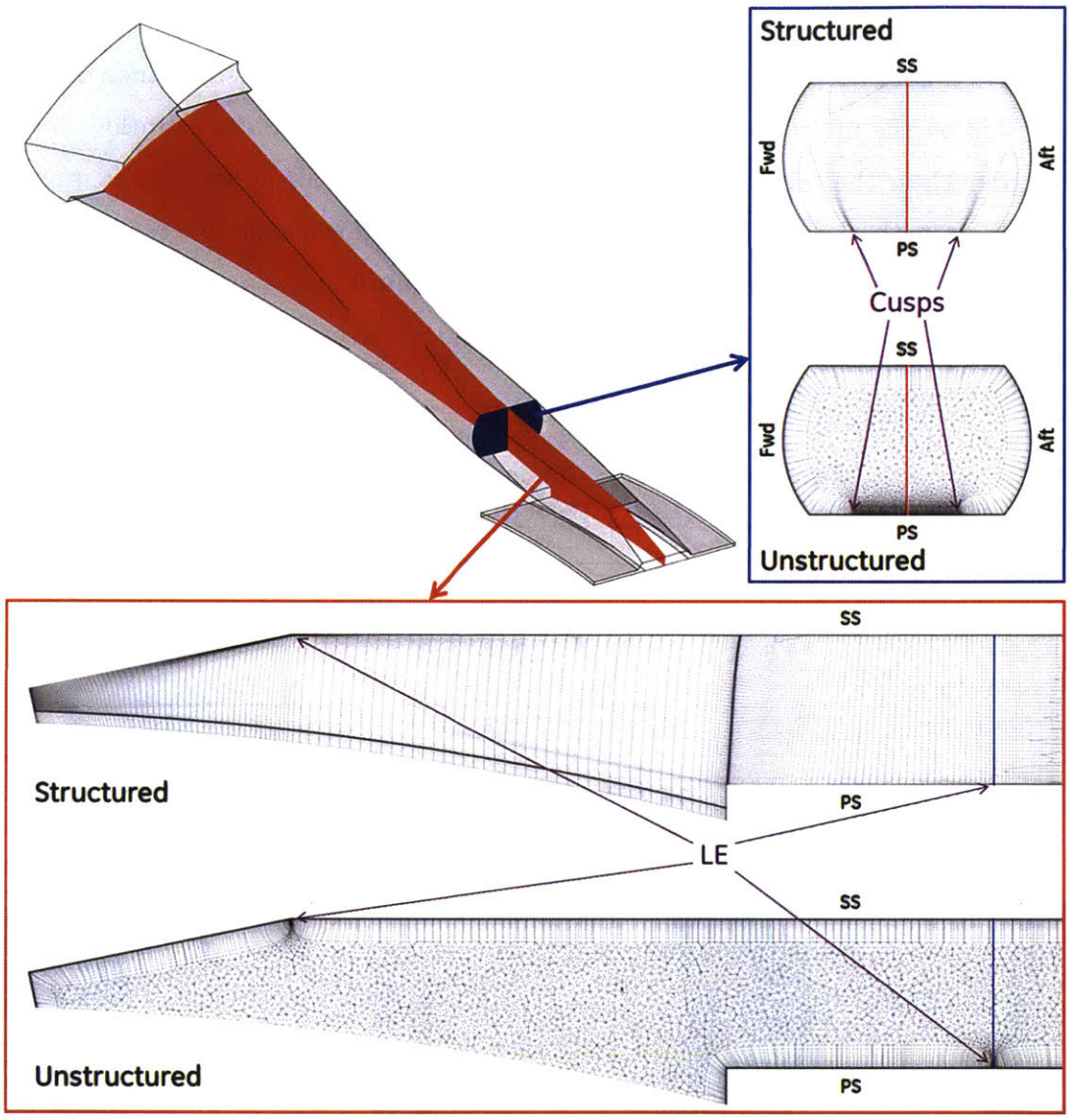


Figure 2.12: Structured and unstructured baseline diffuser grids near inlet. Unstructured grid features more refinement around leading edge and cusps.

Mesh quality statistics are calculated using ANSYS CFD Post and compared against ANSYS recommended values in Table 2.4 [19]. Nearly every node in each grid satisfies ANSYS recommended levels for orthogonality angle and mesh expansion factor, but not for aspect ratio. This is deemed acceptable, since the high aspect ratio cells are the result of refining the grid in the surface-normal direction near the wall to resolve the boundary layer. Wall $y^+$ levels based on the first cell height are shown for each component in Figure 2.13, Figure 2.14, Figure 2.15, Figure 2.16, and Figure 2.17. With $y^+$ values between 1 and 5 on most of the airfoil and flowpath surfaces, the meshes are deemed appropriately refined

for capturing the boundary layer physics. Notice that the diffuser bleed slots are not refined enough to model the bleed boundary layer, but this is not necessary since only the effect of the bleed on the main flow is of concern. Also, because the diffuser inflow velocity is so much higher than the outflow velocity, it is difficult to create a structured mesh with ideal $y^+$ levels at both the inlet and the exit. Secondary flows and reversed flow in this compressor also introduce turbulent shear layers into main flow away from the wall where the grid is not as refined. As a result, future work should investigate other meshing strategies both near and away from the wall.

| Grid | Elements ($10^6$) | Nodes ($10^6$) | Orthogonality Angle > 20 (% of Nodes) | Aspect Ratio < 100 (% of Nodes) | Expansion Factor < 20 (% of Nodes) |
|---|---|---|---|---|---|
| Impeller | 3.7 | 3.8 | 100% | 76% | 100% |
| Base Diffuser, Structured | 7.4 | 7.6 | 100% | 93% | 100% |
| Base Diffuser, Unstructured | 22.5 | 8.6 | 100% | 96% | 100% |
| Trunc Diffuser, Structured | 7.1 | 7.2 | 100% | 94% | 100% |
| Deswirler | 17.3 | 17.7 | 100% | 95% | 100% |

Table 2.4: CFD mesh size and quality statistics. Grids are satisfactory.

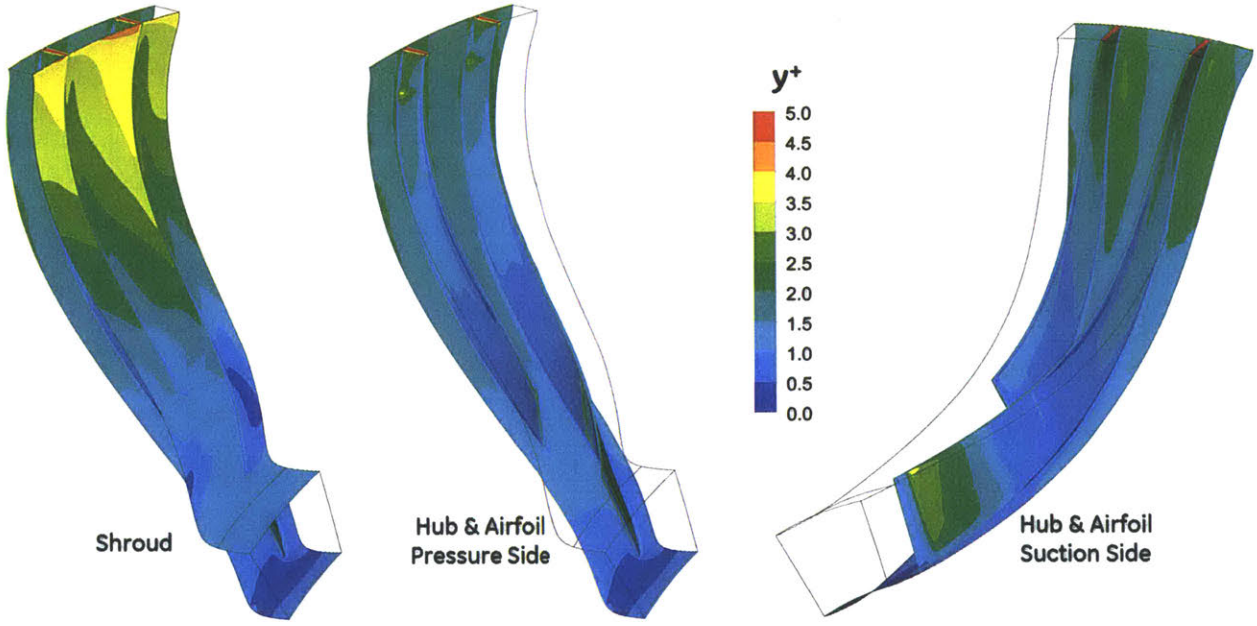


Figure 2.13: Impeller grid $y^+$ levels at 100E operating point. Levels are appropriate for capturing boundary layer physics.

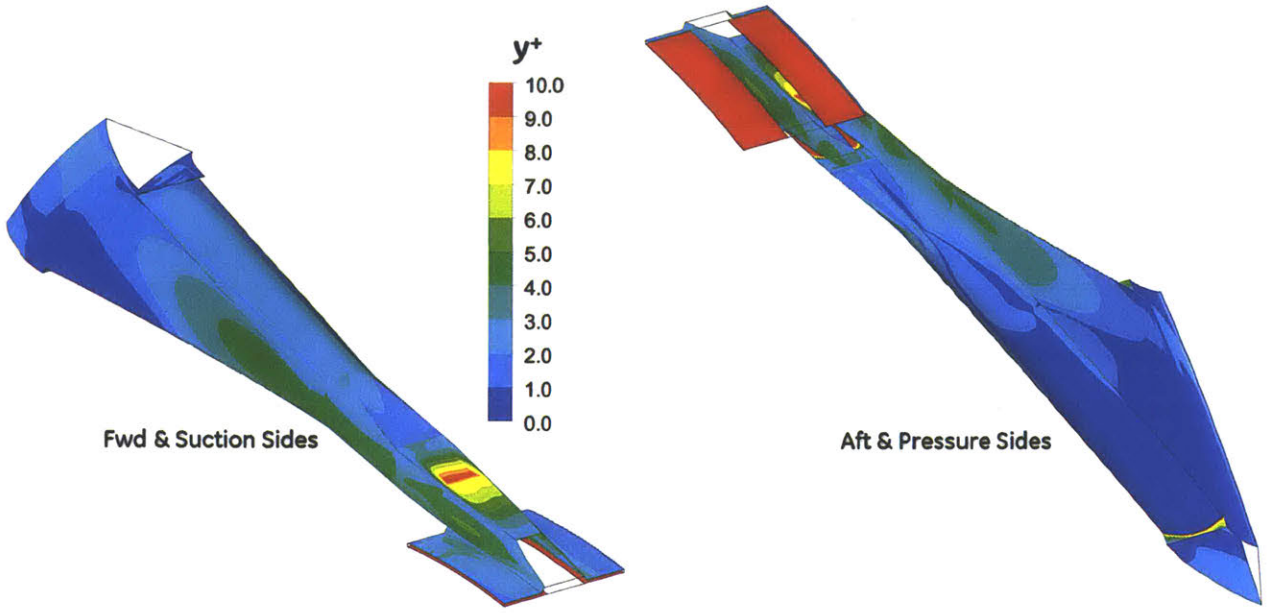


Figure 2.14: Structured baseline diffuser grid $y^+$ levels at 100E operating point. Levels are generally appropriate for capturing boundary layer physics. Local region of high $y^+$ on diffuser inlet suction side due to locally high flow velocities. Bleed slot refinement not necessary given research objectives.

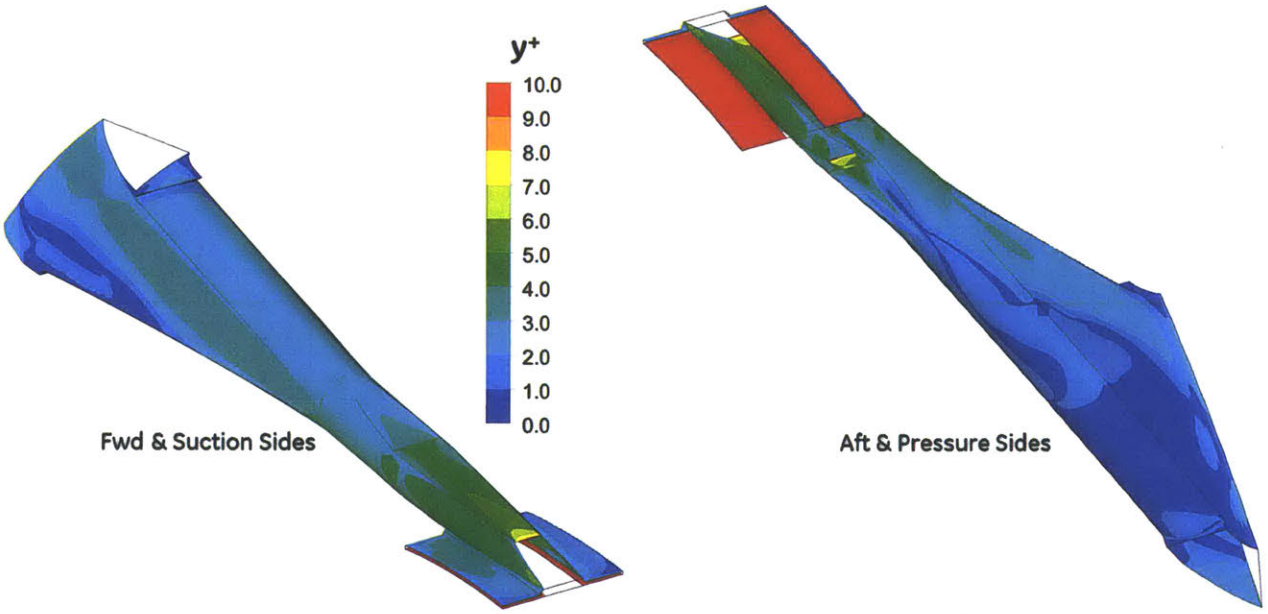


Figure 2.15: Unstructured baseline diffuser grid $y^+$ levels at 100E operating point. Levels are generally appropriate for capturing boundary layer physics. Reduced $y^+$ on diffuser inlet suction side relative to structured grid represents improvement. Bleed slot refinement not necessary given research objectives.

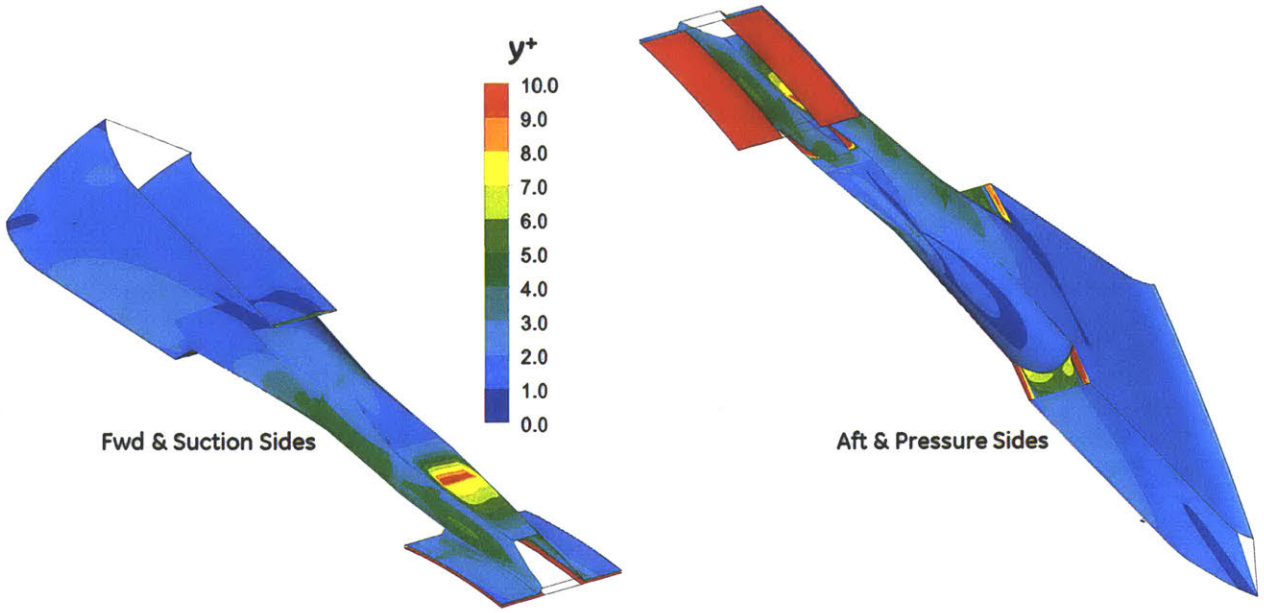


Figure 2.16: Structured truncated diffuser grid $y^+$ levels at 100E operating point. Levels are generally appropriate for capturing boundary layer physics. Local region of high $y^+$ on diffuser inlet suction side due to locally high flow velocities. Bleed slot refinement not necessary given research objectives.

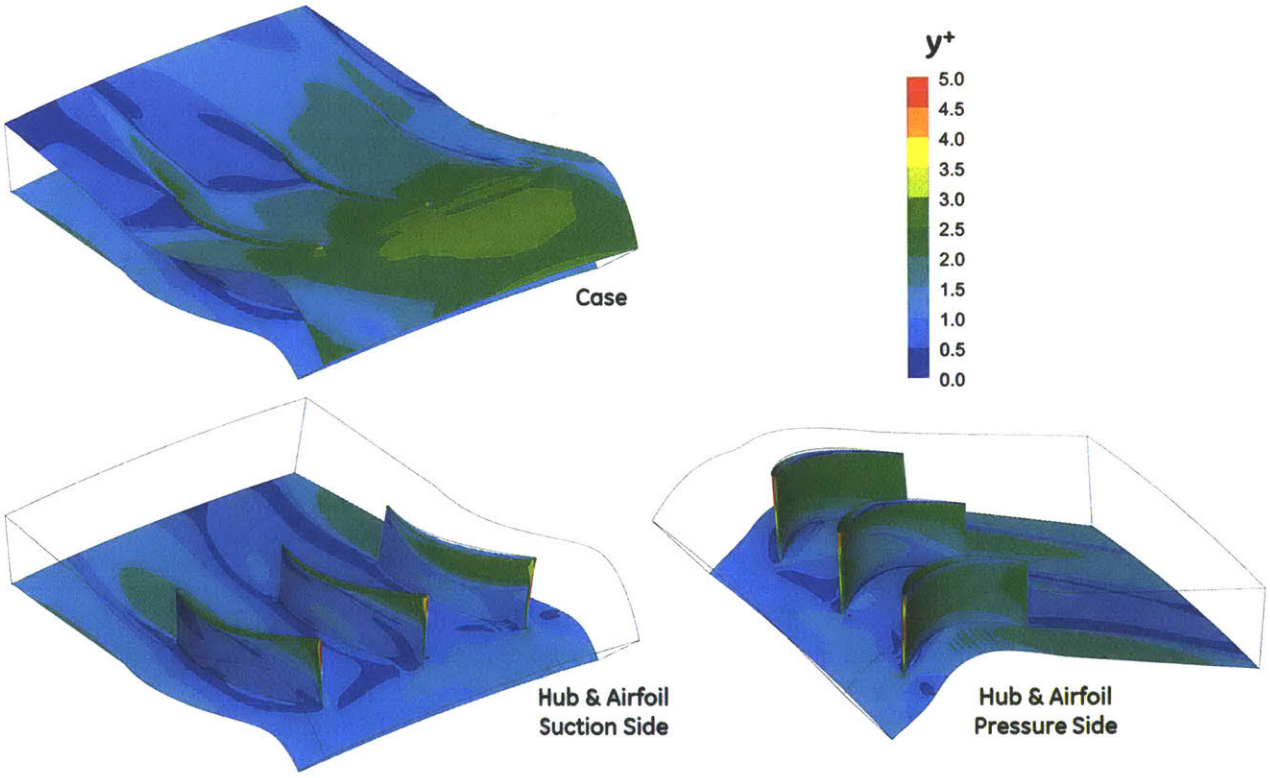


Figure 2.17: Deswirler grid $y^+$ levels at 100E operating point. Levels are appropriate for capturing boundary layer physics.

### 2.5.2 Summary of CFD Cases

CFD simulations are performed for both the baseline and truncated diffusers at 80% $N_{c25}$ and 100% $N_{c25}$. Many simulations are performed at different throttle points along each speed line ranging from choke to stall. Some simulations are even successfully performed at a higher operating line than where the experimental compressor rig stalled, giving insight into possible stall-initiating flow mechanisms.

Additional CFD studies are performed to investigate specific modeling effects or flow mechanisms. Some simulations are performed with an unstructured baseline diffuser grid to examine grid sensitivity effects. Also, to understand the source of vorticity and secondary flows in the diffuser passage, a simulation excluding the impeller is performed on just the diffuser and deswirler utilizing uniform impeller outflow conditions and free-slip diffuser wall boundary conditions. The results of these studies are detailed in Sections 3.3.2 and 6.5.7.3 respectively.

### 2.5.3 CFD Post-processing

The CFD results are post-processed in different ways so as to accommodate each specific objective. First, in order to assess the CFD results relative to the data, the solutions are probed in the same way measurements are taken in the compressor rig. This is done to replicate the static pressure measurements distributed circumferentially near the impeller exit and diffuser leading edge, and those distributed along the diffuser centerline.

For determining changes in high-level performance trends between operating points and diffuser configurations, 1D averaged flow properties are calculated as described in Section 2.2. CFD averaging planes are placed at the major compressor stations described in 2.1, aligned with the test instrumentation or traverses at those stations. Averaging stations are also distributed throughout the entire diffuser, oriented both circumferentially and normal to the diffuser passage centerline as shown in Figure 2.18. An additional circumferential averaging plane is utilized at the impeller trailing edge (station 27) on the impeller side of the mixing plane. This means that any 1D control volume analysis performed on the impeller excludes the mixing plane, but diffuser control volumes beginning at station 27 do include the mixing plane.

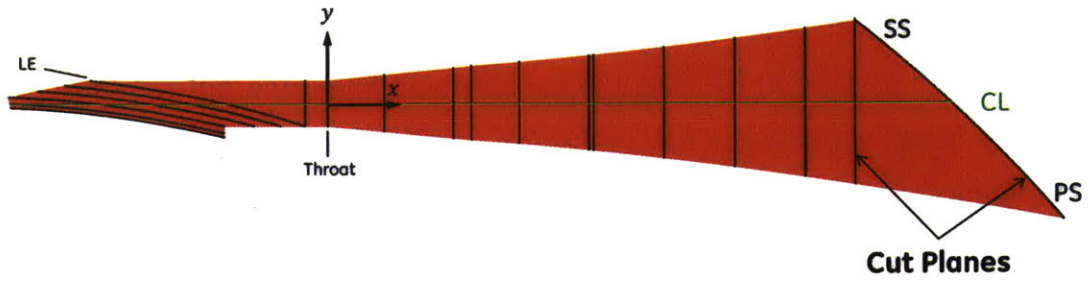


(a) Baseline diffuser.

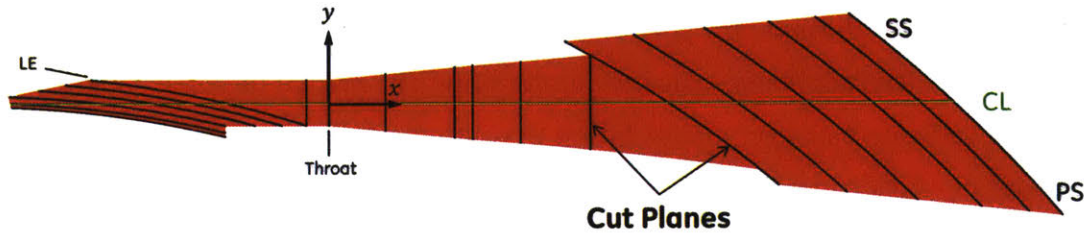


(b) Truncated diffuser.

Figure 2.18: Cut planes used for 1D averaging of diffuser CFD solutions.

The CFD solutions are also post-processed to visualize 3D flow features and spatial distributions of flow properties. This is accomplished by viewing contour plots of flow properties and by viewing vector fields as arrows along evenly spaced cut planes perpendicular to the diffuser passage centerline and compressor centerline, shown in Figure 2.19. These same diffuser throughflow positions are also used to measure boundary layer properties on the diffuser mid plane, $z_2$. Streamlines and vortex lines are viewed in 3D. Although the CFD model is a mirrored version of the actual compressor rig, with the impeller rotating in the opposite direction, the attempt is made to mirror these spatially-dependent CFD results in a way that is consistent with the rig geometry. However, mirroring does not maintain a right-handed coordinate system, so some vector quantities, such as vorticity, can appear to be in the wrong direction.

As discussed in Section 2.4.3.3, additional post-processing of the 100E baseline diffuser CFD results is conducted to develop closure parameters used in post-processing the test data to estimate impeller exit conditions. These closure parameters include impeller inlet and exit mass and angular momentum blockages, the impeller shroud torque as a fraction of rotor torque, and correction factors for the impeller exit radial and axial pressure gradient estimates.

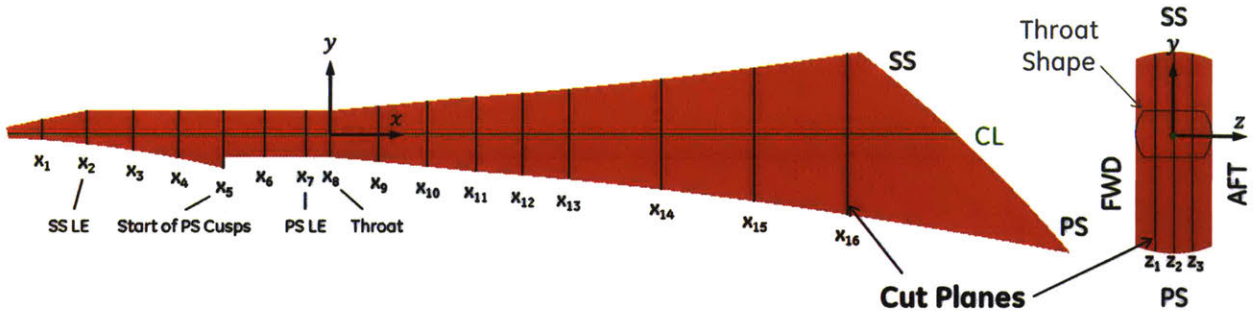


Figure 2.19: Cut planes used for 3D flow field visualization of CFD solutions (baseline diffuser shown). *Left*: planes perpendicular to diffuser passage centerline. *Right*: planes perpendicular to compressor centerline.

## 2.6 Low-Order Flow Modeling

Low-order flow models are developed and utilized to quantify the importance of specific flow mechanisms observed in the CFD while eliminating confounding effects from other mechanisms. Specific effects that are characterized by low-order models include the impacts of inlet flow angle, nonuniformity amplification, nonuniformity mixing, trailing edge solid blockage, and compressibility on the loss and pressure rise in a diffuser. Additionally, a simple model is used to estimate the impact of secondary flows on transverse boundary layer compression in the diffuser, and a modified integral boundary layer model is utilized to estimate the subsequent impact on boundary layer growth and separation. Each model will be described in the sections where they are utilized.

## 2.7 Modular Perspective of Diffusion System

To help differentiate the effects of the many flow mechanisms that contribute to the performance of the centrifugal compressor, the diffusion system is approached from a modular perspective. In this way, the performance, exit conditions, and flow mechanisms present within each module are characterized independently in terms of each module's respective inlet conditions and geometry.

This approach is illustrated in Figure 2.20. Of course, the compressor consists of the impeller, diffuser and deswirler. However, the diffuser itself is further broken down into two sub-components: the diffuser inlet and passage. The diffuser inlet is defined here to extend from the impeller exit (station 27) to the diffuser throat (station T). This is the region which is directly influenced by variations in the impeller exit flow angle. The diffuser

passage is defined here to extend from the diffuser throat (station T) to the trailing edge of the baseline diffuser (station 29). This is the region which differs geometrically between the baseline and truncated diffusers.

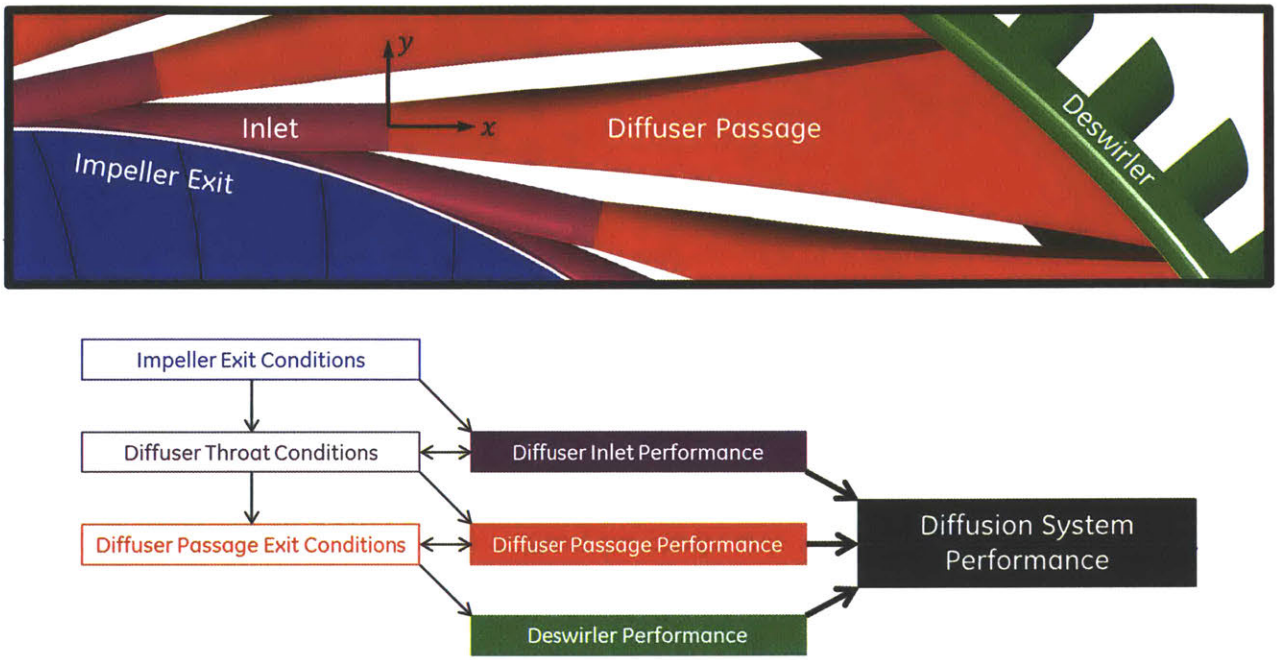


Figure 2.20: Modular perspective of diffusion system. Approach is to understand dependence of each component's performance and exit conditions on influential inlet conditions by characterizing underlying flow mechanisms.

The performance of the overall compressor is summarized in Chapter 3. The impeller performance and exit conditions are then characterized in Chapter 4, and the diffusion system is characterized in Chapter 6. The diffuser inlet and passage are individually characterized in Sections 6.5 and 6.6 respectively. Finally, the overall compressor stability is addressed in Chapter 7, synthesizing the combined effects of the individual components.

## 2.8 Summary of Research Approach

The research approach consists of interrogating in depth a set of experimental data acquired on a research compressor stage rig and a set of well-designed CFD computations, complemented by reduced order flow modeling, directed at addressing the research questions posed. The experimental data is primarily used to determine high-level 1D performance results and trends and to assess where CFD may be used as a tool for detailed investigation. Where CFD and experimental results are determined to follow the same trends, CFD is used to further understand the details of the flow mechanisms present at the 3D

level. Additionally, measurements made from CFD results are used to guide another level of data reduction, allowing for a more useful interpretation of the data. Lastly, low-order models are developed and utilized to quantify the importance of specific flow mechanisms observed in the CFD without confounding effects from other mechanisms, and to gain insight into the process by which these mechanisms influence performance. To simplify the assessment approach and explanation of the compressor performance trends, the compressor is broken into a number of modules which are characterized independently: the impeller, the diffuser inlet, the diffuser passage, and the deswirler. The overall compressor performance characteristics—most notably the stability characteristics—are explained in terms of the specific flow mechanisms present within each module, as well as the interactions between modules.

# Chapter 3 Overall Compressor Performance Assessment

## 3.1 Operating Point Definition

In order to compare CFD results with experimental data, a common operating point definition must first be established. This is important because the experimental measurements and CFD solutions do not match everywhere throughout the compressor. For example, the impeller performance differs between the experiment and CFD. As a result, establishing the compressor operating point based on impeller inlet conditions will mean that the diffuser inlet conditions differ between the experiment and CFD. Since characterizing the performance of the diffusion system is of primary concern, and because Filipenco [9] and Everitt [10] have both determined that diffuser inlet flow angle is the primary variable establishing diffuser performance, it is appropriate to use diffuser inlet flow angle to establish operating point similarity. Impeller corrected speed is also used to define the operating point.

The diffuser inlet flow angle is not measured in the experiment, but it is estimated using the post-processing methodology outlined in Section 2.4.3.3. Instead of relying on this estimation alone to establish diffuser inlet flow angle similarity between CFD and the experiment, the static pressure distribution in the diffuser inlet region can be used as a surrogate for flow angle (assuming stagnation pressure distributions are also similar). The flow angle influences the diffuser inlet static pressure distribution in two major ways. First, the circumferential distribution of static pressure at the diffuser leading edge is affected by the incidence angle; a high flow angle and corresponding positive diffuser incidence means the diffuser suction side experiences a lower static pressure than the pressure side at the leading edge. Second, the streamwise distribution of static pressure is observed to vary from the impeller exit to the diffuser throat as flow angle variations heavily influ-

ence the distribution of effective area ratio throughout the diffuser inlet; a high inlet flow angle means the flow is less perpendicular to the radial impeller exit plane and must diffuse throughout the inlet region to the throat where the flow angle and area are more constrained by the passage geometry. This effect is elaborated on further in Section 6.5.5.

Figure 3.1 shows the locations where the static pressure distributions are interrogated. Figure 3.2 and Figure 3.3 show the pressure recovery coefficients plotted at the diffuser leading edge and along the diffuser centerline for the choke, peak efficiency, and stall operating points. The CFD simulations that most closely match the experimentally measured diffuser inlet static pressure distributions for each operating point are chosen to be representative of those operating points. Recall that the 100E operating line and thus flow angle are higher for the truncated diffuser than they are for the baseline diffuser. Also recall that there is no 100S stall experimental data for the truncated diffuser, so the most representative CFD simulation is chosen based on extrapolation of the stall line from lower speed data.

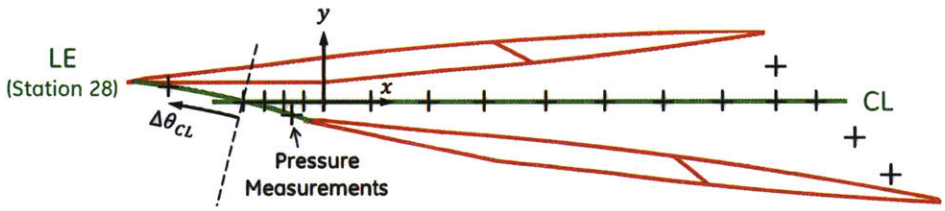


Figure 3.1: Regions along diffuser forward wall where experimental and CFD calculated static pressure distributions are interrogated for comparison.

It is clear that the CFD static pressure distributions do not exactly match the data. It is also apparent that there are some differences between CFD and data in capturing the relative differences between the baseline and truncated diffusers. This is partially because none of the CFD simulations are exactly run to the same operating points as the test. Simulations use deswirler exit static pressure as a boundary condition, which would have to be tediously iterated upon to improve the match in impeller exit flow angle. Nevertheless, these matches are deemed acceptable for considering the CFD operating points to be representative of the experimental operating points. The operating point match will primarily be used to determine the general existence and importance of various flow mechanisms, and their variations between operating points. For comparing 1D performance results between the CFD and experimental data, it is more useful to compare entire speed lines rather than single points. This minimizes the importance of obtaining an exact operating point match.

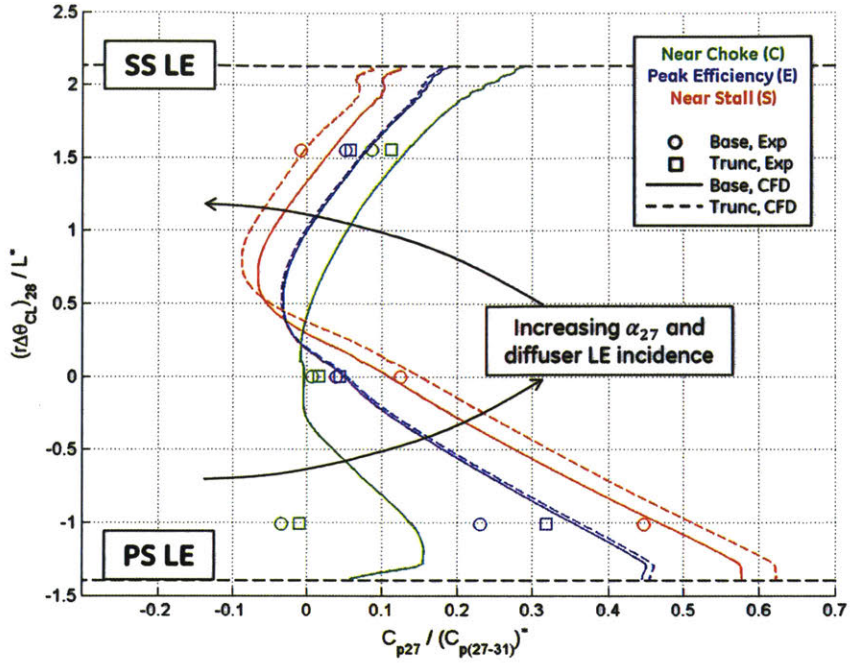


(a) 100% $N_{c25}$.

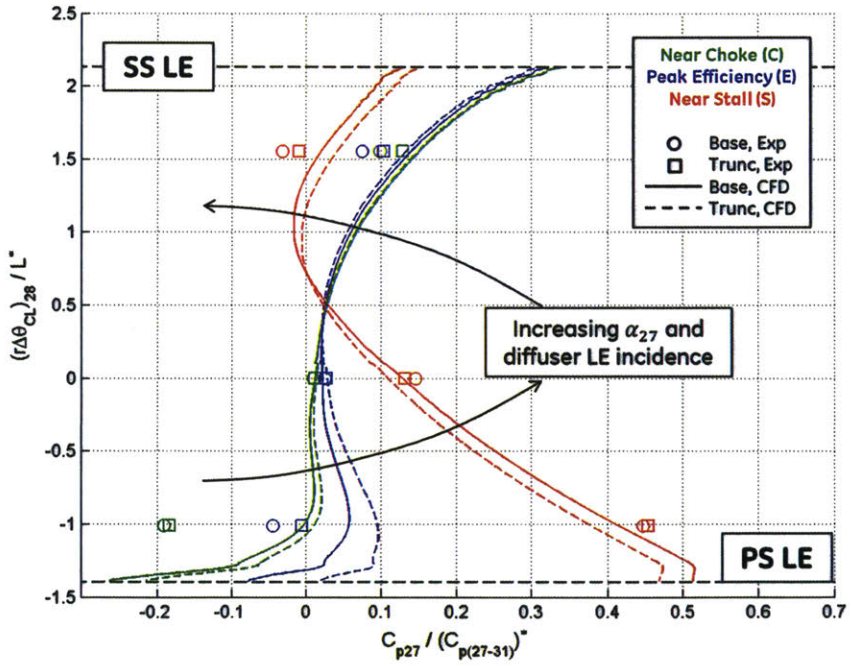


(b) 80% $N_{c25}$.

Figure 3.2: Static pressure recovery coefficient versus circumferential position at diffuser leading edge and forward wall. Symbols and line styles denote diffuser configuration and data source, while colors denote operating point (note: experimental points averaged from multiple tests). Inflow angle influences circumferential gradient of pressure distribution. Pressure gradients exhibited by CFD solutions sufficiently match experimental results, suggesting flow angles also match.

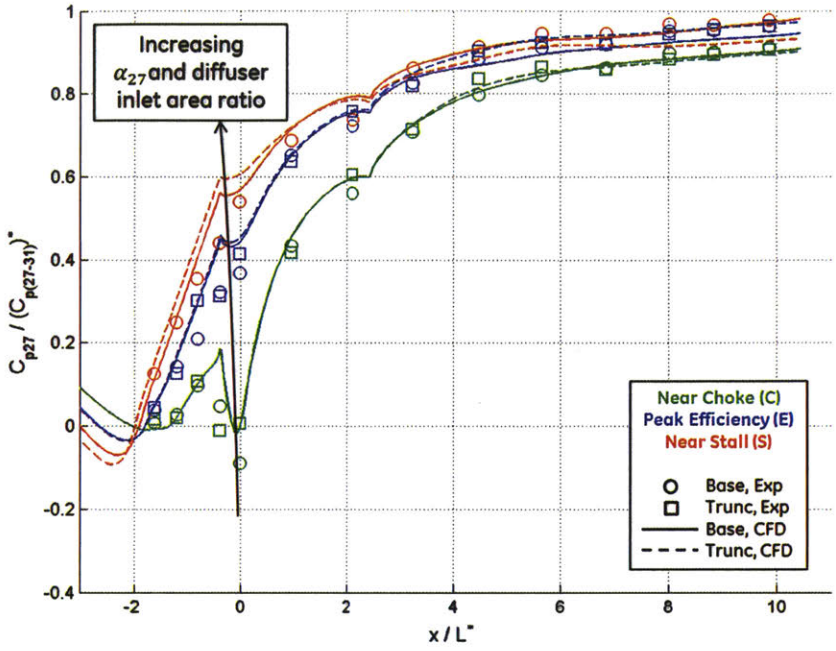


(a) 100% $N_{c25}$.

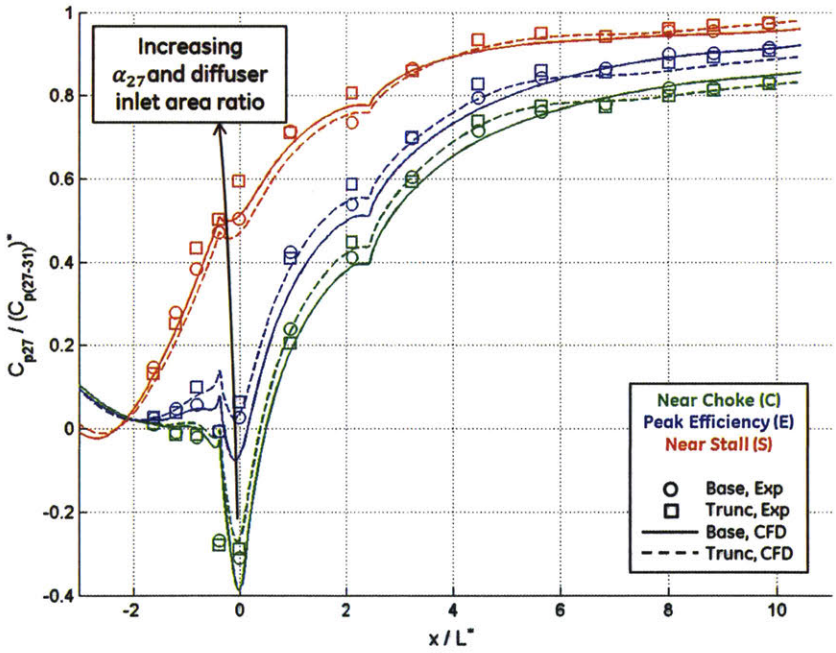


(b) 80% $N_{c25}$.

Figure 3.3: Diffuser static pressure recovery coefficient versus throughflow position along diffuser centerline at forward wall. Symbols and line styles denote diffuser configuration and data source, while colors denote operating point (note: experimental points averaged from multiple tests). Inflow angle influences amount of pressure rise occurring upstream of throat. Throat recoveries exhibited by CFD solutions sufficiently match experimental results, suggesting flow angles also match.

Figure 3.4 shows the 1D impeller exit flow angles calculated at each operating point for both the experiment and CFD. The CFD flow angles come close to matching the experimental estimates at the choke and peak efficiency points, and where mismatches exist they can be explained by actual mismatches in operating point indicated by the static pressure distribution shown in Figure 3.2 and Figure 3.3. Near stall, however, the match in average flow angle is not as good as it appears to be based on Figure 3.2 and Figure 3.3. This may be attributed to reduced off-design applicability of the simplifying assumptions of the experimental impeller exit condition estimation, or of the CFD itself. Another possible explanation is that this is due to a reduced sensitivity of the inlet static pressure distribution to flow angle near stall as shown in Section 6.5 (throat blockage increases with flow angle to negate the impact on diffuser inlet effective area ratio).

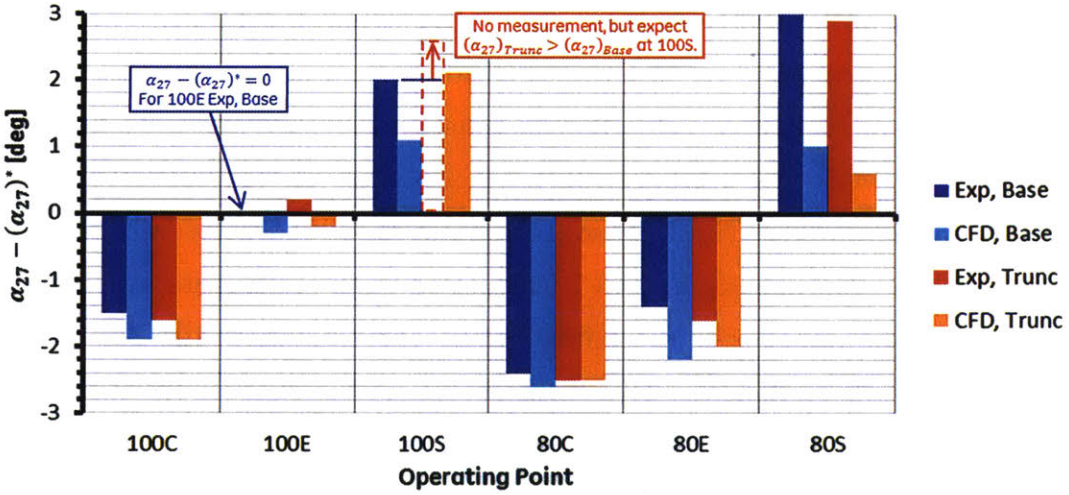


Figure 3.4: 1D average impeller exit flow angles at major operating points (note: experimental points averaged from multiple tests). CFD solutions sufficiently match experimental results, though differences are present.

## 3.2 Overall Compressor Performance

Although this research primarily focuses on the detailed flow mechanisms in the diffuser, it is important to understand the performance of the overall compressor for the following reasons. First, compressor stability is not determined by the diffusion system alone but by the combination of impeller and diffusion system performance characteristics. Second, determining the overall performance of the experimental compressor requires fewer assumptions than determining the performance of the impeller and diffusion system individually. The

latter requires that the impeller exit flow properties be estimated as discussed in Section 2.4.3.3.

Figure 3.5 shows the stagnation pressure ratio and polytropic efficiency maps for this compressor as a function of compressor inlet corrected flow. Experimental and CFD results are shown for both baseline and truncated diffuser configurations. Data points are color-coded according to corrected speed, consistent with many other figures in this thesis. Between 80% $N_{c25}$ and 95% $N_{c25}$, the experimental data shows that the compressor with the truncated diffuser has an improved stability line over the baseline diffuser. While the truncated diffuser configuration wasn't throttled to stall at 100% $N_{c25}$, an estimate of the 100% $N_{c25}$ stall point is estimated by extrapolating the stability line improvement observed between 80% $N_{c25}$ and 95% $N_{c25}$. This estimate is necessary for selecting the CFD solution that is representative of the 100S operating point for the truncated diffuser.

Relative to the experimental results, the CFD calculates a higher pressure ratio at constant corrected flow, or higher corrected flow at constant pressure ratio. To help diagnose this, the compressor work and pressure rise coefficients are plotted against impeller exit flow coefficient in Figure 3.6. The CFD overestimates these characteristics as well. The discrepancy between experimental and CFD calculated work coefficients must be due to a discrepancy within the impeller or the mixing plane approximation; the diffusion system does not influence work coefficient. This work coefficient discrepancy must contribute at least partially to the pressure rise coefficient discrepancy.

The CFD also calculates a higher efficiency than the experiment, as shown in Figure 3.7. Along with the higher work coefficient, this contributes to the higher overall compressor pressure rise coefficient. It is not possible to know whether CFD's overestimation of efficiency is occurring in the impeller or the diffuser, but it is reasonable to infer that the impeller plays a role since an inaccuracy has already been identified with the work coefficient calculation. As a check on the efficiency calculation, a second efficiency calculation is performed using the compressor exit static pressures. This is insightful because the distribution of static pressure is more spatially uniform than stagnation pressure, removing the sensitivity of the 1D average to the measurement locations. Furthermore, the compressor exit static pressure is more representative of the compressor's pressure rise after undergoing a dump loss in the combustor plenum. Both efficiency definitions are shown in Figure 3.7. Clearly, both show similar trends and differences between the experiment and CFD.

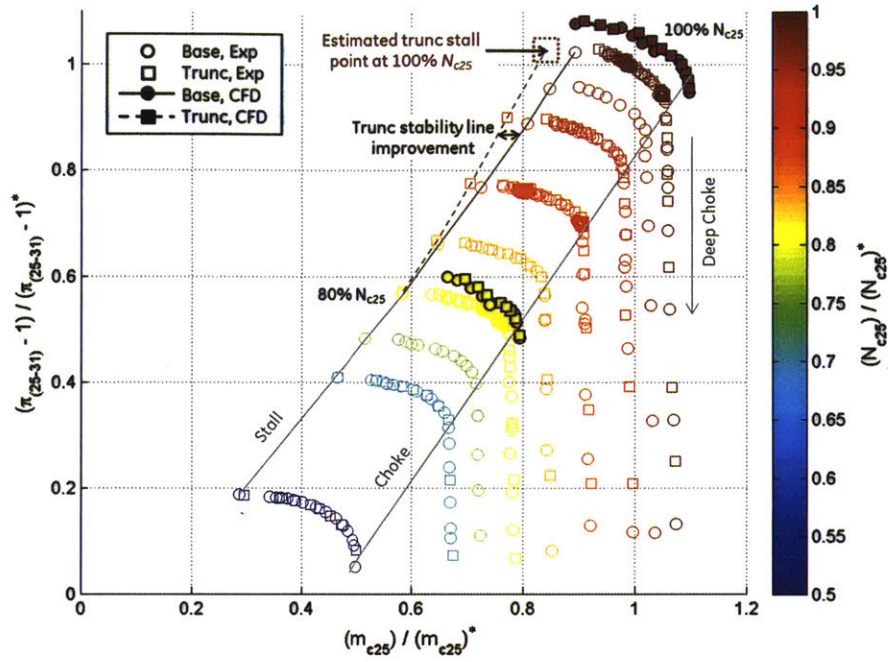


(a) Overall compressor stagnation pressure ratio versus inlet corrected mass flow.

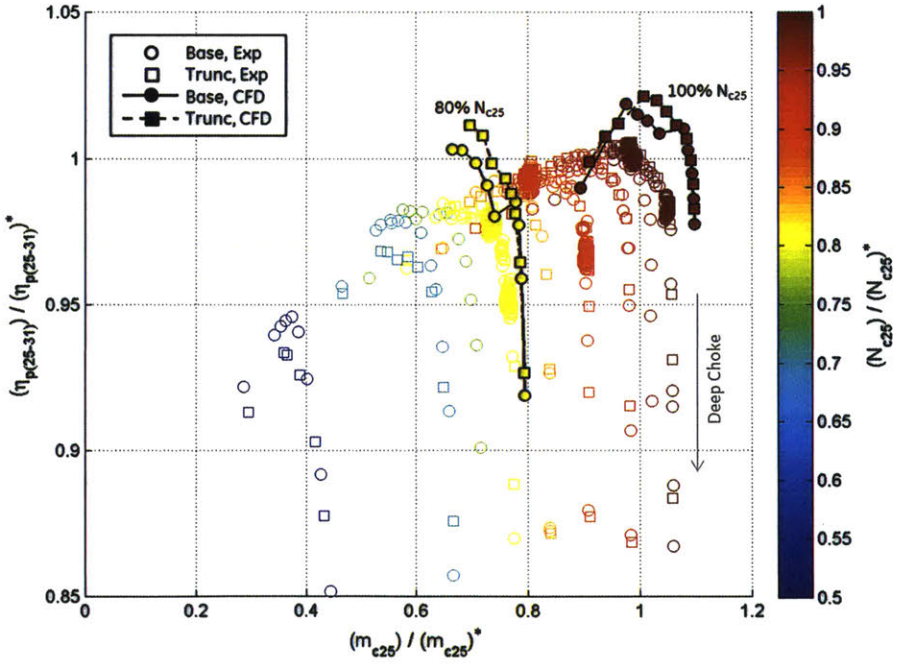


(b) Overall compressor polytropic efficiency versus inlet corrected mass flow.

Figure 3.5: Overall compressor performance versus inlet corrected mass flow. Symbols and line styles denote diffuser configuration and data source, while colors denote rotor speed. Stability line of truncated diffuser configuration is improved relative to baseline diffuser configuration. CFD solutions overestimate pressure ratio and efficiency, but capture overarching trends.

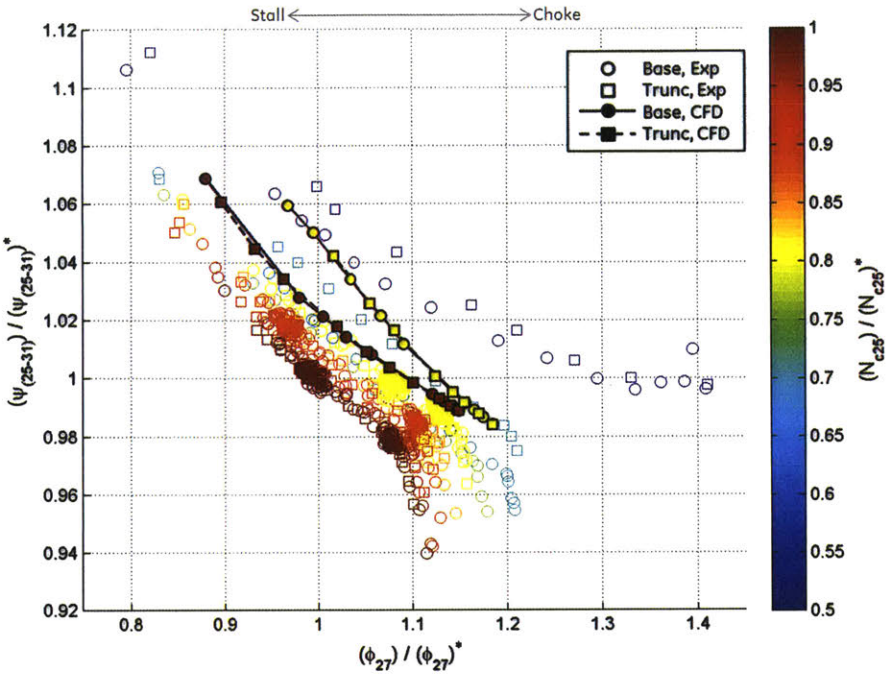


(a) Overall compressor work coefficient versus impeller exit flow coefficient.

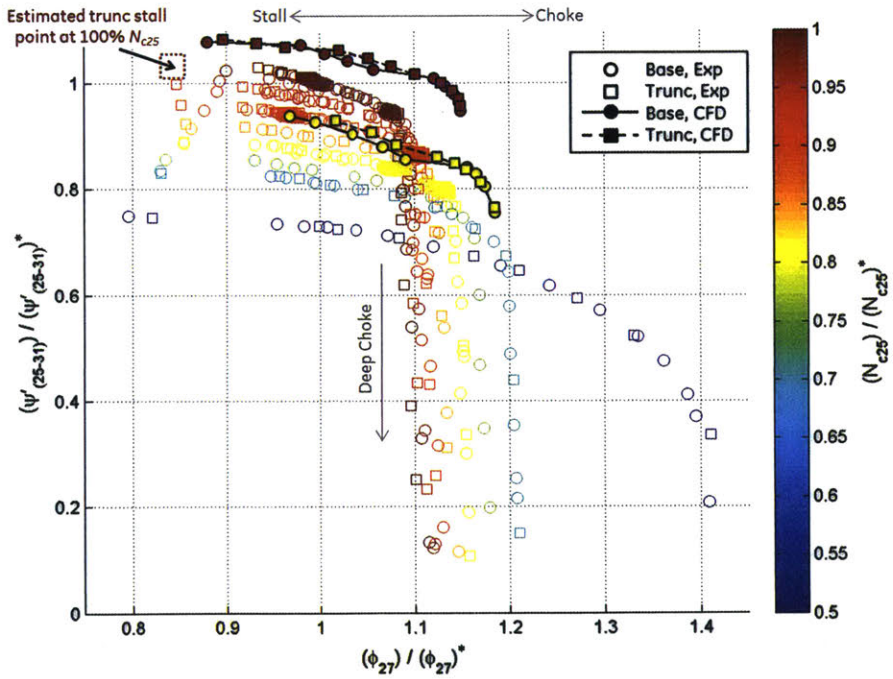


(b) Overall compressor pressure rise coefficient versus impeller exit flow coefficient.

Figure 3.6: Overall compressor performance versus impeller exit flow coefficient. Symbols and line styles denote diffuser configuration and data source, while colors denote rotor speed. Stability line of truncated diffuser configuration is improved relative to baseline diffuser configuration. CFD solutions overestimate work coefficient and pressure rise coefficient, but capture overarching trends.

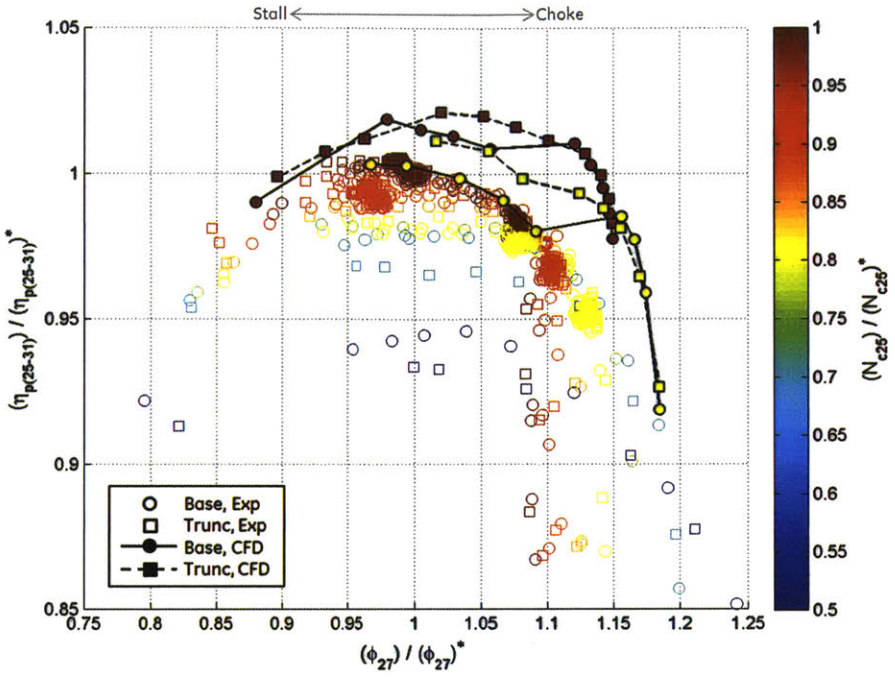


(a) Compressor polytropic efficiency based on deswirler exit stagnation pressure.

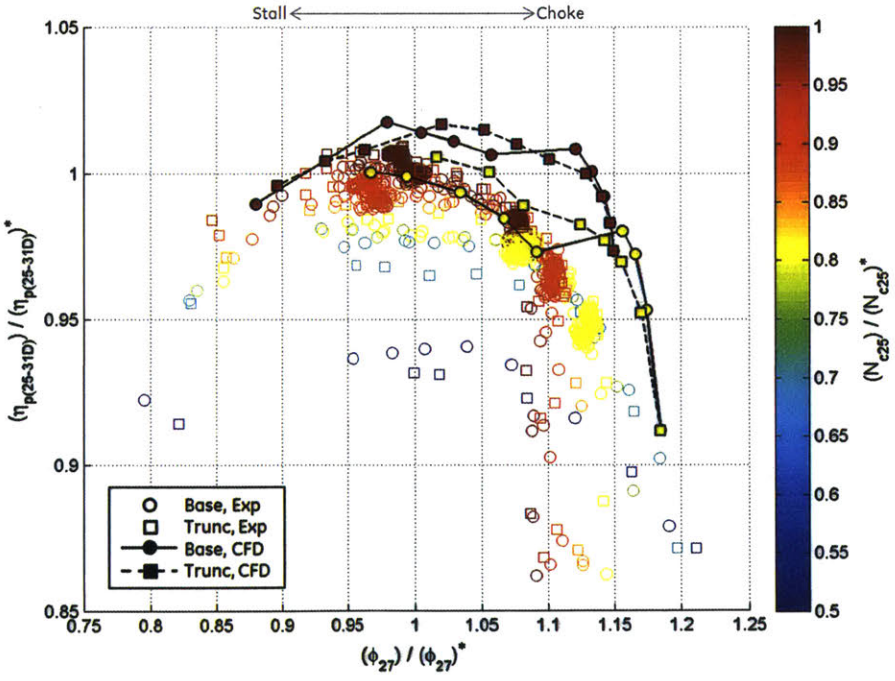


(b) Compressor polytropic efficiency based on deswirler exit stagnation pressure.

Figure 3.7: Overall compressor polytropic efficiency versus impeller exit flow coefficient. Symbols and line styles denote diffuser configuration and data source, while colors denote rotor speed. Trends similar regardless of whether exit static or stagnation pressures are referenced. CFD solutions overestimate efficiency, but capture overarching trends.

To examine these results in more detail, the work coefficients, pressure rise coefficients, and polytropic efficiencies are plotted for 100% $N_{c25}$ and 80% $N_{c25}$ separately in Figure 3.8, Figure 3.9, and Figure 3.10 respectively. The choke, peak efficiency, and near stall operating lines are highlighted along each speed line for the CFD results and the average of the experimental results. The 100S truncated diffuser CFD solution is selected to give a stability line improvement over the 100S baseline diffuser CFD solution, where this improvement is estimated by extrapolating lower speed experimental results as previously discussed.

Looking at the experimental results, the high speed stability line improvement is the most apparent benefit of the truncated diffuser relative to the baseline diffuser configurations. There is also an apparent polytropic efficiency benefit of approximately 0.5% for the truncated diffuser. However, in Section 4.1 this is shown to partially be the result of an impeller improvement hypothesized to be unrelated to the diffuser configuration. There are also some notable differences between the 100% $N_{c25}$ and 80% $N_{c25}$ experimental results. First, the compressor efficiencies are reduced at 80% $N_{c25}$ relative to 100% $N_{c25}$. Second, the throttle range is improved on the choke side for both diffuser configurations at 80% $N_{c25}$. Meanwhile, on the stall side, the truncated diffuser stalls at roughly the same flow coefficient between 100% $N_{c25}$ and 80% $N_{c25}$ while the baseline diffuser stalls at a lower flow coefficient at 80% $N_{c25}$. As a result, the stability line difference observed at high speed between the baseline and truncated diffuser configurations no longer exists at 80% $N_{c25}$. The observation make the 100% $N_{c25}$ and 80% $N_{c25}$ speed lines good case studies for understanding the compressor stall mechanisms.

The CFD solutions show some notable similarities and differences relative to the experimental results. First, notice that stable CFD solutions are able to be found at higher throttle points than those corresponding to the near stall experimental points. At 100% $N_{c25}$, these post-stall operating points are denoted 100S', and they are examined in more detail to understand what flow mechanisms are at play near stall. Regarding the work coefficients shown in Figure 3.8, it is clear that the CFD shows no difference between diffuser configurations, supporting the idea that altering the downstream side of the diffuser should not influence the impeller performance characteristics. At 100% $N_{c25}$, the CFD captures the slope of the work coefficient speed line from choke to stall, while its 80% $N_{c25}$ characteristic is slightly steeper than the experimental characteristic.

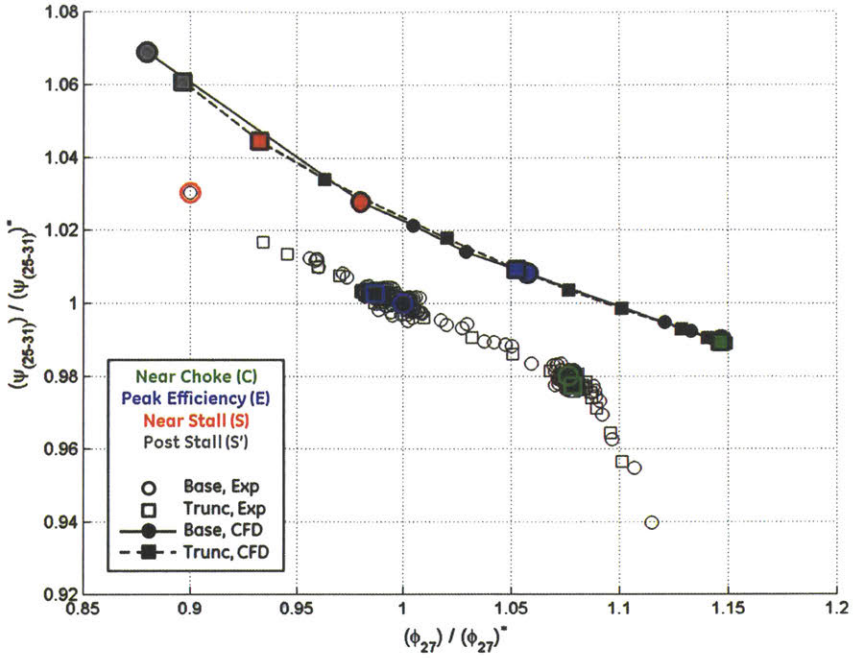


(a) 100% $N_{c25}$.

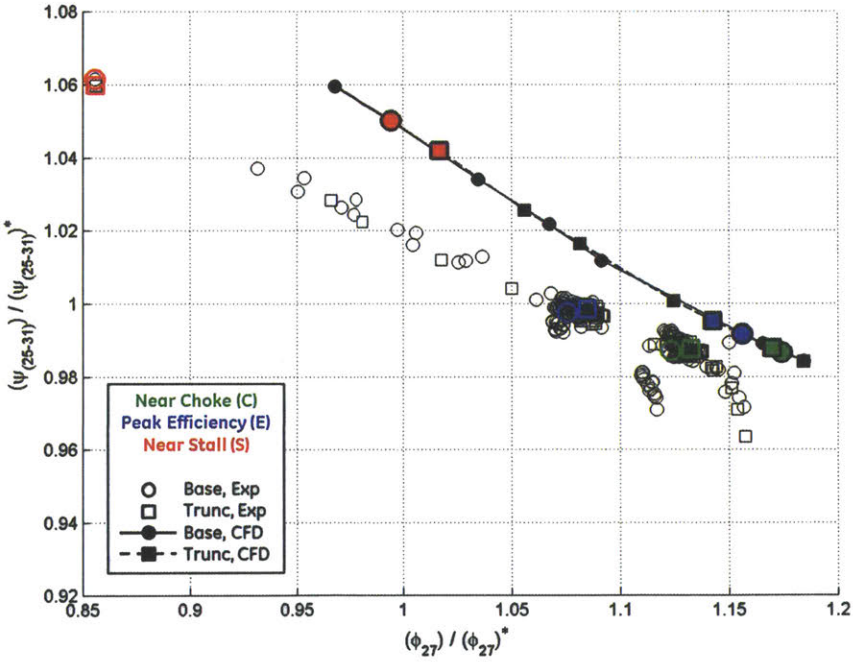


(b) 80% $N_{c25}$.

Figure 3.8: Overall compressor work coefficient versus impeller exit flow coefficient. Symbols and line styles denote diffuser configuration and data source, while colors denote operating point (note: colored experimental points averaged from multiple tests). Experimental and CFD results indicate no difference in characteristics between diffuser configurations. Characteristics also similar between 100% $N_{c25}$ and 80% $N_{c25}$.

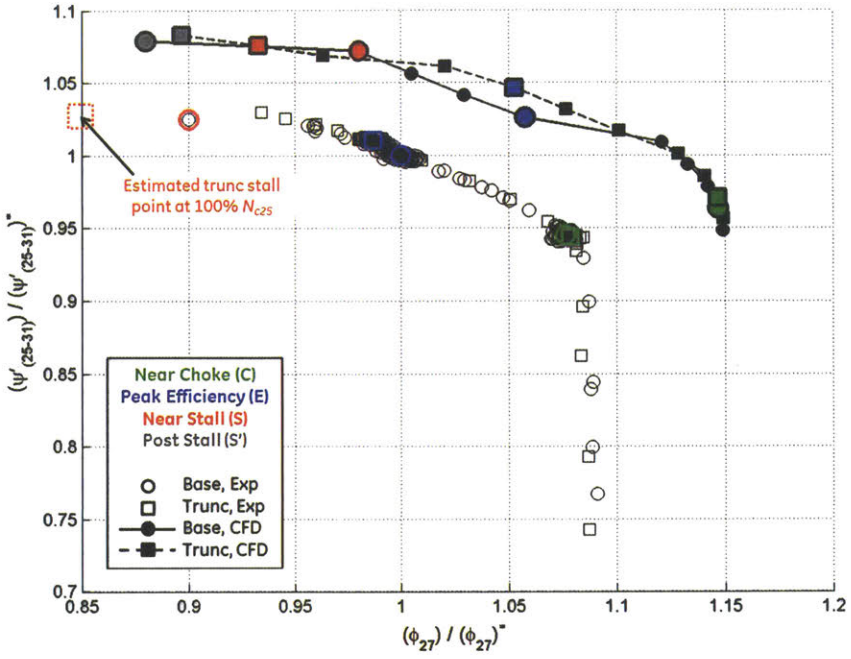


(a) 100% $N_{c25}$.

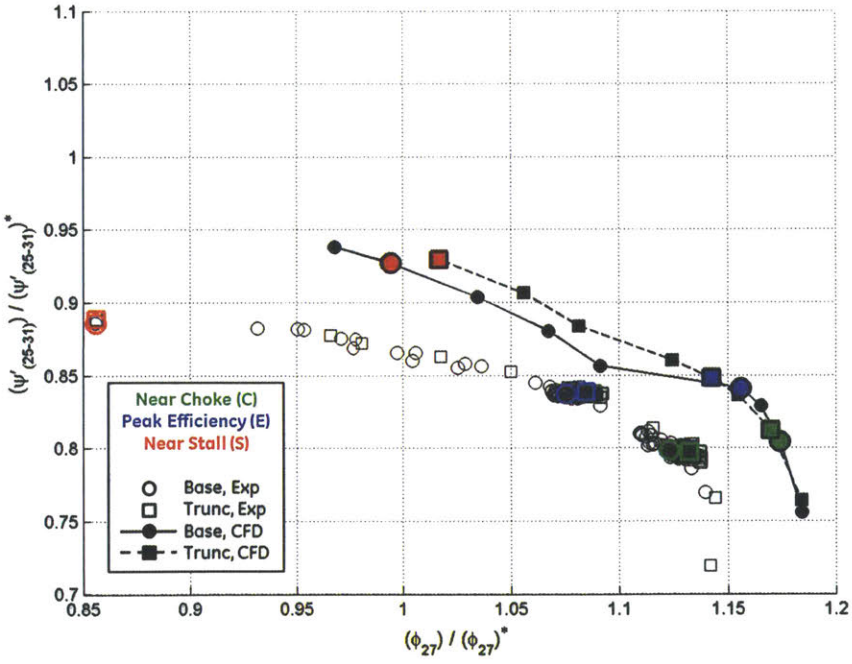


(b) 80% $N_{c25}$.

Figure 3.9: Overall compressor pressure rise coefficient versus impeller exit flow coefficient. Symbols and line styles denote diffuser configuration and data source, while colors denote operating point (note: colored experimental points averaged from multiple tests). Experimental results indicate negligible benefit of truncated diffuser. Note piecewise appearance of CFD solutions.

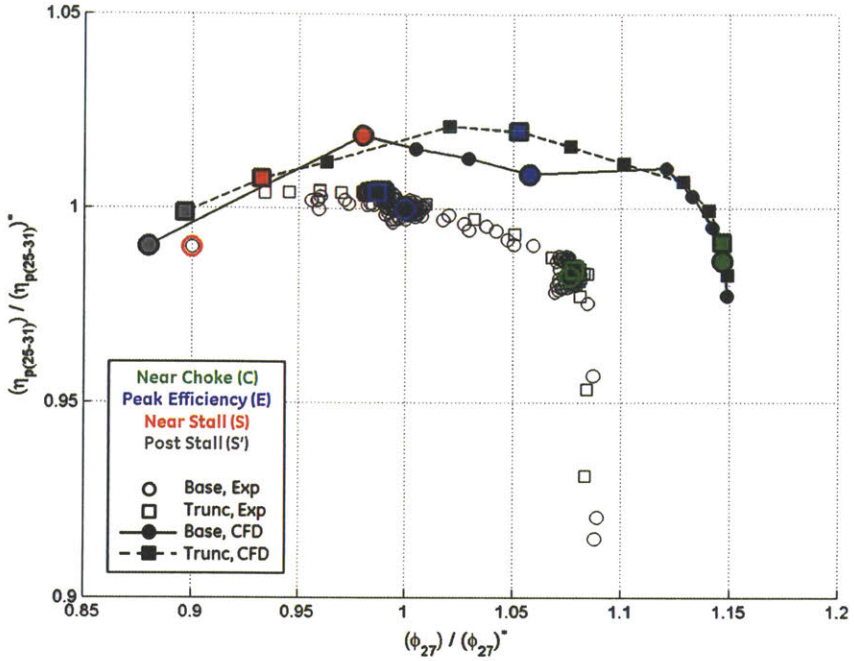


(a) 100% $N_{c25}$.

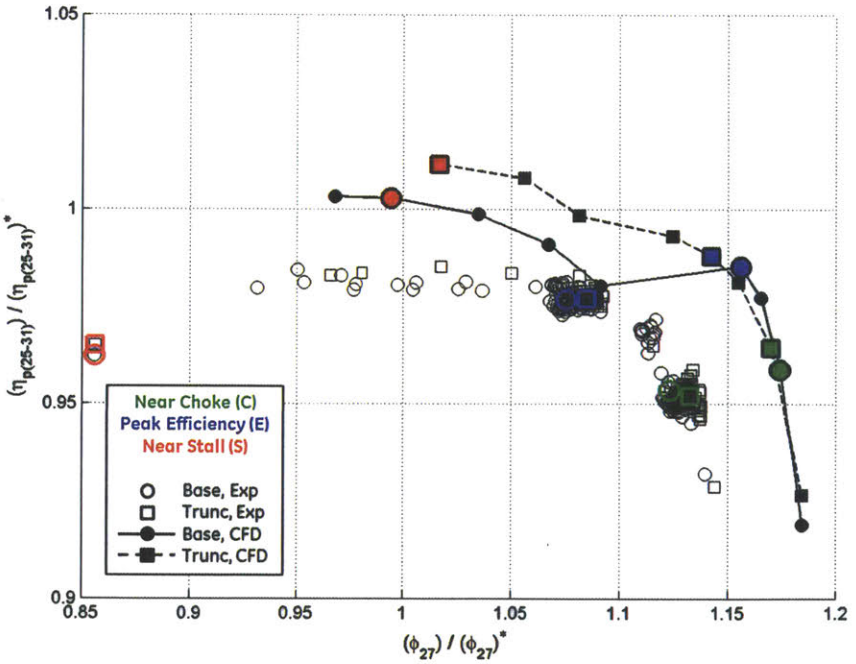


(b) 80% $N_{c25}$.

Figure 3.10: Overall compressor polytropic efficiency versus impeller exit flow coefficient. Symbols and line styles denote diffuser configuration and data source, while colors denote operating point (note: colored experimental points averaged from multiple tests). Experimental results indicate slight benefit of truncated diffuser configuration. Note piecewise appearance of CFD solutions.

Regarding the efficiencies shown in Figure 3.10, the CFD does well at capturing the overarching efficiency trend from choke to stall at 100% $N_{c25}$, and it does well at capturing the reduction in efficiency at lower speed. However, CFD estimates that efficiency at 80% $N_{c25}$ continues to improve toward stall, whereas the experiment shows it falling off in the middle of the operating range. Furthermore, the CFD efficiency trends from choke to stall are not smooth as the experiment shows. Rather, they appear piecewise, with distinct regions apparently exhibiting different characteristics. This piecewise appearance is especially true for the baseline diffuser configuration, though it is also true to a lesser degree for the truncated diffuser. The result of this behavior is that the CFD calculates similar efficiencies for the two diffuser configurations near choke and stall, but in the middle of the operating range it calculates 1% lower efficiency for the baseline diffuser configuration. The causes of these trends and their physical relevance must be addressed by examining the impeller and diffuser in more detail.

## 3.3 Utility of CFD Solutions

It is clear that the CFD solutions do not exactly match the experimental data, which is expected to some degree due to approximations and assumptions of CFD simulations (e.g. spatial discretization, geometry simplifications, boundary condition assumptions, flow modeling simplifications, etc.). However, the CFD captures many of the same trends observed in the data, and one would infer that the CFD solutions are nevertheless useful for identifying the flow mechanisms driving these trends, especially in the diffuser. An assessment is made here to show that CFD captures some of the most influential flow mechanisms observed in the experiment, and to show that the computational grid is adequate.

### 3.3.1 Comparison of CFD Flow Field with Detailed Experimental Measurements

To help assess the usefulness of the CFD results, the spatial distribution of stagnation pressure near the diffuser throat and exit are compared with the experimental traverse measurements. As you can see from the 100E operating point comparison in Figure 3.11, Figure 3.12, and Figure 3.13, the experimental and CFD stagnation pressure distributions match quite well. The strength and positions of the high and low loss flow are captured by CFD for both baseline and truncated diffusers near the throat and exit traverse locations,

keeping in mind the fact that the discrete measurement locations probably do not pick up the exact centers of the jets. The CFD also captures the presence of diffuser passage pressure side separations shown in Figure 3.14, which closely match the experimental PIV measurements extensively documented by Zachau et. al. and Kunte et. al. [1] [2] [3] [4]. Similar comparisons are drawn between the CFD and experimental measurements at the 100C, 80E, and 80C operating points, giving confidence in the applicability of the CFD at these points as well. Unfortunately, detailed experimental traverse or PIV measurements are not taken near stall for comparison with CFD.

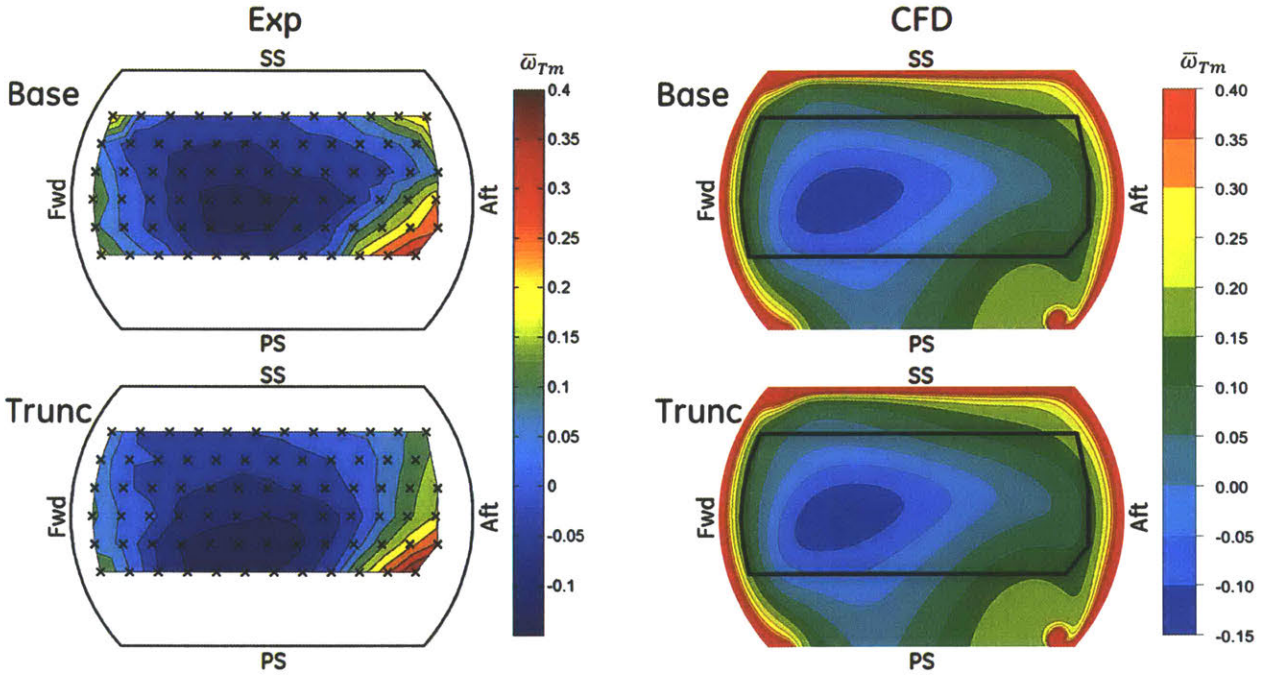


Figure 3.11: Diffuser throat traverse plane (station Tm) stagnation pressure loss coefficient at 100E, $\bar{\omega}_{Tm} = (p_{t(Tm)} - p_t)/(p_{t(Tm)} - p_{(Tm)})$. Experimental and CFD results closely match.

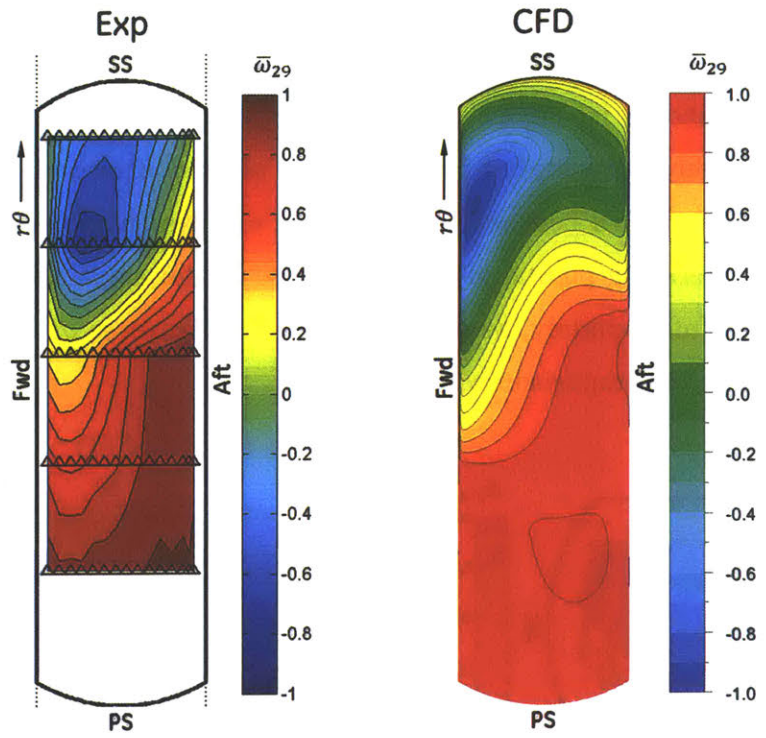


Figure 3.12: Baseline diffuser exit plane (station 29) stagnation pressure loss coefficient at 100E, $\bar{\omega}_{29} = (p_{t29} - p_t)/(p_{t29} - p_{29})$. Experimental and CFD results closely match.

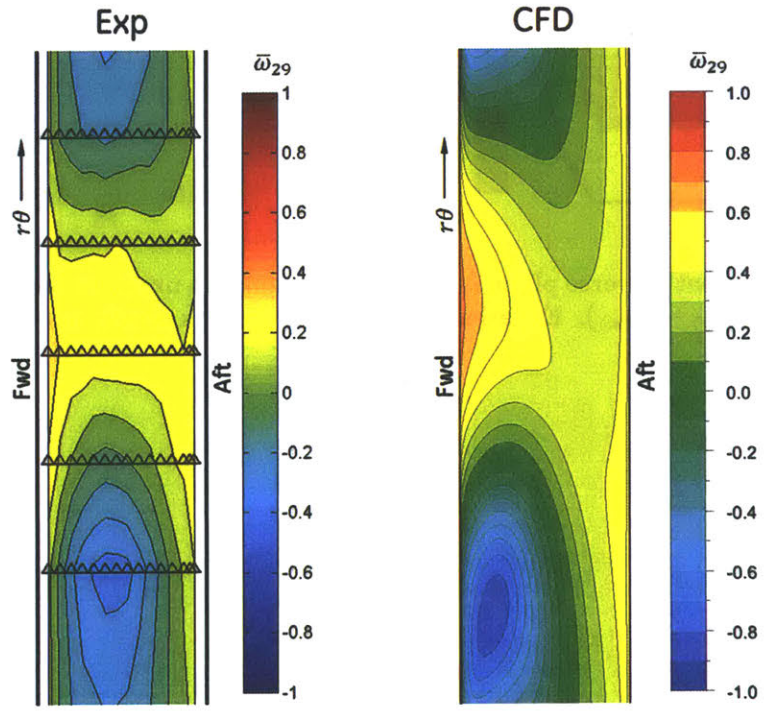


Figure 3.13: Truncated diffuser exit plane (station 29) stagnation pressure loss coefficient at 100E, $\bar{\omega}_{29} = (p_{t29} - p_t)/(p_{t29} - p_{29})$. Experimental and CFD results closely match.

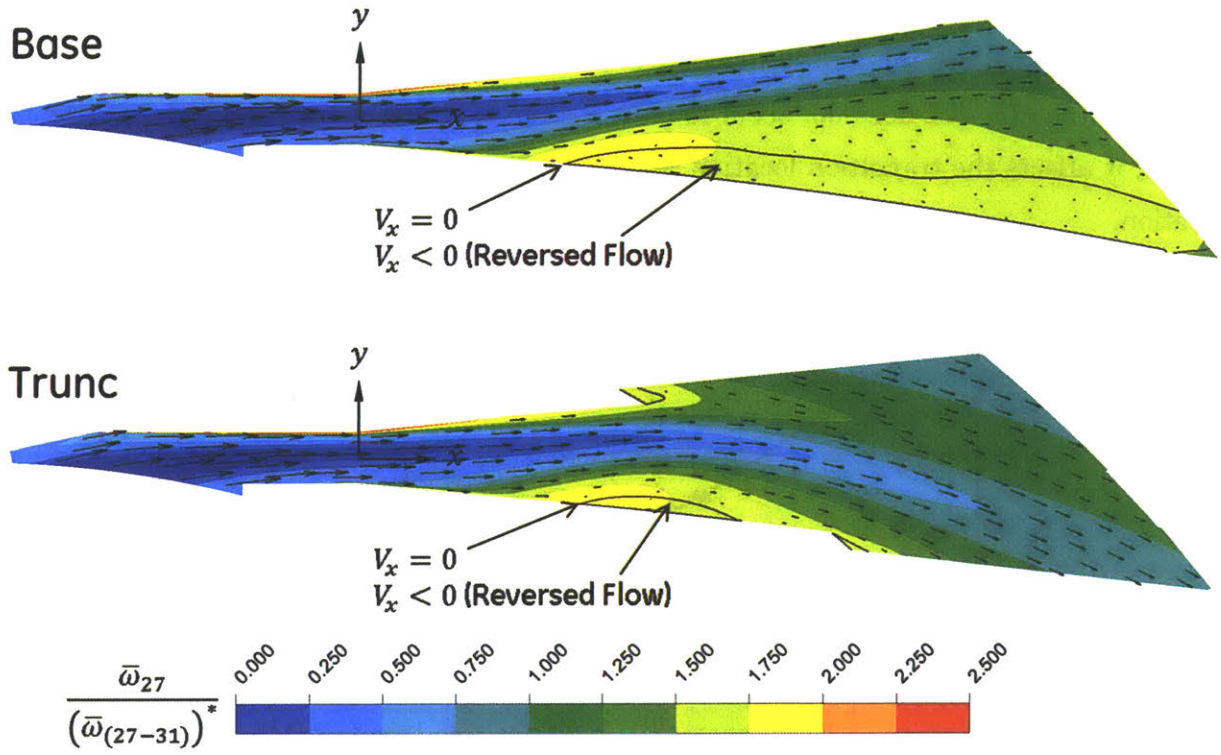


Figure 3.14: CFD calculated diffuser mid plane (Z2) stagnation pressure loss coefficient, velocity vectors, and reversed flow regions at 100E. Known presence of flow reversal is captured by CFD.

### 3.3.2 Effect of Diffuser Grid

To ensure the computational grid is adequate, a 100% $N_{c25}$ speed line is simulated on the baseline diffuser using the unstructured diffuser grid described in Section 2.5.1.4. This unstructured grid is refined more than the structured grid around the diffuser leading edge. The simulations are run with a range of compressor exit static pressure boundary conditions, a subset of the conditions run with the structured diffuser grid.

The CFD calculated compressor work coefficients, pressure rise coefficients, and polytropic efficiencies are shown in Figure 3.15, Figure 3.16, and Figure 3.17 respectively. The work coefficients are identical between the two diffuser grids. The efficiency and pressure rise coefficient are also similar between the two grids. Differences between the structured and unstructured grid results are especially small in comparison to the larger difference between the CFD and experimental results. The trends calculated from both grids are also similar, including their piecewise appearance. Notice that two of the unstructured grid solutions have oscillatory solutions as discussed in Section 2.5.1.2, though only one time-point in the oscillations are shown. These oscillations are hypothesized to be due to the refined

grid, which allows the CFD to resolve small scale flow mechanisms around the diffuser leading edge which are inherently unsteady. This is discussed more in Sections 6.5.7 and 6.6.7. Fortunately, this does not seem to have a large effect on the CFD calculated trends; more so, it affects the transition location between different regimes of steady state diffuser operation.

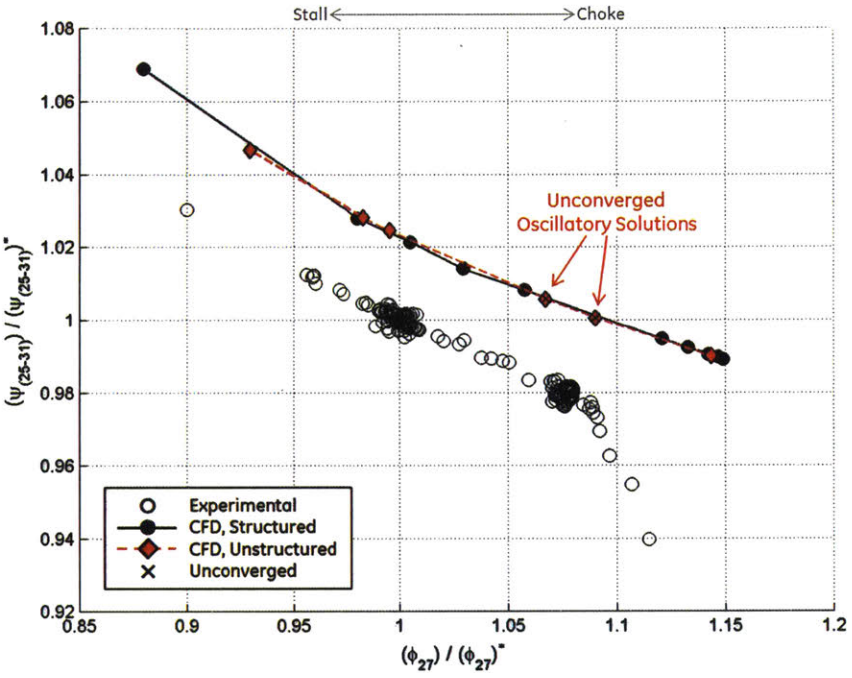


Figure 3.15: Overall compressor work coefficient versus impeller exit flow coefficient at 100% $N_{c25}$. CFD solutions similar for structured and unstructured grids.

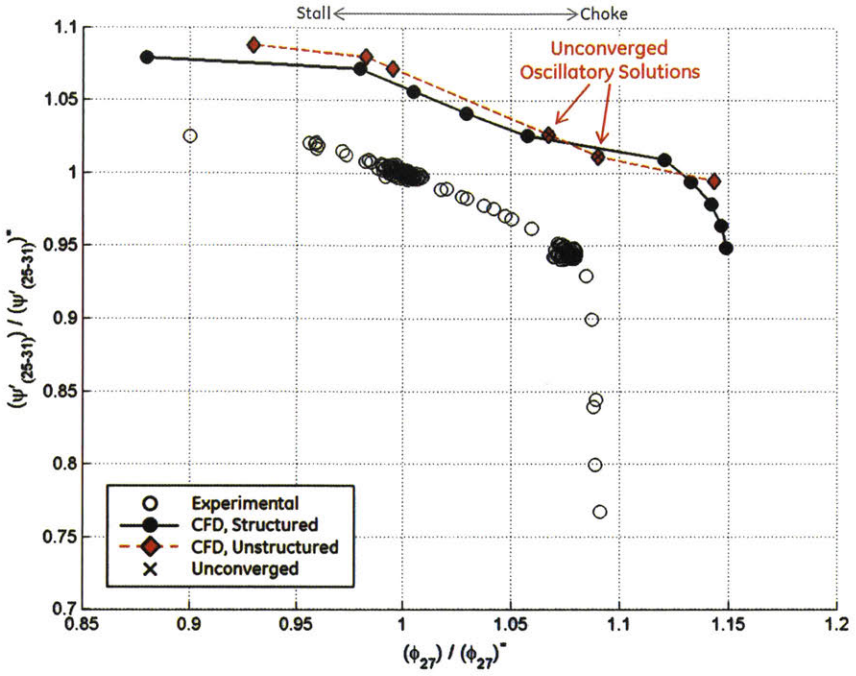


Figure 3.16: Overall compressor pressure rise coefficient versus impeller exit flow coefficient at 100% $N_{c25}$. CFD solutions similar for structured and unstructured grids.

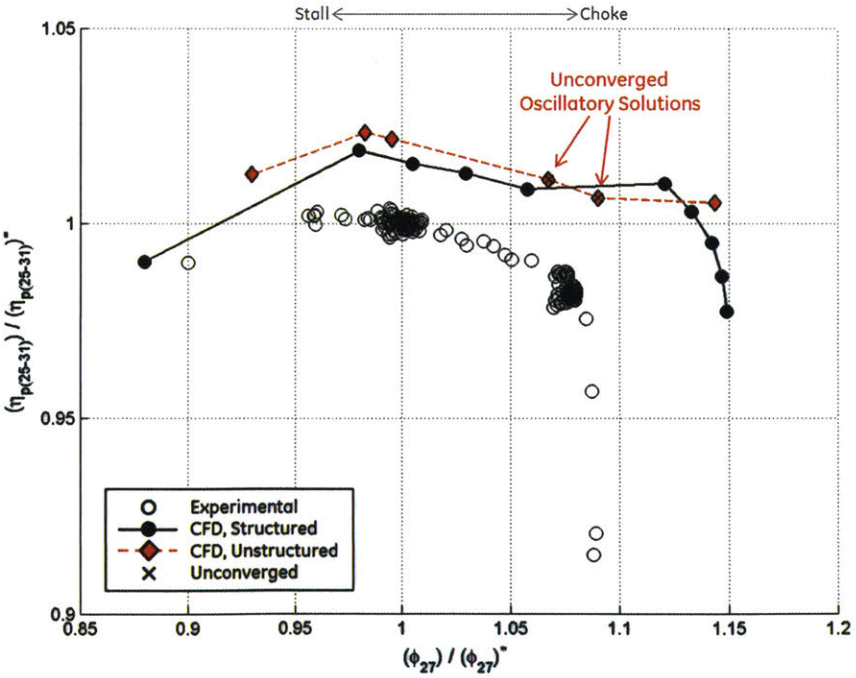


Figure 3.17: Overall compressor polytropic efficiency versus impeller exit flow coefficient at 100% $N_{c25}$. CFD solutions similar for structured and unstructured grids.

# Chapter 4 Impeller Performance Assessment

This research requires understanding the high-level impeller performance characteristics. First, the utility of the CFD simulation and the methodology for estimating the experimental impeller exit conditions must be assessed. Second, the impeller throttle characteristics must be investigated to understand what limits the overall compressor stability. Also, it is necessary to assess whether the baseline and truncated diffuser configurations impact the performance characteristics of the impeller. Lastly, characterizing the diffusion system requires characterizing the impeller exit conditions over a range of operating points.

## 4.1 Impeller Performance

The impeller pressure rise coefficient and polytropic efficiency are shown in Figure 4.1 for both baseline and truncated diffuser configurations at all speeds. The 100% $N_{c25}$ and 80% $N_{c25}$ speed lines highlighting the choke, peak efficiency, near stall, and CFD post stall operating points are shown in Figure 4.2 and Figure 4.3. The impeller work coefficients are the same as for the overall compressor, seen in Figure 3.6 and Figure 3.8.

The CFD calculates higher pressure rise coefficients and efficiencies than the experimental data for the impeller just as it does for the overall compressor. However, recall that there is an estimation procedure for determining the impeller exit stagnation pressure for the experiments discussed in Section 2.4.3.3. This estimation utilizes an assumption that the torque on the impeller shroud is twice the level measured from the 100E baseline diffuser CFD solution. This actually reduces the experimental estimates for impeller efficiency and pressure rise coefficient, increasing the mismatch between CFD and experimental performance levels for the impeller. However, the impeller work coefficient, which is calculated from direct temperature measurements, is also overestimated by CFD solutions. Therefore, it seems reasonable that the impeller pressure rise coefficients and efficiencies calculated by the CFD would also not match experimental data.

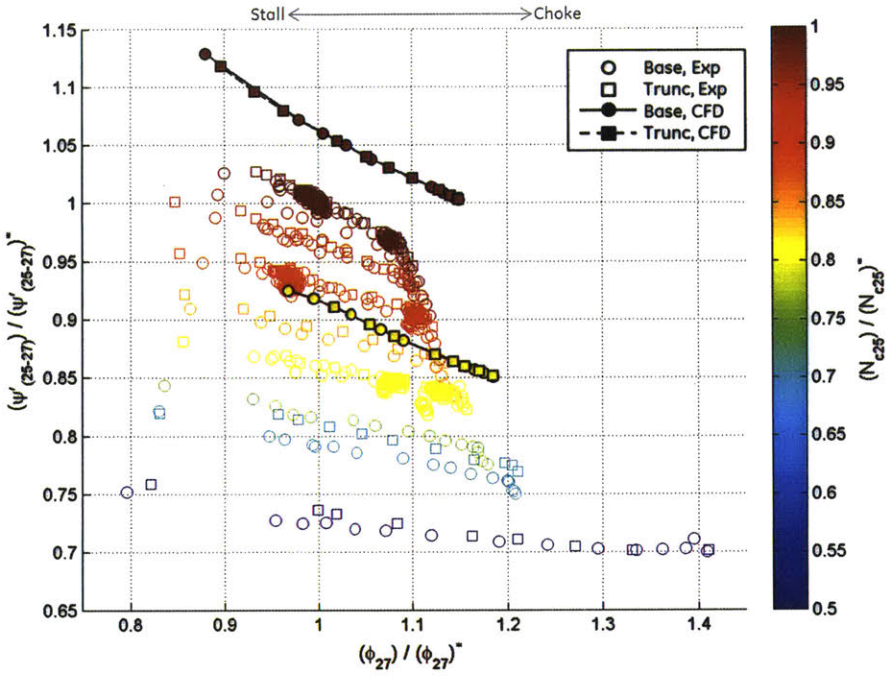


(a) Impeller pressure rise coefficient versus exit flow coefficient.

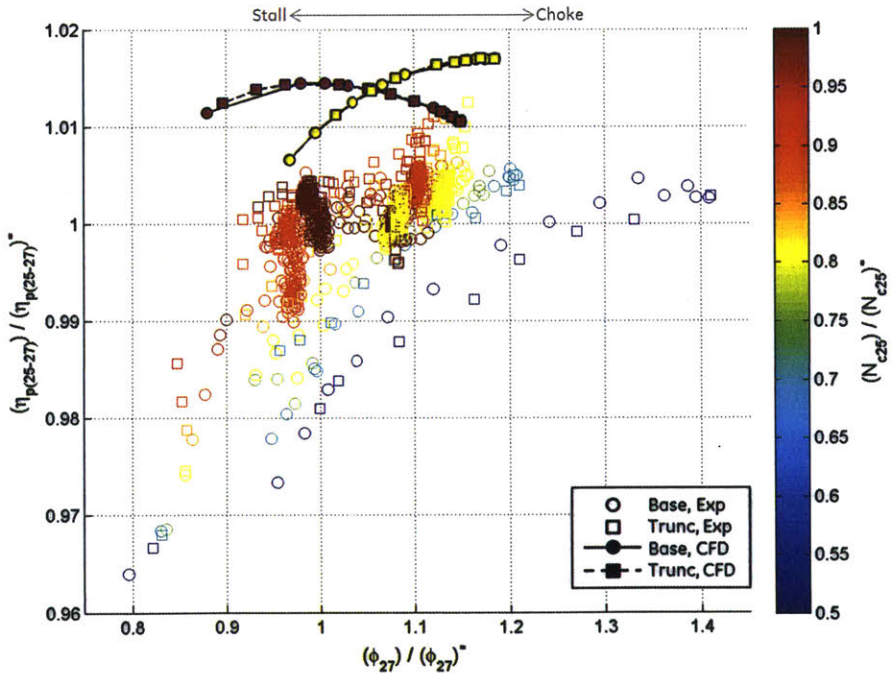


(b) Impeller polytropic efficiency versus exit flow coefficient.

Figure 4.1: Impeller performance versus exit flow coefficient. Symbols and line styles denote diffuser configuration and data source, while colors denote rotor speed. CFD solutions overestimate pressure rise coefficient and efficiency, but capture overarching trends.

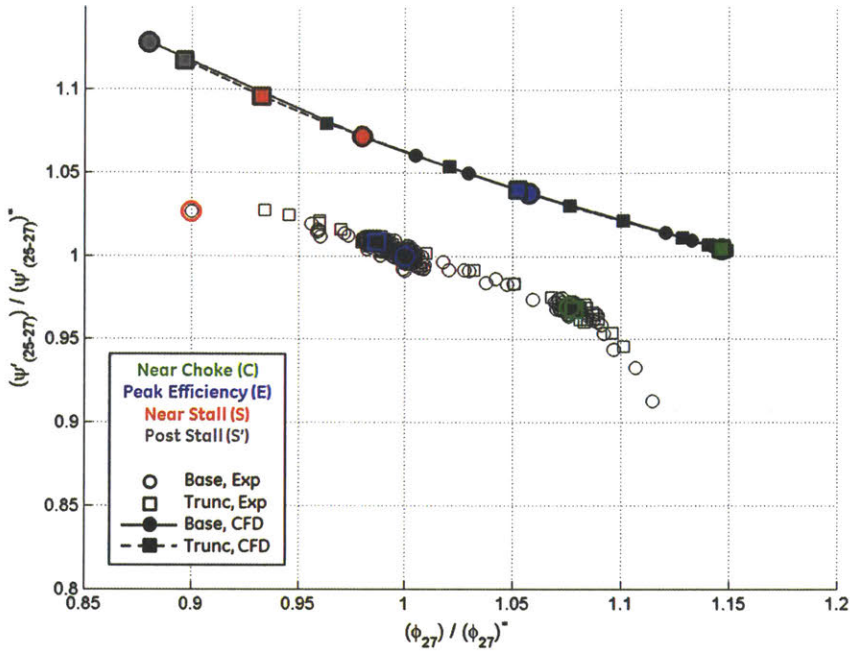


(a) 100% $N_{c25}$.

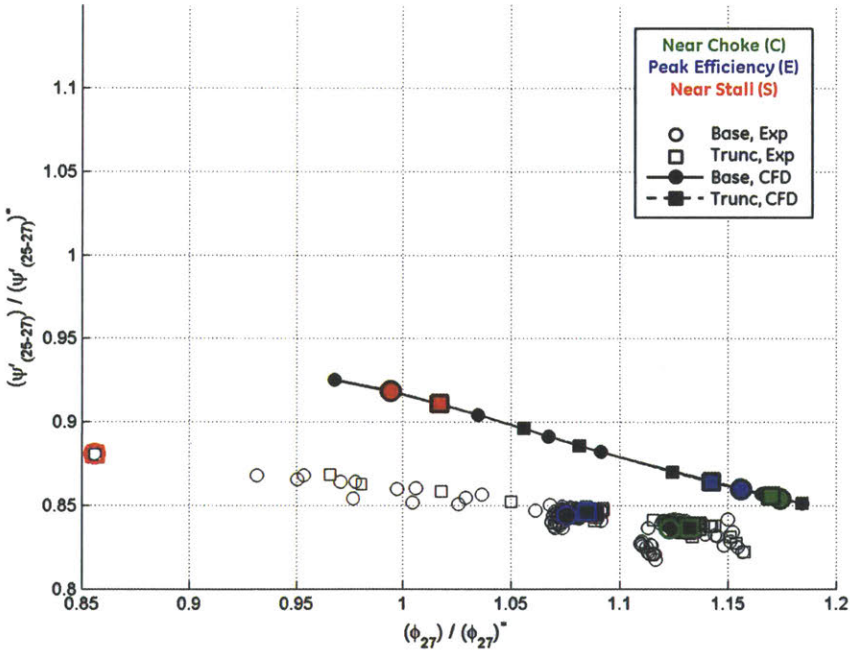


(b) 80% $N_{c25}$.

Figure 4.2: Impeller pressure rise coefficient versus exit flow coefficient. Symbols and line styles denote diffuser configuration and data source, while colors denote operating point (note: colored experimental points averaged from multiple tests). Experimental results indicate negligible benefit of truncated diffuser configuration due to efficiency benefit, whereas CFD shows no impact of diffuser configuration.

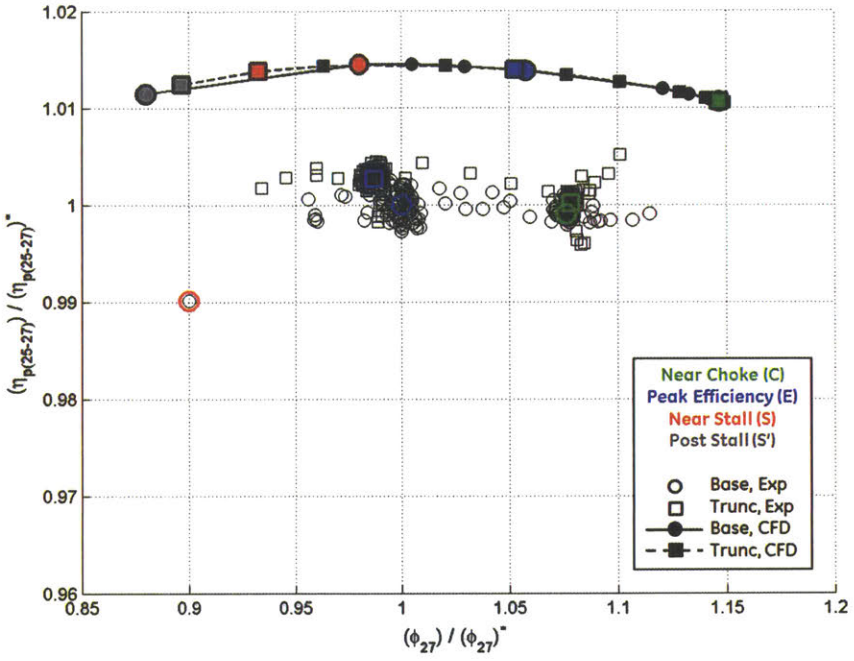


(a) 100% $N_{c25}$.

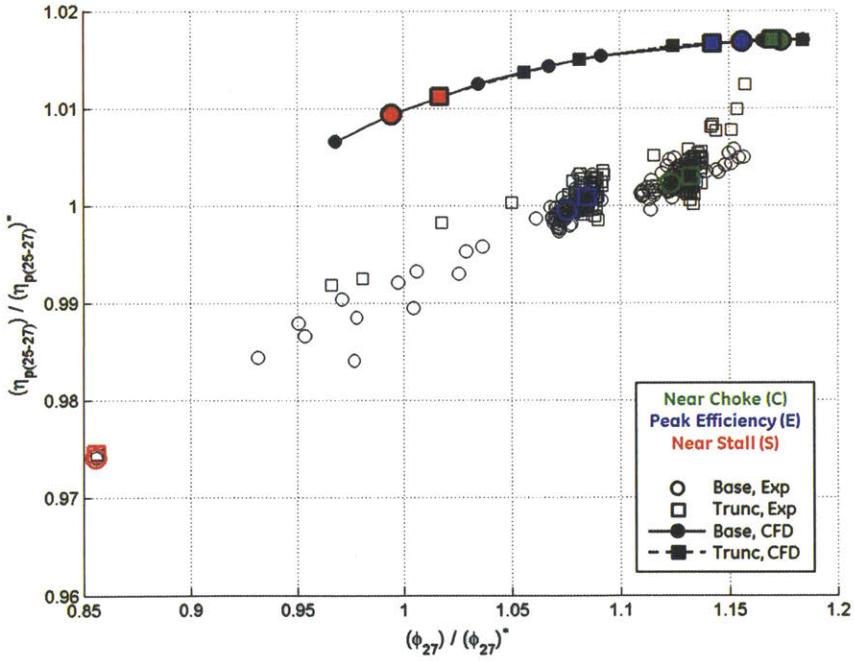


(b) 80% $N_{c25}$.

Figure 4.3: Impeller polytropic efficiency versus exit flow coefficient. Symbols and line styles denote diffuser configuration and data source, while colors denote operating point (note: colored experimental points averaged from multiple tests). Experimental results indicate slight benefit of truncated diffuser configuration, whereas CFD shows no impact of diffuser configuration.

Although the performance levels differ between the CFD and experimental data, trends along speed lines and between speeds are in agreement. Note that the CFD calculated efficiency and pressure rise coefficient characteristics are smooth across the throttle range. This suggests that the diffusion system is causing this piecewise appearance of these characteristics observed for the overall compressor. It is also apparent that the large performance falloff in compressor choke is not due to the impeller, indicating that the diffusion system chokes first. Another observation worth noting is that the peak efficiency is in the middle of the throttle range at 100% $N_{c25}$, but at 80% $N_{c25}$ the peak efficiency is near compressor choke. This means that the efficiency falloff from choke to stall is greater at 80% $N_{c25}$, and as a result, the pressure rise coefficient characteristic is not as steep at 80% $N_{c25}$ as it is at 100% $N_{c25}$. Although these efficiency trends are captured by the CFD, the CFD still calculates a steeper pressure rise coefficient characteristic at 80% $N_{c25}$ due to a corresponding mismatch in the slope of the work coefficient characteristic. The slope of the pressure rise coefficient characteristic has implications for the overall compressor stability, which is discussed in Chapter 7.

Like the work coefficients, the CFD calculated pressure rise coefficients and efficiencies indicate that the diffuser configuration has no impact on the impeller performance. However, the experimental results show otherwise, indicating that the impeller efficiency is up to 0.5% greater with the truncated diffuser than with the baseline diffuser, especially at 100% $N_{c25}$. The impeller pressure rise coefficient is also higher with the truncated diffuser. To verify that this is not the result of the assumptions of the impeller exit stagnation pressure estimation, the impeller near-tip and diffuser leading edge static pressure measurements ($p_{27m}$ and $p_{28}$ respectively) are substituted in place of the impeller exit stagnation pressure in an efficiency calculation and plotted against compressor inlet corrected flow. As one can see from Figure 4.4, these direct measurements also support the observation that the impeller performs differently between the two diffusers. Note that these pressures are actually averages of multiple circumferentially distributed pressure measurements, but the individual measurements are also determined to differ between diffuser configurations.

The question is whether this change in impeller performance characteristics is actually a result of the diffuser configuration impacting the impeller, or whether there is something else that is altering the impeller performance between the baseline and truncated diffuser tests. Any 1D impact of the diffuser truncation on the impeller throttling (e.g. diffuser pas-

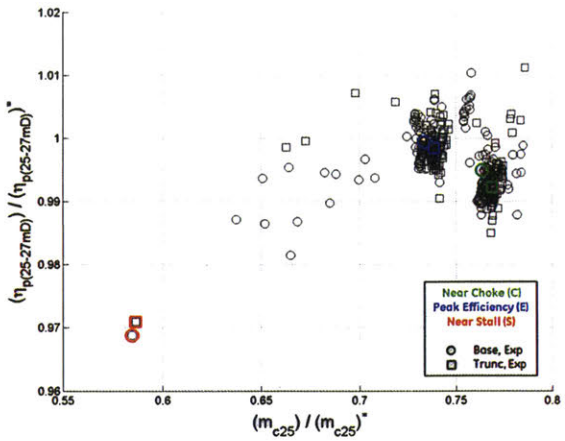


(a) 100% $N_{c25}$ using $p_{27m}$.

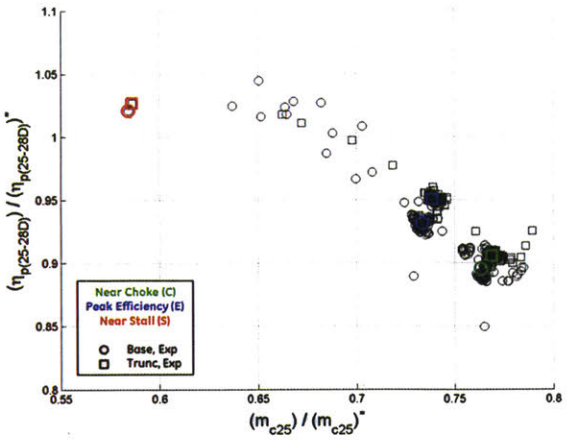


(b) 100% $N_{c25}$ using $p_{28}$.

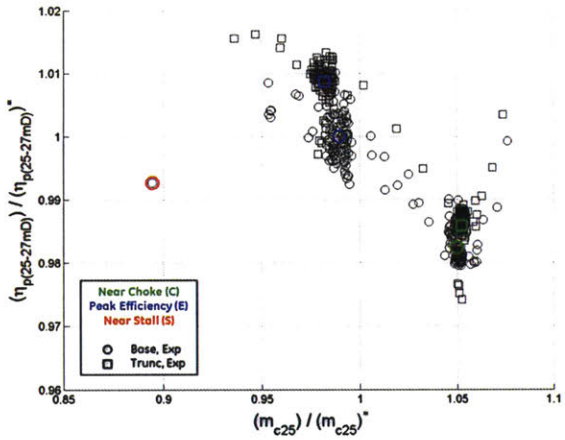


(c) 80% $N_{c25}$ using $p_{27m}$.

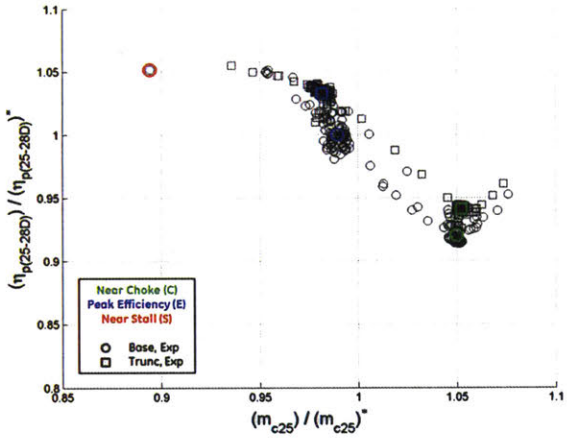


(d) 80% $N_{c25}$ using $p_{28}$.

Figure 4.4: Impeller polytropic efficiency calculated from static pressure measurements versus inlet corrected mass flow. Symbols and line denote diffuser configuration, while colors denote operating point (note: colored points averaged from multiple tests). Confirms impeller performed better for truncated diffuser experiments.

sage loss or blockage) would only move the impeller operating point around on its map, but would not alter its performance characteristics. Any impact of the diffuser truncation on the spanwise static pressure distribution at the impeller-diffuser interface would be captured by the CFD simulation. Therefore, in order for the impeller performance change to be caused by the diffuser configuration in a way that cannot be replicated in the CFD results, the truncation would have to alter the unsteady interaction between the impeller and diffuser. The possibility of this has yet to be investigated. However, it is the author's hypothesis that a more likely cause for the impeller performance change is that something else about the test setup was altered when the rig was disassembled and reassembled to modify

the diffuser. This process involved not only removing the diffuser, but also the impeller shroud, inlet flowpath outer casing, and IGVs. This hypothesis is supported by the observation that the measured near-throat stagnation pressure distributions for the baseline and truncated diffusers are slightly different, as shown in Figure 3.11. This includes differences in the spanwise direction (Forward to Aftward), which should have been captured by the CFD simulations if it were truly due to the diffuser truncation.

## 4.2 Impeller Performance Characterization

While the focus of this thesis is not on understanding the performance-limiting flow mechanisms in the impeller, the impeller does impact the overall compressor stability. The steeper the slope of the impeller pressure rise characteristic, the more it stabilizes the operation of the overall compressor. As noted, the impeller pressure rise coefficient characteristic is steeper at 100% $N_{c25c}$ than at 80% $N_{c25}$, which is driven by the different slopes of the efficiency characteristics at those speeds.

The question, then, is why does the impeller peak efficiency move towards choke with reduced speed? This can be answered by looking at how impeller efficiency changes with respect to the impeller inlet relative flow angle as in Figure 4.5. There is a clear trend which shows the impeller efficiency dropping off for inlet relative flow angles above or below the 100E value, almost independent of compressor speed. This concept of an incidence-dependent "loss bucket" is well established, and there are many detailed flow mechanisms driving this trend. The point here is to understand that because the impeller experiences a higher inlet relative flow angle at lower speeds, peak efficiency moves towards compressor choke at these speeds and compressor stability is reduced. Also note that for large impeller inlet relative flow angles (>5 deg above the 100E value), the slope of this efficiency characteristic with respect to flow angle is approximately constant. This means that the stability of the impeller is virtually unchanged between 50% $N_{c25}$ and 80% $N_{c25}$ before improving between 80% $N_{c25}$ and 100% $N_{c25}$.

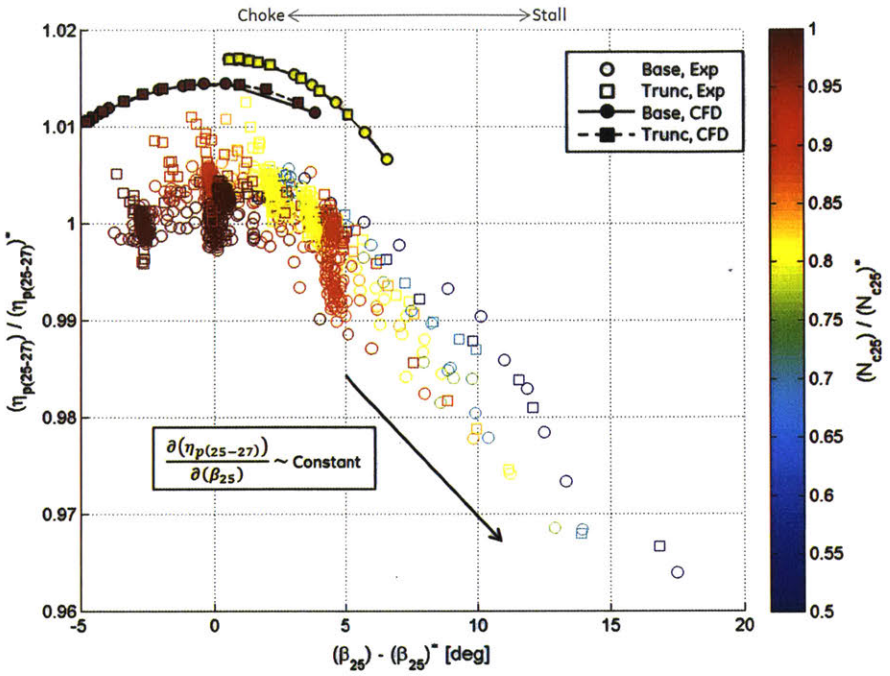


Figure 4.5: Impeller polytropic efficiency versus inlet relative flow angle. Symbols and line styles denote diffuser configuration and data source, while colors denote rotor speed. Efficiency is strongly a function of impeller incidence, such that efficiency generally decreases with reduced speed. However, sensitivity of efficiency to incidence becomes constant for relative flow angles that are 5 deg or more above the design value.

## 4.3 Impeller Exit Conditions

For the purpose of characterizing the diffuser performance, the impeller exit conditions must be understood in the diffuser's stationary frame of reference. The diffuser inlet flow angle has been established by Filipenco and Everitt to be the primary diffuser inlet condition driving its performance [9] [10]. There is nearly a one-to-one relationship between the impeller exit flow coefficient and the absolute flow angle, as shown in Figure 4.6, but flow angle will continue to be used when referring to the diffuser. Note that the CFD and experimental relationships are shifted with respect to one another. This is a result of the differences in impeller work coefficient and efficiency that have already been established.

The impeller exit Mach number is shown in Figure 4.7. Because the impeller exit flow coefficient is relatively small for this compressor, the tangential velocity is the primary velocity component driving the Mach number. As a result, the impeller exit Mach number depends only weakly on the impeller exit flow angle, but there is almost a one-to-one rela-

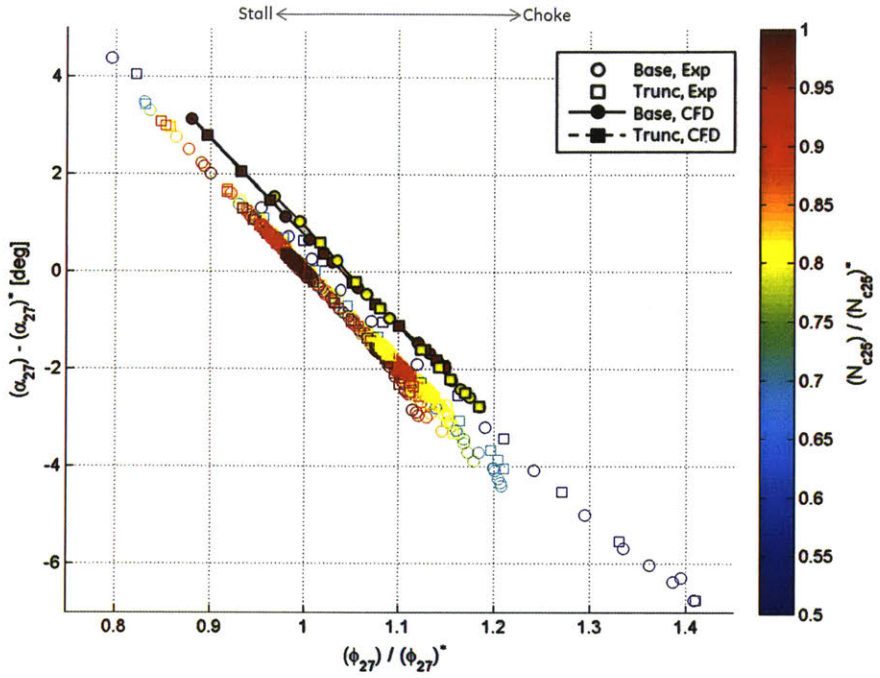


Figure 4.6: Impeller exit flow angle versus flow coefficient. Symbols and line styles denote diffuser configuration and data source, while colors denote rotor speed. Flow coefficient used to characterize impeller and compressor performance, but flow angle used to characterize diffusion system performance. These metrics are strongly correlated to one another.

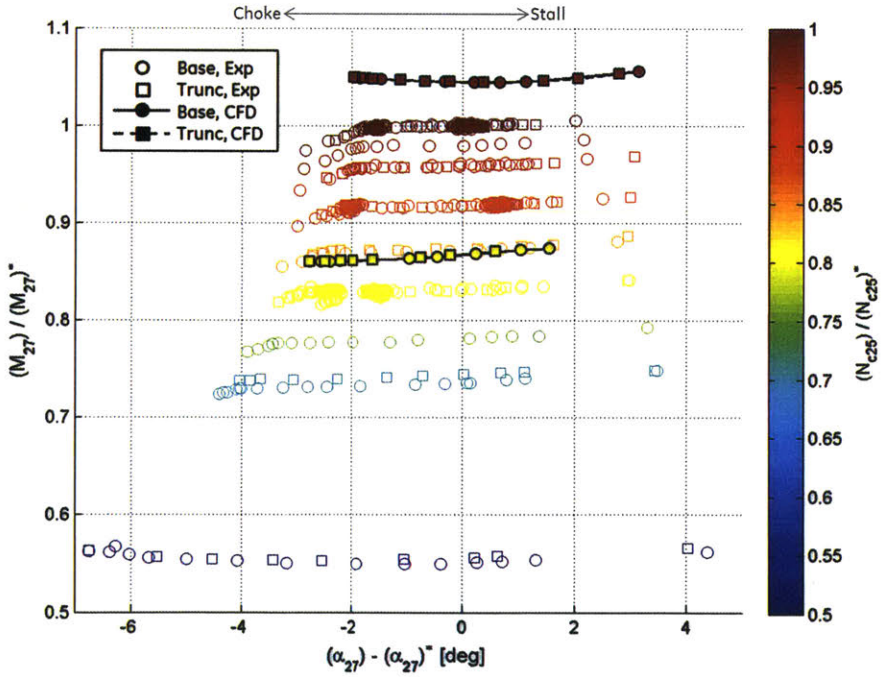


Figure 4.7: Impeller exit Mach number versus flow angle. Symbols and line styles denote diffuser configuration and data source, while colors denote rotor speed. Mach number primarily determined by compressor corrected speed, with weak dependence on flow angle.

tionship between Mach number and compressor speed. This means compressor speed can be used as a surrogate for diffuser inlet Mach number going forward.

Again, the CFD and data do not match, with the CFD Mach numbers overestimating the experimental Mach numbers. If Mach number is a major driver on diffuser performance, a mismatch could mean that the CFD simulations are not representative of their corresponding rig tests. However, flow angle does in fact match between the CFD and experimental data for a given operating point. Furthermore, the effect of Mach number is rather well-understood (see Sections 5.3, 6.5.6, and 6.6.5), so the impact of a mismatch can be accounted for.

In addition to looking at the impeller exit conditions in a 1D sense, it is important to consider how the flow properties vary spatially. One specific category of flow nonuniformity found at the impeller exit is secondary flows. The streamwise component of vorticity at the impeller exit is shown in Figure 4.8 (note that this CFD calculated vorticity has the opposite sign convention as the mirrored experimental rig). High streamwise vorticity is concentrated near the impeller hub and shroud. These secondary flows are later shown to influence the diffuser performance.

All forms of the impeller exit flow nonuniformity can be quantified together as the 1D mass blockage shown in Figure 4.9. The true impeller exit blockages from the experiments are not known, so the CFD calculated 100E blockage value is assumed for the experimental impeller exit condition estimation procedure. This is a good assumption, as the CFD calculated blockages are shown to be nearly constant across the throttle range and between speeds.

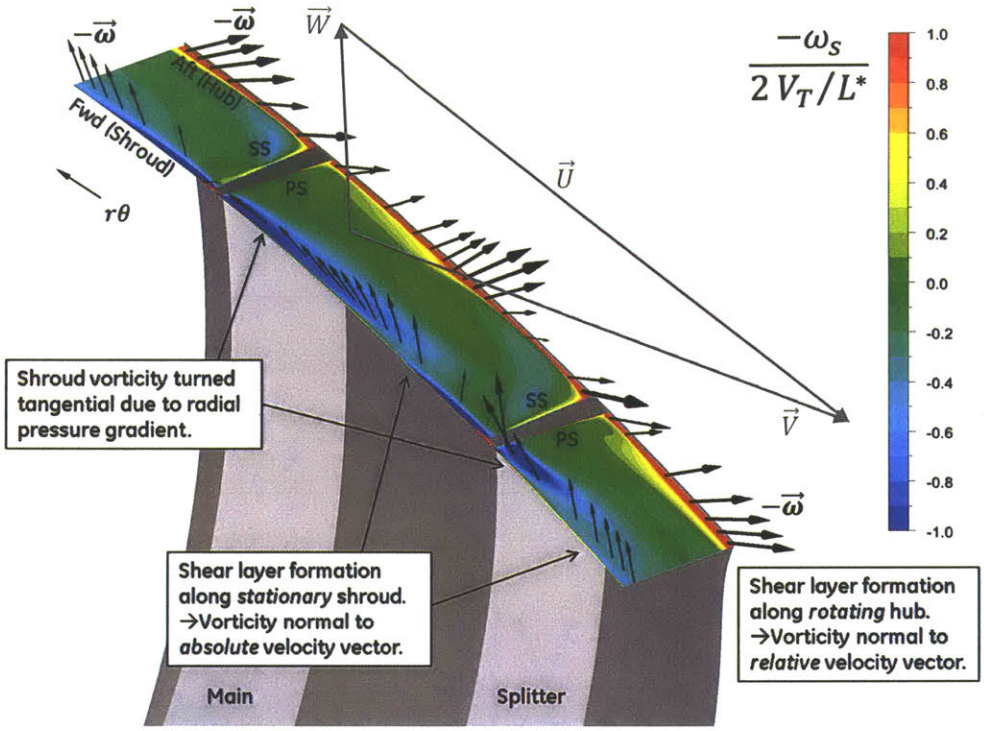


Figure 4.8: Impeller exit endwall vorticity vectors and streamwise vorticity distribution in absolute reference frame, from 100E CFD solution with baseline diffuser. Streamwise impeller exit vorticity present near endwalls due to boundary layers.

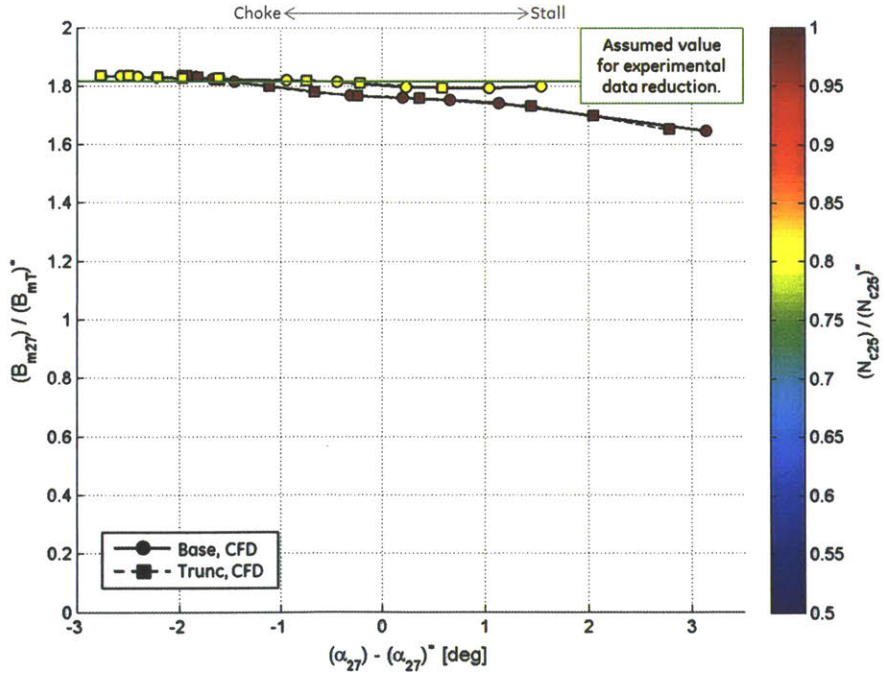


Figure 4.9: Impeller exit mass blockage versus flow angle. Symbols and line styles denote diffuser configuration and data source, while colors denote rotor speed. Blockage nearly constant across all simulated flow angles and speeds.

# Chapter 5 Fundamental Diffuser Flow Mechanisms and Effects

This chapter discusses the general effects of various flow mechanisms present in any diffuser, and explains how they impact pressure recovery and loss. The concepts introduced here are later applied when evaluating the diffusers of interest for this research.

## 5.1 1D Inviscid Incompressible Diffuser Model

A idealized model of a diffuser utilizes the assumptions of 1D inviscid incompressible uniform flow. Such a diffuser is illustrated in Figure 5.1. The density, mass flow, and stagnation pressure are assumed equal between the inlet and exit, as indicated by Equation 5.1, Equation 5.2, and Equation 5.3 respectively. These equations can be manipulated to derive the uniform flow diffuser pressure recovery coefficient as a function of the diffuser's area ratio, Equation 5.4. This is plotted for a range of diffuser area ratios in Figure 5.2. Note that at large area ratios, the marginal benefit of further increasing area ratio diminishes.

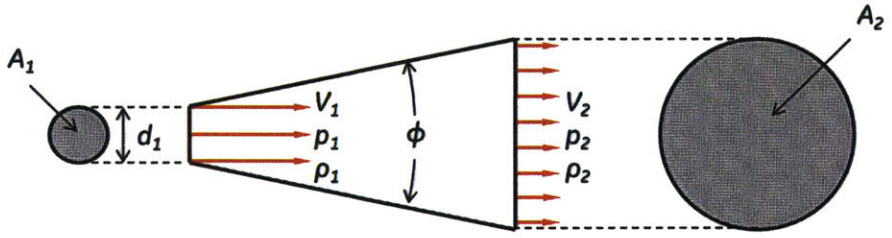


Figure 5.1: 1D uniform flow in a conical diffuser.

$$\rho = \rho_1 = \rho_2 \qquad \text{Equation 5.1}$$

$$\dot{m}_1 = \dot{m}_2 \rightarrow \rho V_1 A_1 = \rho V_2 A_2 \qquad \text{Equation 5.2}$$

$$p_{t1} = p_{t2} \rightarrow p_1 + \frac{1}{2}\rho V_1^2 = p_2 + \frac{1}{2}\rho V_2^2 \qquad \text{Equation 5.3}$$

$$C_{pu0(1-2)} = 1 - \frac{1}{(A_2/A_1)^2} \qquad \text{Equation 5.4}$$

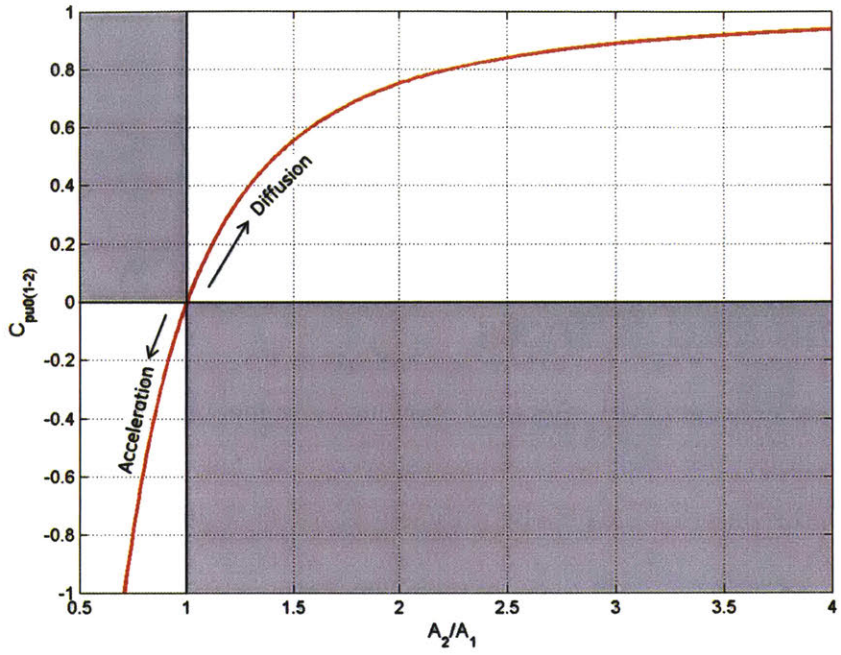


Figure 5.2: Static pressure recovery coefficient versus diffuser area ratio for 1D inviscid incompressible flow. Pressure rise insensitive to area ratio at large area ratios.

## 5.2 Nonideal Effects

Real diffuser flow is not truly 1D or inviscid. In reality, the flow properties are nonuniform and irreversible losses are incurred, reducing the static pressure rise of a diffuser relative to ideal. For the diffusers of interest, velocity nonuniformities and viscous losses are of primary concern. As we have already seen, the flow provided to the diffuser by the impeller already has a nonuniform velocity distribution. This includes spatial nonuniformities in both velocity magnitude and direction, with the latter characterizing the secondary flows. As the flow moves through the diffuser, three mechanisms act to evolve the velocity nonuniformities: nonuniformity amplification via diffusion, streamline shear or mixing, and wall friction.

First, as the static pressure changes throughout the diffuser, the velocity also adjusts in accordance with the momentum conservation, given by Equation 5.5 for an inviscid streamline. Not surprisingly, this says that as pressure increases ($dp > 0$), velocity decreases ($dV < 0$). More interestingly, however, it says that for the same static pressure change the velocity reduction is greater along low velocity streamlines than along high velocity stream-

lines. This means a diffusion process amplifies velocity nonuniformities, while an acceleration process smooths out nonuniformities.

$$\frac{dV}{dp} = -\frac{1}{\rho V} \qquad \text{Equation 5.5}$$

This effect of nonuniformity amplification is demonstrated by creating a simple inviscid two stream model of a conical diffuser. Each stream follows Equation 5.4, with the constraints that the inlet and exit static pressures are equal between the two streams, and the combined area ratio of the two streams is equal to 2. Because the two streams have different inlet dynamic pressures, their pressure recovery coefficients and area ratios must differ. These calculations are well-documented by Greitzer et. al. [17]. Example inlet and exit velocity profiles are shown in Figure 5.3, demonstrating the amplification of nonuniformity due to the diffusion process. In this example, the mass blockage increases from 0.10 to 0.50, and 1D shape factor increases from 1.4 to 6.6.

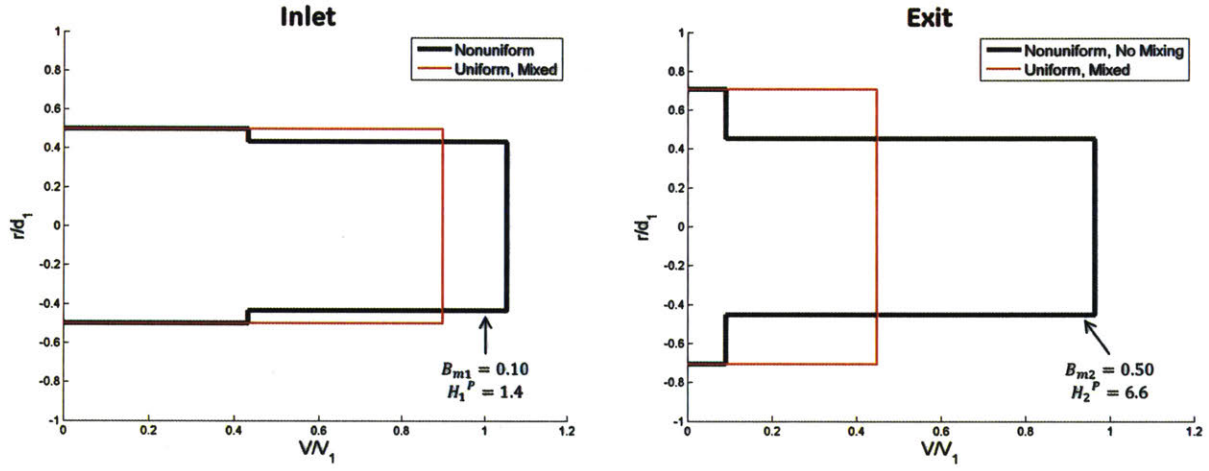


Figure 5.3: Example inlet and exit velocity profiles (normalized by availability average inlet velocity) associated with simulated two stream incompressible diffusion process. Diffuser is conical with $A_1/A_2 = 2$, and inlet conditions are $B_{m1} = 0.10$ and $H_1^P = 1.4$. Without mixing, exit flow is more nonuniform than inlet, as demonstrated by increases in blockage and shape factor.

To show the impact of nonuniformity amplification on pressure rise, different levels of mass blockage and shape factor are imposed at the inlet of this two stream inviscid diffuser model. Each simulated inlet condition is plotted in Figure 5.4, while the resulting static pressure recovery coefficients are shown in Figure 5.5 (black). Clearly the diffuser's pressure rise capability is significantly impaired by the presence of inlet nonuniformity, with inlet shape factor being the primary driver over the blockage.

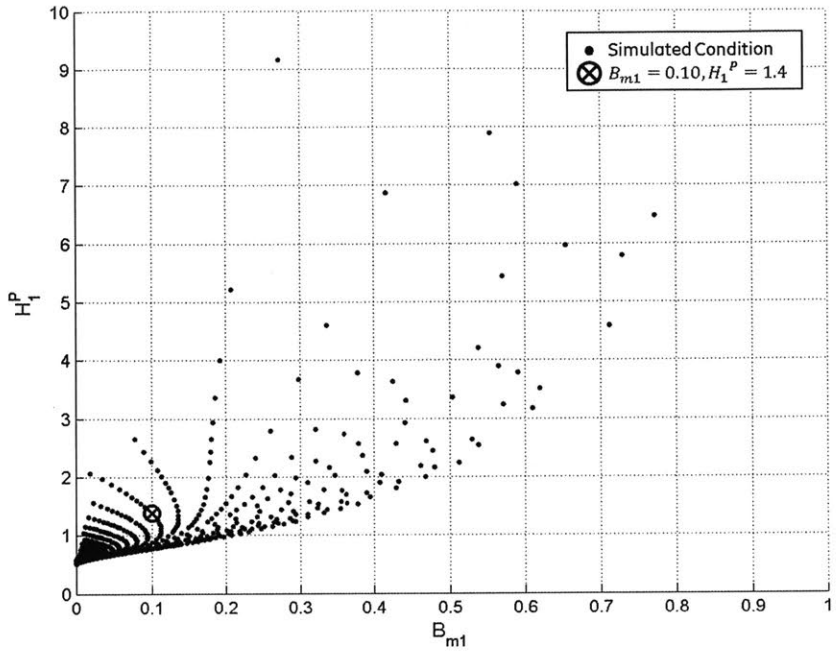


Figure 5.4: Collection of nonuniform flow conditions imposed at inlet of two stream diffuser model to study impacts of nonuniformity amplification and mixing on diffuser pressure recovery and loss. Mass blockages based on availability average, and shape factors based on potential core average.

Nonuniformity amplification predominantly impacts the diffuser throughflow velocity component. However, there is an interaction of the throughflow velocity with the secondary flow field, as described by Greitzer et. al. [17]. As streamtube areas increase with increased pressure, circulating secondary flows in the streamtubes decrease in velocity to preserve angular momentum. Since the secondary flow field and associated streamline curvature is enabled by static pressure gradients in the cross flow plane, the reduction in secondary flows strength reduces this static pressure nonuniformity. This correspondingly impacts the nonuniformity of the throughflow velocity component. This effect can be significant if secondary flows are strong.

The second mechanism impacting the evolution of velocity nonuniformities throughout the diffuser is viscous shear or "mixing" between adjacent streamlines. This mechanism attenuates velocity nonuniformities, tending to make the flow more uniform, and locally increasing the static pressure of the flow. These effects are demonstrated in Figure 5.3 and Figure 5.5, which show the mixed out velocity profiles and pressure recovery coefficients of the two stream diffuser model after completely mixing out nonuniformities. However, mixing is also the mechanism by which losses are generated as the overall kinetic energy of the

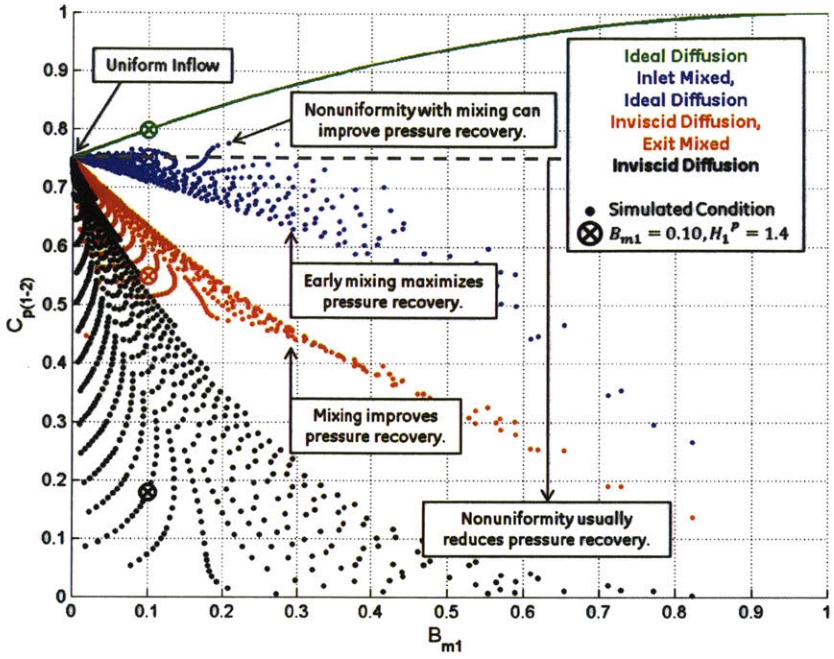


(a) Static pressure recovery coefficient versus inlet mass blockage.

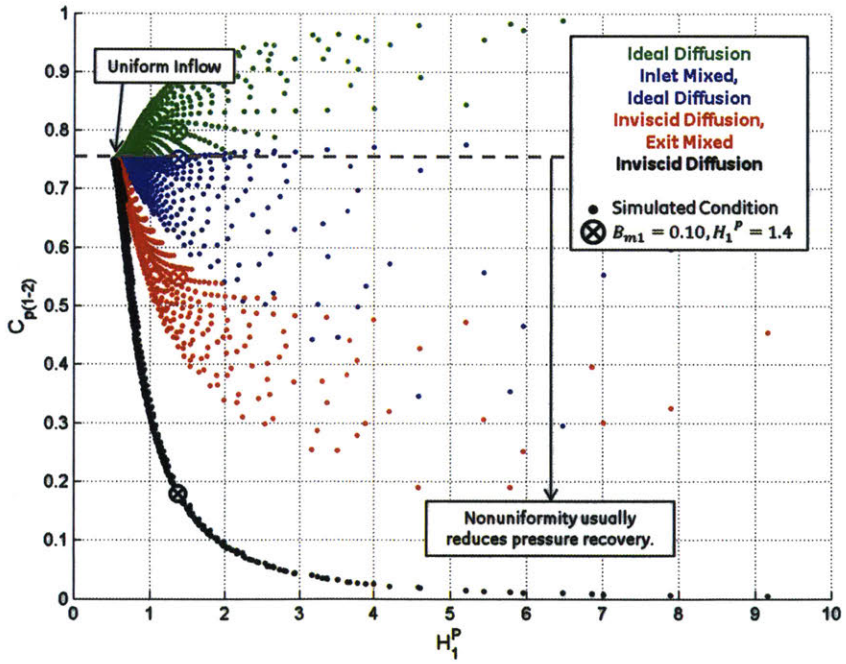


(b) Static pressure recovery coefficient versus inlet 1D shape factor.

Figure 5.5: Effect of flow nonuniformity on diffuser static pressure recovery coefficients with and without mixing. Calculations performed using two stream diffuser model with $A_1/A_2 = 2$. Pressure recovery is reduced with increased inlet nonuniformity and reduced mixing.

flow is reduced irreversibly, shown in Figure 5.6 for the two stream diffuser model. This effect reduces the maximum pressure rise potential of the flow. As one can see from the strong dependency on blockage, the amount of pressure rise and loss incurred during mixing is related to the amount of nonuniformity smoothing that takes place. One implication of this is that rapidly mixing out nonuniformities near the diffuser inlet (blue) results in lower loss generation and greater pressure recovery than if mixing is delayed until the diffuser exit after nonuniformity amplification (red).

It should be noted that the rate at which a flow mixes depends on the arrangement of high and low velocity regions of flow. Mixing will be enhanced with increased surface area of the shear layer boundary between high and low velocity regions of flow. Secondary flows impact the arrangement of these various flow regions in a manner which can either enhance mixing (stretching of shear layer) or diminish it (accumulation and isolation of low or high velocity fluid).

The third mechanism impacting the flow nonuniformity is diffuser wall friction. This is essentially a source for new velocity nonuniformity, extracting momentum from the flow at a rate that is proportional to the wall-normal gradient of velocity at the wall. In the cross-flow plane, the wall friction works with streamline shear to drive secondary flow velocities uniformly toward zero. Conversely, in the throughflow direction, the velocity field can never be completely uniform, reducing the aforementioned benefit of rapid mixing. New nonuniformity generated at the wall is quickly converted to loss via the large shear stresses in the boundary layer.

This scrubbing loss can be estimated using the boundary layer dissipation coefficient, $C_D$. The benefit of this approach is that unlike the friction coefficient, the dissipation coefficient depends only weakly on the boundary layer shape or thickness, with typical values on the order of $1.0 \times 10^{-3}$ for turbulent boundary layers [17]. The relationship between the boundary layer dissipation coefficient and the stagnation pressure loss coefficient is derived by Greitzer et. al. for an incompressible, uniform density flow, given by Equation 5.6. In this equation, $L$ is the diffuser length, $SA$ and $C$ are the shear layer surface area and circumference respectively, and $C_{ref}$ is a reference circumference, equal to $SA/L$. This says that the loss coefficient is proportional to an average of the velocity cubed, weighted by the shear layer surface area. Assuming the circumference of the shear layer is equal to the circumference of the effective area, Equation 5.6 is rewritten as Equation 5.7 for a diffuser

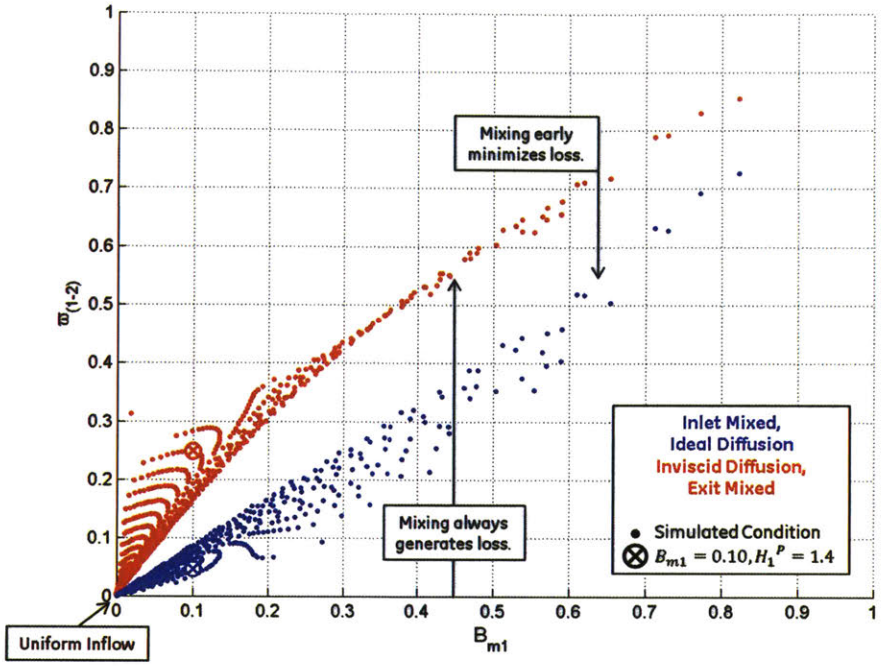


(a) Stagnation pressure loss coefficient versus inlet mass blockage.

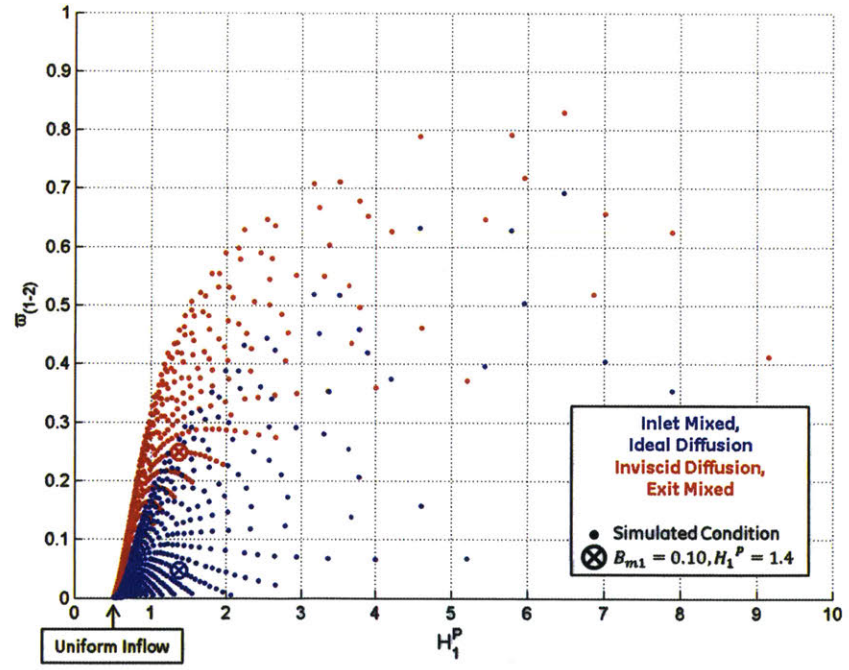


(b) Stagnation pressure loss coefficient versus inlet 1D shape factor.

Figure 5.6: Effect of flow nonuniformity and associated mixing on diffuser stagnation pressure loss coefficients. Calculations performed using two stream diffuser model with $A_1/A_2 = 2$. Loss increases with increased inlet nonuniformity and delayed mixing.

with a circular cross-section and arbitrary area distribution such as the diffuser illustrated in Figure 5.7. This is further simplified for incompressible flows by Equation 5.8. One can see that for a given effective area distribution, the loss scales with the diffuser path length, $L$.

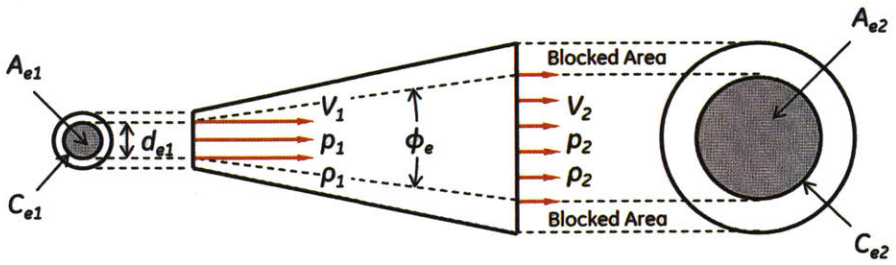


Figure 5.7: 1D representation of nonuniform flow in a conical diffuser showing effective area.

$$\bar{\omega}_{D(1-2)} = 2C_D \frac{SA}{A_{e1}} \int_0^1 \left(\frac{C}{C_{ref}}\right)\left(\frac{V}{V_1}\right)^3 d\left(\frac{s}{L_{(1-2)}}\right) \qquad \text{Equation 5.6}$$

$$\bar{\omega}_{D(1-2)} = 4C_D \frac{L_{(1-2)}}{d_{e1}/2} \int_0^1 \sqrt{\frac{A_e}{A_{e1}}}\left(\frac{V}{V_1}\right)^3 d\left(\frac{s}{L_{(1-2)}}\right) \qquad \text{Equation 5.7}$$

$$\bar{\omega}_{D0(1-2)} = 4C_D \frac{L_{(1-2)}}{d_{e1}/2} \int_0^1 \left(\frac{A_{e1}}{A_e}\right)^{2.5} d\left(\frac{s}{L_{(1-2)}}\right) \qquad \text{Equation 5.8}$$

For a conical diffuser with incompressible flow and thin boundary layer, the integral can be evaluated analytically, and the loss is given by Equation 5.9. This is plotted in Figure 5.8 for a range of diffuser area ratios. For a given nondimensional length and dissipation coefficient, the stagnation pressure loss coefficient reduces with increased area ratio. This is due to the reduction in the average velocity relative to the inlet velocity. Equation 5.9 and Figure 5.8 also show that for a diffuser of constant cone angle, the stagnation pressure loss coefficient increases with area ratio (and length), scaling linearly with the uniform flow static pressure recovery coefficient. Note, however, that the thin boundary layer approximation is not valid for large cone angles due to nonuniformity amplification.

$$\bar{\omega}_{Du0(1-2)} = C_D \frac{L_{(1-2)}}{d_1/2}\left(\frac{(A_2/A_1)^2 - 1}{(A_2/A_1)^{5/2} - (A_2/A_1)^2}\right) = \frac{C_D}{\tan(\phi/2)}\left[1 - \frac{1}{(A_2/A_1)^2}\right] \qquad \text{Equation 5.9}$$

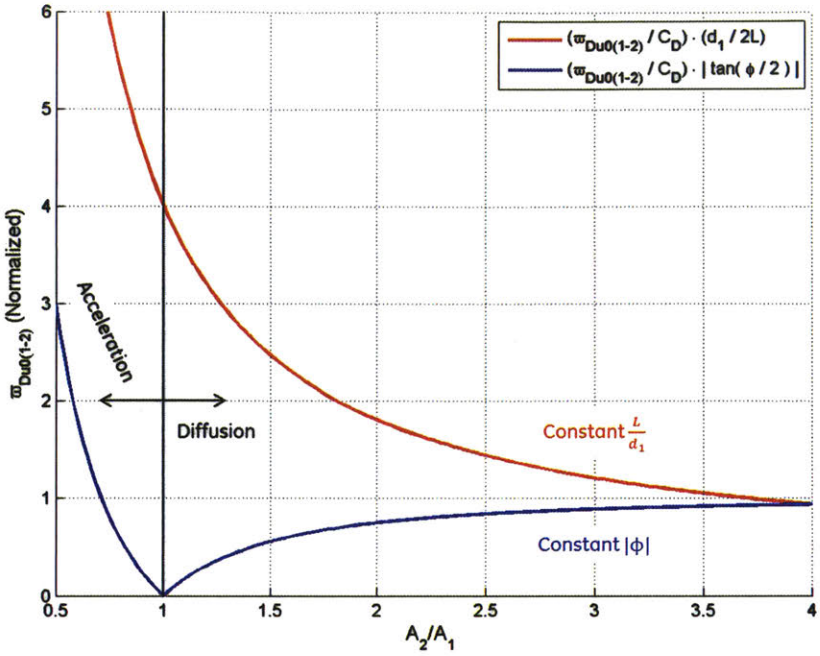


Figure 5.8: 1D uniform flow stagnation pressure loss coefficient due to scrubbing losses versus diffuser area ratio. At constant nondimensional length, increasing area ratio reduces scrubbing losses due to average velocity reduction. At constant cone angle, increasing area ratio increases scrubbing losses due to associated length increase. Assumes thin boundary layer; not valid for large cone angles.

It should be noted that the explanations provided for these three diffuser flow mechanisms above are intentionally simplified. Other forms of flow nonuniformity in the cross-flow plane can impact the evolution of velocity nonuniformities throughout the diffuser as well (e.g. density nonuniformities, or static pressure nonuniformity due to streamline curvature). Unsteadiness is another manifestation of nonuniformity which is not addressed here, but it should be noted that there are reversible mechanisms by which some unsteady nonuniformities can be made uniform (e.g. diffusion of impeller blade wakes through diffuser). In addition, temperature nonuniformity and heat dissipation give rise to a second loss generation mechanism, which may be non-negligible for other applications.

The static pressure recovery coefficient for an incompressible diffuser flow is re-written in Equation 5.10 to account for these real effects. Nonuniformity is characterized by the mass blockage, and loss is characterized by the stagnation pressure loss coefficient. Both of these are calculated using a 1D averaging procedure such as the availability average discussed in Section 2.2. One can see that a loss in stagnation pressure corresponds directly to a reduction in the static pressure recovery. The static pressure recovery is also reduced if the diffuser's 1D effective area ratio is less than its geometric area ratio, or if the diffuser

exit blockage is greater than its inlet blockage. As discussed, this is true of most diffusion processes due to nonuniformity amplification. However, with mixing it is possible for the exit blockage to be reduced relative to the inlet, increasing the effective area ratio above the geometric area ratio. In this way, a greater pressure recovery coefficient may be achieved with nonuniform inflow than with uniform inflow. A classic example of this is a constant area mixing process. This effect is also seen in Figure 5.5 for the two stream diffuser model when inlet blockage and shape factor are low and mixing occurs at the diffuser inlet (blue). An ideal pressure recovery coefficient is therefore best defined according to Equation 5.11, which incorporates the inlet blockage, but assumes an isentropic diffusion process with zero exit blockage. The ideal pressure recovery coefficient for the two stream diffuser model is plotted in Figure 5.5 (green).

$$C_{p(1-2)} = 1 - \bar{\omega}_{(1-2)} - \frac{1}{\left[\frac{A_2(1-B_{m2})}{A_1(1-B_{m1})}\right]^2} \qquad \text{Equation 5.10}$$

$$C_{p(1-2i)} = 1 - \frac{(1-B_{m1})^2}{(A_2/A_1)^2} \qquad \text{Equation 5.11}$$

## 5.3 Effect of Compressibility

For the compressor being studied in this research, the impeller exit Mach number at the 100E operating point is subsonic, but high. Therefore, compressibility is important in the diffuser. It has already been shown that the diffusion system chokes before the impeller, which is one impact of compressibility. One can infer from quasi-1D compressible flow theory that shocks must also form downstream of the diffuser throat when the diffuser backpressure is further reduced into deep choke. Of greater interest, however, is how compressibility plays a role during normal subsonic diffuser operation between choke and stall.

Because density changes are inversely proportional to velocity changes in a compressible flow, one can infer from mass conservation that velocity changes in a 1D diffusion process will be amplified by compressibility. Greitzer et. al. provide a table of influence coefficients, employing all the governing 1D compressible flow equations to relate changes in independent flow variables to changes in dependent variables [17]. The relation between static pressure changes and 1D area changes is given by Equation 5.12. Normalizing changes in static pressure by the dynamic pressure gives Equation 5.13, which represents fractional changes in the pressure recovery coefficient for fractional changes in 1D area.

This equation is plotted in Figure 5.9 for Mach numbers less than one. For Mach numbers near unity, an incremental change in area results in a proportionally large static pressure rise. For a diffusion process, this static pressure rise will also decrease the Mach number such that the influence of compressibility is reduced throughout the length of the diffuser. This means that proportionally speaking, the amount of static pressure recovered near the inlet of a subsonic diffuser will increase with compressibility, and the amount of pressure recovered toward the exit will decrease. This can be inferred from Figure 5.10. It also means that the effect of compressibility is most apparent when the diffuser area ratio is small. Conversely, for large diffuser area ratios, the ideal pressure recovery coefficient will approach unity whether or not the flow is compressible (of course the absolute pressure rise will still be larger for high Mach number flows due to greater inlet dynamic pressure).

$$\frac{dp}{p} = \frac{\gamma M^2}{1 - M^2}\frac{dA}{A} \qquad \text{Equation 5.12}$$

$$\frac{dp/(p_t - p)}{dA/A} = \frac{\gamma M^2}{1 - M^2}\left[\left(1 + \frac{\gamma - 1}{2}M^2\right)^{\frac{\gamma}{\gamma - 1}} - 1\right]^{-1} \qquad \text{Equation 5.13}$$

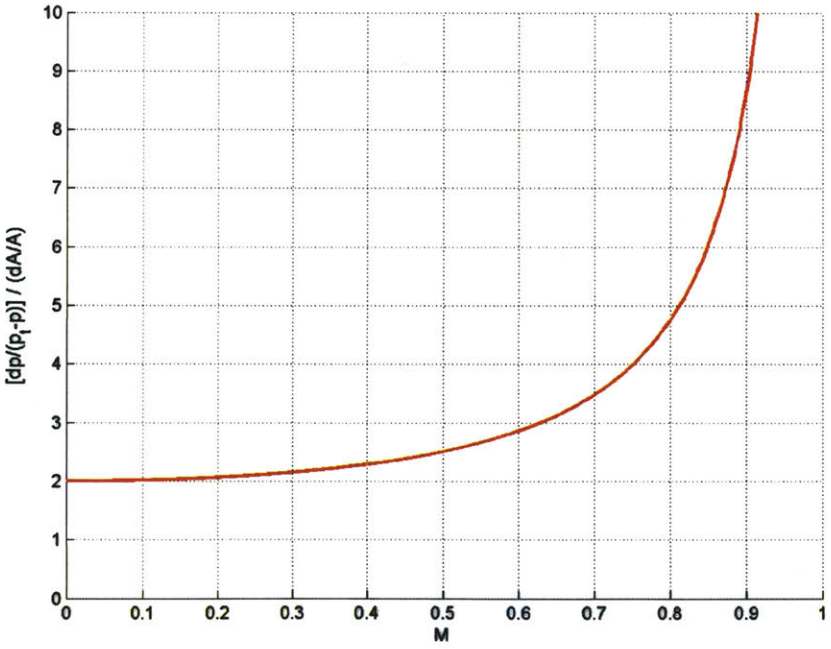


Figure 5.9: Sensitivity of pressure recovery coefficient changes to area changes versus Mach number. Pressure changes are most sensitive to area changes at Mach numbers near unity.

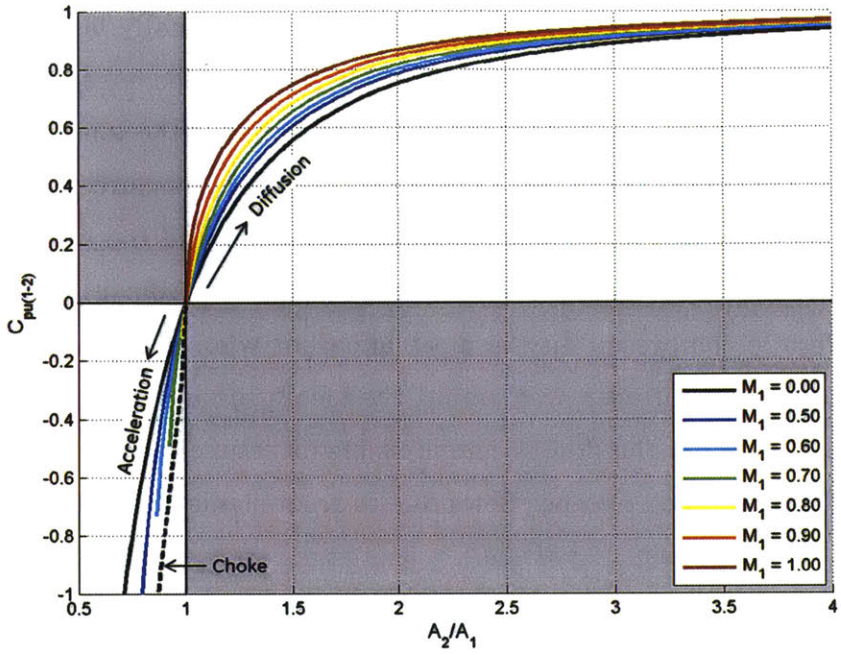


Figure 5.10: Static pressure recovery coefficient versus diffuser area ratio for 1D inviscid compressible flow. Compressibility magnifies pressure recovery coefficient, especially for low area ratios.

With the knowledge about the effect of compressibility on the static pressure distribution throughout a diffuser, one can infer what effects this has on the three nonideal effects: nonuniformity amplification, mixing, and nonuniformity introduction via wall friction. First, compressibility will further amplify nonuniformity in a diffusion process. This can be illustrated by considering what would happen to a two stream compressible diffusion process if the individual streamtube areas were held equal to what they would be in an incompressible flow situation. In this case, the higher Mach number streamtube would increase in pressure more rapidly than the lower Mach number streamtube. Therefore, the higher Mach number streamtube must contract and the lower Mach number streamtube must expand in order to maintain a uniform static pressure across the diffuser. It was already shown that the area ratio of the high velocity streamtube is lower than the low velocity streamtube in the incompressible case, so compressibility only amplifies this effect. However, it is not a large effect. For the sample two stream diffusion case with inlet blockage of 0.10 and 1D shape factor of 1.4, increasing the availability averaged inlet Mach number from 0 to 0.9 only increases the exit blockage and shape factor from 0.50 to 0.54 and from 6.6 to 6.9 respectively.

Because nonuniformity is amplified by compressibility, it makes sense that loss due to mixing should also be amplified. This will be true if the inlet nonuniformity is the dominant source of nonuniformity in the diffusion process. However, the wall friction also acts as a source of new nonuniformity. Since the wall-normal velocity gradient can be expected to scale with the velocity itself, which is reduced more rapidly in compressible flow diffusion, the wall friction has a smaller impact than the incompressible case. This can be inferred from Equation 5.7, which shows the strong dependence of loss coefficient on velocity. Although the derivation of this equation assumes constant density, it can be used to elucidate the effect of compressibility on loss. This is in contrast to Equation 5.8 and Equation 5.9, which use the additional assumption of constant density cubed. Assuming a conical diffuser with inviscid uniform flow velocity distributions and a thin boundary layer, and assuming compressibility does not impact the dissipation coefficient, the stagnation pressure loss coefficient is calculated as a fraction of the equivalent loss coefficient in an incompressible flow. This is plotted in Figure 5.11 over a range of Mach numbers. This demonstrates that compressibility can significantly decrease the stagnation pressure loss coefficient in a diffusion process. Unlike the static pressure recovery coefficient, compressibility impacts loss the most at large area ratios. This is because the loss is cumulative, or path-dependent, so the benefit of reduced velocities experienced near the inlet translates to loss reduction everywhere downstream as well.

Everitt found in his studies that diffuser performance was independent of compressibility when using the effectiveness as the performance measure, which he defined according to Equation 5.14 [10]. However, the results of analyses presented here suggest that Everitt's finding is not necessarily true of all diffusers. An example is a diffuser with large 1D geometric area ratio and large exit blockage. Because $C_{pu(1-2)}$ is calculated using the large geometric area ratio, it is proportionally not as affected by compressibility as the recovery of the true diffuser, which has the smaller effective area ratio. Fortunately, blockage itself is not found to be significantly impacted by compressibility, so using the effective area ratio to calculate $C_{pu(1-2)}$ is a reasonable refinement to Everitt's proposal if blockage is the primary mechanism reducing the static pressure recovery. However, if loss also significantly reduces the static pressure, then this modified effectiveness cannot accurately correct for compressibility since the loss does not scale with $C_{pu(1-2)}$. Correcting the loss requires an additional simplifying assumption about whether it is dominated by the wall friction or by mix-

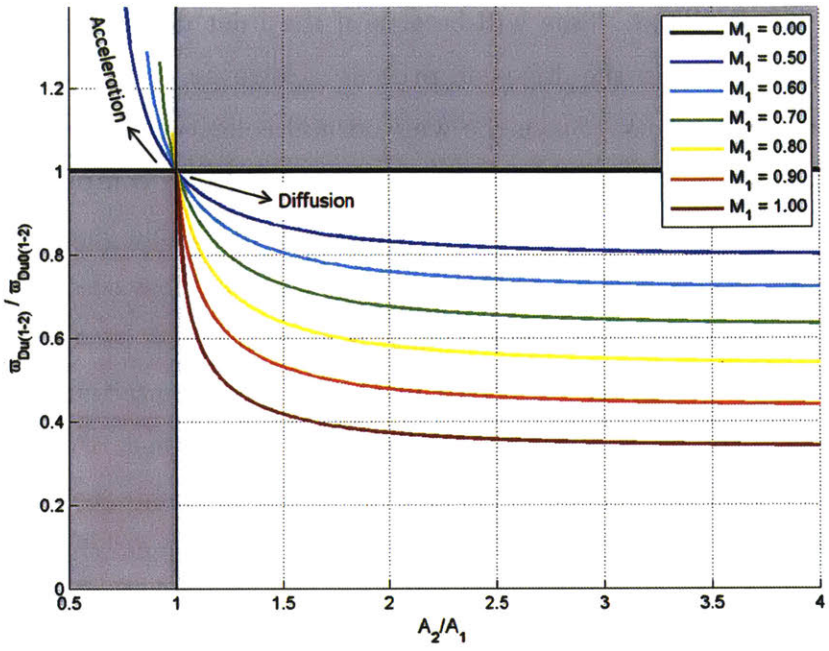


Figure 5.11: 1D uniform flow stagnation pressure loss coefficient due to scrubbing losses normalized by equivalent incompressible loss versus diffuser area ratio. Compressibility reduces loss coefficient in diffusion processes. Assumes thin boundary layer; not valid for large cone angles.

ing of bulk flow nonuniformities. If the scrubbing losses dominate, a compressibility correction can be performed if velocity distributions are assumed throughout the diffuser, both for the compressible flow and the equivalent incompressible flow. These distributions must be accurate, since the loss is highly sensitive to them.

$$E_{(1-2)} = \frac{C_{p(1-2)}}{C_{pu(1-2)}} \qquad \text{Equation 5.14}$$

Attempts are not made in this thesis to correct performance metrics for compressibility. Rather, the goal is simply show where and to what degree compressibility does have an effect on the diffuser flow and resulting performance metrics.

## 5.4 Summary of Fundamental Flow Mechanisms

This chapter discusses the general effects of various flow mechanisms present in any diffuser, and quantifies them using 1D flow examples. The static pressure distribution is largely determined by the area distribution. However, nonideal effects reduce the static pressure relative to what is ideal. These effects include nonuniformity amplification (an inviscid effect), as well as mixing and wall friction, viscous effects which also result in stag-

nation pressure loss. While mixing does introduce loss, it is shown that a uniformly mixed flow improves the static pressure rise over that of a nonuniform flow. Lastly, compressibility is shown to increase the ideal static pressure recovery coefficient in a diffusion process, especially at low area ratios, while reducing the stagnation pressure loss coefficient, especially at large area ratios.

# Chapter 6 Diffusion System Performance Assessment

The purpose of this chapter is to provide an understanding of how the diffusion system performance affects the overall compressor performance. In general, the objective is to explain why the diffusion system performs the way it does. Specifically, this involves addressing what flow mechanisms drive diffusion system performance changes across a range of operating conditions, and why the baseline and truncated diffuser configurations perform differently especially with respect to compressor stability.

The diffusion system consists of the diffuser and the deswirler, as shown in Figure 6.1. To investigate the diffuser performance in more detail, it is further broken down into two sub-components: the diffuser inlet and passage. The diffuser inlet is defined here to extend from the impeller exit (station 27) to the diffuser throat (station T). This is the region which is directly influenced by variations in the impeller exit flow angle. The diffuser passage is defined here to extend from the diffuser throat (station T) to the trailing edge of the baseline diffuser (station 29). This is the region which differs geometrically between the baseline and truncated diffusers.

Figure 6.1 illustrates the interactions between each of these diffusion system components, and it demonstrates the approach for characterizing the diffusion system in this research. Each box represents a boundary condition or performance metric, while the arrows connecting the boxes represent the specific flow mechanisms that cause the interaction. The idea behind this framework is that each component can be characterized by understanding the driving flow mechanisms within that component and how they relate the most influential inlet conditions to the exit conditions and performance metrics. To characterize the diffuser inlet for example, the impeller exit flow angle, Mach number, and flow nonuniformities are cast in terms of their effects on the inlet 1D area ratio, path length, incidence, compressibility, shocks, blockage, and mixing. These mechanisms are then used to charac-

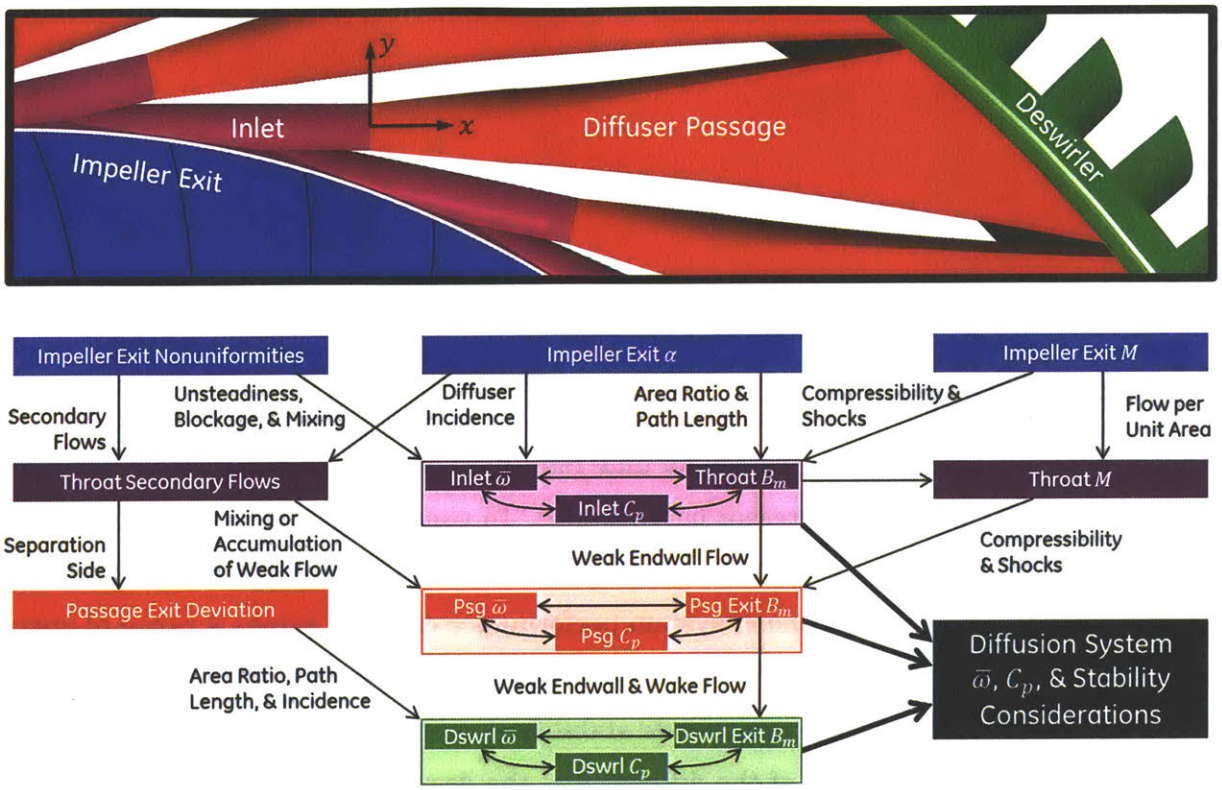


Figure 6.1: Modular perspective of diffusion system performance illustrating most influential boundary conditions (boxes), performance metrics (boxes), and flow mechanisms (arrows). Each component's performance metrics and exit conditions can be characterized in terms of inlet conditions by understanding influential flow mechanisms. System performance metrics may be understood by linking components together.

terize the diffuser inlet loss and pressure recovery trends, and to describe the effects on the secondary flows, blockage, and Mach number at the diffuser throat. It should be noted that the effect of unsteadiness, while noted in Figure 6.1 as a potentially influential flow mechanism, is not investigated in this research since its influence is hypothesized to be limited as explained in Sections 1.3 and 2.5.1.2. Furthermore, only those mechanisms relating to the performance of the diffuser inlet and passage are investigated in this thesis, while the deswirler is not investigated. This is because the deswirler is shown in Section 6.1 to play a relatively small role in the overall diffuser system performance.

It might seem unusual that this chain of causality includes no mention of diffusion system geometry, or of the three fundamental mechanisms influencing diffuser flow nonuniformity and loss discussed in Section 5.2. Diffusion system geometry is not included as a flow mechanism because it is not one. Rather, it influences each mechanism (e.g. the diffuser leading edge geometry influences the secondary flows, where the secondary flows are

the actual mechanisms). If the individual mechanisms are understood, then the impact of geometry on the mechanisms will also be understood. As for the three noted nonuniformity and loss mechanisms (nonuniformity amplification, streamline shear or mixing, and nonuniformity introduction via wall friction), these are not mentioned because they are understood to be the fundamental sub-mechanisms through which inefficiencies are incurred. However, they are influenced by the other mechanisms listed. Understanding these interactions will result in an understanding of why the compressor performance changes with operating point and diffusion system geometry.

## 6.1 Diffusion System and Diffuser Performance

To investigate what drives the performance of the diffusion system, this research focuses primarily on the diffuser as opposed to the deswirler. This is because the deswirler contributes less much less to the compressor performance than the diffuser. Figure 6.2 shows that 95% of the overall diffusion system's static pressure rise occurs in the diffuser, leaving only 5% for the deswirler. The diffuser also incurs 75%-85% of the diffusion system's stagnation pressure loss. Therefore, most of the performance-limiting mechanisms driving the performance trends for this diffusion system are present in the diffuser. Furthermore, focusing on the diffuser offers a large potential for future design improvement. Previous work at RWTH Aachen University has already identified a large separation in the baseline diffuser, as well as strong secondary flows introduced in the diffuser inlet [1] [2] [3] [4] [18]. It is hypothesized that an improved understanding of the causes and impacts of these mechanisms and others will provide some insights that could be leveraged in future designs.

This is not to say that the deswirler performance is not worth considering. In fact, because it generates 15%-25% of the overall diffusion system's stagnation pressure loss with only 5% of the static pressure rise, it makes sense that greater physical understanding of the deswirler will yield opportunities for improvement. For the truncated diffuser experiments in particular, the diffuser exit flow angle and deswirler leading edge incidence are increased above the deswirler's design intent. Experiments conducted at RWTH Aachen University matching new deswirlers with the truncated diffuser have in fact shown improvements [4]. That said, this research focuses on the diffuser for the reasons noted.

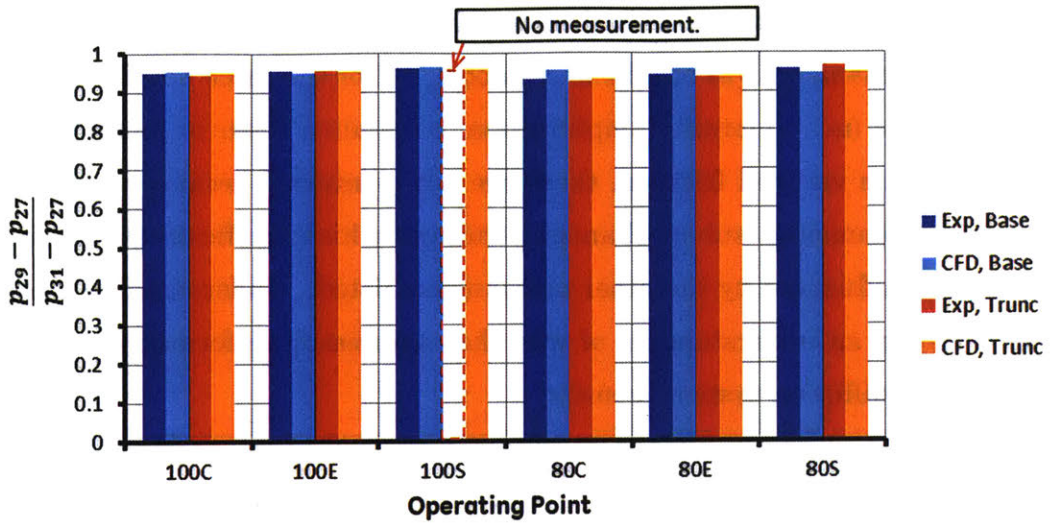


(a) Diffuser static pressure rise fraction.

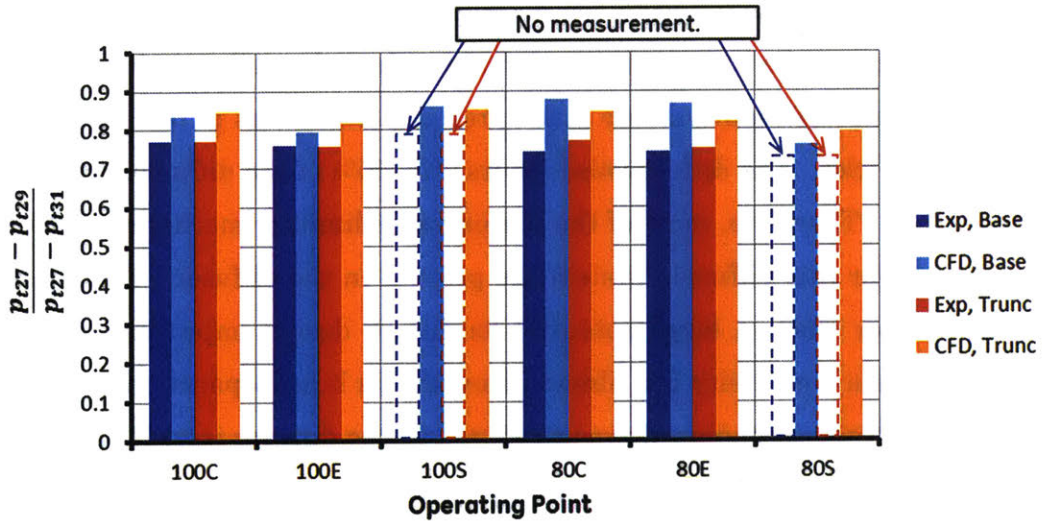


(b) Diffuser stagnation pressure loss fraction.

Figure 6.2: Fraction of diffusion system performance attributable to diffuser. Because most of the diffusion system performance is attributable to the diffuser, this research will not investigate details of the deswirler.

Upon performing this same analysis for the diffuser inlet and passage, it is clear that both sub-components are important for explaining the diffuser performance. This is seen in Figure 6.3. Approximately half of the diffuser's stagnation pressure loss is incurred in the inlet. Similarly, the inlet contributes up to 60% of the diffuser's static pressure rise near stall, while reducing it significantly for the 80C operating point. Unlike the deswirler, neither the diffuser inlet nor the passage can be ignored in this research.

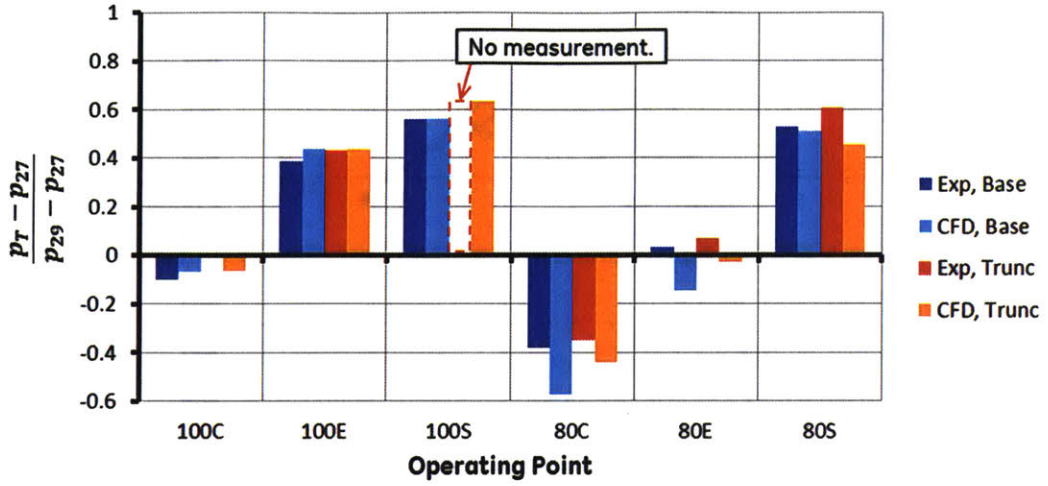


(a) Diffuser inlet static pressure rise fraction.

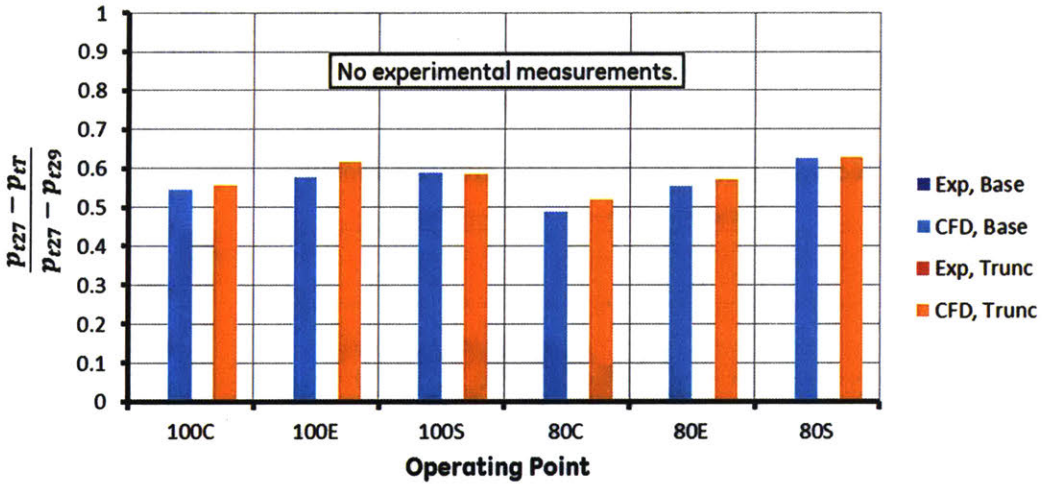


(b) Diffuser inlet stagnation pressure loss fraction.

Figure 6.3: Fraction of diffuser performance attributable to inlet. Because both diffuser inlet and passage contribute significantly to diffuser performance, both are investigated further in this research.

The static pressure recovery coefficients for the overall diffusion system and the diffuser by itself, including both baseline and truncated diffuser configurations, are shown in Figure 6.4. Because the deswirler contributes little to the pressure rise of the diffusion system, the diffuser and diffusion system pressure recovery trends are the same. The same is nearly true of the stagnation pressure loss coefficients shown in Figure 6.5, though there are some small differences. Recall that diffuser exit stagnation pressure is only measured at the 80C, 80E, 90C, 90E, 100C, and 100E operating points.

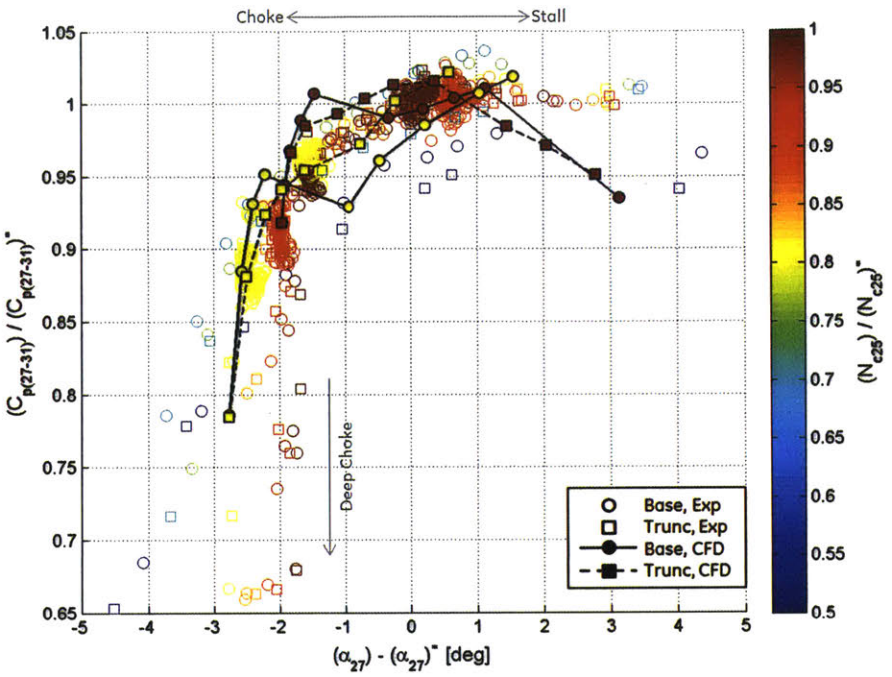


(a) Static pressure recovery coefficient for overall diffusion system.

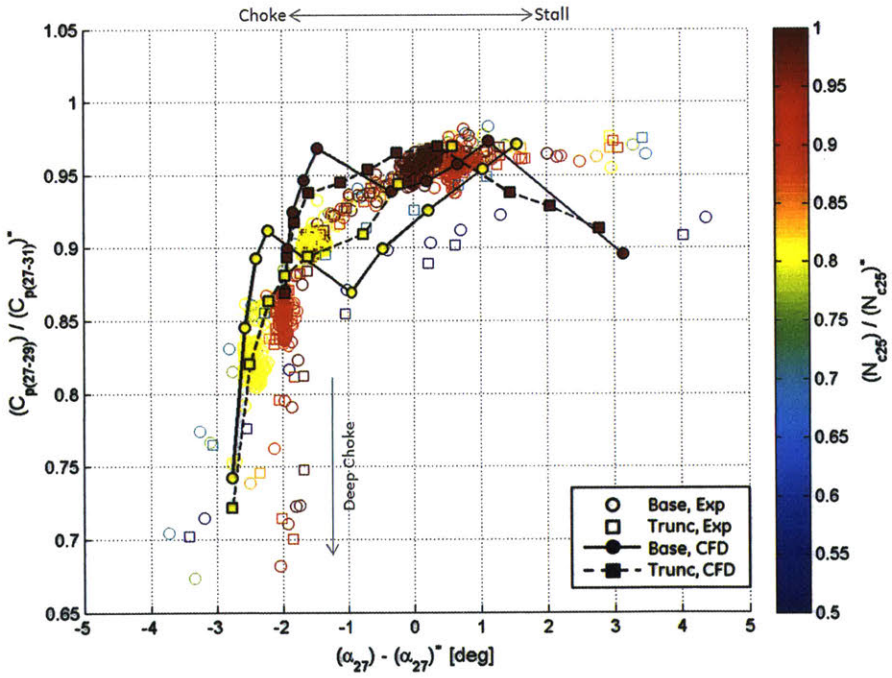


(b) Static pressure recovery coefficient for diffuser only.

Figure 6.4: Static pressure recovery coefficient versus impeller exit flow angle. Symbols and line styles denote diffuser configuration and data source, while colors denote rotor speed. Diffusion system and diffuser trends comparable. Overarching positive correlation between flow angle and pressure recovery coefficient. Pressure recovery most sensitive to flow angle and speed at low flow angles. Acceptable agreement between experimental and CFD trends.

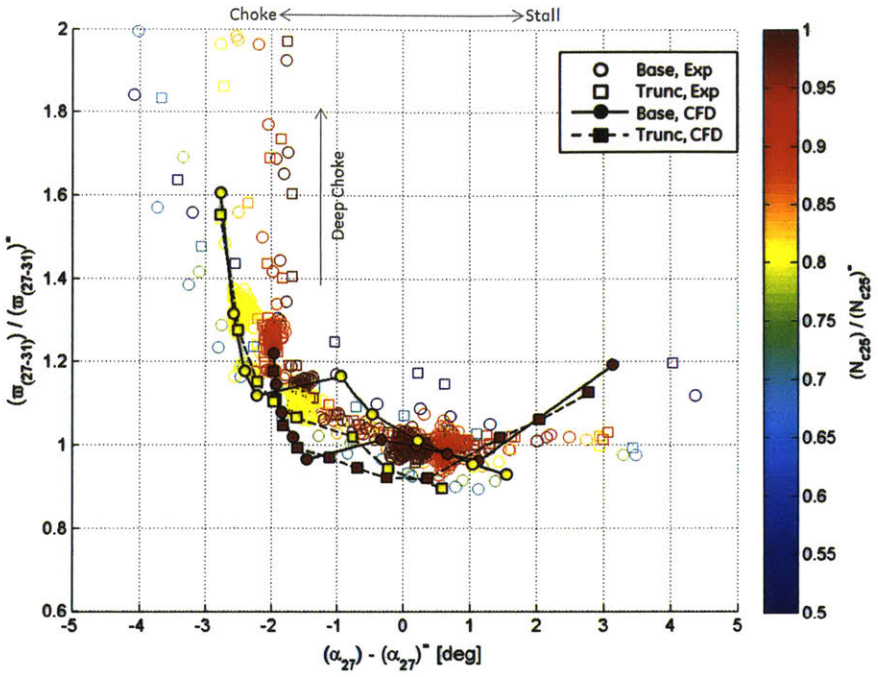


(a) Stagnation pressure loss coefficient for overall diffusion system.

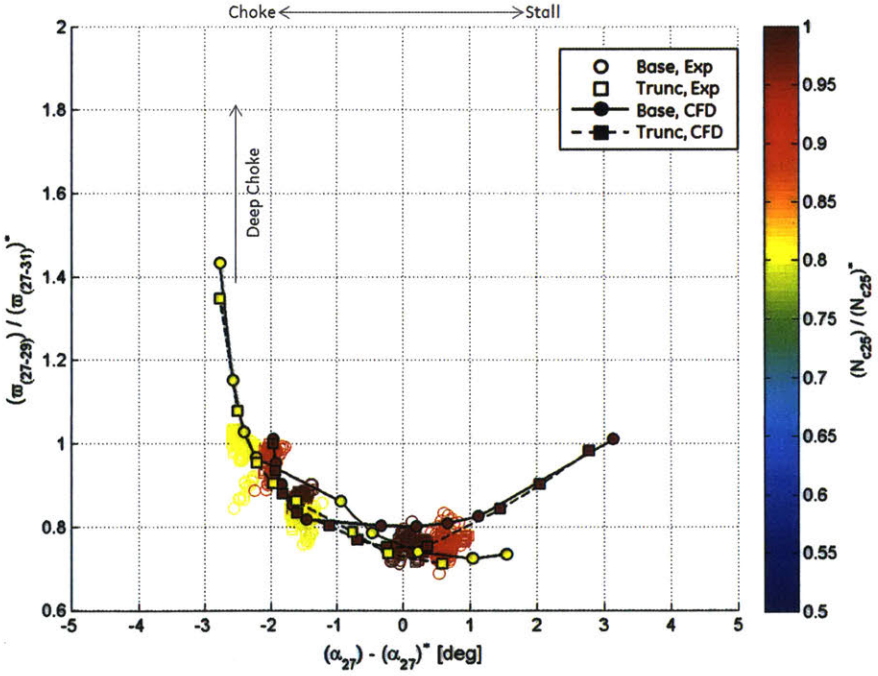


(b) Stagnation pressure loss coefficient for diffuser only.

Figure 6.5: Stagnation pressure loss coefficient versus impeller exit flow angle. Symbols and line styles denote diffuser configuration and data source, while colors denote rotor speed. Diffusion system and diffuser trends comparable. Minimum loss near design flow angle, with increased loss off-design. Pressure recovery most sensitive to flow angle and speed at low flow angles. Acceptable agreement between experimental and CFD trends.

Consistent with Filipenco's finding, the experimental data shows the diffuser pressure recovery characteristic having an increasing trend with respect to diffuser inlet flow angle. This trend has two segments. At low flow angles, the pressure recovery is lowest and decreases rapidly with reduced flow angle, reaching a minimum flow angle when the diffuser chokes. This drop-off effect is observed at lower flow angles when the compressor speed is also low than when the compressor speed is high. At higher flow angles between choke and stall, the compressor pressure recovery increases more gradually with respect to flow angle. Also consistent with Filipenco's finding, the level and slope of the pressure recovery characteristic at high flow angles is largely independent of compressor speed, with the exception of the 50% $N_{c25}$ experiments where a reduction in pressure recovery is observed. It should be noted that the positive correlation between diffuser inlet flow angle and static pressure rise contributes beneficially to the overall compressor stability, as discussed in Chapter 7.

The CFD solutions show diffuser performance levels that are consistent with the experimental results (within 5% for static pressure recovery coefficient, and within 10% for stagnation pressure loss coefficient). However, recall that there is an estimation procedure for determining the impeller exit stagnation pressure for the experiments discussed in Section 2.4.3.3. This estimation utilizes an assumption that the torque on the impeller shroud is twice the level measured from the 100E baseline diffuser CFD solution. This assumption essentially places the discrepancy between experimental and CFD compressor performance levels on the impeller, while improving the match between experimental and CFD results for the diffuser. As discussed in Section 4.1, this assumption is believed to be reasonable since there is already a known mismatch between the experimental and CFD calculated impeller work coefficients, and because instrumentation is present on the experimental impeller shroud. However, other assumptions could also be reasonably made to estimate the impeller exit conditions, which would alter the match between experimental and CFD calculated performance levels in the diffuser. That said, what matters most for this research is that the CFD solutions capture experimental performance trends with respect to operating point and diffuser configuration, regardless of whether pressure and loss coefficient magnitudes are also captured.

To investigate the diffuser static pressure recovery and stagnation pressure loss trends in more detail, the 100% $N_{c25}$ and 80% $N_{c25}$ speed lines are shown in Figure 6.6 and Figure 6.7 highlighting the choke, peak efficiency, near stall, and CFD post stall operating points.

The CFD solutions do in fact show that the overarching performance trends are consistent with the experimental results; namely, the generally positive correlation between flow angle and pressure recovery coefficient. However, there is a piecewise appearance to the CFD trends not seen in the experimental results, such that the CFD pressure recovery characteristic varies along the speed line. This gives rise to the piecewise appearance of the overall compressor CFD performance trends discussed in Section 3.2. Three different regimes of behavior—regions 1, 2, and 3—are identified and denoted in Figure 6.6. These regions will be referenced throughout the remainder of this thesis.

Figure 6.6 and Figure 6.7 also demonstrate that according to the experimental data, there is negligible difference between the static pressure rise and stagnation pressure loss of the baseline and truncated diffusers. However, the CFD shows the stagnation pressure loss of the baseline diffuser being lower than the truncated diffuser at some operating conditions. Also, the piecewise appearance of the CFD calculated pressure recovery trend is much more pronounced for the baseline diffuser than for the truncated diffuser, such that the baseline diffuser static pressure recovery is higher than the truncated diffuser at some flow angles, and lower at others. In addition, the fact that the CFD calculates different slopes for the baseline and truncated diffuser pressure rise characteristics has implications for compressor stability.

The causes of the diffuser performance trends and the physical relevance of the piecewise appearance of the CFD solution must be addressed by examining the diffuser in more detail. This will be done for the diffuser as a whole, as well as for the diffuser inlet and passage separately.

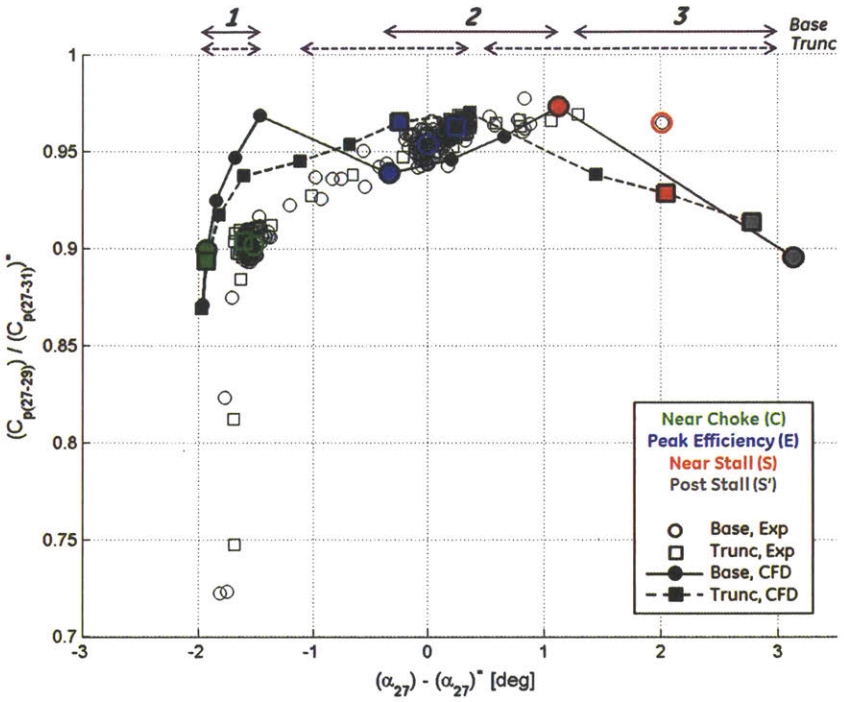


(a) 100% $N_{c25}$.

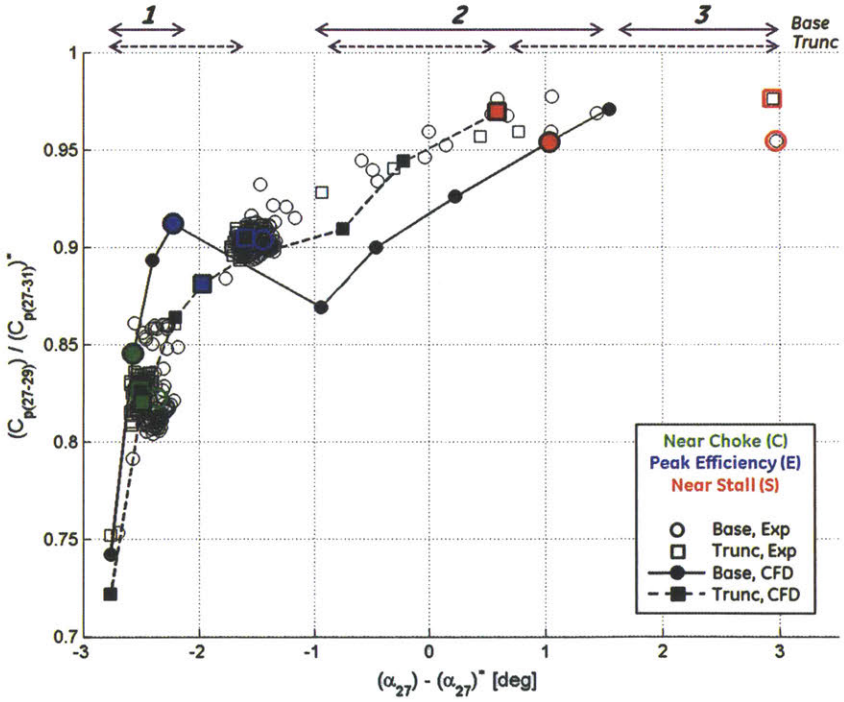


(b) 80% $N_{c25}$.

Figure 6.6: Diffuser static pressure recovery coefficient versus impeller exit flow angle. Symbols and line styles denote diffuser configuration and data source, while colors denote operating point (note: colored experimental points averaged from multiple tests). Experimental data indicates no difference between diffuser configurations, while CFD indicates differences which vary between operating points. Note piecewise appearance of CFD trend (regimes of behavior denoted 1, 2, and 3).

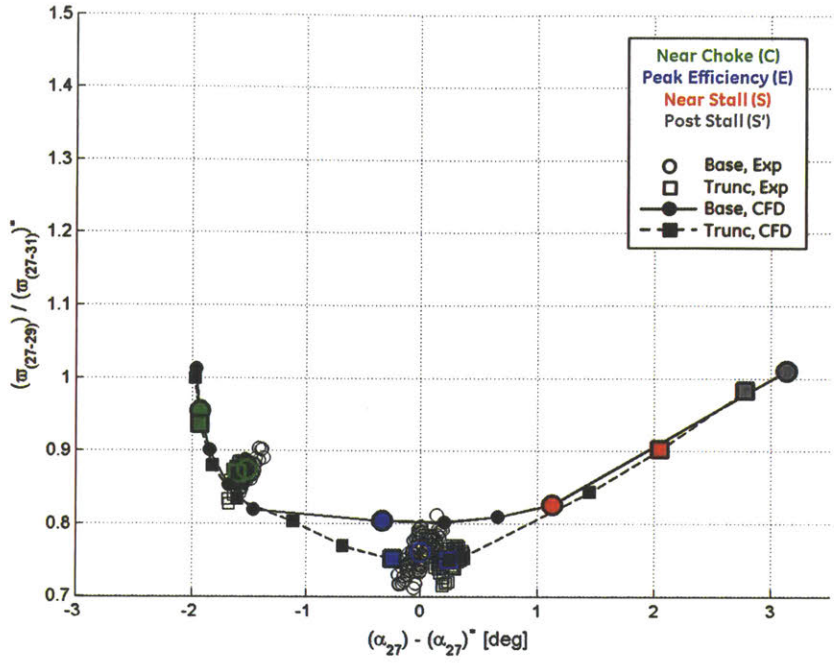


(a) 100% $N_{c25}$.

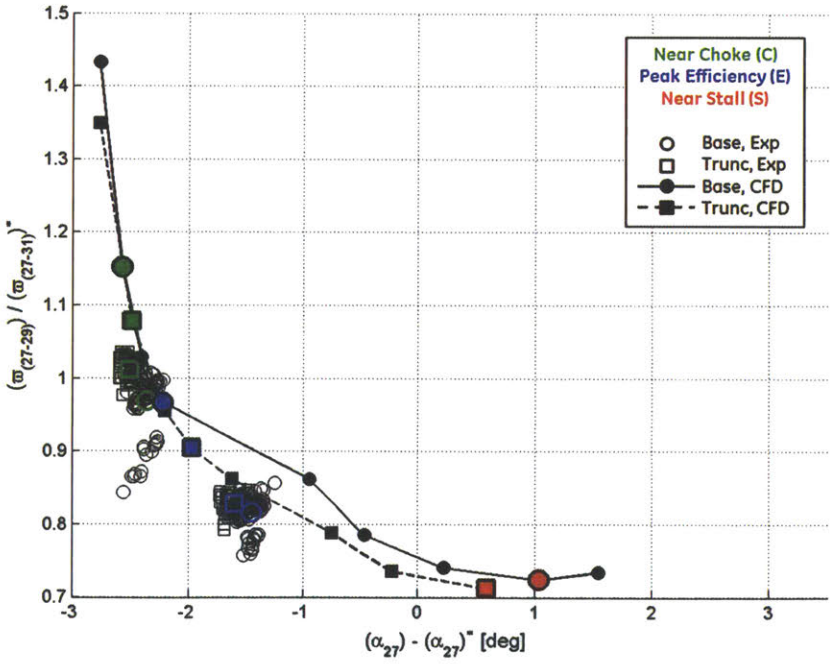


(b) 80% $N_{c25}$.

Figure 6.7: Diffuser stagnation pressure loss coefficient versus impeller exit flow angle. Symbols and line styles denote diffuser configuration and data source, while colors denote operating point (note: colored experimental points averaged from multiple tests). Experimental data indicates no difference between baseline and truncated diffuser pressure recovery coefficients, while CFD indicates truncated diffuser loss is lower than baseline.

## 6.2 Identification of Diffuser Flow Mechanisms

Some of the specific loss and blockage mechanisms in the diffuser can be seen by looking at the distributions of stagnation pressure loss coefficient and entropy generation rate calculated by the CFD simulations. These are shown for the baseline diffuser in Figure 6.8 and Figure 6.10, and for the truncated diffuser in Figure 6.9 and Figure 6.11 (notice that the entropy generation rate is color-coded using a logarithmic scale). The passage separations mentioned in Sections 1.3 and 3.3.1 are clearly visible, characterized by large areas high loss coefficient and reversed flow ($V_x < 0$). High loss fluid is also observed in the attached boundary layers, and on the downstream side of the trailing edge. Each of these mechanisms contributes to the flow blockage, and each forms a corresponding shear layer between the high loss region and the low loss jet. These shear layers may be identified by their high entropy generation rates. For the separation regions in particular, the corresponding shear layer is located away from the wall. Other less influential loss mechanisms that can be seen in these figures are shocks, occurring near choke or at low flow angles, and flow shear around the diffuser leading edge due to the presence of high velocity gradients.

There is a clear progression in the intensity of these various mechanisms as the compressor is throttled from choke to stall, or between low and high impeller exit flow angle. Conversely, between 100% $N_{c25}$ and 80% $N_{c25}$ the flow mechanisms appear similar. Note that due to the lower impeller exit Mach number at 80% $N_{c25}$, a lower flow angle is achieved before the diffuser chokes and before shocks develop (to compare 100% $N_{c25}$ and 80% $N_{c25}$ CFD solutions at the same flow angle, compare 100C with 80E).

Comparing the baseline and truncated diffusers, we see distinctly significant differences between the influential flow mechanisms. For the baseline diffuser, the majority of the loss is generated in the shear layer between the region of reversed flow and the main jet. The flow also exits the diffuser with a low level of swirl, but with a high level of nonuniformity. For the truncated diffuser, the region of weak flow is still large enough to generate significant losses in the shear layer, but because the separation is smaller these losses are lower than for the baseline diffuser. However, the truncated diffuser generates more loss than the baseline diffuser in the shear layer between the jet and the weak trailing edge flow. The extended vanless space allows the nonuniformities to mostly mix out by the diffuser exit, but the exit flow angle is higher.

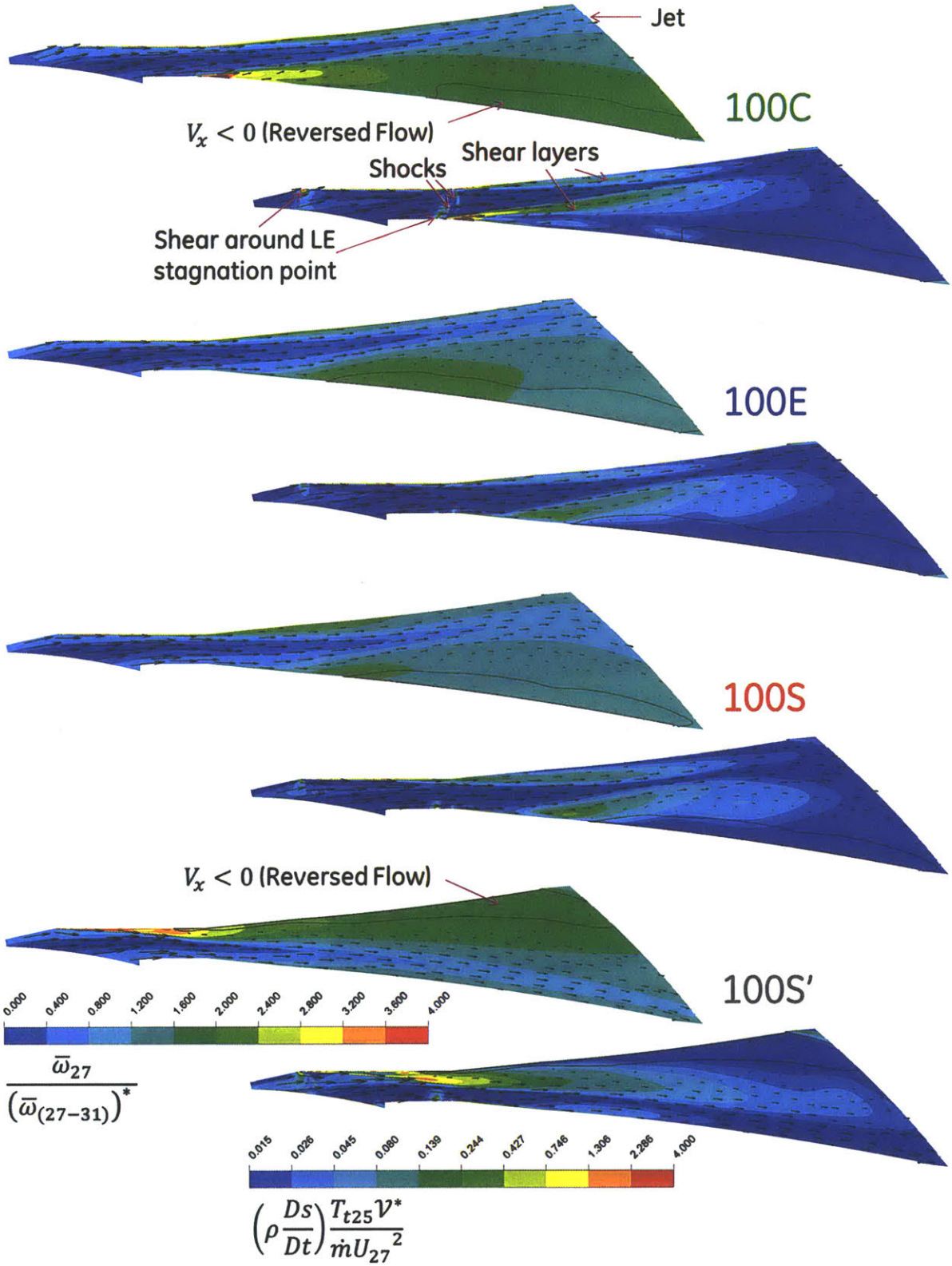


Figure 6.8: CFD calculated distributions of stagnation pressure loss coefficient (*left*) and entropy generation rate (*right*) at 100% $N_{c25}$ for baseline diffuser. Notable flow mechanisms indicated. Note nonlinear color scale on entropy generation rate.

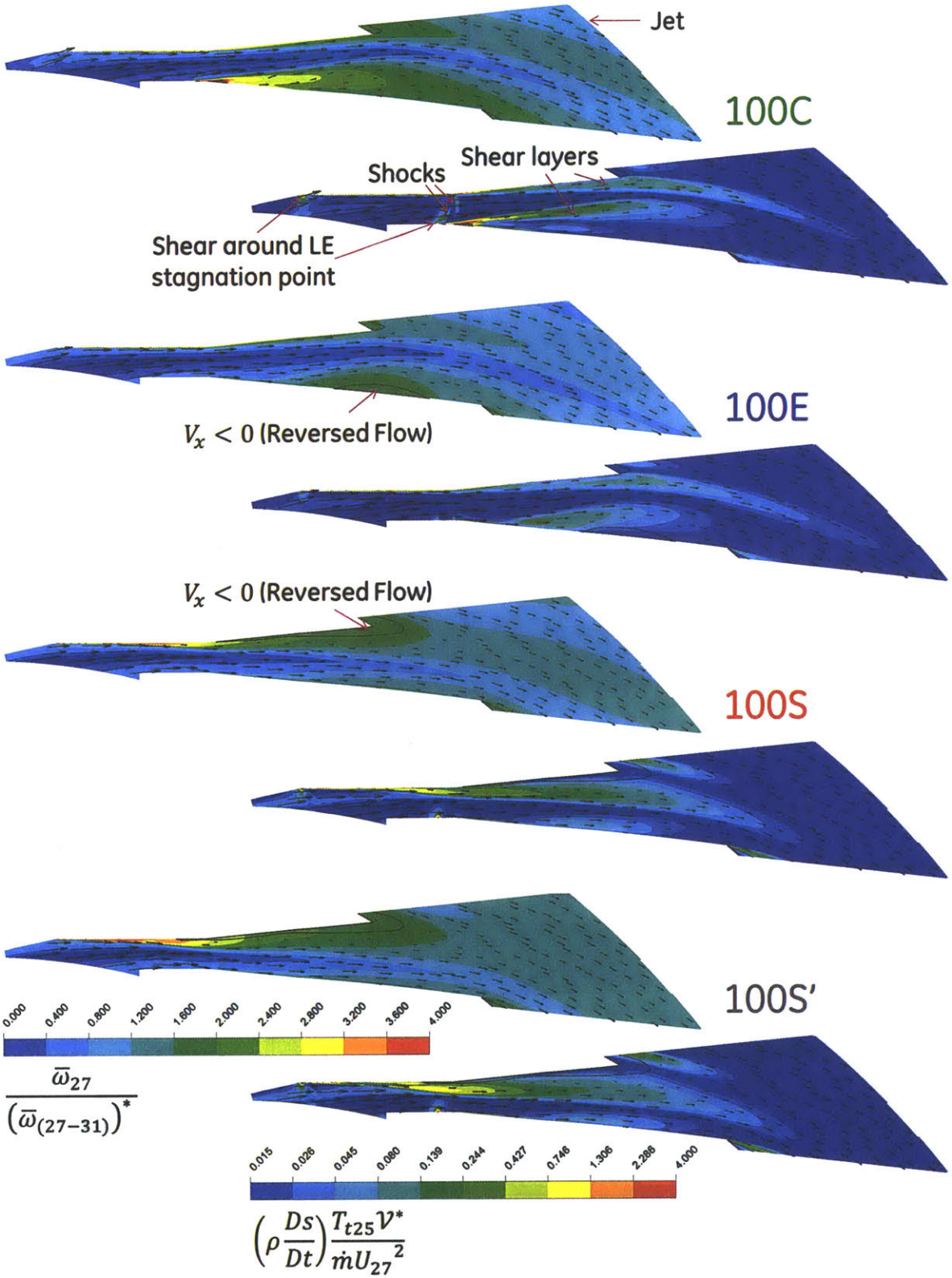


Figure 6.9: CFD calculated distributions of stagnation pressure loss coefficient (*left*) and entropy generation rate (*right*) at 100% $N_{c25}$ for truncated diffuser. Notable flow mechanisms indicated. Note nonlinear color scale on entropy generation rate.

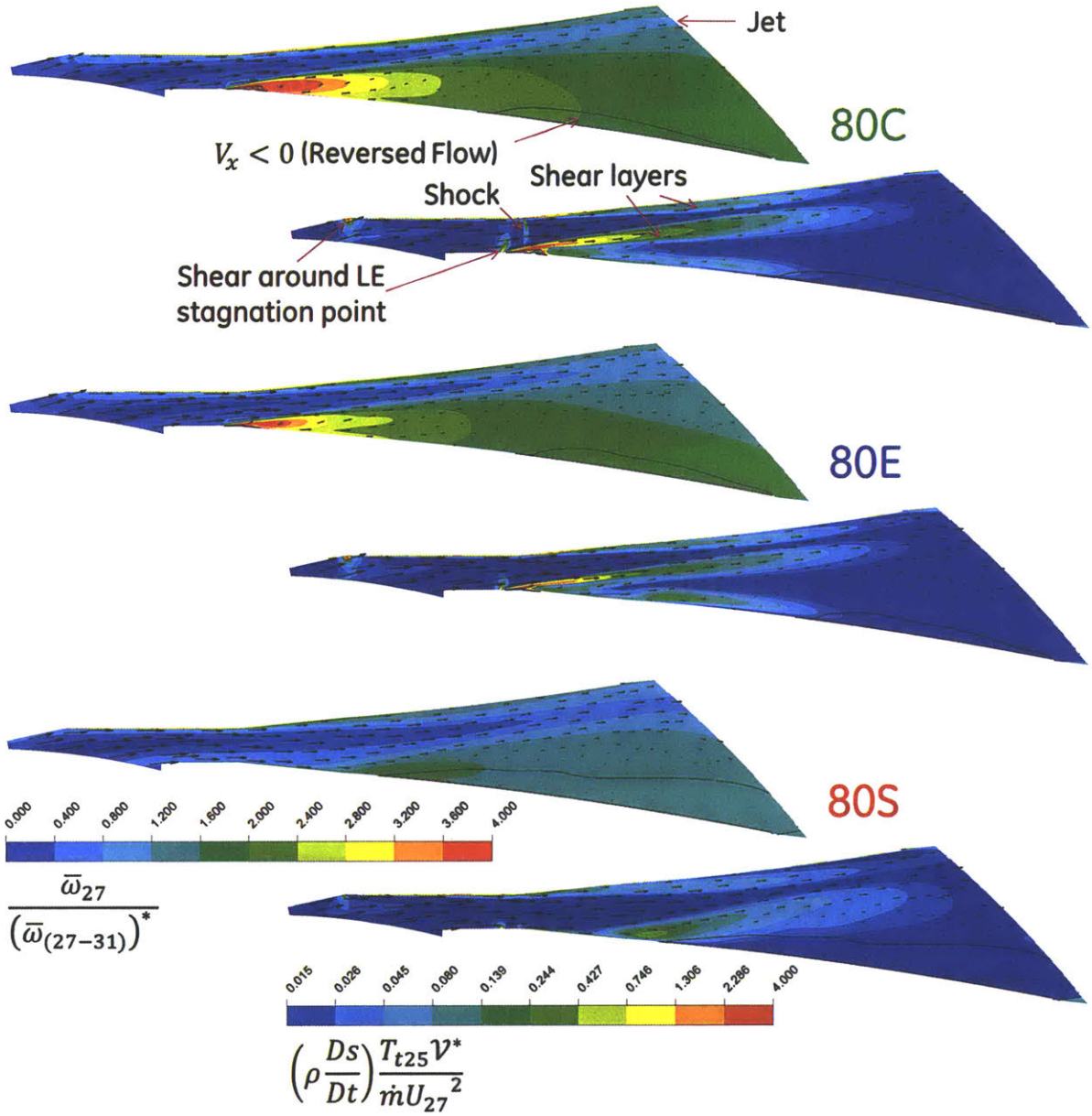


Figure 6.10: CFD calculated distributions of stagnation pressure loss coefficient (*left*) and entropy generation rate (*right*) at 80% $N_{c25}$ for baseline diffuser. Notable flow mechanisms indicated. Note nonlinear color scale on entropy generation rate.

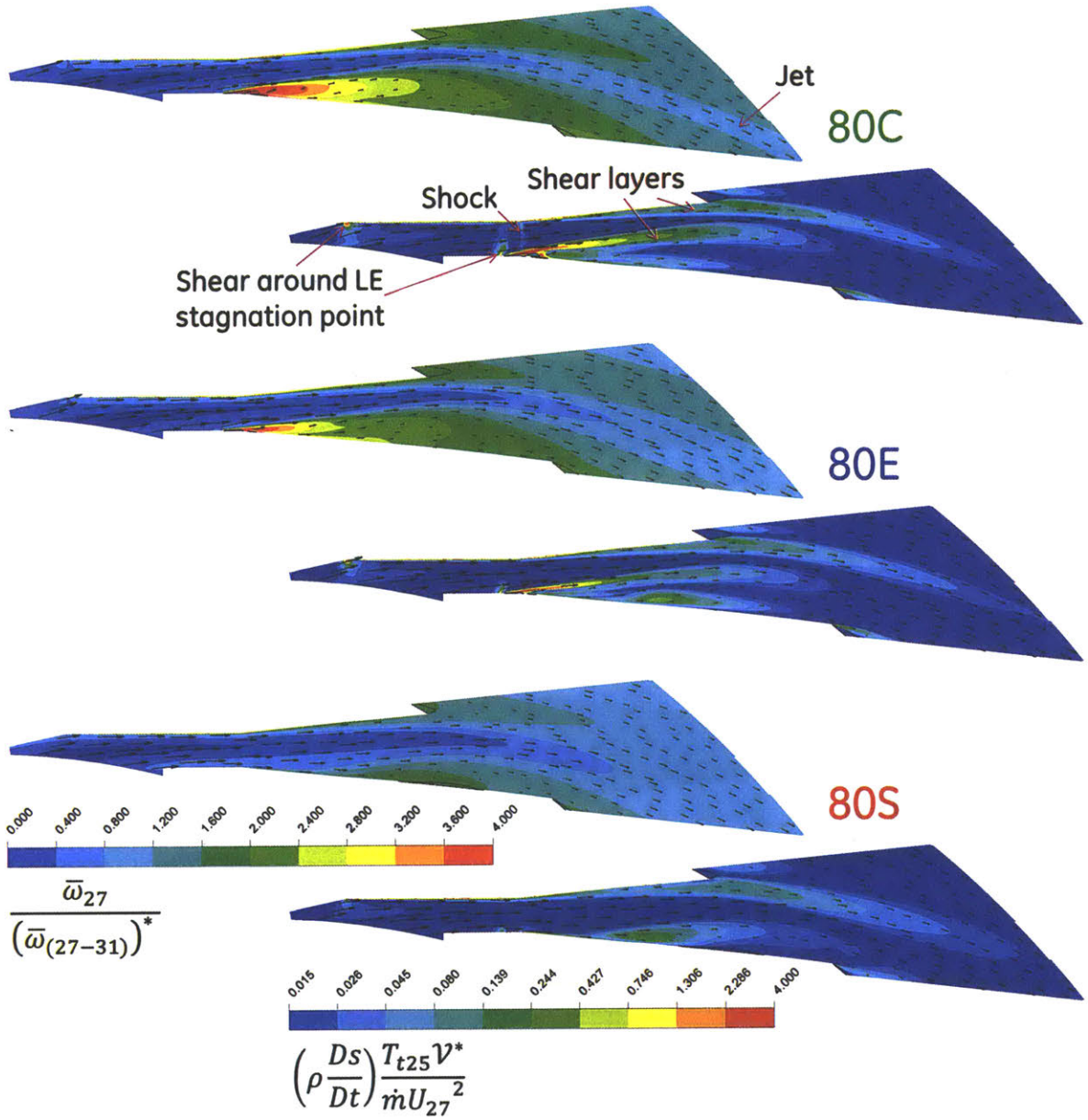


Figure 6.11: CFD calculated distributions of stagnation pressure loss coefficient (*left*) and entropy generation rate (*right*) at 80% $N_{c25}$ for truncate diffuser. Notable flow mechanisms indicated. Note nonlinear color scale on entropy generation rate.

The various flow mechanisms, most notably the separation, switch location between the diffuser pressure side and suction side as the compressor is throttled. For the baseline diffuser, the CFD solution shows the switch in separation side occurring just after stall. This is seen by comparing the baseline diffuser 100S and 100S' CFD solutions. For the truncated diffuser at 100% $N_{c25}$, the switch in separation side occurs before stall such that stable operation with a suction side separation is possible. This is seen by comparing the truncat-

ed diffuser 100E and 100S CFD solutions. At 80% $N_{c25}$, CFD simulations shows the separation side switching for both baseline and truncated diffusers when throttled slightly past stall, but solution convergence is not able to be achieved for either configuration. This switch in separation side corresponds to a sudden change in slope of the diffuser's CFD calculated pressure recovery characteristic, as shown in Figure 6.6 between regions 2 and 3. For this reason, this switch in separation side is hypothesized to impact the stability of the true compressor, as explained in Chapter 7. It certainly impacts the stability of the simulated CFD compressor, explaining why CFD convergence is difficult to achieve with a suction side diffuser separation. Notably, because the baseline diffuser's separation is larger than the truncated diffuser's, this effect is more pronounced for the baseline diffuser.

If one looks closely, it is apparent that the size of the separation does not vary smoothly with flow angle. The region of reversed flow on the diffuser pressure side is actually greater near the design flow angle (e.g. 100E or 80S) than it is at flow angles lower by only 1-2 deg (e.g. 100C or 80C/E). The CFD solutions "jump" between these two separation regimes, corresponding to the piecewise shift in the diffuser's CFD calculated pressure recovery characteristic, as shown in Figure 6.6 between regions 1 and 2. Also characterizing this jump is the amount of loss generated immediately downstream of diffuser leading edge on the separation side. Again, because the baseline diffuser's separation is larger than the truncated diffuser's, this effect is more pronounced for the baseline diffuser.

## 6.3 Evolution of 1D Flow Conditions along Diffuser

To simplify our understanding of these various mechanisms, 1D averages of flow variables are calculated from the CFD solutions at various cut planes along the diffuser length. As a reminder, these cut planes are shown in Figure 2.18. Figure 6.12 shows the diffuser static pressure recovery coefficient along the diffuser length. As has already been demonstrated, the amount of pressure rise occurring in the diffuser inlet varies significantly with operating point, but the overall diffuser pressure rise does not vary as drastically due to the large overall 1D area ratio. Towards the diffuser exit, the diffuser becomes less effective as the pressure rise coefficient levels off with length. Meanwhile, the stagnation pressure loss coefficient increases steadily throughout the entire diffuser, as shown in Figure 6.13. There is also a significant amount of loss incurred between the impeller exit and the mixing plane exit due to the impeller exit nonuniformity.

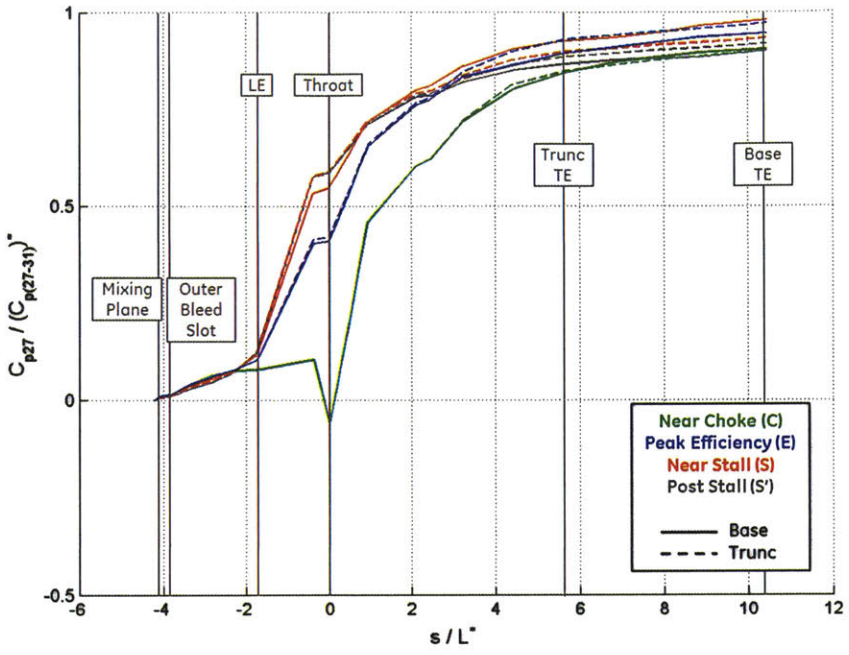


(a) 100% $N_{c25}$.

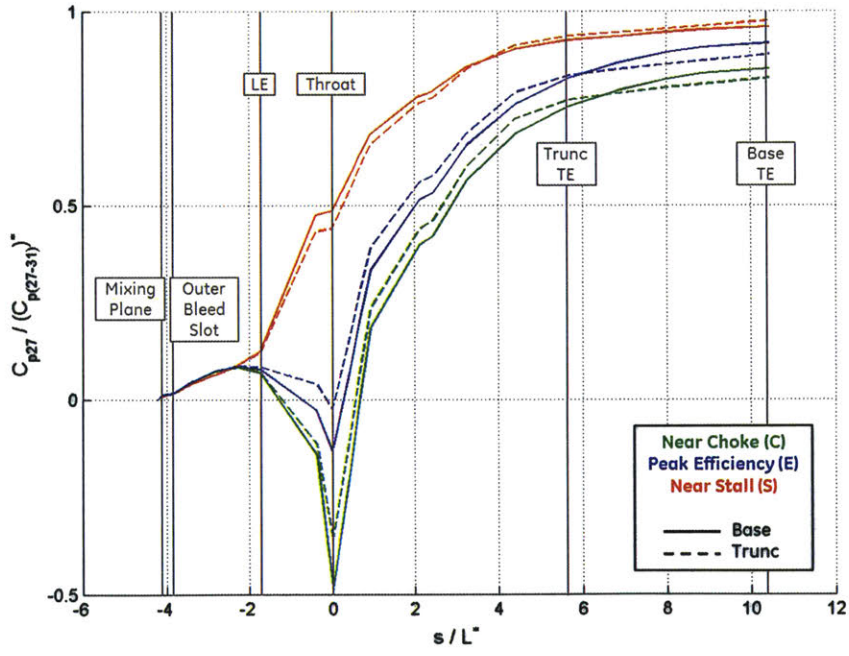


(b) 80% $N_{c25}$.

Figure 6.12: CFD calculated 1D static pressure recovery coefficient throughout diffuser. Line styles denote diffuser configuration, while colors denote operating point. Baseline and truncated diffusers are indistinguishable. Large variations between inlet and passage pressure recovery with operating point. Portion of diffuser downstream of truncated diffuser trailing edge is ineffective for both diffuser configurations.

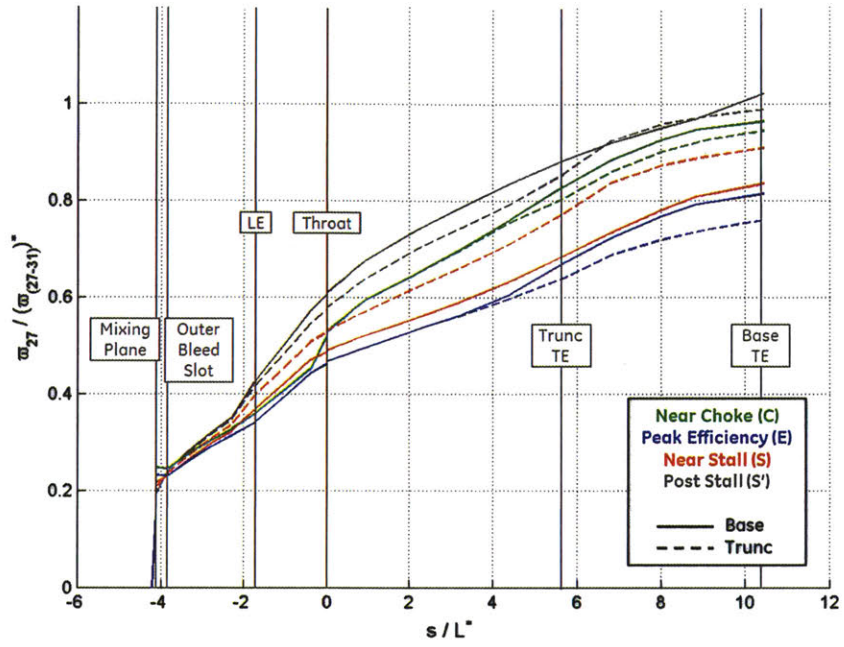


(a) 100% $N_{c25}$.

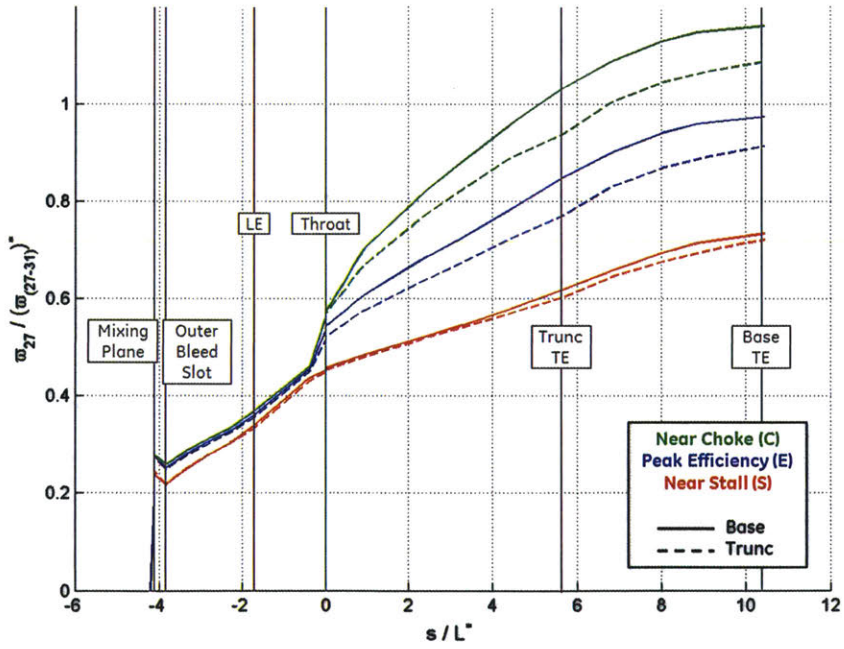


(b) 80% $N_{c25}$.

Figure 6.13: CFD calculated 1D stagnation pressure loss coefficient throughout diffuser. Line styles denote diffuser configuration, while colors denote operating point. Baseline and truncated diffusers are indistinguishable. Loss increases steadily throughout diffuser, especially for off-design flow angles.

Referring to Figure 6.12 and Figure 6.13, it is not appropriate to compare the baseline and truncated diffusers performance levels too closely due to differences in averaging planes, imperfect matching of operating conditions, and the previously noted shortfalls of the CFD solutions with respect to the experimental data. However, despite the large differences in their 1D area distributions, the pressure rise and loss trends observed near the diffuser exit are generally similar between the two configurations. To understand this better, Figure 6.14 and Figure 6.15 show the 1D aerodynamic mass blockage and shape factor respectively throughout the diffuser. These indicate that the baseline diffuser exit blockage is larger than it is for the truncated diffuser, compensating for the differences in exit area. This is the result of the large separation pointed out previously in the mid-passage contour plots and indicated by the high shape factor. A shape factor of $H > 4$ is a typical separation criteria for turbulent boundary layers, though this criteria is high for this 1D shape factor since the separation is only localized to portions of the averaging plane perimeter.

The baseline and truncated diffusers exhibit similar blockage and shape factor trends throughout the inlet region. First, due to mixing, the flow becomes more uniform between the impeller exit and the mixing plane exit. Then, it increases abruptly across the bleed slot as the flowpath width changes discontinuously, indicating the presence of flow reversal on the forward and aftward endwalls near the inlet to the bleed slots. Throughout the remainder of the inlet to the throat, the blockage and shape factor generally decrease. However, the nonuniformity does increase around the diffuser cusps and leading edge for flow angles higher and lower than the design point. In the semi-vaneless space between the leading edge and the throat, the rate at which the blockage decreases is inversely related to the amount of static pressure rise occurring over the same region.

In the diffuser passage, the blockage and shape factor trends differ between the baseline and truncated diffusers. For the baseline diffuser, they increase between the throat and exit as the nonuniformity grows. There is also a small increase in the nonuniformity as the flow passes over the trailing edge and the solid blockage becomes aero blockage, but this is negligible. For the truncated diffuser, the blockage and shape factor increase through the passage, but decrease beginning just upstream of the trailing edge. As the flow passes over the truncated diffuser's thick trailing edge, the aerodynamic blockage and shape factor increase such that they are momentarily larger than those of the baseline diffuser. However, they decrease again as the flow mixes throughout the vaneless space to the diffuser exit.

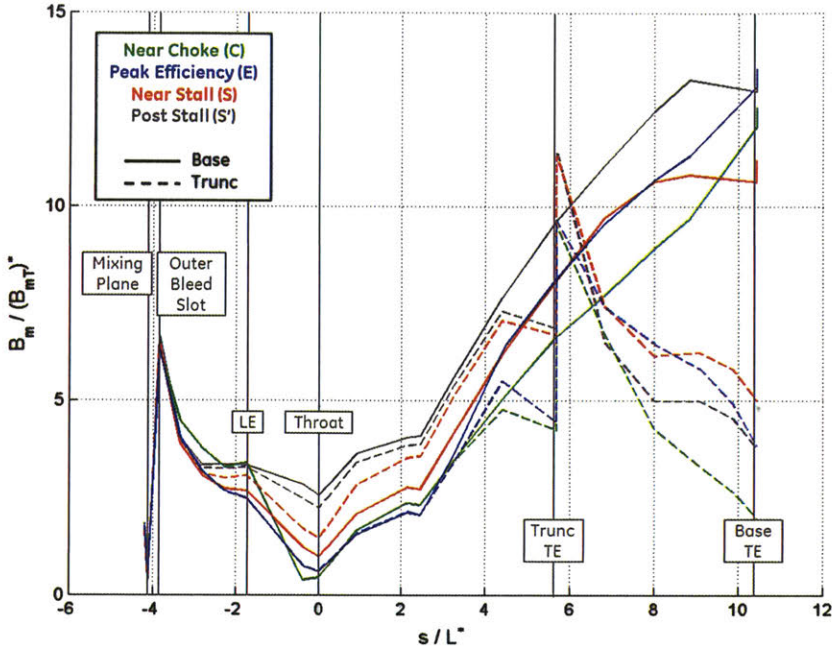


(a) 100% $N_{c25}$.

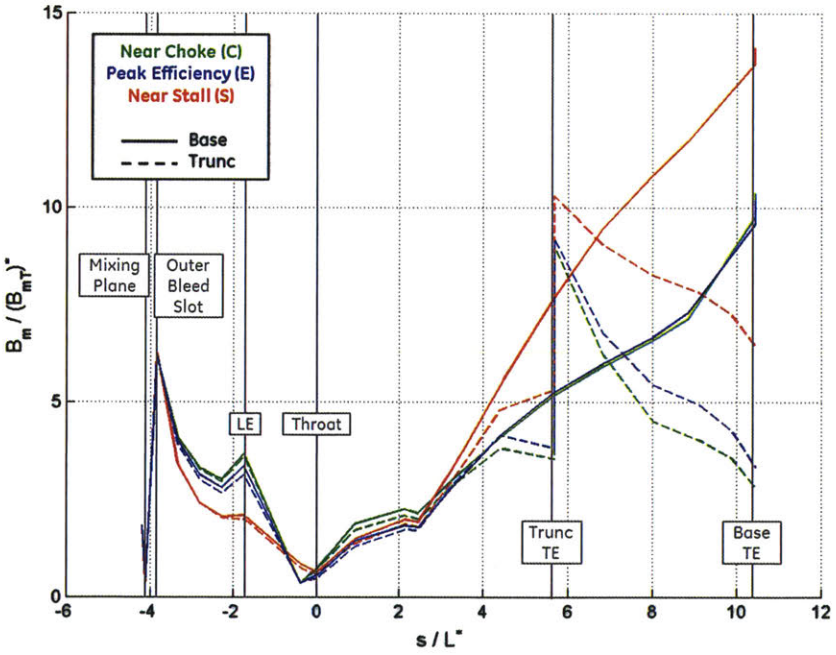


(b) 80% $N_{c25}$.

Figure 6.14: CFD calculated 1D aerodynamic mass blockage throughout diffuser. Line styles denote diffuser configuration, while colors denote operating point. Baseline and truncated diffusers are indistinguishable until near truncated diffuser trailing edge. Large blockage present at impeller-diffuser interface due to discontinuous passage width, but decreases throughout inlet even for diffusing flows. Leading edge blockage is dependent on operating point. Greatest blockage is at diffuser exit for baseline diffuser, and at trailing edge for truncated diffuser. Truncated diffuser blockage reduces downstream of trailing edge due to mixing.

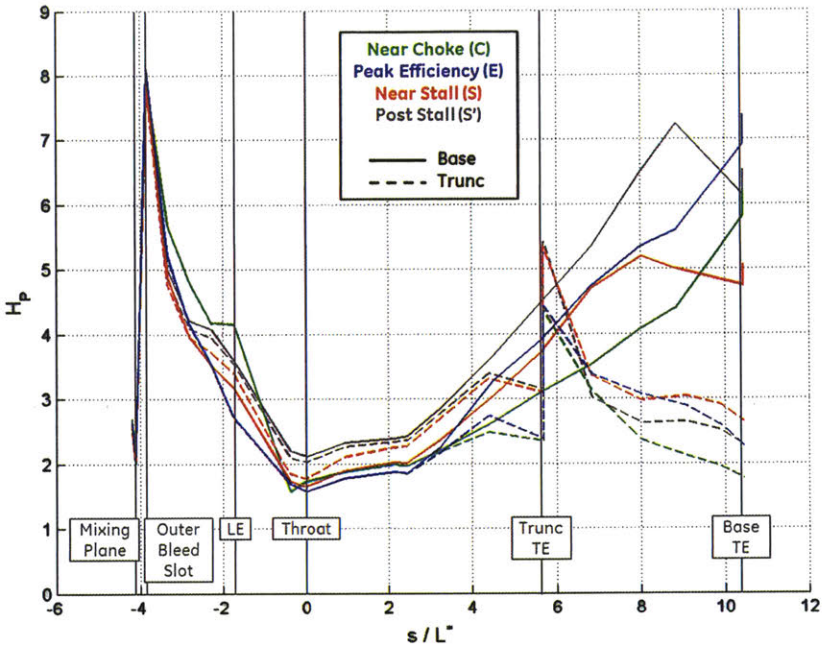


(a) 100% $N_{c25}$.

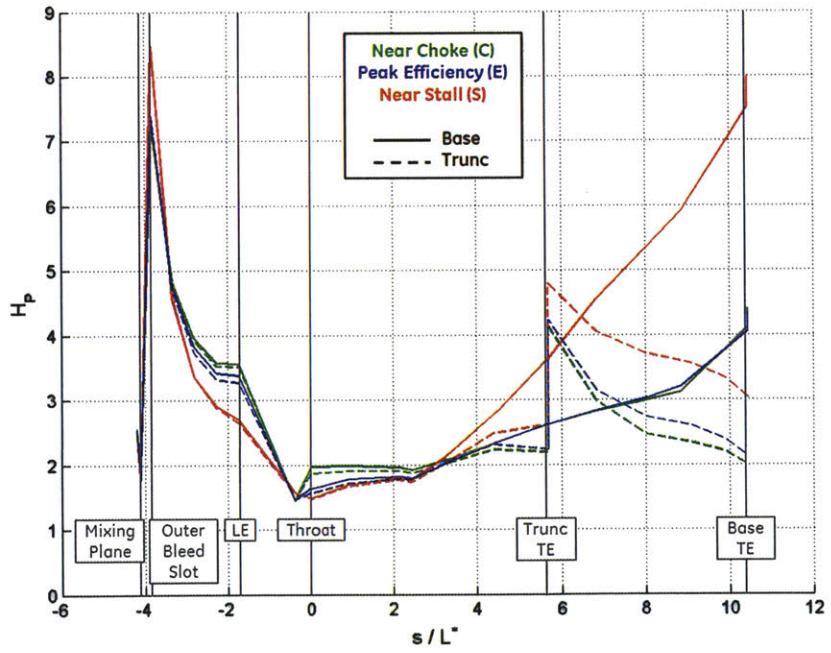


(b) 80% $N_{c25}$

Figure 6.15: CFD calculated 1D shape factor throughout diffuser. Line styles denote diffuser configuration, while colors denote operating point. Baseline and truncated diffusers are indistinguishable until near truncated diffuser trailing edge. Large shape factor present at impeller-diffuser interface due to discontinuous passage width and reversed flow, but decreases throughout inlet even for diffusing flows. Leading edge shape factor is dependent on operating point. Separation indicated at diffuser exit for baseline diffuser, and at trailing edge for truncated diffuser. Truncated diffuser shape factor reduces downstream of trailing edge due to mixing.

## 6.4 Evaluation of Nonideal Effects

As discussed in Section 1.3, one way to gauge the optimality of a diffuser design is to spot it on a diffuser design chart, relating simple geometric parameters to 1D performance parameters. Sovran and Klomp showed that for a diffuser to achieve the greatest possible pressure rise, it must have a specific 1D area ratio that depends only on its length normalized by its inlet height. This relationship is independent of diffuser inlet blockage and diffuser configuration, whether 2D, conical, or annular [7]. The particular diffusers being studied in the present work do fall close to this line, as shown by Wilkosz, making them good choices for further study [18].

To estimate the hypothetical performance level of the diffusers of interest with their particular inlet conditions, performance data generated by Cockrell and Markland is utilized. This is shown in Figure 6.16, where loss coefficient is defined by Cockrell and Markland to be equal to one minus the diffuser effectiveness, $C_p/C_{pu}$ [5]. While this data was generated on conical diffusers, our diffusers have similar lengthwise 1D area distributions as a conical design making the conical diffuser a good comparison. The diffuser cone angle, $\phi$, can be estimated by considering equivalent conical diffusers with the same 1D area ratios and lengths of the diffusers of interest. To estimate the inlet momentum thickness, the CFD calculated momentum blockage is used, such that $\theta_1/d_1 \approx B_{P1}/4$. Applying all of these approximations, the loss coefficient given by Figure 6.16 for an equivalent conical diffuser is found to be 15% higher than the experimentally measured loss coefficient for the baseline diffuser at the 100E operating point. This is at least partially the result of compressibility increasing the pressure rise potential of our diffusers relative to Cockrell and Markland's incompressible experiments. This effect is described in Sections 5.3, 6.5.6, and 6.6.5. Whether there are actual advantages or disadvantages of these diffuser designs relative to others of similar inlet Mach number will not directly be addressed. Rather, the focus will be on explaining the performance drivers of these diffusers in themselves, and generalizing where possible.

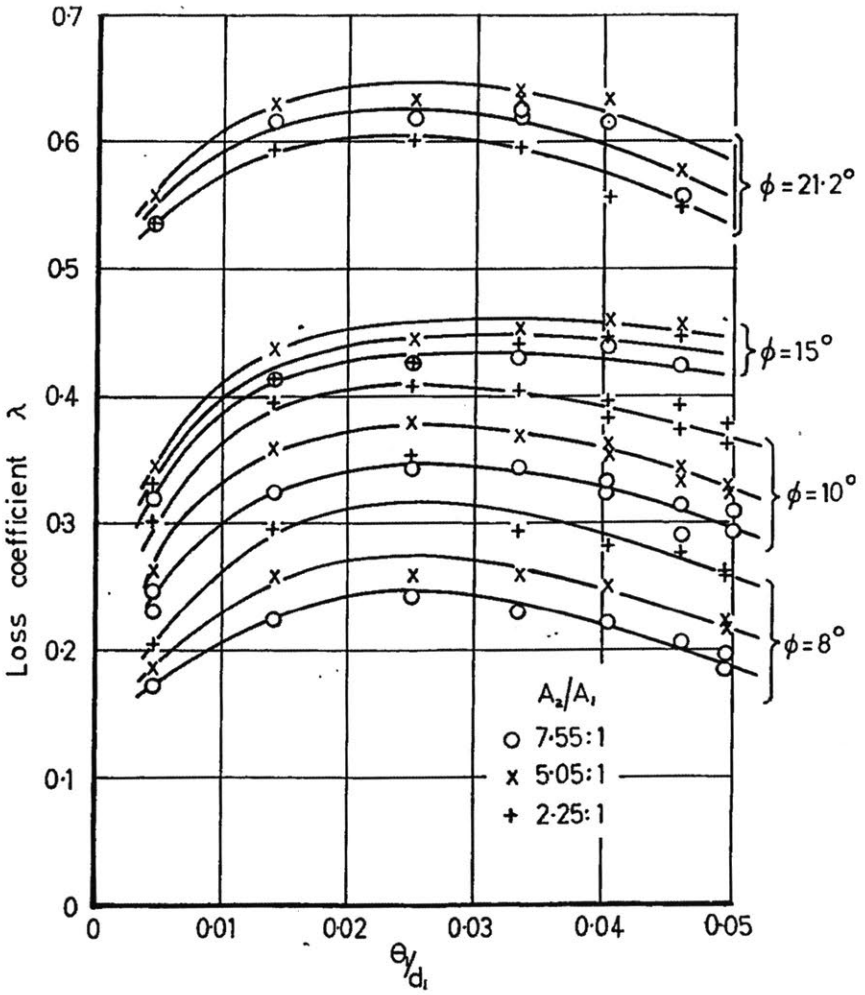


Figure 6.16: Measurements of conical diffuser loss coefficients, defined as $\lambda = 1 - (C_p/C_{pu})$, versus inlet boundary layer momentum thickness, showing effects of area ratio and cone angle [5].

To weigh the relative detrimental influences of diffuser exit nonuniformity and loss on the static pressure rise of the diffuser, the 1D diffuser exit conditions are calculated from the CFD results using three different assumptions, plotted in Figure 6.17. The first set, of course representing the actual diffuser exit conditions, is the availability average (black). The second set, representing the ideal diffuser exit conditions, is calculated from the impeller exit availability averaged stagnation pressure and stagnation pressure, as well as the diffuser exit momentum averaged flow angle and mass flow rate per unit area (green). The third set of exit conditions is calculated in the same way as the second but uses the diffuser exit 1D effective area, which includes the exit blockage (blue).

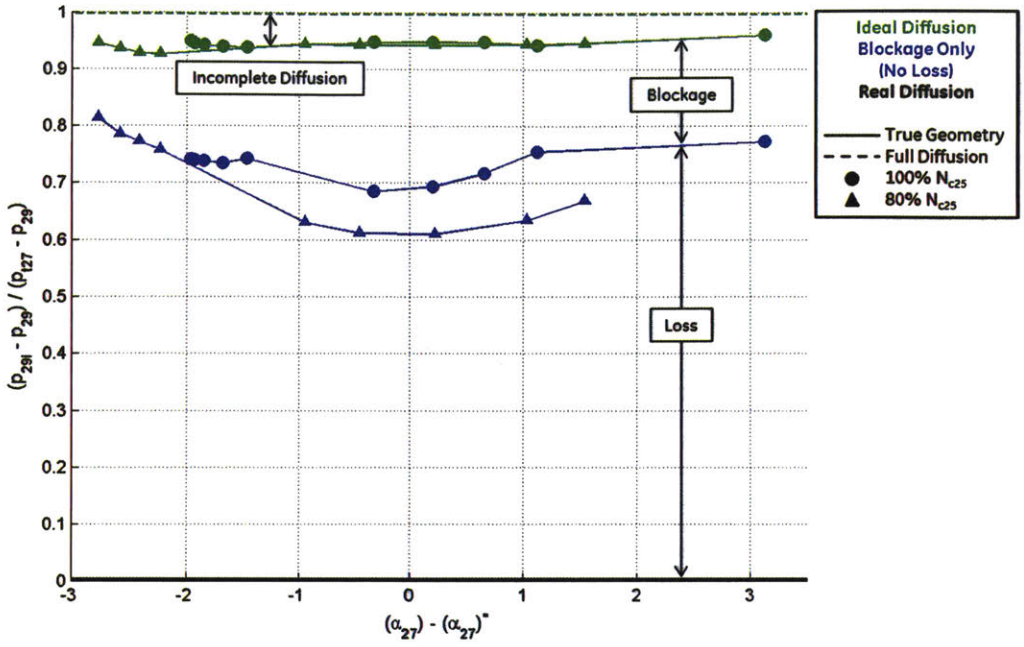


(a) Baseline diffuser.

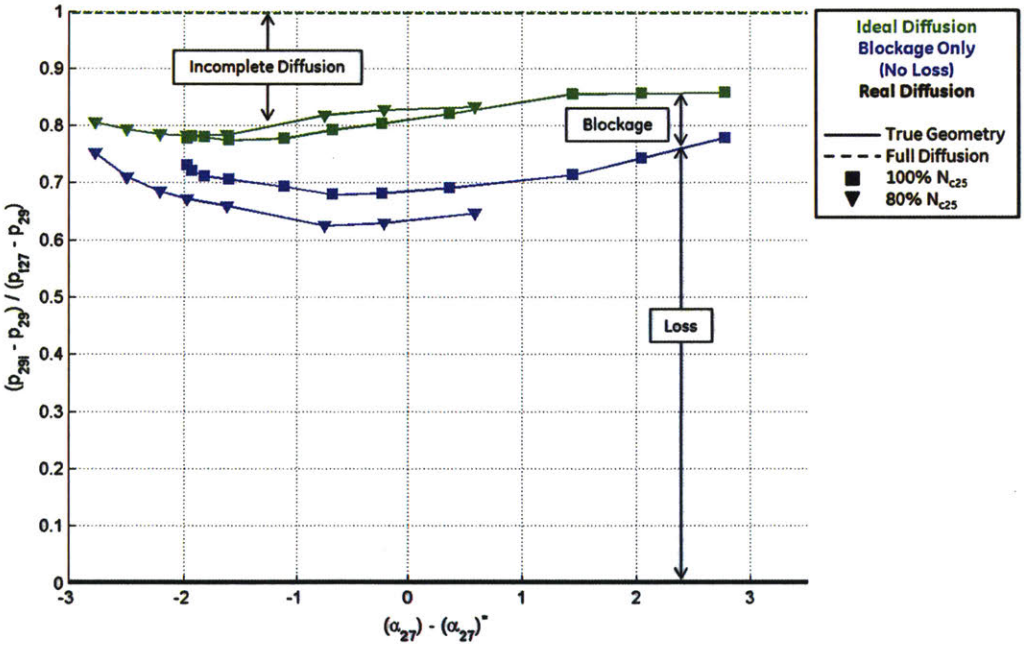


(b) Truncated diffuser.

Figure 6.17: Relative influence of nonideal effects on diffuser pressure rise versus impeller exit flow angle, based on CFD solutions. Symbols denote compressor speed, line styles denote use of static pressures (incomplete diffusion constrained by true geometry) or stagnation pressures (full diffusion), colors denote different nonideal effects. Results normalized between true pressure rise (0) and ideal full diffusion pressure rise (1). Loss is primary source of inefficiency for both configurations, followed by blockage for baseline diffuser and limited 1D area ratio for truncated diffuser.

The pressures plotted in Figure 6.17 are normalized such that the actual diffuser exit static pressure corresponds to zero and the ideal diffuser exit stagnation pressure corresponds to one. As one can see, the gap between these two is created by the diffuser loss, the diffuser exit blockage, and incomplete diffusion due to the diffuser's finite 1D area ratio. The diffuser loss makes up the largest contributor to the deficit for both baseline and truncated diffusers. The difference between the two diffusers is due to the remaining two effects, which can be summarized as a limitation in the diffuser effective area ratio. For the baseline diffuser, this limitation primarily comes about due to the large exit blockage. For the truncated diffuser on the other hand, it comes about primarily due to the lower 1D area ratio, or high exit flow angle. At 80% $N_{c25}$, the impact of loss is reduced relative to 100% $N_{c25}$, and the impact of blockage is increased. There is also some dependence on inlet flow angle, most notably for the baseline diffuser which experiences increased inefficiency due to blockage in the middle of the operating range.

Splitting the diffuser inefficiencies into blockage and loss aids in conceptually understanding what limits the diffuser static pressure rise. However, it has been demonstrated that the two are related; nonuniformity can only be reduced via a mixing process, which inevitably results in increased loss. Therefore, these two nonideal effects should not be thought of as independent mechanisms, but rather the mixed out average can be used to combine them into a single measured impact on the static pressure recovery. By defining new hypothetical diffusion processes using the mixed out average, one can break the diffuser inefficiencies into components that are less dependent on each other.

First, one can define a process where the nonuniform diffuser inflow mixes instantaneously and diffuses isentropically through the remainder of the diffuser. This process results in the diffuser's maximum attainable static pressure rise and the associated stagnation pressure loss given the nonuniform inlet conditions. The resulting diffuser exit static and stagnation pressures are shown in Figure 6.18 (blue). This pressure rise is less than the ideal pressure rise (green), with the difference between the two representing opportunity that is actually not available to the diffuser. Rather, this source of inefficiency should be attributed to the impeller exit nonuniformity.

The mixed out average can also be applied to the diffuser exit (red). Because mixing increases static pressure of the flow, the diffuser exit nonuniformity represents a pressure rise potential that could be realized with additional downstream mixing. This additional

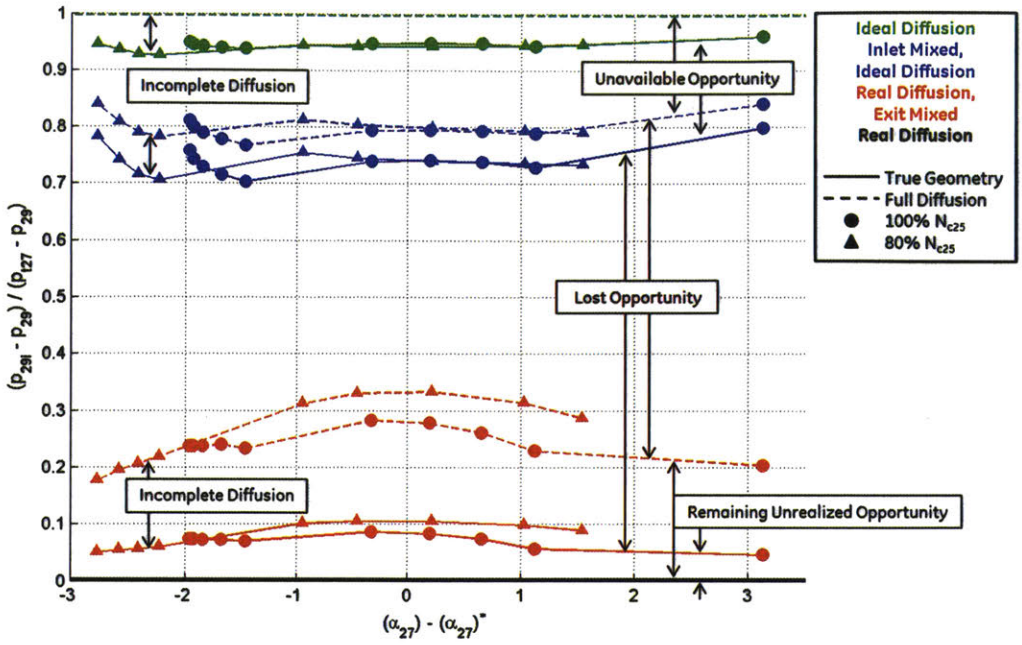


(a) Baseline diffuser.

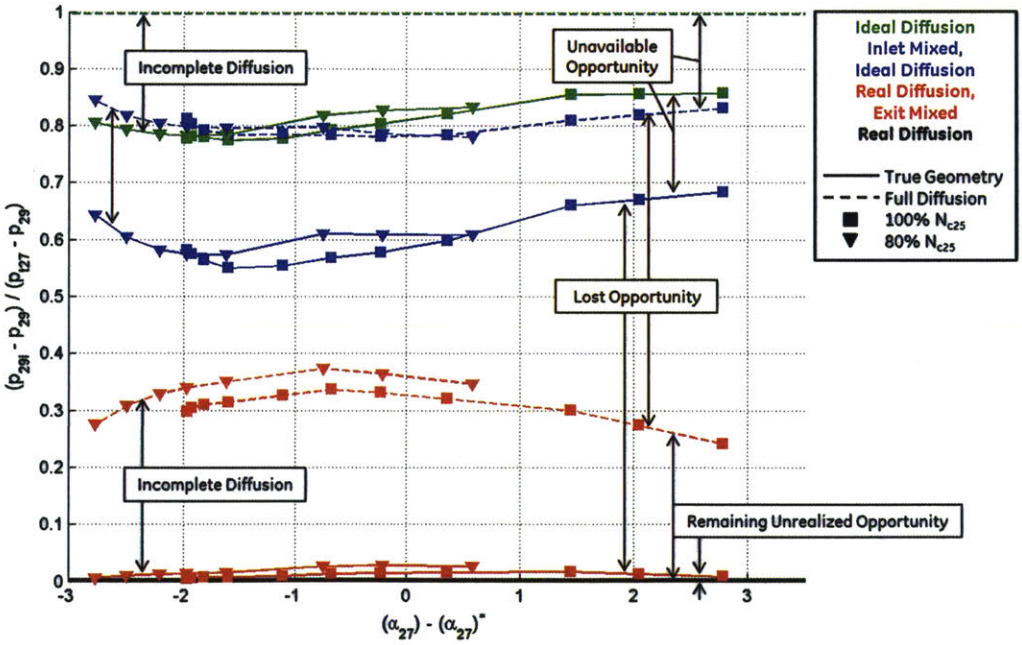


(b) Truncated diffuser.

Figure 6.18: Relative influence of nonideal effects on diffuser pressure rise versus impeller exit flow angle, based on CFD solutions. Symbols denote compressor speed, line styles denote use of static pressures (incomplete diffusion constrained by true geometry) or stagnation pressures (full diffusion), and colors denote different nonideal effects. Results normalized between true pressure rise (0) and ideal full diffusion pressure rise (1). Lost pressure rise opportunity is greater for baseline diffuser than truncated diffuser, while truncated diffuser offers greater unrealized pressure rise opportunity for deswirler.

pressure rise potential and associated stagnation pressure loss can be credited to the diffuser. Whether this pressure rise is actually achieved depends on the efficiency of the deswirler, not the diffuser.

The amount by which the diffuser exit mixed out static pressure (red) is lower than the maximum attainable static pressure (blue) represents actual inefficiencies due to the diffuser. These inefficiencies can only come from two sources: delayed mixing (i.e. mixing occurring after diffusion has already amplified nonuniformities), and wall friction. The impacts of nonuniform inlet flow and incomplete mixing are excluded from this comparison, removing the dependency of diffuser pressure rise on the upstream and downstream components.

Curves based on static pressures and stagnation pressures are both shown in Figure 6.18, representing diffusion processes that are respectively limited and not limited by the diffuser's true 1D area ratio. Again, pressures are normalized such that the actual diffuser exit static pressure (black) corresponds to zero in this figure and the ideal diffuser exit stagnation pressure (green) corresponds to one.

There are a number of observations that can be made from Figure 6.18 about the sources of inefficiency within the diffusers of interest. Not surprisingly, the greatest source of inefficiency for both diffuser configurations is the lost opportunity resulting from nonideal effects attributable to the diffuser itself. However, this lost opportunity is about 5% greater for the baseline diffuser than for the truncated diffuser. Because Figure 6.17 indicates that the true stagnation pressure loss contributions are equal between the two diffuser configurations, this difference can be attributed to the larger exit nonuniformity of the baseline diffuser. This difference is offset by the fact that the baseline diffuser has a larger 1D area ratio than the truncated diffuser, and thus has a higher ideal pressure recovery.

For both baseline and truncated diffusers, approximately 15-25% of the pressure rise deficit can be attributed to the nonuniform exit flow of the impeller, something the diffuser design cannot influence. Additionally, the remaining diffuser exit dynamic pressure, in the form of diffuser exit nonuniformity and incomplete diffusion, remains as available opportunity for the deswirler to increase static pressure. Because the baseline diffuser has greater exit nonuniformity, the additional pressure rise that could be achieved in the deswirler due to mixing at constant area is approximately 5% larger than for the truncated diffuser. However, due to the lower exit nonuniformity, the truncated diffuser leaves the

deswirler with 5% greater pressure rise opportunity if the deswirler continues to diffuse the flow completely. This suggests that if each diffuser were paired with a deswirler that was optimized for its respective diffuser configuration, the diffusion system incorporating the truncated diffuser could achieve the greater pressure rise. It is hypothesized that the reason this isn't observed in the experiments and CFD simulations documented here is that the deswirler design is held constant.

These patterns are generally the same for 80% $N_{c25}$ as for 100% $N_{c25}$, but again the impact of inefficiencies attributable to the diffuser itself is reduced slightly at 80% $N_{c25}$. Regarding the effect of flow angle, a large swing is observed in the lost opportunity resulting from the diffuser itself. At extreme low or high flow angles, it can account for up to 75% of the pressure rise deficit. However, at flow angles closer to the design value, it can account for as little as 40% of this deficit. Clearly, the effects of flow angle must be understood. Note that the other effects appear to vary with flow angle as well, but this is only in proportional terms.

## 6.5 Diffuser Inlet Performance Assessment

The diffuser inlet is the portion of the diffuser over which the flow angle varies as the compressor is throttled between choke and stall, starting at the impeller exit (station 27) and ending at the diffuser throat (station T). Because inlet flow angle is known to heavily influence the diffuser performance, it makes sense to identify the dominant mechanisms in the diffuser inlet, and explain how they relate to inlet performance and throat conditions. The major effect of flow angle is found to be its effect on the 1D area ratio of the diffuser inlet. Compressibility and mixing of impeller exit circumferential nonuniformities are also found to have significant impacts on the diffuser inlet performance. The development of secondary flows in the diffuser inlet and its dependence on inflow angle is also investigated. These secondary flows are shown in Section 6.6.6 to have a detrimental impact on the pressure recovery of the diffuser passage, as they result in accumulation of high loss flow and reduced mixing effectiveness.

Note that for some of the experimental test points, static pressure was not measured at the throat. As a result, the population of experimental data that can be used to characterize inlet performance is smaller than the larger set of data used to investigate the overall diffuser performance.

### 6.5.1 Diffuser Inlet Performance

The purpose of this section is to simply show the performance of the diffuser inlet and highlight trends. Some explanation will be provided for these trends here, but more detailed explanations are reserved for the following sections.

The diffuser inlet static pressure recovery coefficient up to the diffuser throat is shown in Figure 6.19. Some similarities between the inlet and overall diffuser pressure recovery characteristics are identifiable. There is a positive correlation between inlet flow angle and pressure recovery coefficient as the inlet 1D area ratio varies, with greater sensitivity to flow angle on the choke side. The choking flow angle for each speed line is also apparent.

There are also some new observations that can be made about the inlet pressure recovery characteristic. First, it is clear that the inlet pressure recovery varies between both positive and negative values, denoting diffusing and accelerating processes respectively. Around the transition point where recovery is zero, it is apparent that the pressure recovery characteristic is more sensitive to flow angle for higher inlet Mach numbers (i.e. compressor speed). There is also a minimum pressure recovery at choke, corresponding to the minimum flow angle. Like the choking flow angle, the choking pressure recovery is also higher at high inlet Mach numbers.

Figure 6.19 also shows the pressure recovery coefficient up to the diffuser leading edge (station 28). The positive correlation between inlet flow angle and recovery is observed at the leading edge just as it is at the throat. However, in comparison to the throat pressure recovery coefficient, the leading edge recovery is smaller. This suggests that most of the pressure recovery variation between choke and stall occurs in the small region between the diffuser leading edge and throat, furthermore suggesting that this is where most of the flow angle adjustment and 1D area change occurs. This effect is also apparent in Figure 6.12.

The stagnation pressure loss coefficient is shown for the CFD solutions in Figure 6.20 (the inlet loss is not measured experimentally). Again, loss coefficients at the leading edge and throat are both shown, but unlike the pressure recovery coefficient, which varies significantly in magnitude between the two stations, the loss coefficient does not. Most of the loss occurs upstream of the leading edge. The loss bucket shape seen in the overall diffuser loss characteristic is also apparent in the inlet loss characteristic, with the minimum loss corresponding to the design point flow angle. However, it is noteworthy that the shape of the loss bucket manifests itself upstream of the leading edge. This suggests that the higher

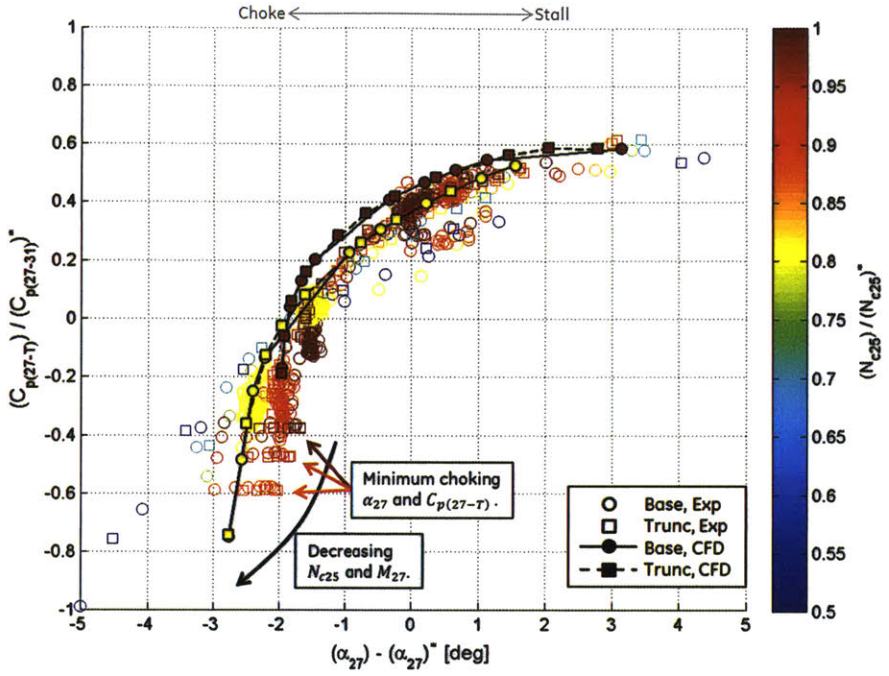


(a) Pressure recovery coefficient between impeller exit and diffuser throat.

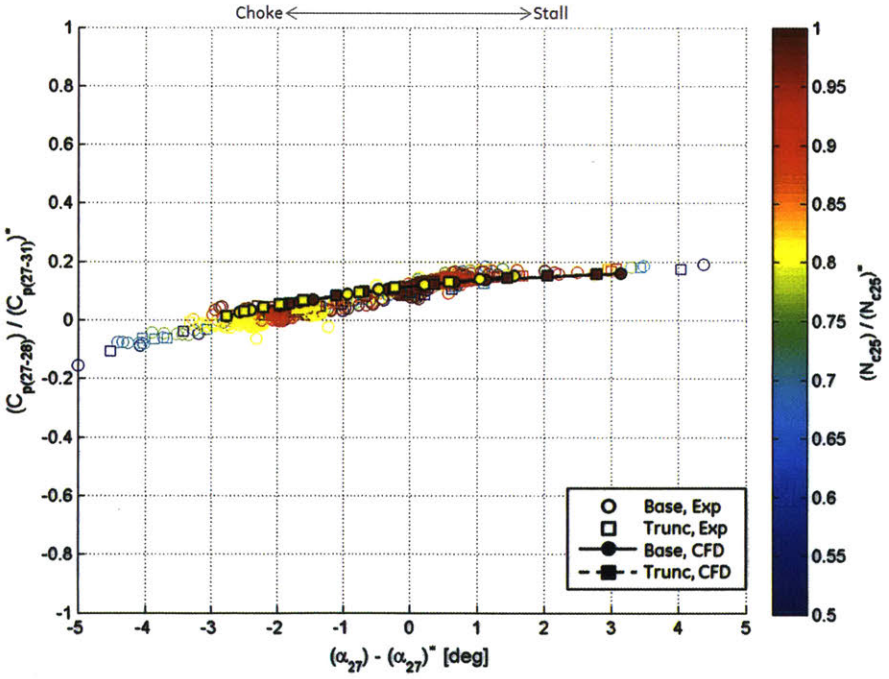


(b) Pressure recovery coefficient between impeller exit and diffuser leading edge.

Figure 6.19: Diffuser inlet pressure recovery coefficient versus impeller exit flow angle. Symbols and line styles denote diffuser configuration and data source, while colors denote rotor speed. Pressure recovery generally increases with flow angle, with most pressure rise occurring between leading edge and throat.

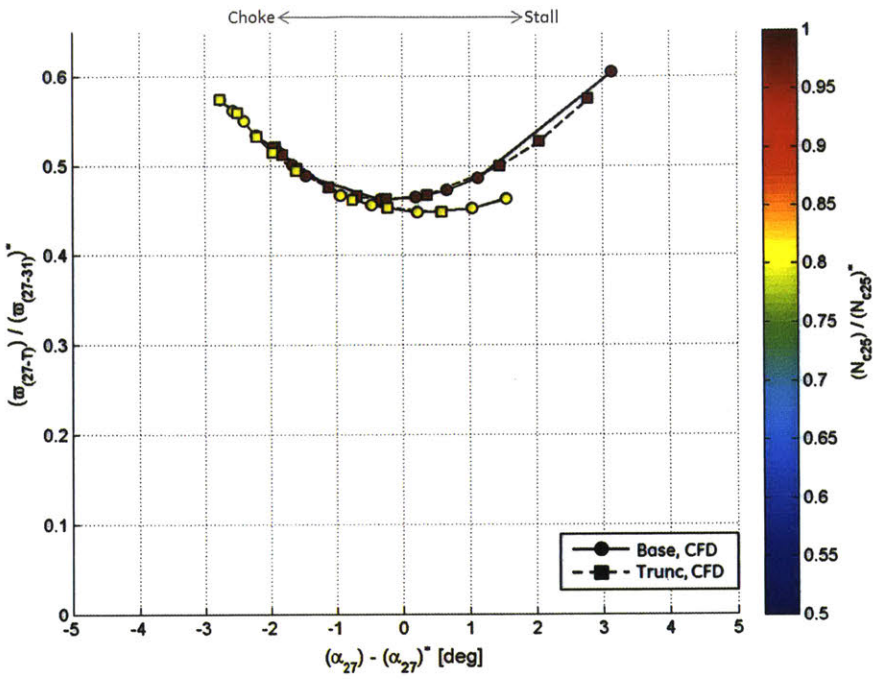


(a) Stagnation pressure loss coefficient between impeller exit and diffuser throat.

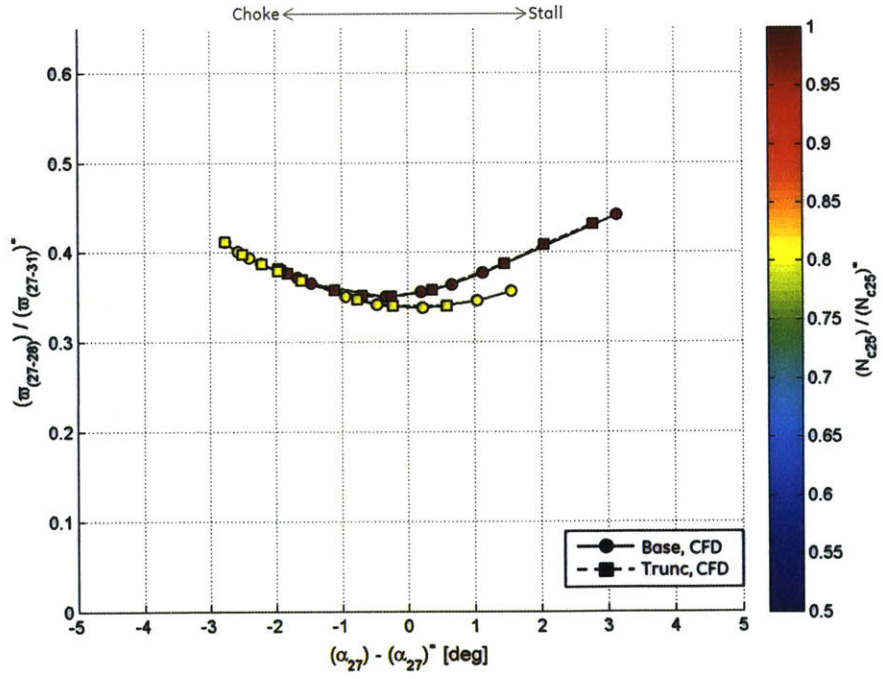


(b) Stagnation pressure loss coefficient between impeller exit and diffuser leading edge.

Figure 6.20: Diffuser inlet stagnation pressure loss coefficient versus impeller exit flow angle. Symbols and line styles denote diffuser configuration and data source, while colors denote rotor speed. Minimum loss observed near design flow angle, with increases in loss for higher or lower flow angles. Loss bucket trend also observed upstream of leading edge, indicating leading edge incidence is not the driver.

losses observed at extreme high and low flow angles is not due to leading edge incidence effects alone. This does not rule out other upstream incidence effects, such as leading edge cusp or bleed slot incidence.

To make some additional observations, the inlet static pressure recovery coefficients for the 100% $N_{c25}$ and 80% $N_{c25}$ speed lines are shown individually in Figure 6.21. Comparing the baseline and truncated diffusers, there is no difference in the CFD calculated pressures. This is also reflected by the CFD loss calculations shown in Figure 6.20. The experimental results on the other hand do indicate some differences between the two diffusers. There is some skepticism about these experimental differences, however, since the observations are reversed when looking at the diffuser passage static pressure recovery coefficients (see Section 6.6.1). It is hypothesized that this is either due to an error between the true and measured throat static pressures, or it may be due to a difference in throat static pressure distribution caused by differences in the impeller setup (see Section 4.1 discussion).

Another difference between the CFD and experimental results is that at 100% $N_{c25}$ the experimental results show the flow angle continuing to drop with reduced diffuser backpressure after the diffuser is in deep choke, defined as the constant mass flow portion of the compressor's characteristic associated with high diffusion system losses. This effect is also observed at other speeds in Figure 6.19. However, if the diffuser truly is choked, then by definition it is not possible for the compressor backpressure to influence the impeller exit angle. Recall that the impeller exit flow angle is calculated from other measurements along with a set of assumptions. Upon further investigation, it is determined that these flow angle changes are themselves driven by changes in the measured compressor exit stagnation temperature (see compressor work coefficient in Figure 3.8). The cause of the lower compressor exit stagnation temperature measurements in deep choke needs to be investigated. However, because static pressure measurements upstream of the diffuser throat are not affected the same way, it is hypothesized that the impeller work input is not truly changing as it seems. Therefore, the perceived changes in impeller exit conditions in deep choke should be disregarded.

The CFD solutions agree well with the experimental data on the other observations made about the diffuser inlet performance characteristics. Note that the piecewise appearance of the overall diffuser performance characteristics calculated by the CFD is not apparent in the inlet, indicating that it is the diffuser passage which gives rise to this trend.

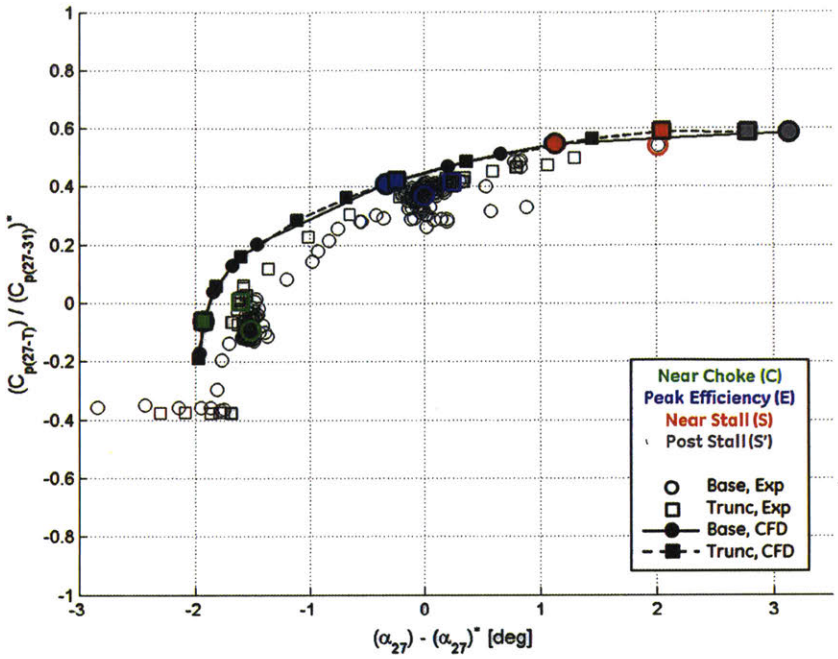


(a) 100% $N_{c25}$.

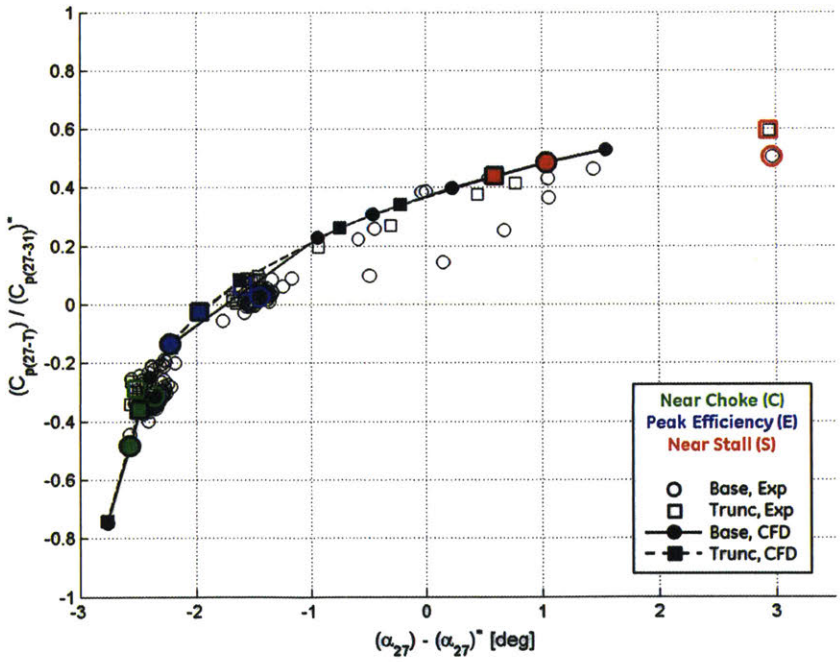


(b) 80% $N_{c25}$.

Figure 6.21: Diffuser inlet static pressure recovery coefficient versus impeller exit flow angle. Symbols and line styles denote diffuser configuration and data source, while colors denote operating point (note: colored experimental points averaged from multiple tests). Experimental difference between baseline and truncated diffuser pressure recovery coefficients disregarded due to opposite trend observed in passage. CFD calculates identical trends for baseline and truncated diffusers.

### 6.5.2 Diffuser Throat Conditions

The flow conditions at the diffuser throat are presented to better understand what drives the performance trends of the diffuser inlet, and because they represent the inlet conditions to the diffuser passage. First, the throat Mach number is shown in Figure 6.22. The throat Mach number and diffuser inlet flow angle are inversely related to one another, as flow angle sets the inlet 1D area ratio. The highest achievable Mach number of course corresponds to choke, and is independent of compressor speed (note that experimental throat static pressures are not measured in deep choke for all compressor speeds). At a fixed inlet 1D area ratio (i.e. flow angle), the throat Mach number is higher for high diffuser inlet Mach numbers (i.e. compressor speed). This explains why the choking flow angle is lowest at low speeds.

The diffuser throat blockage is shown in Figure 6.23. In general, the CFD and experimental results seem to correlate with one another, though there is significant variability in the experimental results. This is because the blockage estimate is sensitive to the many

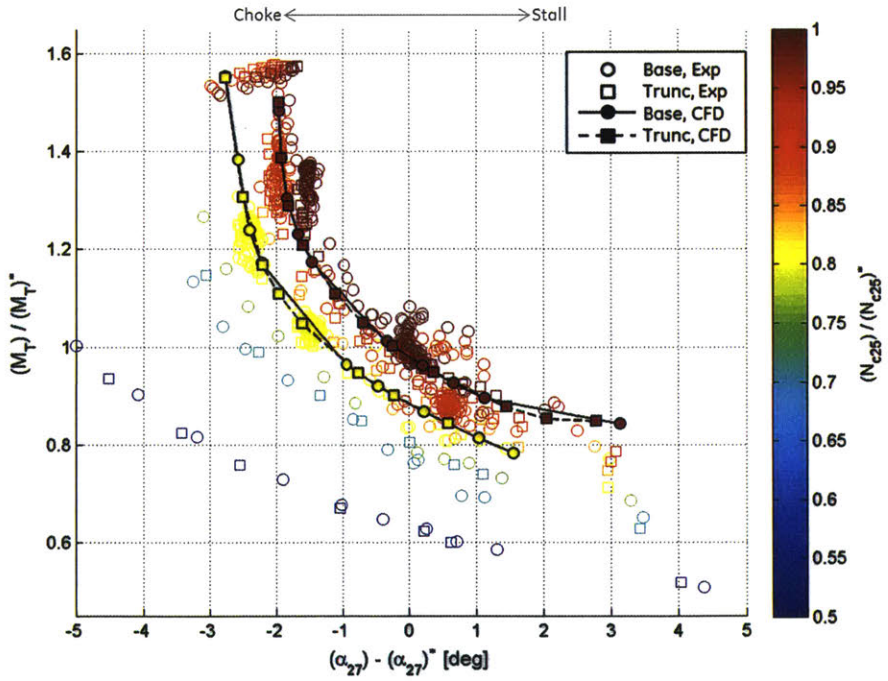


Figure 6.22. Diffuser throat Mach number versus impeller exit flow angle. Symbols and line styles denote diffuser configuration and data source, while colors denote rotor speed. Negative correlation between throat Mach number and flow angle due to 1D area ratio effects. Throat Mach number increases with compressor speed, or inlet Mach number. Maximum Mach number and therefore minimum flow angle limited by choking. Thus, range reduces with increased speed.

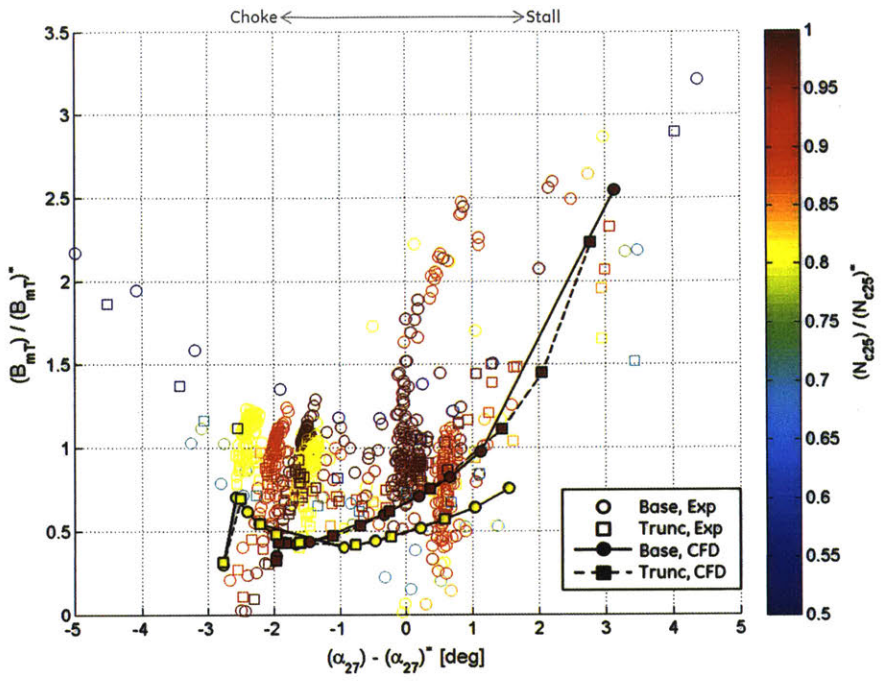


(a) Diffuser throat mass blockage.

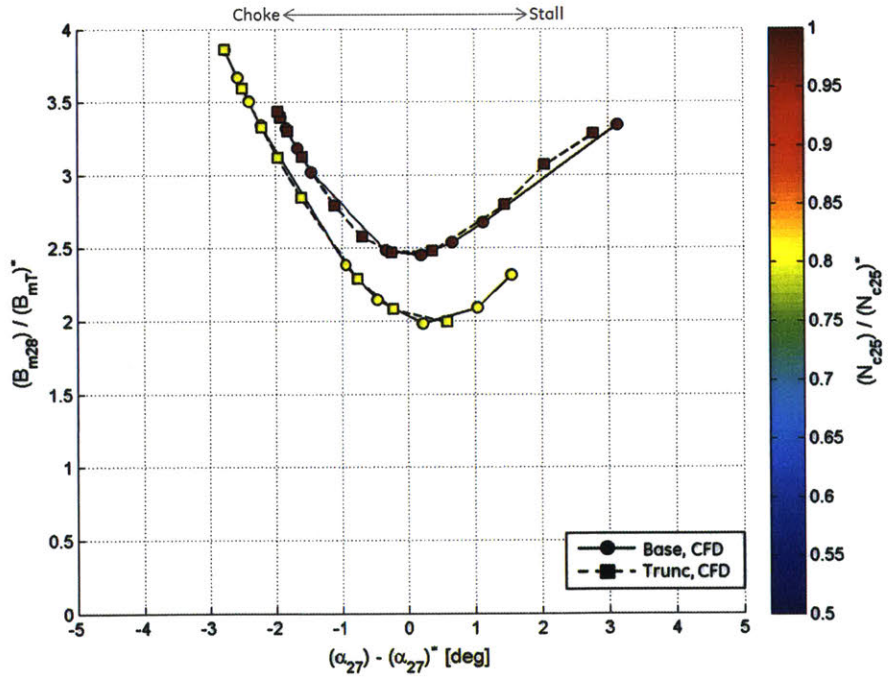


(b) Diffuser leading edge mass blockage.

Figure 6.23: Diffuser mass blockage versus impeller exit flow angle. Symbols and line styles denote diffuser configuration and data source, while colors denote rotor speed. Blockage reduces between leading edge and throat. Minimum blockage observed near design flow angle, with increases in blockage for higher or lower flow angles. Bucket trend also observed at leading edge. Relation between leading edge and throat blockages unclear due to circumferential static pressure nonuniformity that contributes to leading edge blockage at off-design incidence angles.

assumptions that go into its calculation. Recall from the CFD results that the diffuser inlet blockage is constant across the operating range. This is the result of the constant impeller exit blockage (see Figure 4.9) combined with a constant blockage increases across the bleed slot, which is essentially a geometric effect determined by a discontinuity in passage width (see Figure 6.14). Due to nonuniformity amplification, it makes sense that the throat blockage would be largest at high flow angles, or 1D area ratios. However, there is also increased blockage at very low flow angles when the flow is accelerating. This appears to be the result of high negative incidence losses manifested on the diffuser pressure side immediately downstream of the leading edge. These losses can be seen in Figure 6.10 and Figure 6.11 for the 80C CFD simulations.

Figure 6.23 also shows the blockage at the diffuser leading edge. This suggests that the larger blockage at both high and low flow angles may originate upstream of the diffuser leading edge. This is followed by a reduction in blockage between the leading edge and throat, which is indeed greater for accelerating flows. However, recall that blockage represents all forms of nonuniformity, including static pressure nonuniformity. At extreme flow angles, a circumferential gradient in static pressure is present at the diffuser leading edge plane due to streamline curvature. This type of nonuniformity is eliminated between the leading edge and throat simply by straightening the streamlines independent of nonuniformity amplification or mixing. Therefore, it is difficult to draw conclusions that relate the blockage at the diffuser leading edge with the blockage at the throat.

Secondary flows are also present at the diffuser throat, and are captured to some degree by the blockage. However, because these secondary flows are later shown to influence the flow downstream in the diffuser passage, their formation and characterization is a special topic of discussion reserved for Section 6.5.7. The claims made in the literature that the secondary flows enhance inlet mixing and thus reduce the throat blockage are further addressed in Sections 6.6.6 and 6.7.

### 6.5.3 Evaluation of Nonideal Effects

Using the same procedure discussed in Section 6.4 for evaluating nonideal effects in the diffuser, the diffuser inlet pressure recovery coefficient is calculated from the CFD solutions using three sets of assumptions, and the results are plotted in Figure 6.24. These include the actual (black) and ideal (green) pressure recoveries as well as a pressure recovery calcu-

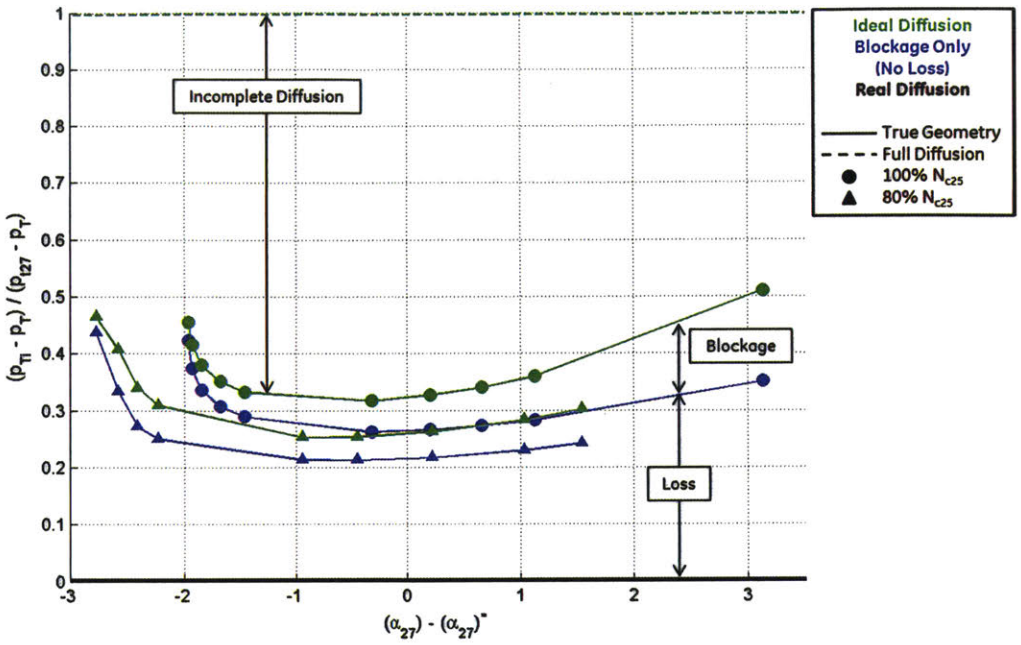


(a) Baseline diffuser.

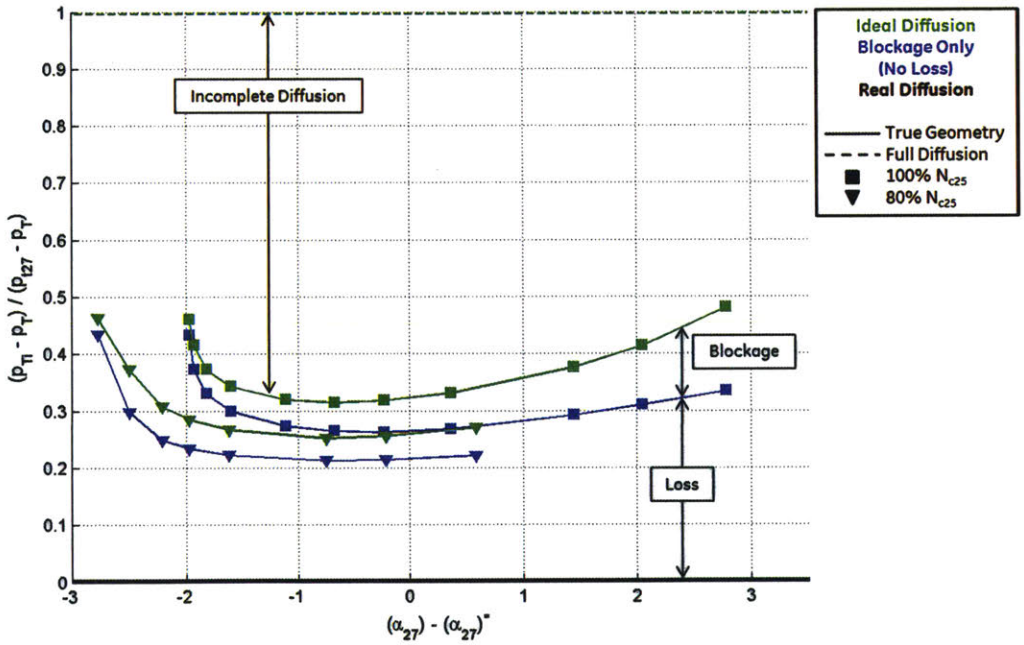


(b) Truncated diffuser.

Figure 6.24: Relative influence of nonideal effects on diffuser inlet pressure rise versus impeller exit flow angle, based on CFD solutions. Symbols denote compressor speed, line styles denote use of static pressures (incomplete diffusion constrained by true geometry) or stagnation pressures (full diffusion), and colors denote different nonideal effects. Results normalized between true pressure rise (0) and ideal full diffusion pressure rise (1). Baseline and truncated diffusers are indistinguishable. Diffusion is incomplete due to limited throat area. Remainder of inefficiency is dominated by stagnation pressure loss.

lated using the actual diffuser throat blockage but assuming no stagnation pressure loss in the diffuser inlet (blue). These are normalized in Figure 6.24 to show the gap between the actual static pressure rise in the diffuser inlet and the ideal static pressure rise after complete diffusion.

Not surprisingly, the inlet diffusion is far from complete, but the passage and deswirler follow downstream to generate the remainder of the pressure rise. The deficit between actual and ideal diffusion is primarily due to the loss in the inlet. The throat blockage is secondary, but it does have a larger impact at high flow angles. The breakdown of nonideal effects in the inlet again proves to be identical between baseline and truncated diffusers. However, there is a difference between the 100% $N_{c25}$ and 80% $N_{c25}$ simulations, with the ideal recovery being higher at 100% $N_{c25}$ due to compressibility.

Using the second procedure discussed in Section 6.4 for evaluating nonideal effects, the diffuser inlet pressure recovery coefficient is calculated by defining hypothetical flow processes which utilize the mixed out average, and plotted in Figure 6.25. In addition to the actual (black) and ideal (green) pressure recoveries, this includes the maximum attainable pressure recovery for a frictionless diffusion process given the nonuniform inlet conditions (blue), and the recovery that could be obtained if the throat nonuniformity were mixed (red). These pressure recovery coefficients are normalized in Figure 6.25 to show the gap between the actual static pressure rise in the diffuser inlet and the ideal static pressure rise if diffusion were complete. Again, a large deficit is clear due to incomplete diffusion in the inlet. Approximately half of the remaining pressure rise deficit in the diffuser inlet can be attributed to the nonuniform impeller exit conditions. Note that this includes the effect of the mixing plane, which may or may not be a good approximation of what happens with the impeller exit flow. This is discussed in Section 6.5.4. Wall friction and inefficient or incomplete mixing in the diffuser inlet itself cause the remainder of the pressure deficit in the diffuser inlet, having the largest impact at high flow angles. Note that near choke, where the diffuser inlet actually accelerates the flow, it is not accurate to say that mixing nonuniformities at the inlet yields the maximum pressure rise potential. This is because acceleration actually smooths rather than amplifies nonuniformities. Therefore, wall friction rather than delayed mixing must be the primary cause of the lost opportunity near choke.

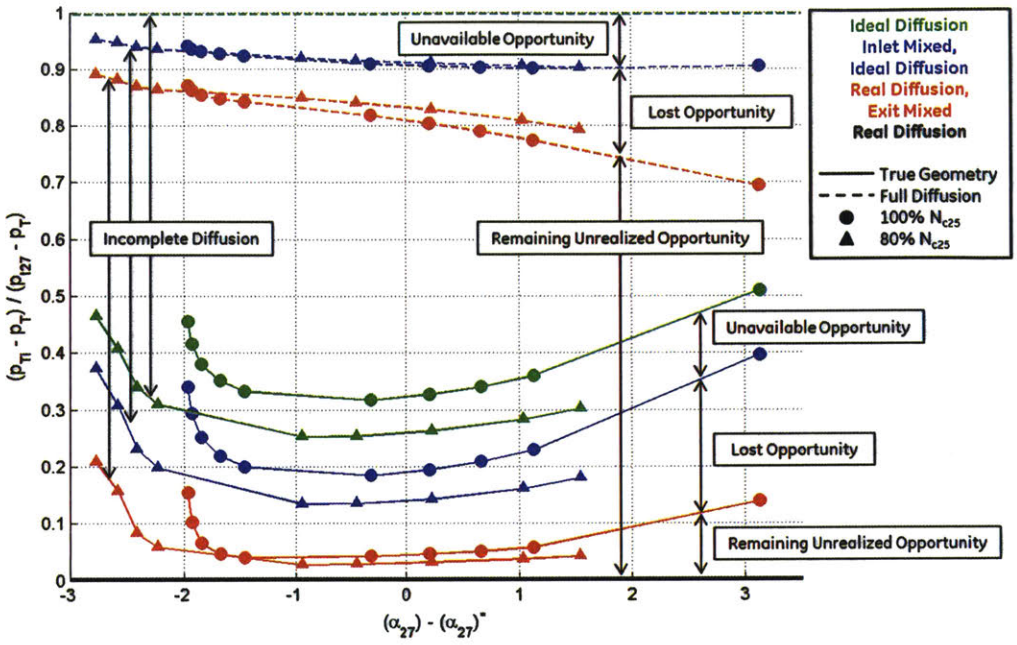


(a) Baseline diffuser.

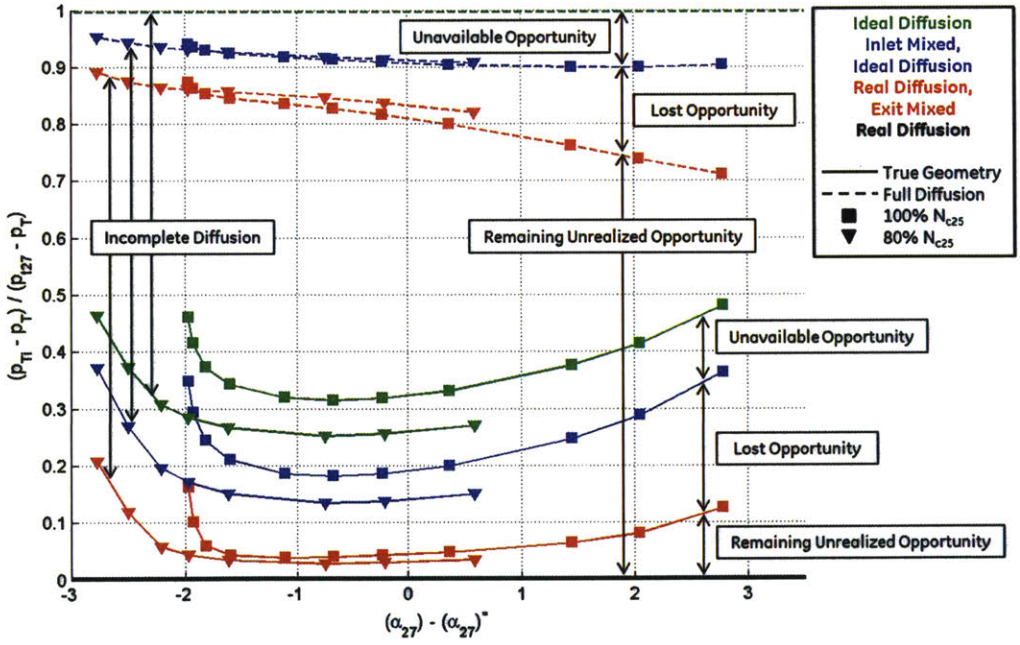


(b) Truncated diffuser.

Figure 6.25: Relative influence of nonideal effects on diffuser inlet pressure rise versus impeller exit flow angle, based on CFD solutions. Symbols denote compressor speed, line styles denote use of static pressures (incomplete diffusion constrained by true geometry) or stagnation pressures (full diffusion), and colors denote different nonideal effects. Results normalized between true pressure rise (0) and ideal full diffusion pressure rise (1). Baseline and truncated diffusers are indistinguishable. Diffusion is incomplete due to limited throat area. Near the design flow angle, half of remaining inefficiency is due to impeller exit nonuniformity (unavailable opportunity).

There is a small amount of available pressure rise opportunity that remains at the diffuser throat due to the dynamic pressure associated with the throat nonuniformity. It makes sense that this opportunity is greater at high flow angles, since the blockage is greater. However, a large opportunity is also visible near choke, despite the fact that the blockage is small. This is because the static pressure change is sensitive to variations in the effective flow area and loss at high Mach numbers. In other words, the real diffusion process with nonuniform flow at the throat chokes at a higher flow angle and 1D area ratio than the other hypothetical diffusion processes with uniform throat flow. This also explains why this increase in remaining unrealized opportunity appears at a lower flow angle at 80% $N_{c25}$ than at 100% $N_{c25}$.

### 6.5.4 Mixing of Impeller Exit Circumferential Nonuniformity

As discussed in Section 2.5.1.3, this research utilizes RANS CFD simulations by placing a mixing plane between the impeller and diffuser. The spatial distribution of flow conditions at the impeller trailing edge and on the diffuser side of the mixing plane are shown in Figure 6.26 and Figure 6.27 respectively for the 100E operating point. One can see that nonuniformities in the spanwise (forward-aftward) direction are preserved across the mixing plane, but circumferential nonuniformities are not. The mixing plane thus incurs a reduction in blockage and a corresponding loss as the circumferentially nonuniform impeller exit flow is mixed out.

Figure 6.28 shows the blockages calculated at the impeller trailing edge as well as on the diffuser inlet side of the impeller-diffuser mixing plane. The blockage downstream of the mixing plane is much lower than the blockage immediately at the impeller exit. This implies that much of the impeller exit nonuniformity is in the circumferential direction. To evaluate this further, the impeller trailing edge blockage is broken into solid blockage and aero blockage components, with the solid blockage representing slightly more than half of the total blockage. Because the solid blockage becomes aerodynamic blockage as the flow passes over the trailing edge, it can be thought of purely as circumferential nonuniformity which gets completely mixed out by the mixing plane. Of the remaining impeller trailing edge aero blockage, only half is mixed out by the mixing plane and the other half remains as spanwise nonuniformity. Note that the remaining blockage is smaller for the 80% $N_{c25}$ simulations than at 100% $N_{c25}$. This suggests that the impeller exit flow structures are ar-

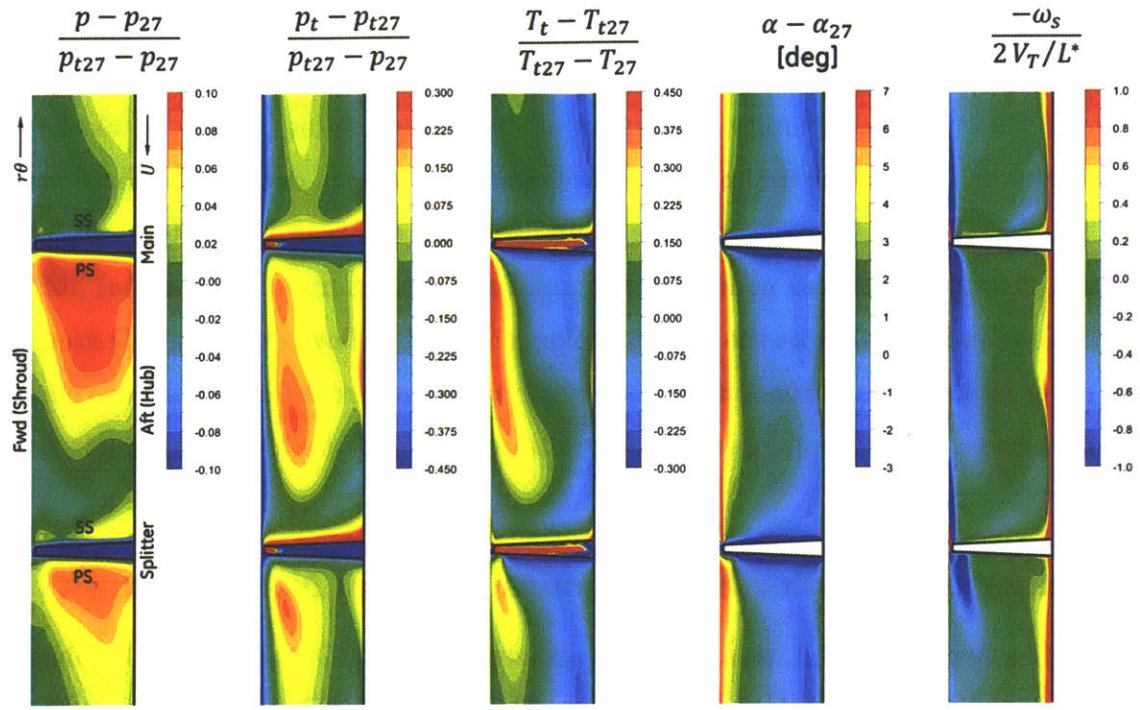


Figure 6.26: Flow nonuniformity at the impeller trailing edge plane from baseline diffuser 100E CFD simulation. Both spanwise and pitchwise nonuniformities exist. Impeller trailing edge wakes contribute only to pitchwise nonuniformity. Flow angle nonuniformity gives rise to streamwise vorticity.

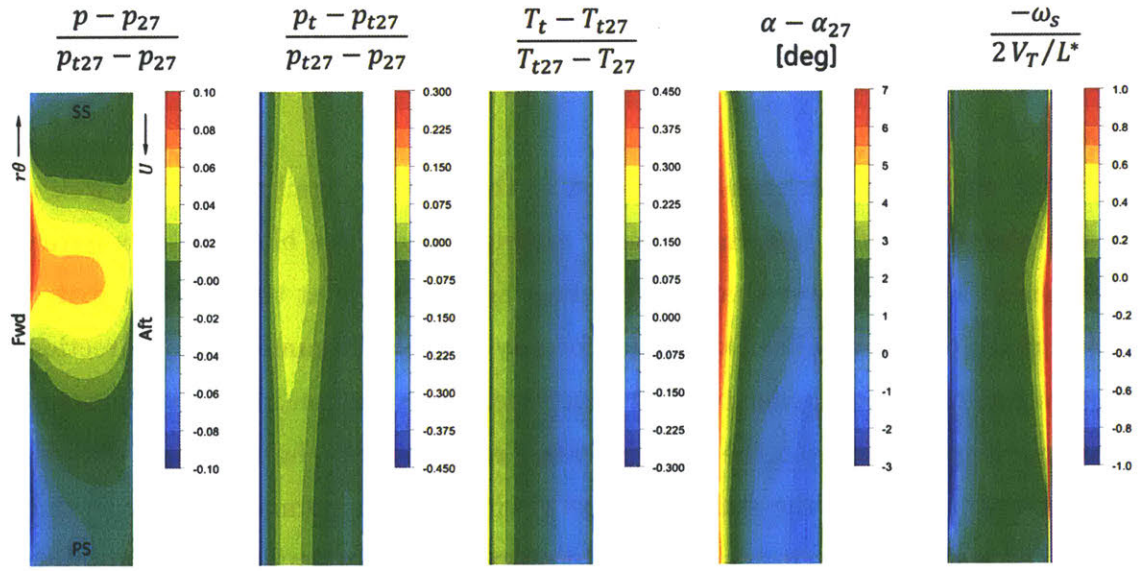


Figure 6.27: Flow nonuniformity at the diffuser inlet, immediately downstream of the impeller-diffuser mixing plane from baseline diffuser 100E CFD simulation. Impeller exit spanwise nonuniformities preserved by mixing plane. Impeller exit pitchwise nonuniformities mixed out, though some circumferential nonuniformities exist due to upstream influence of diffuser. Flow angle nonuniformity gives rise to streamwise vorticity.

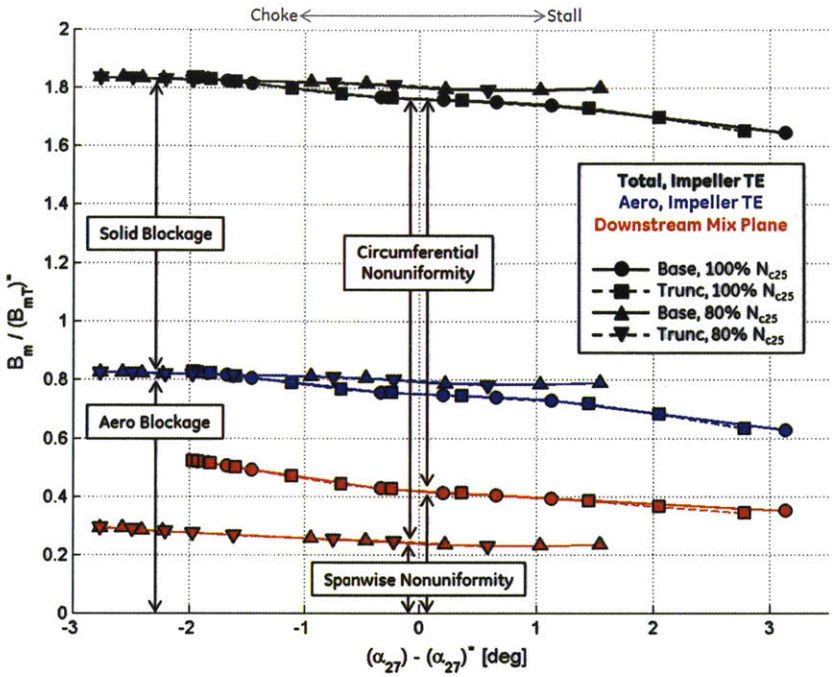


Figure 6.28: Impeller exit blockage versus flow angle, based on CFD solutions. Symbols and line styles denote diffuser configuration and compressor speed, while colors denote different cut planes and blockage definitions. Half of impeller trailing edge blockage attributable to solid blockage. Of remaining nonuniformity, half remains downstream of mixing plane as spanwise nonuniformity.

ranged differently at 80% $N_{c25}$ such that less of the total nonuniformity is considered spanwise. Upon further comparing the spatial distributions of impeller exit flow properties between the 80% $N_{c25}$ and 100% $N_{c25}$ CFD solutions, the primary difference is identified to be a more uniform spanwise flow angle distribution at 80% $N_{c25}$ than at 100% $N_{c25}$.

The stagnation pressure loss coefficient between the impeller trailing edge and the downstream side of the mixing plane is shown in Figure 6.29, along with the loss calculated from the impeller trailing edge mixed out average. The fact that these are nearly equal indicates that most of the loss potential in the impeller trailing edge nonuniformity is manifested across the mixing plane. The loss to the diffuser throat is also plotted for comparison, supporting the previous observation that the impeller exit nonuniformity accounts for half of the total inlet inefficiency. Note that the mixing loss is approximately 50% greater near choke than near stall, skewing the observed loss bucket towards higher flow angles.

The remaining diffuser inlet stagnation pressure loss coefficient between the mixing plane and throat is recalculated and shown in Figure 6.30. This will be referenced to evaluate the remaining flow mechanisms throughout the diffuser inlet.

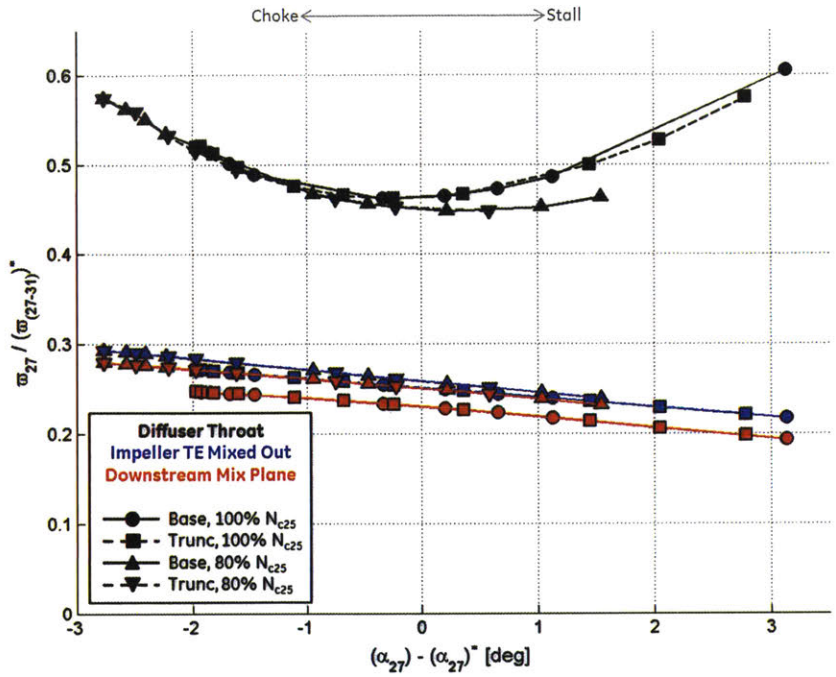


Figure 6.29: CFD calculated diffuser inlet stagnation pressure loss coefficient versus impeller exit flow angle, showing effects of impeller exit nonuniformity and CFD mixing plane on loss. Symbols and line styles denote diffuser configuration and compressor speed, while colors denote different cut planes and averaging schemes. Mixing plane loss accounts for approximately half of diffuser inlet loss, manifesting almost all loss potential associated with impeller exit nonuniformity.

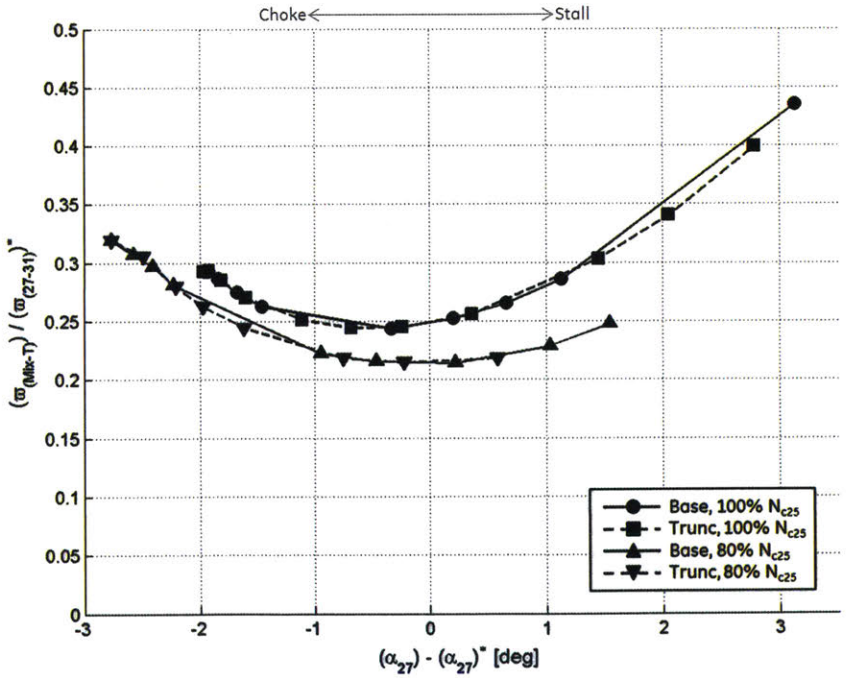


Figure 6.30: CFD calculated diffuser inlet stagnation pressure loss coefficient beginning downstream of mixing plan versus impeller exit flow angle. Symbols and line styles denote diffuser configuration and compressor speed.

Clearly the impeller exit circumferential nonuniformity and the mixing plane approximation have significant impacts on the stage simulation results. However, because this nonuniformity subjects the true centrifugal stage to unsteady effects, including the ability to recover some of the impeller exit circumferential nonuniformity in a reversible manner, the mixing plane approximation has the potential to be inaccurate. This can especially be true for a closely-coupled stage such as this. Fortunately, the unsteady simulations performed by Wilkosz do support the idea that the mixing plane approximation is sufficient for the goals of this research [18].

### 6.5.5 Effect of Impeller Exit Flow Angle

The impeller exit flow angle impacts the diffuser inlet performance via three major mechanisms: the inlet 1D area ratio, the inlet path length, and the incidence on the diffuser leading edge or inlet cusps. These effects are illustrated in Figure 6.31, demonstrating their dependence on the impeller exit flow angle. The 1D area ratio, path length, and incidence are calculated from the CFD solutions according to Equation 6.1, Equation 6.2, and Equation 6.3 respectively. Note that the path length is integrated numerically using momentum averaged flow angles calculated on the discrete averaging planes throughout the inlet region, which are shown in Figure 2.18. Also note that incidence is defined with respect to the cusp angle, which varies with radius throughout the inlet region and is equal to the diffuser pressure side angle at the leading edge. The variations in these parameters are plotted in Figure 6.32 over the range of relevant flow angles.

$$\frac{A'_T}{A'_{27}} = \frac{A_T}{A_{27}\cos\alpha_{27}} \qquad \text{Equation 6.1}$$

$$L_{(27-T)} = \int_{r_{27}}^{(r_{CL})_T} \frac{1}{\cos\alpha}\, dr \qquad \text{Equation 6.2}$$

$$i = \alpha - \alpha_{Cusp} \qquad \text{Equation 6.3}$$

The main impact of the diffuser inlet 1D area ratio is that it sets the ideal uniform flow static pressure recovery of the inlet. One can see that the inlet 1D area ratio is only a small fraction of the overall diffuser effective area ratio, but the effect on pressure recovery is still large due to compressibility. The combined effect of flow angle (i.e. 1D area ratio) and compressibility on static pressure rise is discussed further in Section 6.5.6.

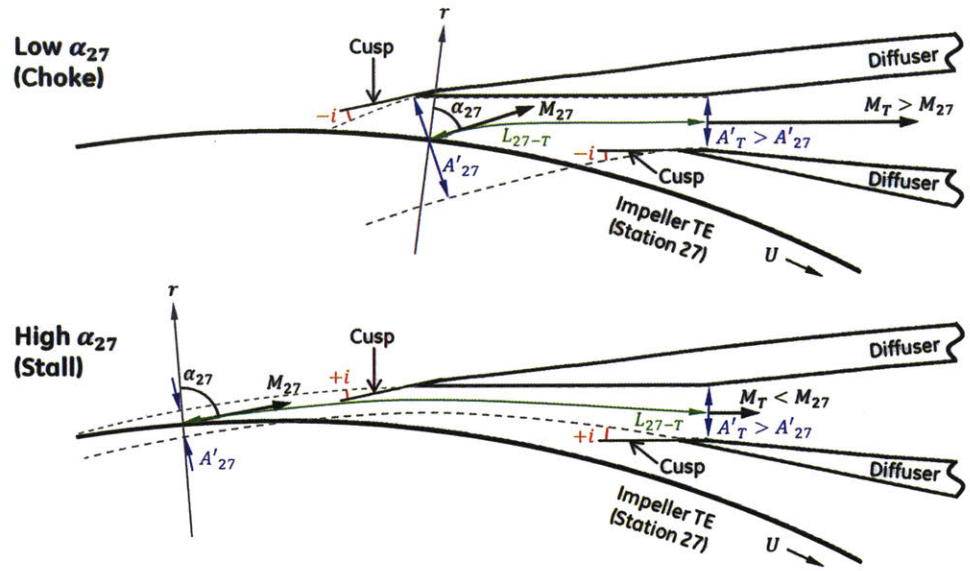


Figure 6.31: Illustration showing influence of diffuser inlet flow angle on 1D area ratio ($A'_T/A'_{27}$), path length ($L_{(1\text{-}2)}$), and incidence ($i$).

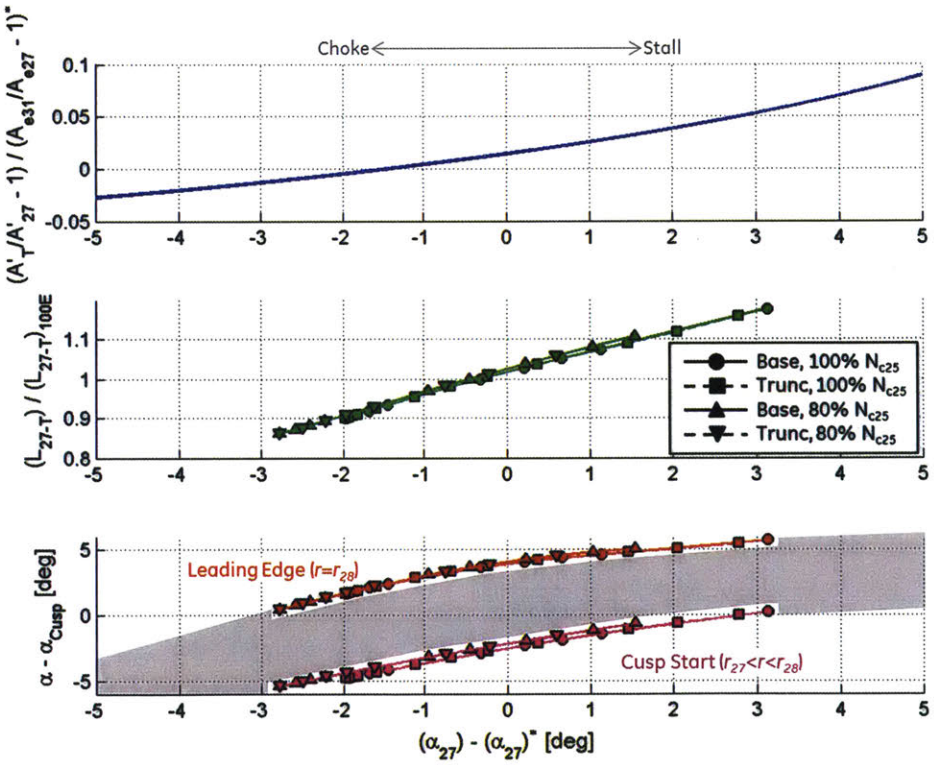


Figure 6.32: CFD calculated diffuser inlet 1D area ratio, path length, and cusp incidence versus impeller exit flow angle. Each mechanism increases with flow angle. Note that cusp angle and therefore incidence depend on radius. It is possible to have negative cusp incidence near start of cusps and positive cusp incidence near diffuser leading edge.

One hypothesized consequence of increased flow angle and associated pressure recovery is that it leads to nonuniformity amplification, contributing partially to the growth in throat blockage observed at high flow angles in Figure 6.23. Another consequence is that the pressure gradient reduces the average velocity throughout the inlet region relative to the inflow velocity, decreasing the loss associated with the boundary layer dissipation. This effect can be estimated from the integral in Equation 5.7, which is calculated numerically from the CFD solutions using the distributions of effective area and 1D average velocity throughout the diffuser inlet. As one can see from Figure 6.33, the effect is to reduce the stagnation pressure loss coefficient at high flow angles (diffusing flow), and reduce the loss at low flow angles (accelerating flow). There is also a difference with respect to compressor speed due to compressibility effects, but this is discussed in Section 6.5.6.

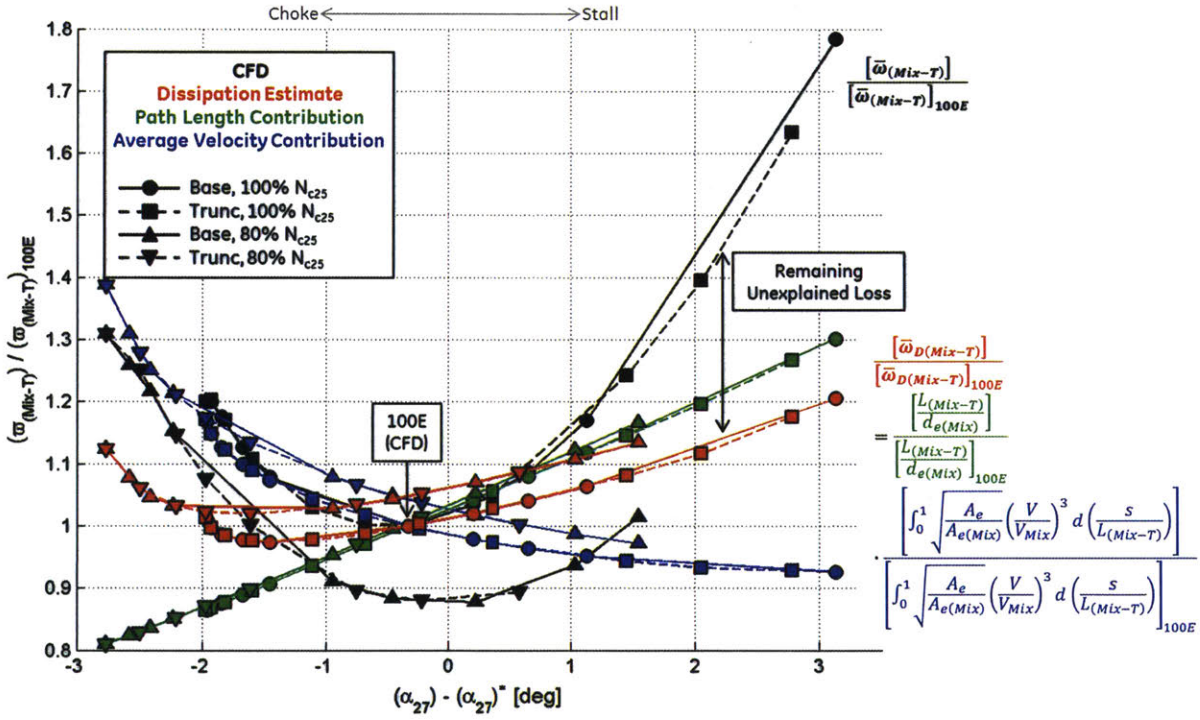


Figure 6.33: Stagnation pressure loss coefficients downstream of mixing plane versus impeller exit flow angle. Symbols and line styles denote diffuser configuration and compressor speed, while colors denote different calculation assumptions. Loss coefficients based on CFD (black) and Equation 5.7 dissipation estimate (red), normalized by 100E values. Flow angle has opposite effects on average velocity (blue) and path length (green) contributions to loss. Remaining unexplained loss hypothesized to be result of incidence effects and associated variations in dissipation coefficient associated and 3D velocity field.

Counteracting the effect of reduced inlet velocities on the stagnation pressure loss coefficient at high flow angles is the increase in path length. This is also shown in Figure 6.33, along with the combined contribution of both path length and average velocity. One can see that the higher average velocities dominate the stagnation pressure loss coefficient at low flow angles, whereas the longer path length dominates the loss at high flow angles. However, the steepness of the loss bucket walls with respect to flow angle and the variation in loss with compressor speed as calculated by the CFD are not captured by these two effects alone.

In general, there are a number of effects that can explain this difference, which are not accounted for in the simple 1D loss estimate based on the boundary layer dissipation coefficient. First, the dissipation coefficient itself is not uniform, but it is inversely related to the Reynold's number based on shear layer thickness [17]. The shear layer is of course thinnest near the diffuser leading edge where a boundary layer freshly forms, but thickness can also be influenced by secondary flows which stretch or compress the shear layer through cross-flow migration. The perimeter of the shear layer also varies with transverse stretching and compression, working together with variations in dissipation coefficient to influence the loss. Finally, static pressure non-uniformity causes local increases or decreases in flow velocity, varying the loss associated with those shear layers.

These effects—leading edge boundary layers, secondary flows, and local flow accelerations—are all present in the diffuser inlet and are most pronounced at high and low incidence angles. Figure 6.8 and Figure 6.10 clearly show additional loss generation taking place near the diffuser leading edge for high and low incidence angles. However, recall from Figure 6.20 that the loss bucket trend is also visible upstream of the diffuser leading edge. This means it cannot be caused by the leading edge incidence alone, but also by cusp incidence or even bleed slot incidence. Figure 6.32 shows that the cusp incidence varies from being negative along most of the cusp length at low flow angles to being positive near stall. Secondary flows in particular and their relation to cusp incidence are described more in Sections 6.5.7, 6.6.6, and 6.7. These sections also establish a link between the secondary flows and the observed throat blockage trends, which mimic the loss trends. However, more work is required to understand the other incidence effects in more detail.

### 6.5.6 Effect of Compressibility

The diffuser inflow angle (i.e. 1D area ratio) and compressibility together govern the ideal uniform flow static pressure recovery coefficient of the diffuser inlet. For the diffusers of interest in this research, the ideal uniform flow static pressure recovery coefficient is shown in Figure 6.34 as a function of impeller exit flow angle over a range of impeller exit Mach numbers. Because the diffuser inlet 1D area ratio is small allowing Mach numbers to remain transonic throughout, compressibility results in proportionally large changes in ideal pressure recovery relative to an equivalent incompressible flow. This effect is explained in Section 5.3.

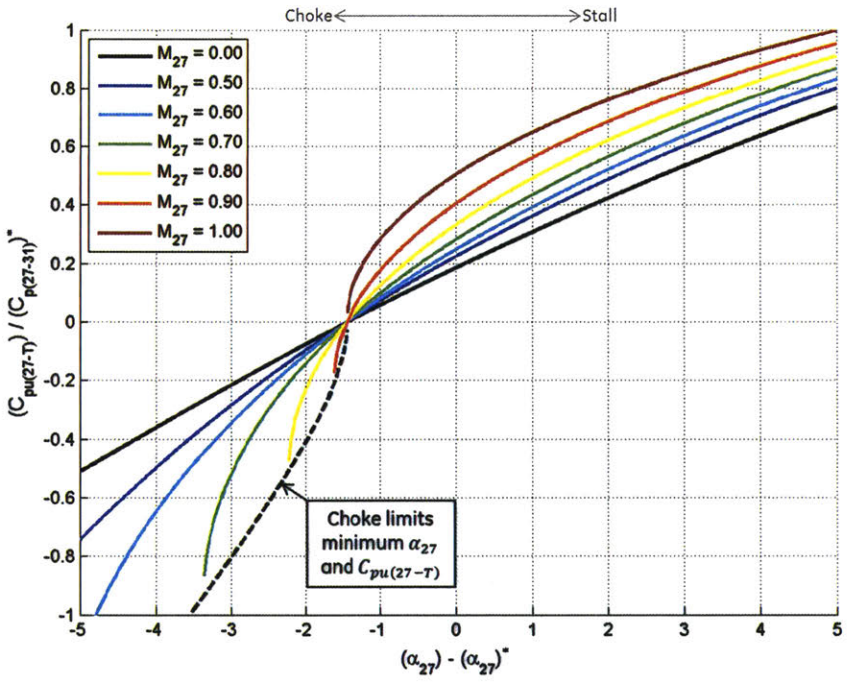


Figure 6.34: Ideal uniform diffuser inlet pressure recovery coefficient versus impeller exit flow angle, showing effect of compressibility. Compressibility increases pressure recovery potential at high flow angles, but choking limits minimum recovery and flow angle.

Of course this idealized pressure rise is greater than the experimental or CFD results due to the absence of loss and blockage. However, it does explain some real effects observed in the experimental and CFD results. First, for diffusing flows, high Mach numbers yield greater pressure recovery potential than low Mach number flows. Second, for accelerating flows, the pressure recovery falls off rapidly with reduced flow angle, with this effect being observed at higher flow angles for higher Mach number flows. Lastly, minimum flow an-

gles and pressure recovery coefficients are reached when the diffuser chokes, both of which are higher for larger Mach numbers.

Note that for diffusing flows, if the inlet pressure recovery coefficient increases via this mechanisms, the throat dynamic pressure is correspondingly reduced. This reduces the pressure rise potential of the diffuser passage relative to the diffuser inlet, even if the pressure recovery coefficient of the passage also increases due to compressibility. The reverse is true as well. For accelerating flows, compressibility in the inlet increases the dynamic pressure at the throat and increases the pressure recovery potential of the diffuser passage. In this way, some of the trends observed for the diffuser inlet pressure recovery coefficient are counteracted by changes in the diffuser passage recovery coefficient such that the overall diffuser pressure recovery changes only slightly via this mechanism.

By influencing the velocity distribution throughout the diffuser inlet, compressibility also influences the wall friction and corresponding amount of scrubbing loss incurred in the inlet. This effect is explained in Section 5.3, and can be estimated by comparing the scrubbing loss estimated in Section 6.5.5, which utilizes Equation 5.7, with an incompressible scrubbing loss estimated using Equation 5.8. These estimates are plotted in Figure 6.35 assuming the dissipation coefficient is constant. Compressibility clearly has a big effect on the stagnation pressure loss coefficient, reducing it by approximately 20-30% at high flow angles (diffusing flow). Compressibility also influences the trend, shifting the minimum loss coefficient to higher flow angles.

Unlike the impact of compressibility on the ideal pressure recovery coefficient, its effect on inlet loss is not counteracted by an opposite effect on the diffuser passage loss. In this way, the effects of compressibility on loss via this particular mechanism compounds throughout the diffuser.

Because the diffuser inlet Mach number is greater at 100% $N_{c25}$ than it is at 80% $N_{c25}$, this estimate indicates that compressibility reduces the stagnation pressure loss coefficient more at 100% $N_{c25}$. However, this effect is not observed in the CFD results. This is hypothesized to be due to other mechanisms possibly related to the differences in inlet nonuniformity between the two speeds, as seen in Figure 6.28.

Everitt hypothesized that increased Mach number increases the incidence losses, or increases the sensitivity of loss to incidence angle at low flow angles [10]. This is reflected in the overall diffuser experimental data shown in Figure 6.4 and Figure 6.5, but it is not re-

flected upstream of the throat by the CFD results shown in Figure 6.35. These incidence losses will be shown in Section 6.6 to actually be incurred downstream of the throat.

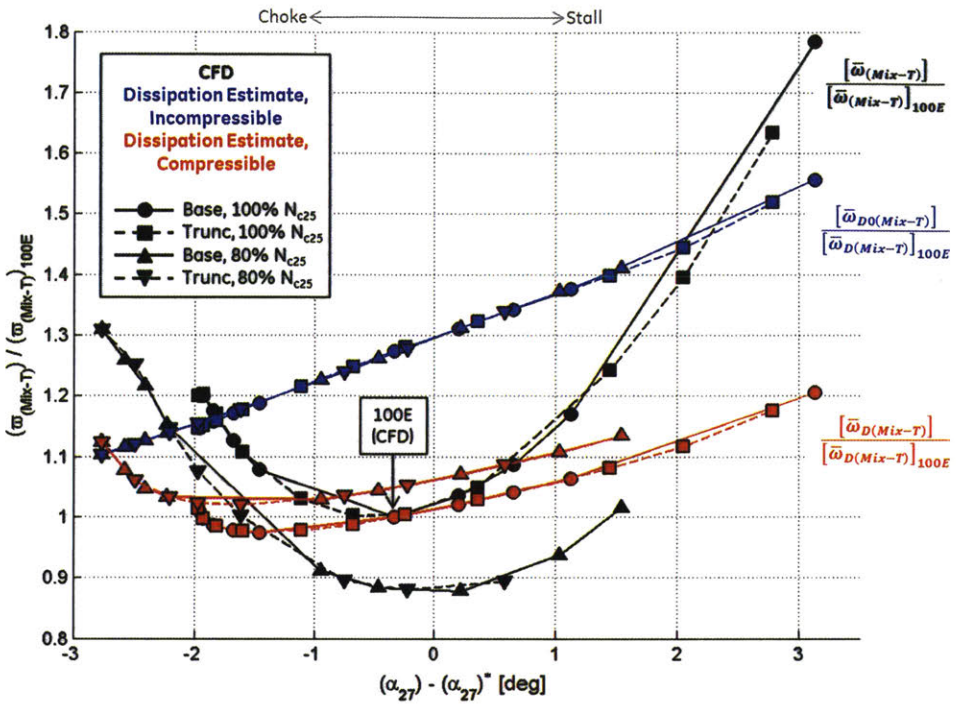


Figure 6.35: Diffuser inlet stagnation pressure loss coefficient versus impeller exit flow angle, showing effect of compressibility. Symbols and line styles denote diffuser configuration and compressor speed, while colors denote different calculation assumptions, including both incompressible (blue) and compressible (red) scrubbing loss estimates. Compressibility reduces loss coefficient associated with scrubbing, especially at high flow angles.

## 6.5.7 Secondary Flows

This section details the characteristics, sources, and development of secondary flows in the diffuser inlet. The motivation for this is that the secondary flows persist throughout the diffuser passage, and are shown in Section 6.6.6 to have a detrimental impact on the pressure recovery of the diffuser passage by accumulating high loss flow and reducing mixing effectiveness.

The existence of streamwise vorticity near the endwalls at the impeller exit has been shown in Section 4.3. However, the diffuser inlet also plays an important role in the development of secondary flows by altering the magnitude and direction of the vorticity exiting the impeller and by generating new vortices as flow separates off the leading edge cusps. Both of these effects are strongly influenced by the impeller exit flow angle.

As mentioned, Section 6.6.6 further discusses the impacts of these secondary flows within the diffuser passage.

### 6.5.7.1 Characteristics of Secondary Flows

Figure 6.36 and Figure 6.37 show the distributions of vorticity throughout the diffuser inlet over a range of operating conditions. Specifically these figures show the component of vorticity in the diffuser passage lengthwise direction, which is nearly the same as the streamwise component. The secondary flow structures are clearly visible, occurring as counter-rotating vortex pairs positioned on either the diffuser pressure side, suction side, or both. The influence of operating point on the strength or even the existence of these vortex pairs

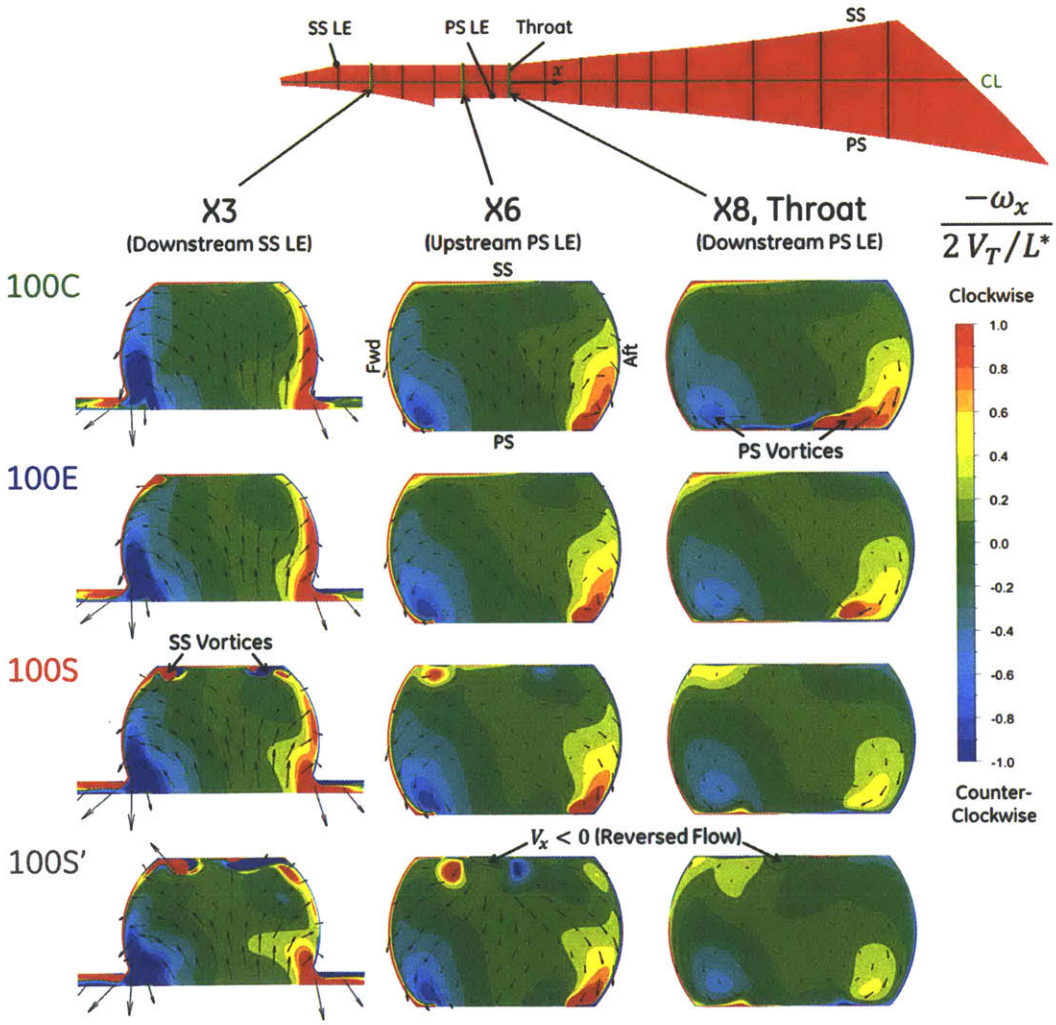


Figure 6.36: Distribution of vorticity in diffuser passage direction at 100% $N_{c25}$ for baseline diffuser. Presence and strength of counter-rotating vortices on diffuser pressure and suction sides depends on operating point or incidence angle.

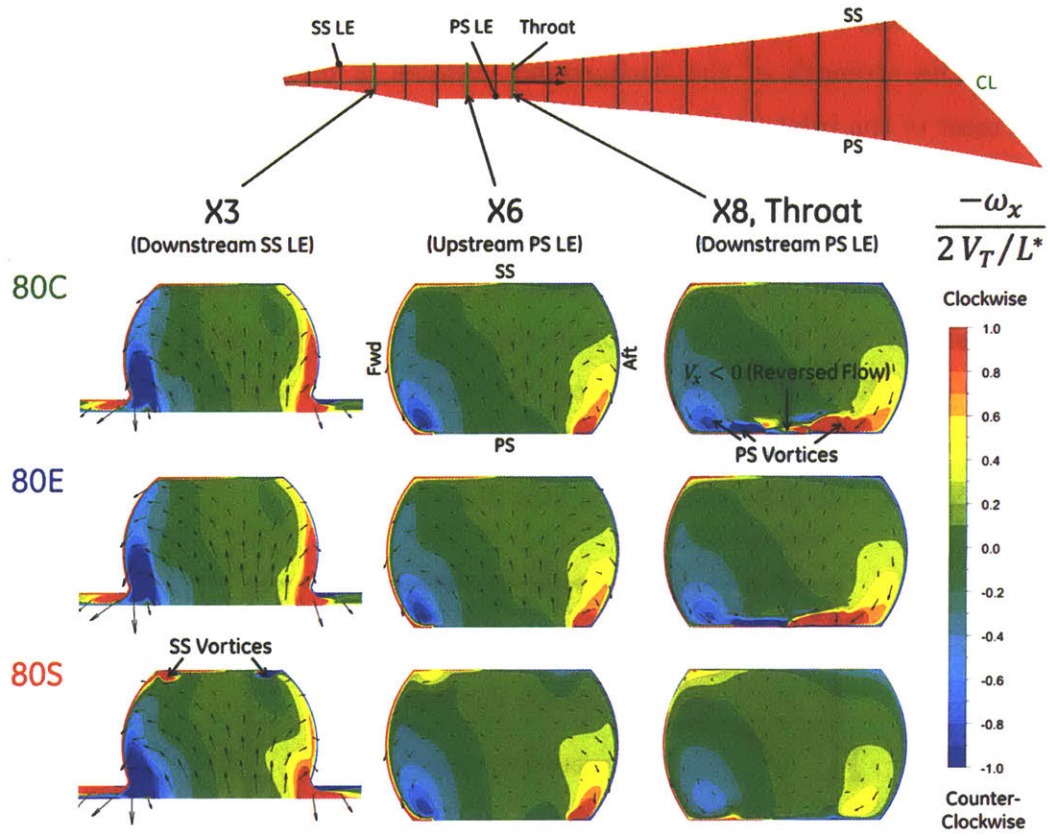


Figure 6.37: Distribution of vorticity in diffuser passage direction at 80% $N_{c25}$ for baseline diffuser. Presence and strength of counter-rotating vortices on diffuser pressure and suction sides depends on operating point or incidence angle.

is also clear. Note that the baseline and truncated diffusers exhibit identical secondary flow structures (truncated diffuser vorticity is not shown). Also, recall that the CFD results are mirrored to correspond to the rig geometry, so vorticity quantities derived from the CFD coordinate system are re-labeled as negative to reflect the rig's coordinate system.

The observable secondary flow structures can be characterized into three sets of vortex pairs, which are also illustrated in Figure 6.38. At high flow angles, strong vortices are observed on the diffuser suction side immediately downstream of the leading edge (cut plane X3), and are almost completely diffused out by the throat (X8). These are referred to as the suction side incidence vortices, as they are later shown to result from positive incidence on the leading edge cusps. Similarly, at low flow angles, strong pressure side incidence vortices are observed downstream of the diffuser leading edge (X8). Lastly, streamwise vorticity accumulates on the forward and aftward walls near the impeller exit and diffuser pressure side. These are referred to as background vortices, since they are less concentrated than

the incidence vortices, but instead they represent weaker vorticity which is spread over a larger area. The strength of the background vortices is unaffected by operating point throughout most of the inlet (up to cut plane X6), but a change in strength with respect to flow angle is finally observed downstream of the throat (X8). The background vortices are also associated with the flow reversal and large 1D shape factors observed near the bleed slots. A fourth category of vorticity is observed in the boundary layers as a necessary reaction to the crossflow and no-slip condition at the wall, but only a small fraction of this induced vorticity is in the streamwise direction. Notice that the vorticity distributions are similar between 100% $N_{25}$ and 80% $N_{c25}$, although lower flow angles and thus stronger pressure side vortices are able to be achieved at 80% $N_{c25}$.

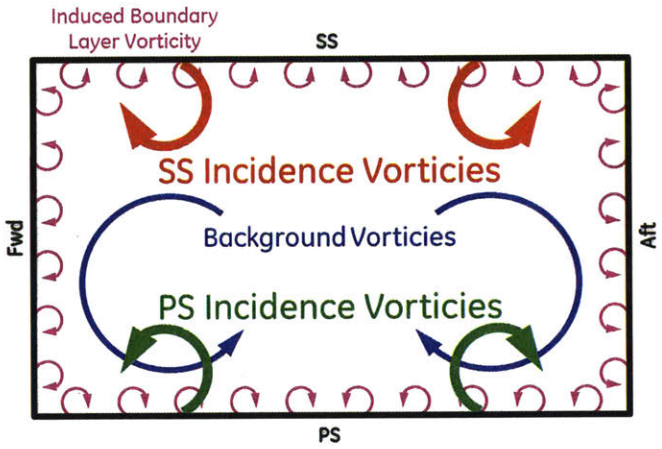


Figure 6.38: Diffuser secondary flow structures.

To weigh the importance of each of these vortex pairs, the circulation of each vortex is calculated from the CFD solutions at cut planes downstream of the suction side leading edge (X3) and pressure side leading edge (X8). The vortex passage is divided into different regions attributed to each vortex, and the vorticity is integrated over the area of these regions. These regions are defined for each vortex pair in two steps. First, regions of the diffuser passage where the streamwise component is less than 50% of the total vorticity magnitude are neglected. This filters out the induced boundary layer vorticity near the diffuser walls which, if included, would necessitate that the net circulation around the diffuser passage be equal zero. These regions are shown in Figure 6.39 for the lowest simulated flow angle (80C) and the highest simulated flow angle (100S'). Next, the incidence vortices are distinguished from the background vortices. This is accomplished by dividing the diffuser passage into four quadrants: PS-Fwd, PS-Aft, SS-Fwd, and SS-Aft. In quadrants where

incidence vortices can be expected (SS-Fwd, and SS-Aft on X3, and PS-Fwd, and PS-Aft on X8), regions with normalized vorticity greater than 1 are attributed to the incidence vortices. This threshold is chosen after observing in Figure 6.36 and Figure 6.37 that, unlike the background vortices, the incidence vortices are associated with concentrated zones of high vorticity. This is a good approximation due to their small size, although it is recognized that the incidence vortices are truly superimposed on the background vortices, and they are not spatially distinct. The resulting incidence vortex regions are also shown in Figure 6.39, clearly showing the suction side and pressure side incidence vortices at high and low flow angles respectively.

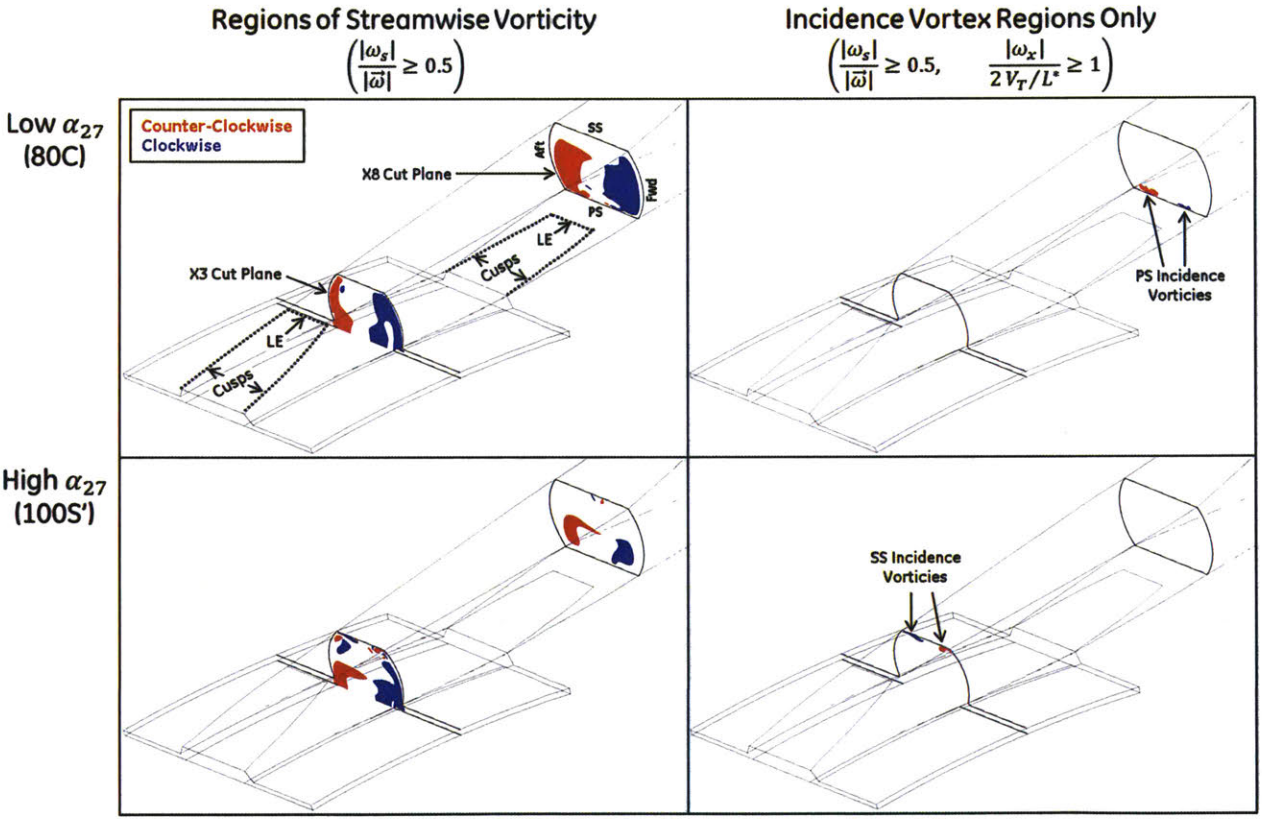


Figure 6.39: Vortex zones at low (80C) and high (100S') diffuser inlet flow angles for baseline diffuser.

The circulations of each vortex are plotted in Figure 6.40 downstream of the leading edge on both suction and pressure sides. Each vortex pair is separated into individual forward and aftward vortices, and the sums of the clockwise and counterclockwise circulations are also shown. At the X3 plane immediately downstream of the suction side leading edge, the background vortices have greater circulation than the incidence vortices, with strength

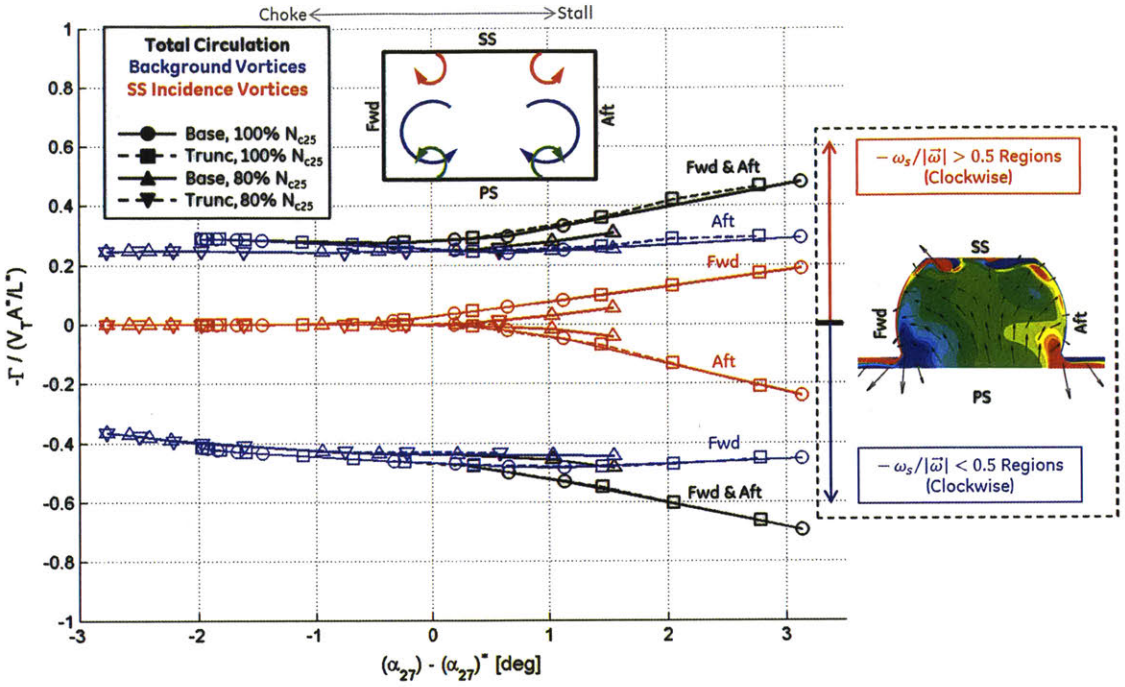


(a) X3 cut plane (downstream of suction side leading edge).

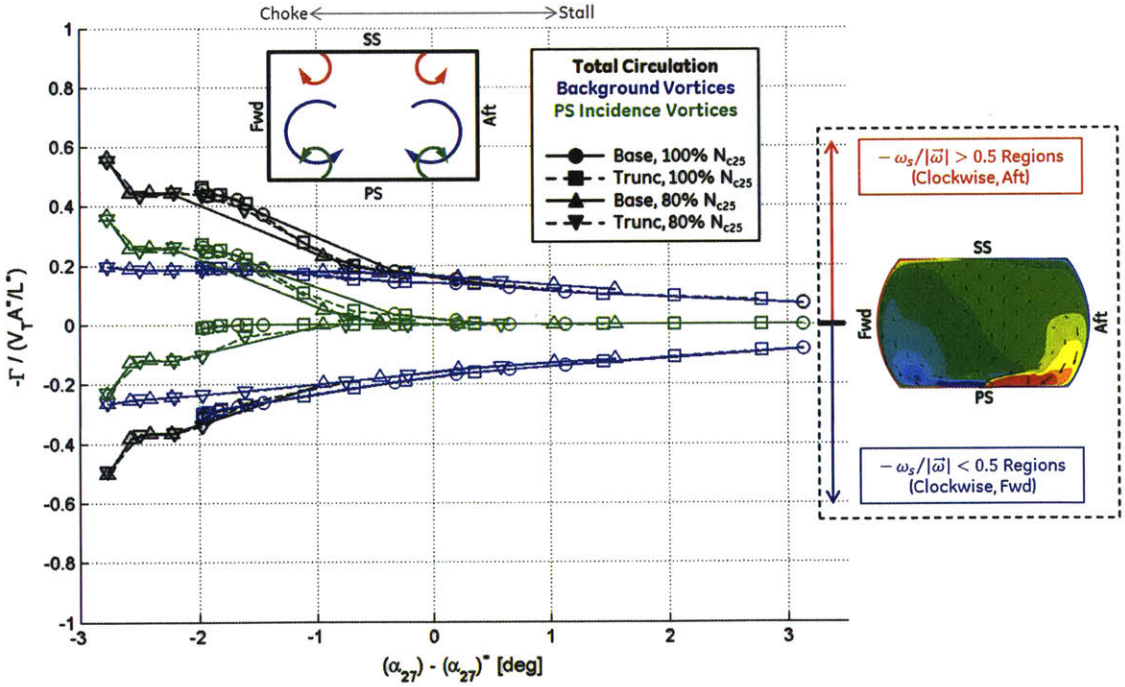


(b) X8 cut plane (downstream of pressure side leading edge).

Figure 6.40: Normalized circulation around vortex regions versus impeller exit flow angle. Symbols and line styles denote diffuser configuration and compressor speed, while colors denote different vortex sources. Pressure and suction side incidence vortices rapidly increase in strength below and above threshold flow angle. Background vortex strength unaffected by flow angle at X3, but increases with reduced flow angle at X8.

that is unaffected by flow angle. The suction side incidence vortices are nonexistent at low flow angles, but above a threshold flow angle they begin to steadily increase in strength. At the diffuser throat (X8), the background vortices are weaker than they are further upstream, with increased flow angle having the effect of weakening them even more. The pressure side incidence vortices are nonexistent at high flow angles, but they increase below the same threshold flow angle identified for the suction side incidence vortices, surpassing the background vortices in circulation at the lowest flow angles despite their smaller size. It should be noted that the appearance of the pressure side incidence vortices corresponds approximately to the piece-wise change in the overall diffuser pressure recovery trend from region 1 to region 2 (Figure 6.6).

In general, the clockwise and counterclockwise vortex counterparts follow the same patterns. However, the forward background vortex is stronger than the aftward background vortex at X3, and the aftward incidence vortex is stronger than the forward incidence vortex at the throat (X8). This is the result of the forward-to-aftward asymmetry in diffuser inlet conditions. All of these patterns are common between 100% $N_{c25}$ and 80% $N_{c25}$, though there are minor differences in the vortex strengths between the two speeds. These differences are also likely attributable to differences in spanwise inlet velocity or flow angle profiles between the two speeds.

#### 6.5.7.2 Development of Secondary Flows

There are a number of ways secondary flows could develop in the diffuser inlet. First, the origin of the vorticity must be determined. It can either be a result of the impeller exit nonuniformity, or new vorticity can be generated in the diffuser inlet boundary layer. Once vorticity exists, it is convected throughout the flow, behaving the same way as fluid material lines. Vorticity can thus be strengthened and reoriented as the nonuniform velocity field stretches and bends the vortex lines. In this manner, boundary layer vorticity can become streamwise vorticity. Eventually, vorticity diffuses, weakening the secondary flows. These vorticity kinematics are described in detail by Greitzer et. al. [17].

The origin of the secondary flows in the diffuser can be investigated by tracing the CFD calculated streamlines and vortex lines that pass through the established vortex regions. These are shown in Figure 6.41 for the background vortices, color coded according to the strength of the streamwise vorticity. Illustrations are shown below the CFD results to sim-

plify the CFD observations. The streamlines that pass through the background vortices can be traced directly and smoothly back to the impeller exit, with nearly constant streamwise vorticity. This suggests that the background vortices are predominantly the result of the impeller exit secondary flows and not due to new or modified vorticity sources. One can also see from the vortex lines that although new boundary layer vorticity formed in the diffuser inlet does modify the direction of the vortex lines, the streamwise component from the impeller exit is still preserved. The fact that the impeller exit secondary flows give rise to the background vortices explains why they are not strongly impacted by diffuser inlet flow angle. Another inference that can be drawn from this observation is that the existence of background vortices doesn't depend on the diffuser leading edge geometry or the presence of cusps.

While the circulation of the background vortices has been shown to be independent of flow angle at the X3 cut plane immediately downstream of the diffuser suction side leading edge, flow angle does impact the background vortex strength at the throat (X8). This can be explained by the vortex kinematic effect illustrated in Figure 6.42. If the flow enters the diffuser with some incidence angle relative to the leading edge, a circumferential static pressure gradient will form due to streamline curvature, decelerating the flow on one side of the passage while accelerating it on the other side. This skews the fluid lines and vortex lines entering the diffuser, which correspondingly strengthens or weakens the secondary flows. As a result, the background vortices are weakened at low flow angles relative to high flow angles.

Figure 6.43 shows the streamlines and vortex lines passing through the pressure side incidence vortices at negative flow angles, and through the suction side incidence vortices at high flow angles. These lines are also color coded according to the streamwise vorticity, which is two orders of magnitude stronger for the incidence vortices than it is for the background vortices (note the color scale). Tracing the streamlines upstream, one can see that they originate from the opposite sides of the leading edge cusps. Upon further investigation it is also observed that the strength of the streamwise vorticity changes rapidly across the cusps. The vortex lines show that the streamwise vorticity is only localized to small regions aligned with the edges of the cusps.

The incidence vortices are hypothesized to form when flow separates off the cusps, introducing boundary layer vorticity into the main flow stream as illustrated in Figure 6.44.

These vortex lines are then stretched in the streamwise direction as the separated flow gains velocity, with more stretching at more extreme flow angles. At very low flow angles, the vortex lines are further stretched by high flow accelerations around the diffuser leading edge on the pressure side.

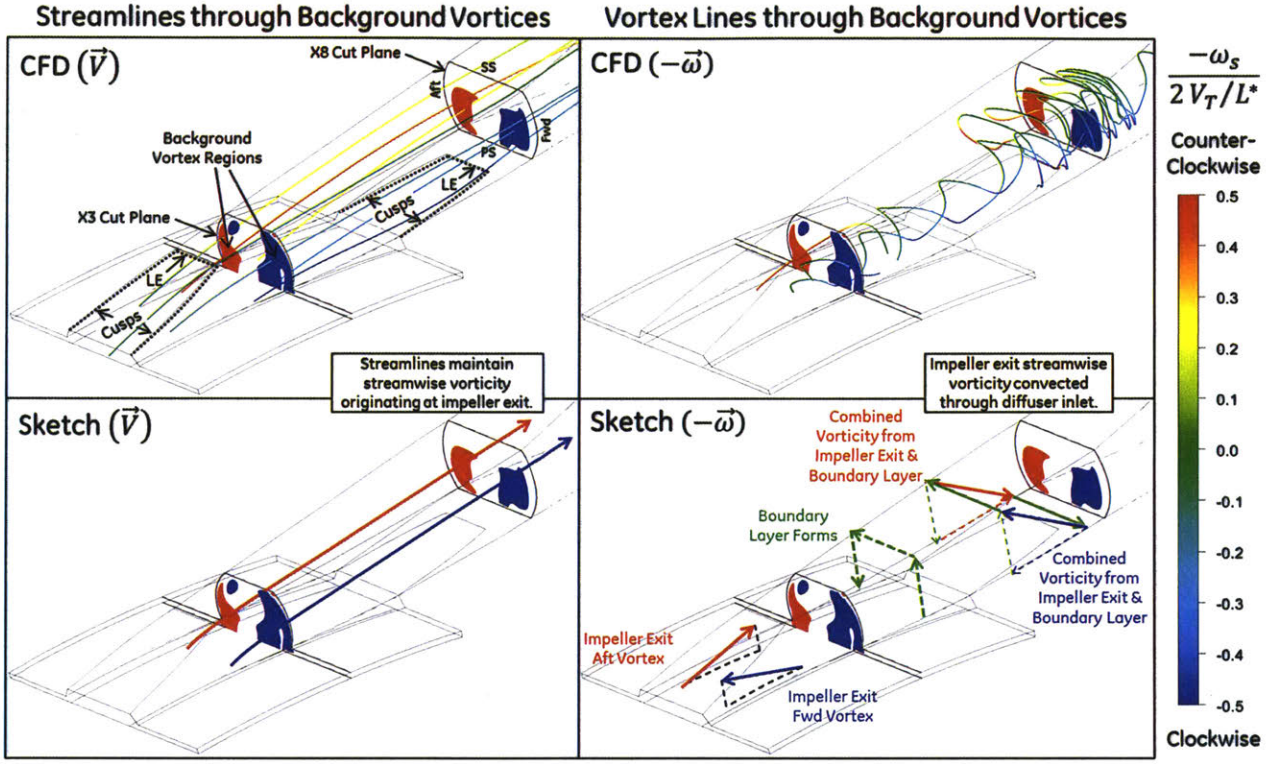


Figure 6.41: Streamlines and vortex lines through background vortex regions for baseline diffuser 100E CFD simulation. Background vortices originate with impeller exit streamwise vorticity.

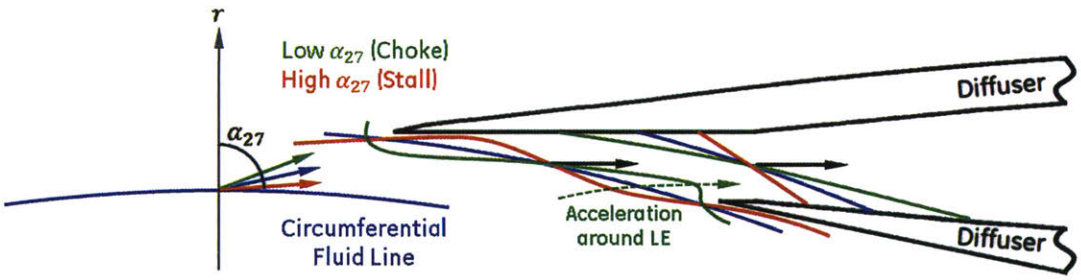


Figure 6.42: Convection of circumferential fluid line through diffuser. Streamline curvature skews fluid line, altering length in streamwise direction. Streamwise vorticity is similarly impacted by vortex line stretching and skewing. Therefore, strength of background vortices is increased with reduced incidence angle.

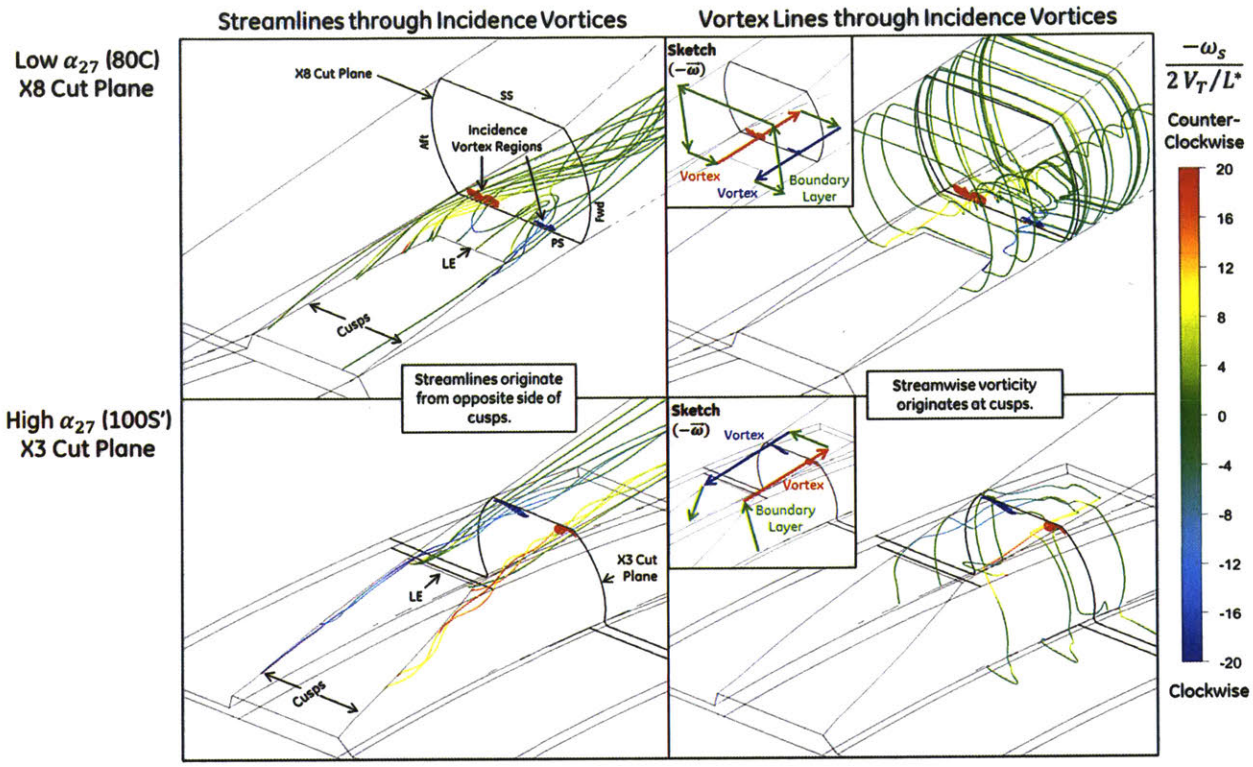


Figure 6.43: Streamlines and vortex lines through incidence vortex regions. Pressure side incidence vortices shown at low flow angle (80C) and suction side incidence vortices shown at high flow angle (100S'). Incidence vortices originate with separation off leading edge cusps, and associated introduction of boundary layer vorticity into main flow stream.

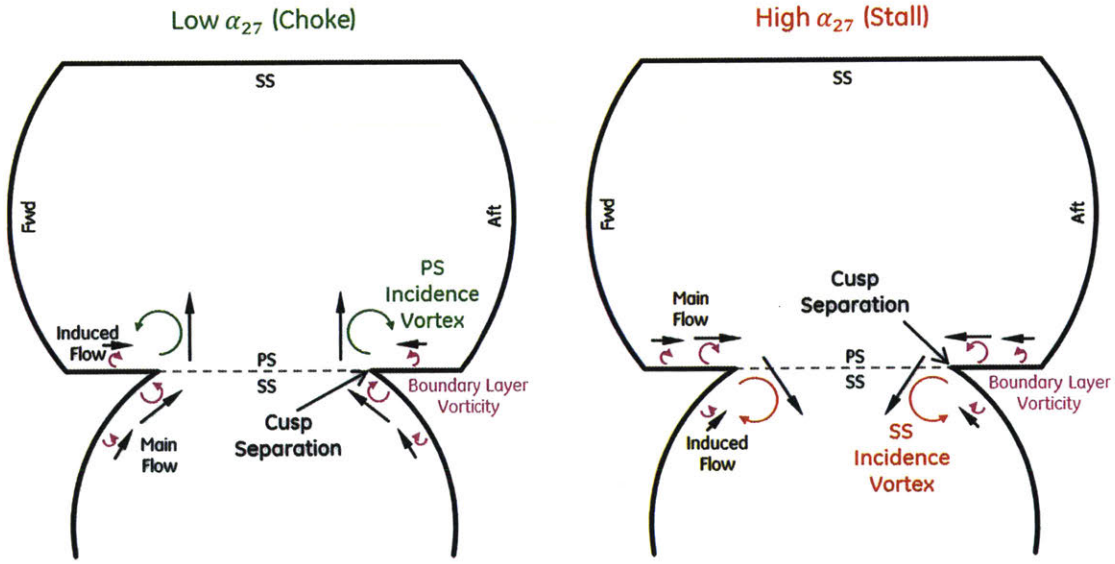


Figure 6.44: Formation of incidence vortices due to flow separation off diffuser cusps and introduction of boundary layer vorticity into main flow stream.

### 6.5.7.3 Effect of Flow Nonuniformity on Secondary Flows Development

The background vortices and incidence vortices are found to originate with the impeller exit streamwise vorticity and diffuser inlet boundary layer vorticity respectively. Therefore, it is hypothesized that these secondary flows are influenced by variations in the impeller exit spanwise nonuniformity and boundary layer thickness. This is found to be true. However, in the limiting case, one might infer that there would be no vortices if there were no inlet flow nonuniformities or inlet boundary layer growth. This is found to be false.

To test the hypothesis that the secondary flows are influenced by the diffuser inlet nonuniformity and boundary layer growth, these mechanisms are varied in CFD simulations of the 100E operating point performed on the diffuser and deswirler alone (no impeller). Two sets of diffuser inlet conditions are simulated: one including all circumferential and spanwise nonuniformities resulting from the full stage simulation, and one in which these inlet conditions are availability averaged in the spanwise direction, leaving only small circumferential variations in flow properties to accommodate the upstream influence of the diffuser. The 1D momentum averaged diffuser inflow angle is preserved. In addition, two sets of diffuser wall boundary conditions are simulated: one being the standard no-slip condition and one being a free-slip (no wall friction) condition that does not allow new vorticity generation at the inlet walls. Note that the simulations utilize different deswirler exit static pressure boundary conditions, since the simulations without the wall friction experience a greater static pressure recovery coefficient.

The four different combinations of inlet conditions and wall boundary conditions are simulated, and the resulting vorticity distributions are shown in Figure 6.45. It is clear there are differences in the strengths of the vortices. The greatest difference is a change in the pressure side incidence vortices at the diffuser throat for the free-slip diffuser inlet wall simulations (note that the 100E operating point does not have strong incidence vortices to begin with, so operating points near choke and stall should be simulated to better evaluate the impact on incidence vortices). This confirms the hypothesis that flow nonuniformity influences the vortices. Furthermore, this suggests that the difference in diffuser inlet nonuniformity between 80% $N_{c25}$ and 100% $N_{c25}$ gives rise to the observed differences in vortex strengths at the same average diffuser inflow angle.

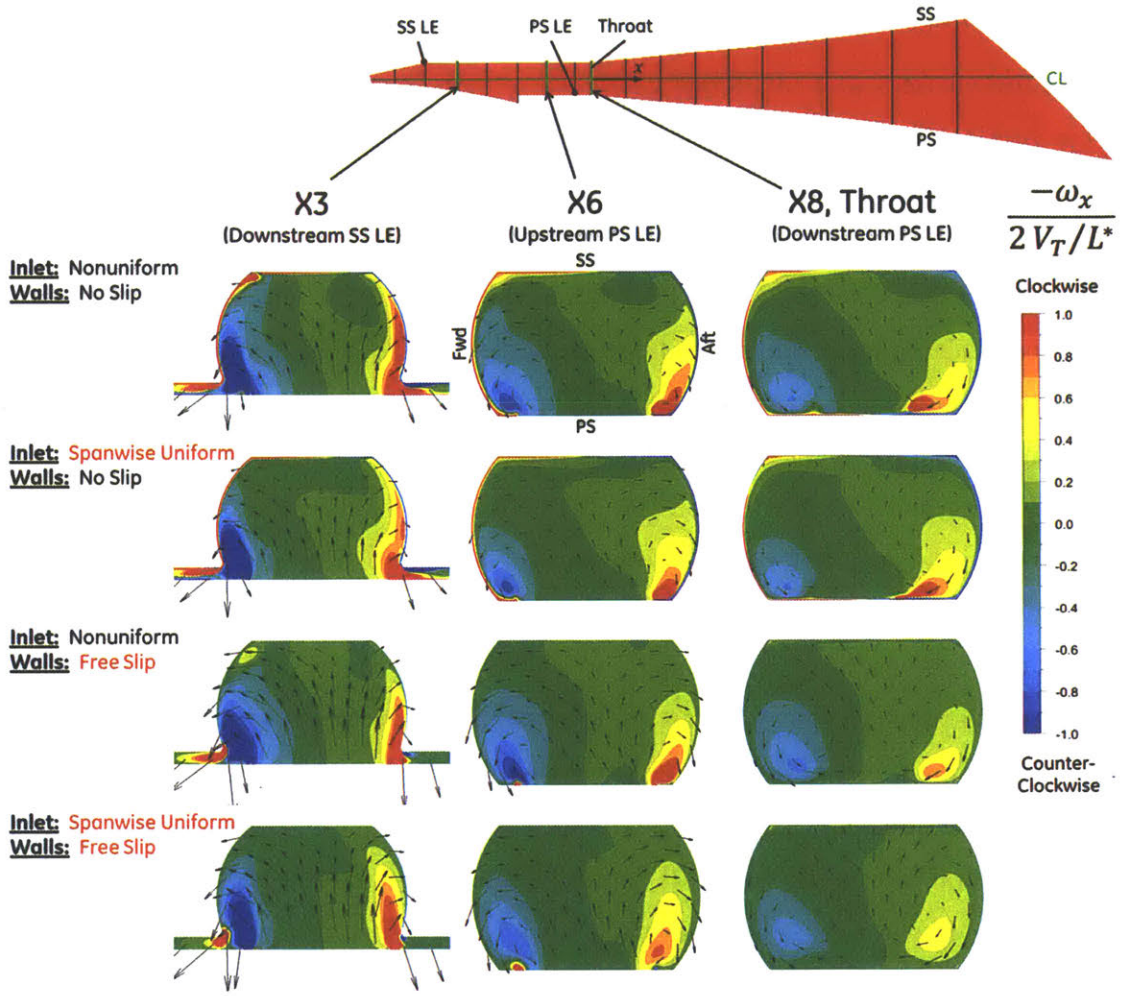


Figure 6.45: Effect of wall friction and impeller exit spanwise nonuniformity on throat secondary flow structures for baseline diffuser 100E CFD simulation. Vortex strength is affected by nonuniformity. However, vortex structures are generally present regardless of boundary condition uniformity.

The hypothesis is not completely confirmed, however. Even though these experiments completely remove vorticity introduced at the diffuser inlet and generated in the boundary layer, the secondary flows are still clearly present with the same general characteristics in each case. Therefore, there must be another mechanism by which vorticity is introduced into the flow. Even without nonuniformities or wall friction, vorticity still exists between the flow and the wall because the wall itself is stationary. This vorticity can enter the main flow as a result of separation, which can occur even in the absence of a simulated boundary layer due to the Kutta condition. This is illustrated in Figure 6.46. As previously mentioned, the incidence vortices are hypothesized to result from cusp separation. The background vortices, on the other hand, have been attributed to the impeller exit streamwise

vorticity. However, in the absence of impeller exit nonuniformity the background vortices can be interpreted as a result of flow separating off the impeller shroud and hub at the discontinuous transition to the diffuser inlet.

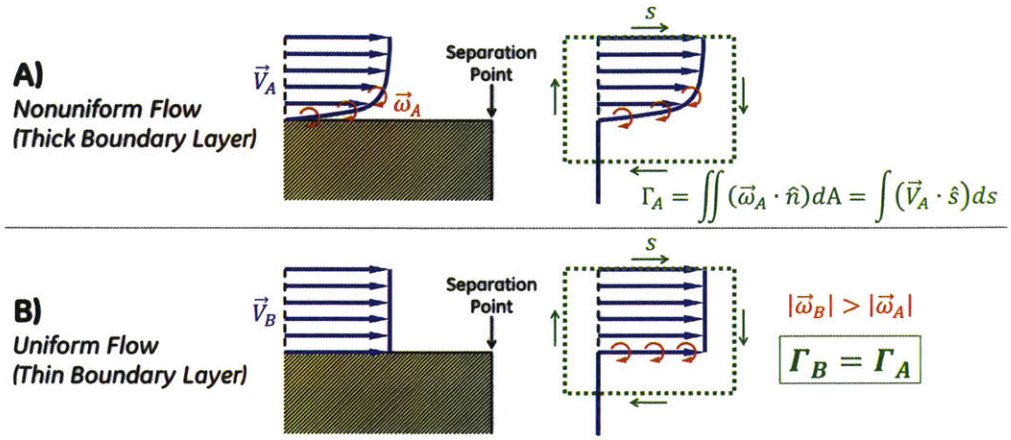


Figure 6.46: Introduction of vorticity into main flowstream via separation. Circulation about a contour enclosing shear layer is independent of shear layer thickness.

This way of thinking about the secondary flows development yields another insight. The circulation around a contour passing through the wall is not affected by the details of the enclosed shear layer. In other words, the thicker the shear layer is, the weaker the vorticity will be to maintain constant circulation. Therefore, the hypothesis is revised to assert that the secondary flows should only depend weakly on the details of the flow nonuniformity (an example of a weak effect is the impact of blockage growth on throughflow velocity, and thus cusp incidence angle). Filipenco and Everitt both observed in their experiments that the diffuser performance is insensitive to spanwise variations in flow properties [9] [10]. The arguments presented here could explain the reason for these observations. However, it is still necessary to establish a link between the secondary flows and the diffuser performance. This is done in Section 6.6.6.

### 6.5.8 Summary of Diffuser Inlet Performance Assessment

The diffuser inlet, representing the region of the diffuser over which impeller exit flow angle has the greatest influence, contributes a significant fraction of the overall diffuser pressure rise. However, the performance is highly dependent on operating point. The ideal uniform static pressure recovery coefficient is determined primarily by the impeller exit flow angle, which sets the inlet 1D area ratio, and secondarily by compressibility. The greatest

pressure recovery coefficients are experienced at high inlet flow angles and Mach numbers. Choking at the diffuser throat limits the minimum achievable static pressure recovery, flow angle, and thus compressor flow range, with high inlet Mach numbers being more limiting.

Approximately half of the inlet loss is incurred in the mixing plane, attributable to the impeller exit circumferential nonuniformities. The remainder of the inefficiency is attributed primarily to loss and secondarily to blockage growth in the inlet boundary layer. The boundary layer loss is driven by path length, which increases loss at high flow angles, and compressibility, which increases the average velocities and corresponding losses at low flow angles. Incidence effects contribute additional loss at high and low flow angles. These effects are not limited to leading edge incidence, but cusp incidence and possibly bleed slot incidence are also hypothesized to play a role.

Secondary flows in the diffuser inlet are characterized and categorized in to two groups according to their origin: background vortices, which result from the impeller exit streamwise vorticity, and incidence vortices, which originate due to separation off the diffuser leading edge cusps at high and low incidence angles. The incidence vortices are observed on the diffuser pressure side at low flow angles, and on the diffuser suction side at high flow angles. The characteristics and strength of the secondary flows are only found to depend weakly on the details of the vorticity sources, since circulation around a contour that bounds a shear layer is independent of its thickness.

## 6.6 Diffuser Passage Performance Assessment

The diffuser passage is the portion of the diffuser that differs between the baseline and truncated configurations, beginning at the throat (station T) and ending at the exit (station 29). As previously established in Section 6.5.1, the diffuser inlet performance is not affected by the differences in passage geometry, so differences in the overall diffuser and compressor performance trends can be attributed to differences in the performance of the diffuser passage itself. The boundary conditions at the throat have also been shown in Section 6.5.2 to be independent of the baseline and truncated diffuser geometry differences, only varying with operating point.

The Mach number and secondary flows at the diffuser throat are found to have the largest influence on the diffuser passage performance. The secondary flows in particular heavily influence the passage separation, and thus they are more influential for the baseline dif-

fuser than the truncated diffuser, which has a smaller separation. The impact of the diffuser trailing edge thickness on diffuser performance is also evaluated and found to account for 6-16% of the inefficiencies within the truncated diffuser passage. For the baseline diffuser, trailing edge thickness has a negligible impact on performance, but the additional inefficiency associated with the large separation make up the difference between the two configurations.

Note that for some of the experimental test points, static pressure is not measured at the throat. As a result, the population of experimental data that can be used to determine passage performance is smaller than the larger set of data used to investigate the overall diffuser performance.

### 6.6.1 Diffuser Passage Performance

The purpose of this section is to simply show the performance of the diffuser passage and highlight performance trends. Performance metrics are plotted relative to diffuser inlet flow angle for consistency with the other diffuser performance plots. Although the flow angle itself doesn't have a direct physical influence over the diffuser passage performance, it does have an indirect influence by governing the throat blockage and secondary flows strength, as discussed in Sections 6.5.2 and 6.5.7. Recall that the diffuser inlet flow angle and throat Mach number are also inversely related to one another for a given compressor speed.

The diffuser passage static pressure recovery coefficient is shown in Figure 6.47. In deep choke, the experimental data indicates that the pressure recovery falls off sharply due to the formation of a passage shock downstream of the throat. More interestingly, between choke and stall there is an overarching trend showing pressure recovery decreasing with flow angle.

The stagnation pressure loss coefficient is not experimentally measured, but the CFD calculated loss is also shown in Figure 6.47. Although deep choke conditions are not simulated by the CFD, it can be inferred that there are high losses corresponding to the shocks and the sharp reduction in experimentally measured static pressure recovery. The CFD results do show the loss decreasing further as the compressor is throttled slightly out of choke. Between choke and stall, the CFD calculated loss trend varies with the compressor speed. Everitt referred to this effect as an incidence loss [10]. At higher flow angles, the

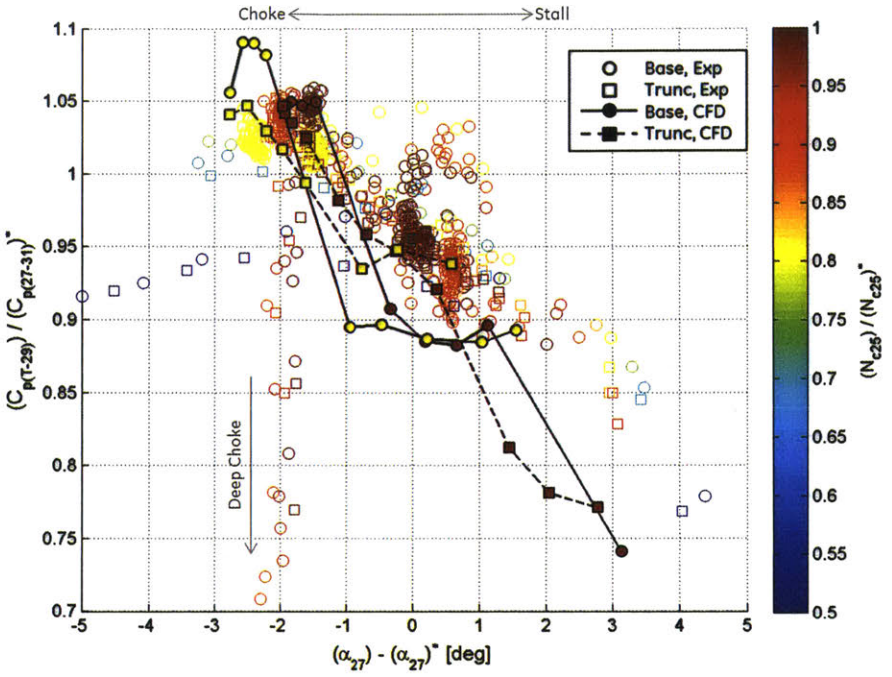


(a) Static pressure recovery coefficient.

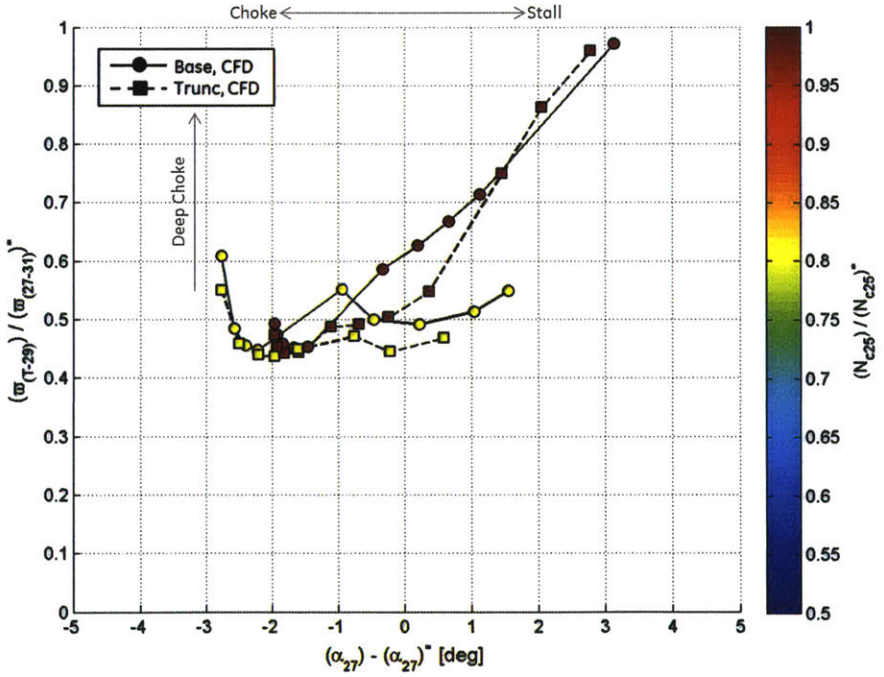


(b) Stagnation pressure loss coefficient.

Figure 6.47: Diffuser passage performance versus impeller exit flow angle. Symbols and line styles denote diffuser configuration and data source, while colors denote rotor speed. Poor pressure recovery and high losses at low flow angles, dependent on compressor speed. Reduction in pressure recovery and increase in loss also observed with increased flow angle between choke and stall. Combined effects of incidence and compressibility confound simple determination of causality.

loss increases steadily toward stall at 100% $N_{c25}$, whereas it is nearly constant across the operating range for the 80% $N_{c25}$ simulations.

The differences between the experimental and CFD results, and between baseline and truncated diffusers are investigated by isolating the 100% $N_{c25}$ and 80% $N_{c25}$ static pressure recovery coefficients individually in Figure 6.48. Clearly, the diffuser passage is the origin of the piecewise appearance of the CFD calculated performance trends referenced in Sections 3.2 and 6.1. The three apparent performance regimes denoted as regions 1, 2, and 3 in Figure 6.48, will be referred to more in the following sections as the cause of this trend is investigated. Again, one can see that the piecewise appearance of the CFD calculated performance trends is more pronounced for the baseline diffuser than it is for the truncated diffuser.

The CFD calculates a lower loss for the truncated diffuser than for the baseline diffuser across much of the operating range, as shown in Figure 6.47. The experimental data also shows a slight difference between the baseline and truncated diffusers. However, recall that the opposite difference is observed in the diffuser inlet experimental performance trend, so this is hypothesized to be the result of differences in the diffuser throat static pressure measurement rather than the differences in diffuser geometry. Furthermore, recall from Section 6.1 that differences in the baseline and truncated diffuser pressure recovery and loss levels are not reflected by the overall diffuser experimental loss measurements.

The causes of the diffuser performance trends and the physical relevance of the piecewise appearance of the CFD solution must be addressed by examining the diffuser in more detail.

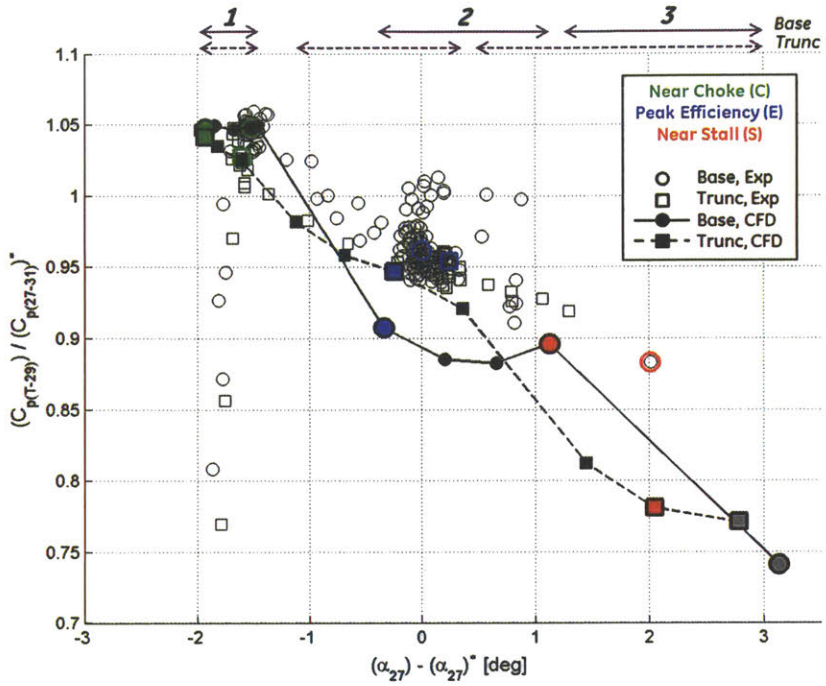


(a) 100% $N_{c25}$.

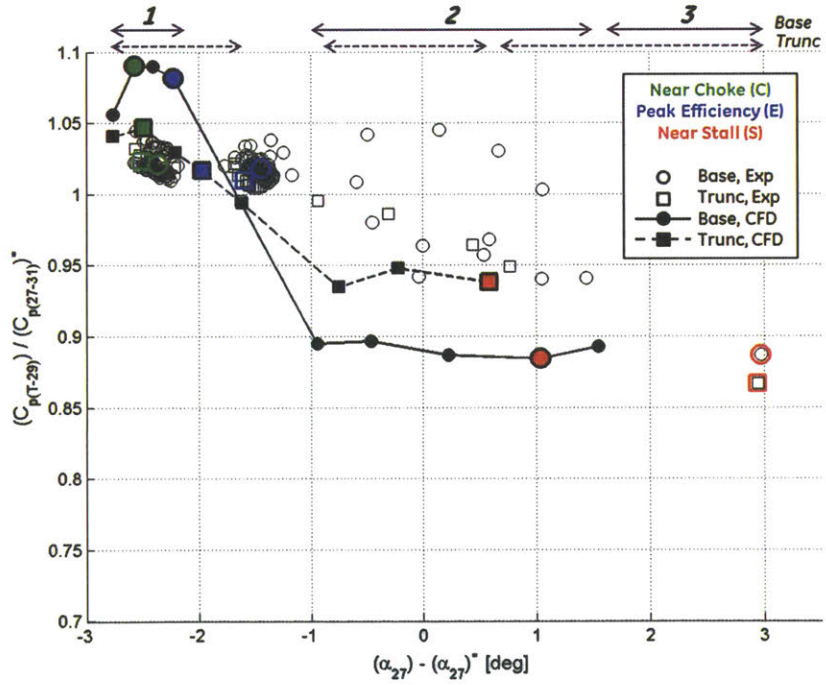


(b) 80% $N_{c25}$.

Figure 6.48: Diffuser passage pressure recovery coefficient versus impeller exit flow angle. Symbols and line styles denote diffuser configuration and data source, while colors denote operating point (note: colored experimental points averaged from multiple tests). Experimental difference between baseline and truncated diffuser pressure recovery coefficients disregarded due to opposite trend observed in inlet. CFD indicates differences between baseline and truncated diffuser, but note piecewise appearance of trend (regimes of behavior denoted 1, 2, and 3).

### 6.6.2 Diffuser Exit Conditions

The flow conditions at the diffuser exit are presented to better understand what drives the performance trends of the diffuser passage, and because they represent the inlet conditions to the deswirler. The diffuser exit flow angle is plotted in Figure 6.49, showing that the truncated diffuser has a higher exit flow angle than the baseline diffuser by approximately 20 deg. Again, this implies that in the truncated diffuser configuration, the deswirler leading edge incidence angle is much higher than design intent. The fact that the deswirler operates off-design with the truncated diffuser upstream is one of the reasons why the deswirler performance is not closely studied here.

The diffuser exit mass blockage is shown in Figure 6.50. Both diffusers have a much higher blockage at the exit than at the throat, with the baseline diffuser exit blockage being 2 to 5 times greater than that of the truncated diffuser. The effects of increased exit flow angle and blockage both reduce the 1D effective area at the diffuser exit such that the two diffuser configurations have nearly equal effective area ratios. This is one reason the static pressure recovery of the two diffuser configurations are so similar despite the large geometry differences. Notice how the baseline diffuser exit blockage trend has a piecewise appearance as the levels and slopes of the characteristic vary sharply across the operating range. This behavior corresponds to the piecewise appearance of the baseline diffuser static pressure recovery coefficient trend.

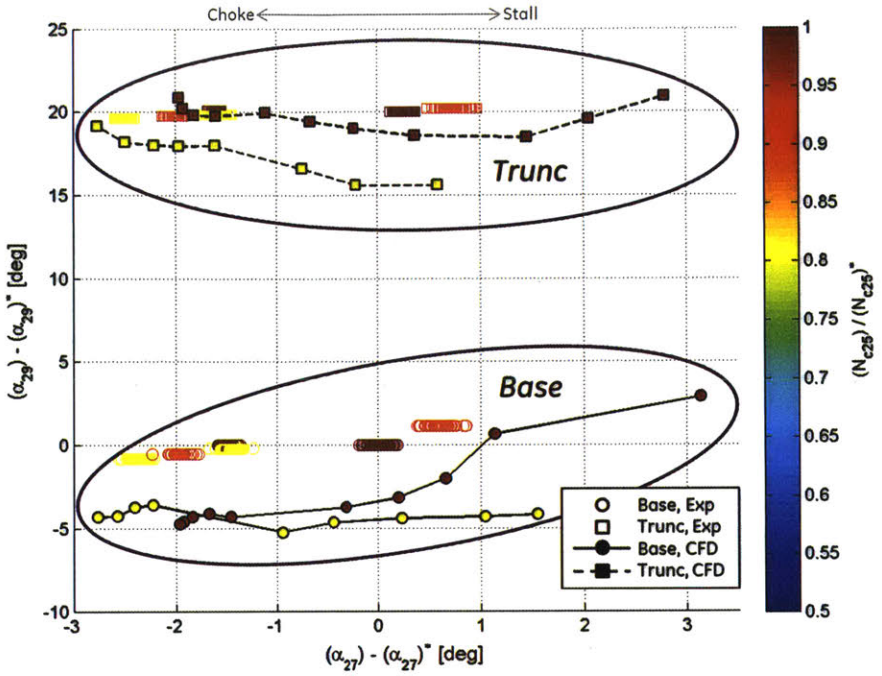


Figure 6.49: Diffuser exit flow angle versus impeller exit flow angle. Symbols and line styles denote diffuser configuration and data source, while colors denote rotor speed. Truncated diffuser exit flow angle approximately 20 deg greater than baseline diffuser.

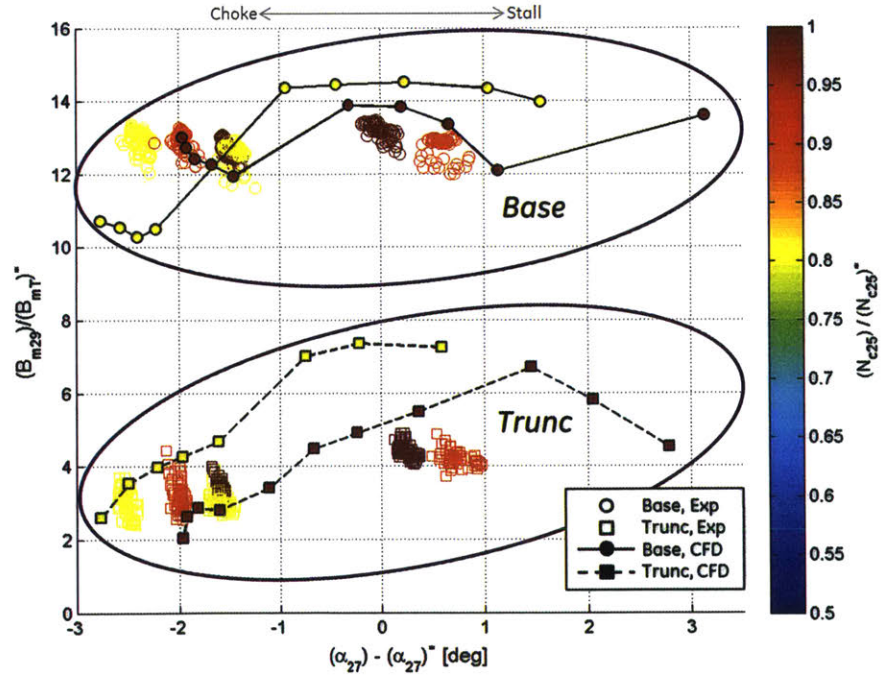


Figure 6.50: Diffuser exit mass blockage versus impeller exit flow angle. Symbols and line styles denote diffuser configuration and data source, while colors denote rotor speed. Baseline diffuser exit blockage 2-5 times greater than truncated diffuser.

### 6.6.3 Evaluation of Nonideal Effects

Using the same procedure discussed in Section 6.4 for evaluating nonideal effects in the diffuser, the diffuser passage pressure recovery coefficient is calculated from the CFD solutions using three sets of assumptions, and plotted in Figure 6.51. These include the actual (black) and ideal (green) pressure recoveries as well as a pressure recovery calculated using the actual diffuser exit blockage but assuming no stagnation pressure loss in the diffuser passage (blue). These are normalized in Figure 6.51 to show the gap between the actual static pressure rise in the diffuser passage and the ideal static pressure rise after complete diffusion.

The 1D area ratio of the baseline diffuser is large enough that an ideal diffusion process would recover all but 10% of the pressure rise deficit. The remaining inefficiencies in the baseline diffuser passage are split between the stagnation pressure loss (35-70%) and blockage (20-55%). For the truncated diffuser, the impact of the stagnation pressure loss is comparable to that of the baseline diffuser. However, the impact of exit blockage is reduced to just 10-25% of the pressure rise deficit. The remaining 25-40% of the truncated diffuser's pressure rise deficit comes from the reduction in effective area ratio caused by the increased exit flow angle. These patterns vary noticeably with respect to flow angle and compressor speed.

Using the second procedure discussed in Section 6.4 for evaluating nonideal effects, the diffuser passage pressure recovery coefficient is calculated by defining hypothetical flow processes which utilize the mixed out average, and plotted in Figure 6.52. In additional to the actual (black) and ideal (green) pressure recoveries, this includes the maximum attainable pressure recovery for a frictionless diffusion process given the nonuniform throat conditions (blue), and the recovery that could be obtained if the exit nonuniformity were mixed out (red). These pressure recovery coefficients are normalized in Figure 6.52 to show the gap between the actual static pressure rise in the diffuser passage and the ideal static pressure rise if diffusion were complete.

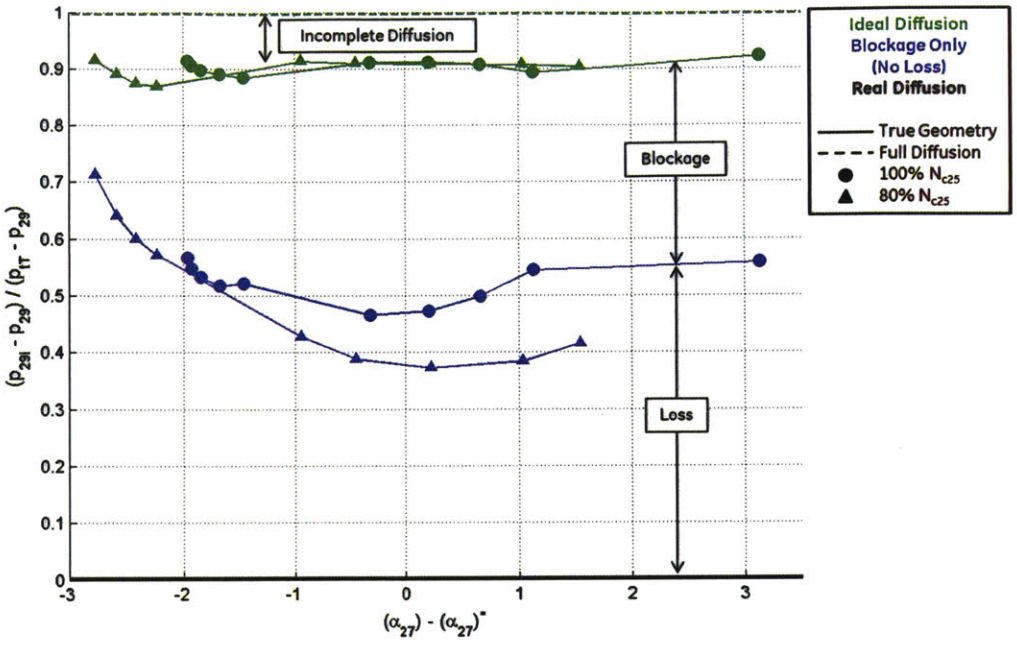


(a) Baseline diffuser.

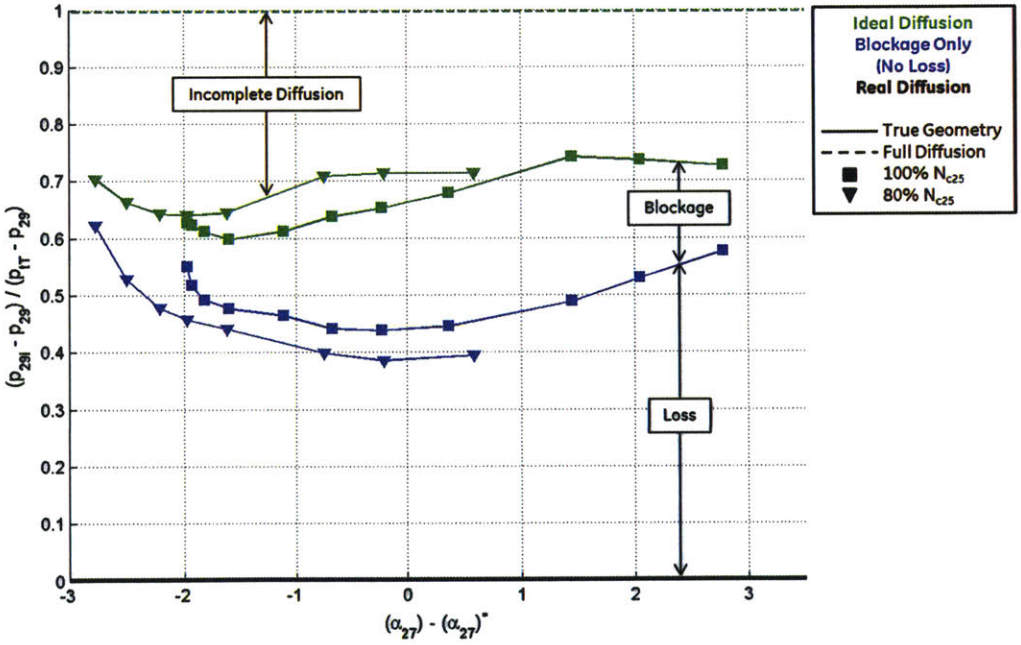


(b) Truncated diffuser.

Figure 6.51: Relative influence of nonideal effects on diffuser passage pressure rise versus impeller exit flow angle, based on CFD solutions. Symbols denote compressor speed, line styles denote use of static pressures (incomplete diffusion constrained by true geometry) or stagnation pressures (full diffusion), and colors denote different nonideal effects. Results normalized between true pressure rise (0) and ideal full diffusion pressure rise (1). Loss accounts for half of inefficiency for both diffuser configurations, followed by blockage for baseline diffuser and limited 1D area ratio for truncated diffuser.

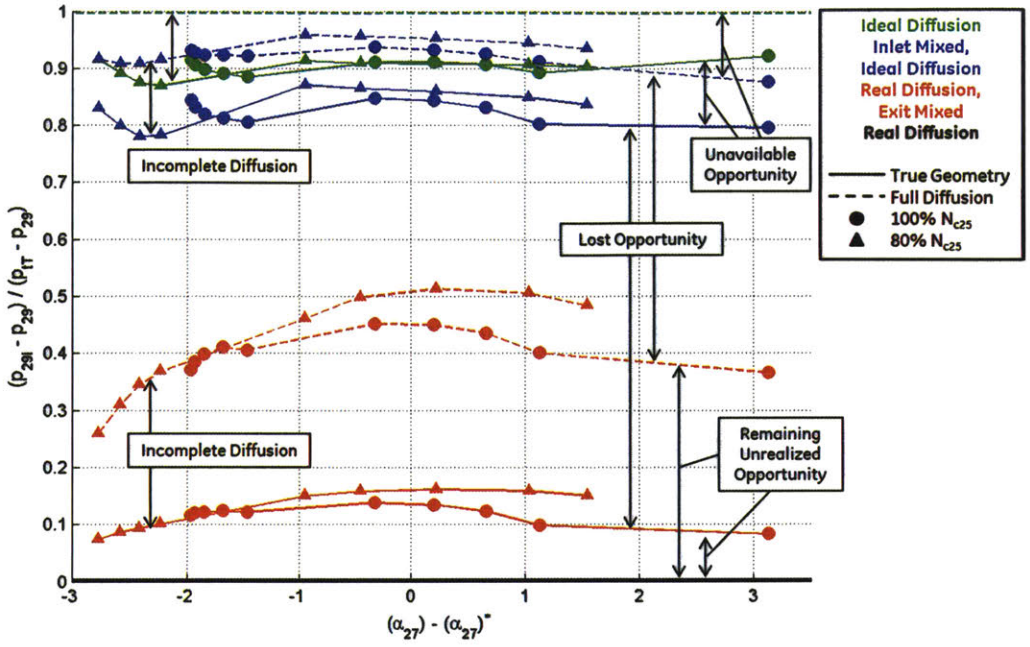


(a) Baseline diffuser.

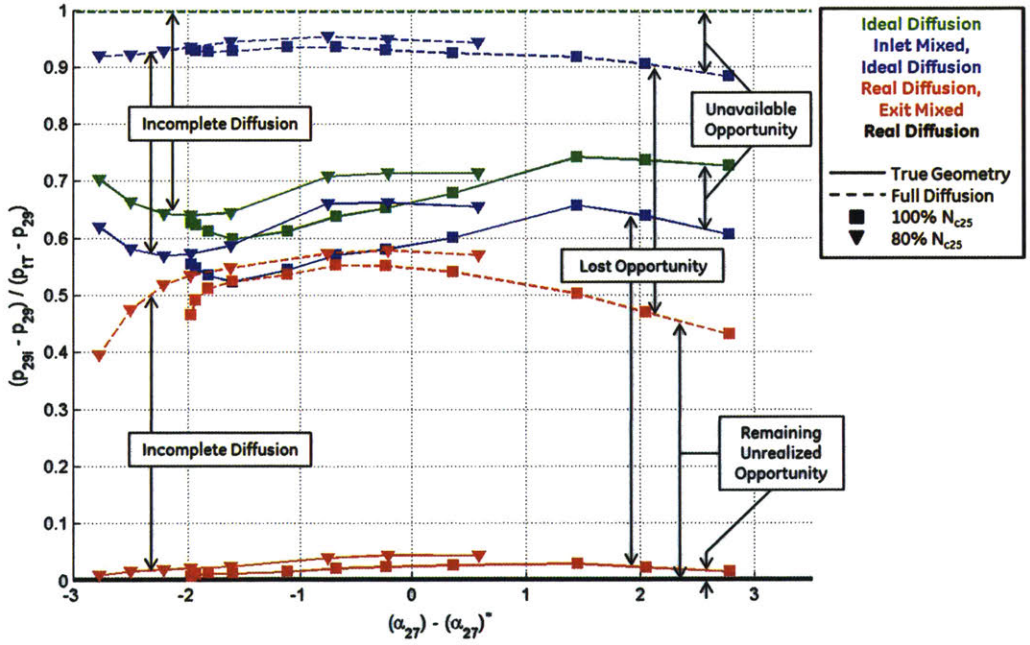


(b) Truncated diffuser.

Figure 6.52: Relative influence of nonideal effects on diffuser passage pressure rise versus impeller exit flow angle, based on CFD solutions. Symbols denote compressor speed, line styles denote use of static pressures (incomplete diffusion constrained by true geometry) or stagnation pressures (full diffusion), and colors denote different nonideal effects. Results normalized between true pressure rise (0) and ideal full diffusion pressure rise (1). Lost pressure rise opportunity is greater for baseline diffuser than truncated diffuser, while truncated diffuser offers greater unrealized pressure rise opportunity for deswirler.

Because all of the performance differences between the two diffusers are manifested in the diffuser passage, the observations made in Section 6.4 regarding differences between the baseline and truncated diffuser inefficiencies are relevant to Figure 6.52 as well. However, the relative contributions of each inefficiency category (unavailable opportunity, lost opportunity, and remaining opportunity) are different. The pressure rise potential that is unavailable due to throat nonuniformity is small, since throat flow properties are relatively more uniform than properties at the impeller trailing edge. Similarly, opportunity that is lost in the diffuser passage due to wall friction and delayed or incomplete mixing is only a fraction of the overall lost opportunity shown for the overall diffuser. The result is that the pressure rise potential remaining at the diffuser exit due to nonuniformity (especially for the baseline diffuser) and the limited 1D area ratio (especially for the truncated diffuser) represent larger portions of the pressure rise deficit for the diffuser passage.

### 6.6.4 Effect of Trailing Edge Thickness

Recall from Figure 6.14 that there is a discontinuous increase in aerodynamic mass blockage across the diffuser trailing edge due to the finite thickness of the trailing edge. At the diffuser trailing edge, the solid blockage accounts for 3-6% of the total blockage for the baseline diffuser, and 35-65% for the truncated diffuser. This additional nonuniformity reduces the mixed out average stagnation pressure, contributing to the loss in pressure rise opportunity incurred within the diffuser passage shown in Figure 6.52.

Figure 6.53 shows the loss in mixed out average stagnation pressure across the trailing edge as a fraction of the total loss in mixed out average stagnation pressure between the throat and exit. For the baseline diffuser, the trailing edge thickness accounts for less than 1.5% of this lost opportunity, while the thicker truncated diffuser trailing edge accounts for 6-16% of the lost pressure rise opportunity within the passage. Despite the differences in contributions from the trailing edge, the baseline and truncated diffusers have been shown in Figure 6.52 to differ only slightly in mixed out average stagnation pressure loss (in fact, the CFD calculates a slightly lower loss for the truncated diffuser). This means that the baseline diffuser makes up this difference via additional wall friction and delayed or incomplete mixing. This is another way to view the fundamental difference between the baseline and truncated diffusers.

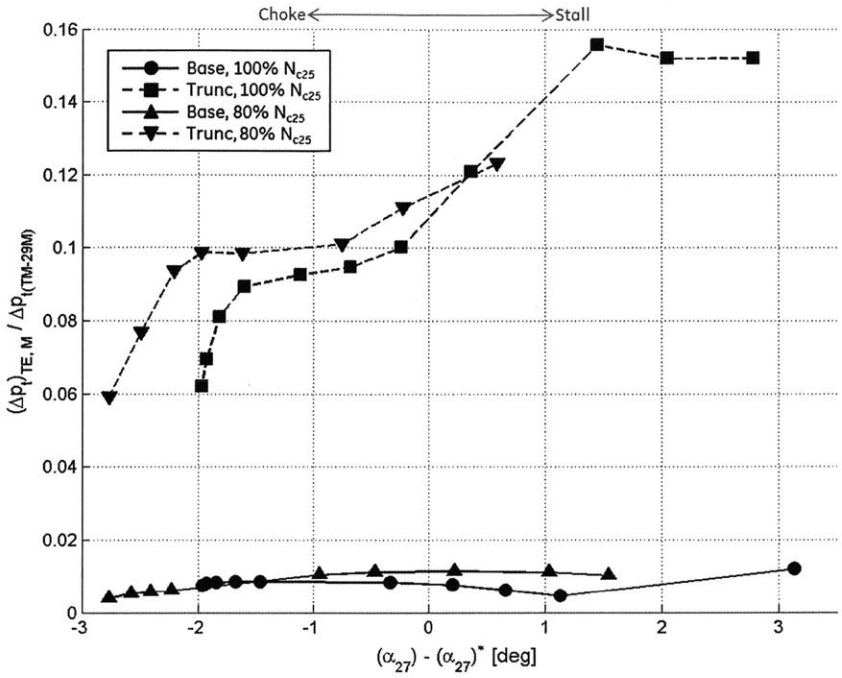


Figure 6.53: Mixed out average stagnation pressure loss across diffuser trailing edge normalized by mixed out stagnation pressure loss between diffuser throat and exit versus impeller exit flow angle. This represents the fraction of lost pressure rise opportunity in the diffuser passage attributable to trailing edge thickness. Symbols and line styles denote diffuser configuration and compressor speed. Truncated diffuser trailing edge accounts for 6-16% of overall passage loss, while contribution is negligible for baseline diffuser.

### 6.6.5 Effect of Compressibility

The diffuser passage static pressure recovery and stagnation pressure loss coefficients are plotted in Section 6.6.1 with respect to the diffuser inlet flow angle. However, recall that the diffuser inflow angle is correlated with the blockage, secondary flows, and Mach number at the diffuser throat. Therefore, the attempt is made here to separate the effect of compressibility, and show its contribution to these diffuser passage performance trends.

To begin, the diffuser passage pressure recovery and loss coefficients are replotted against the throat Mach number in Figure 6.54 and Figure 6.55 respectively, normalized by the baseline diffuser performance measures at 100E. As discussed in Section 5.3, compressibility can be expected to increase the ideal pressure recovery coefficient and reduce the loss coefficient due to scrubbing losses. This general effect is in fact observed in Figure 6.54 and Figure 6.55. However, there are still other effects at play.

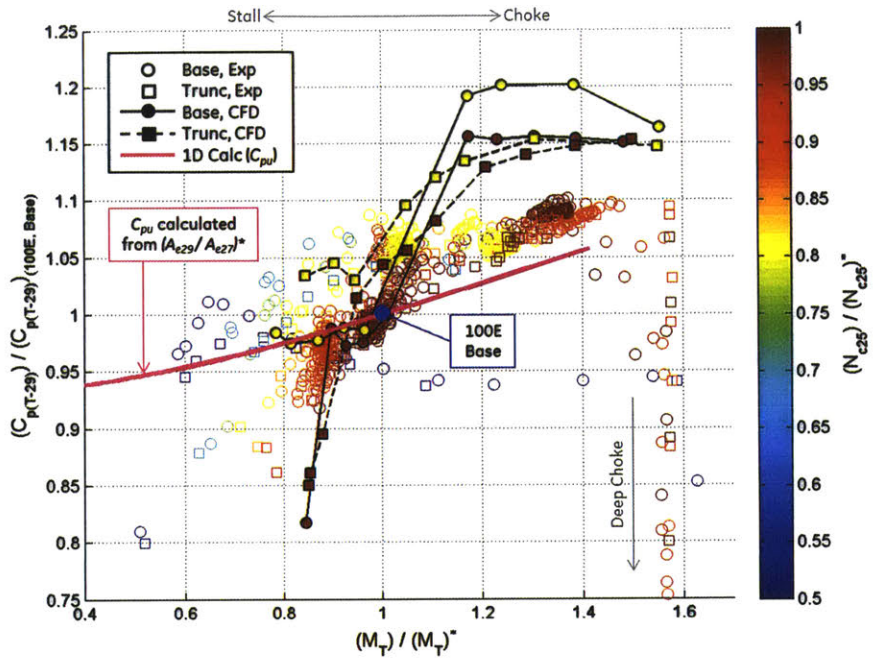


Figure 6.54: Diffuser passage static pressure recovery coefficient versus throat Mach number, showing effect of compressibility on pressure rise. Symbols and black line styles denote diffuser configuration and data source, while symbol colors denote rotor speed. Magenta line represents ideal uniform pressure recovery coefficient calculated from design point effective area ratio. Compressibility increases pressure rise potential.

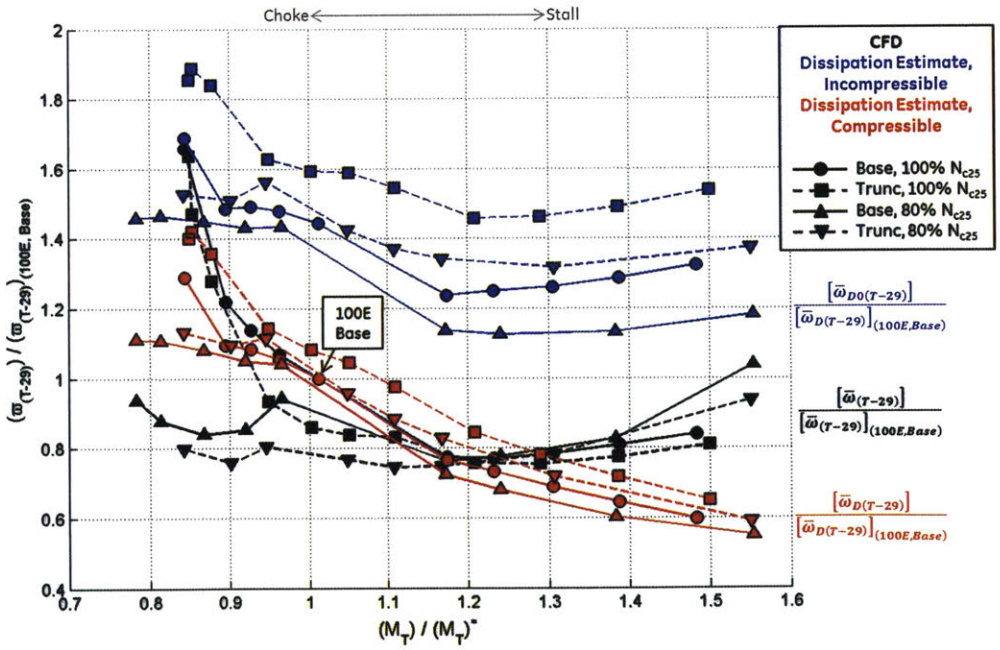


Figure 6.55: Diffuser passage stagnation pressure loss coefficient versus throat Mach number, showing effect of compressibility. Symbols and line styles denote diffuser configuration and compressor speed, while colors denote different calculation assumptions, including both incompressible (blue) and compressible (red) scrubbing loss estimates. Compressibility reduces loss coefficient associated with scrubbing.

Figure 6.54 also shows the 1D uniform flow ideal static pressure recovery coefficient for the diffuser passage. This is calculated over a range of throat Mach numbers using the diffuser passage effective area ratio estimated from the 100E experimental measurements on the baseline diffuser (the effective area ratio of the truncated diffuser is similar due to the combination of lower exit blockage and higher exit flow angle). This idealization helps to quantify the effect of compressibility, which one can see increases the pressure recovery coefficient at higher Mach numbers. However, it does not exhibit a trend as steep as the experimental data or CFD results.

Also contributing to the static pressure recovery trend is the stagnation pressure loss trend. This partially accounts for the difference in slopes between the 1D ideal static pressure recovery coefficient and the experimental or CFD results, since the stagnation pressure loss coefficient is reduced at higher Mach numbers due to compressibility. The impact of compressibility on the loss coefficient due to scrubbing is quantified by applying and comparing Equation 5.7 (compressible) and Equation 5.8 (incompressible), which are based on the dissipation coefficient. These are plotted in Figure 6.55. One can see that the compressible flow loss coefficient estimate is only 50% of the incompressible flow estimate, and it is indeed lowest at higher Mach numbers.

The effect of compressibility on scrubbing loss does not explain everything about the static pressure recovery or stagnation pressure loss coefficient trends, notably their piecewise nature or the differences between the loss at 80% $N_{c25}$ and 100% $N_{c25}$. However, it does account for the general increase in pressure recovery coefficient and reduction in stagnation pressure loss coefficient at higher Mach numbers. As previously mentioned, another effect of compressibility is the high losses and low pressure recoveries incurred when the diffuser chokes due to passage shocks that form downstream of the throat within the diffuser passage. Even at low flow angles approaching coke, the sensitivity of incidence loss to Mach number described by Everitt [10] and observed in Figure 6.5 and Figure 6.47 is also the result of compressibility. Though they are not the full passage shocks that form in deep choke, smaller shocks like those observed in Figure 6.8 and Figure 6.10 form due to localized regions of supersonic flow near the diffuser leading edge or at the transition between the throat and the diverging passage. Near choke, the throat Mach number and corresponding presence of these shocks are extremely sensitive to small changes in inflow angle

or 1D area ratio. This is what drives the sensitivity of incidence loss to Mach number at low flow angles approaching choke.

It is worth recalling the combined effects of compressibility in the diffuser inlet and passage subcomponents, as discussed in Section 6.5.6. While it is true that for the same diffuser inlet flow angle, a higher diffuser inlet Mach number will result in greater ideal static pressure recovery coefficients for both the inlet and passage, the overall diffuser ideal static pressure recovery coefficient is only weakly impacted. This is due to the reduced dynamic pressure at the throat associated with improved diffuser inlet recovery. Essentially, for a large 1D area ratio diffuser with ideal pressure recovery coefficient near unity, compressibility only shifts the ideal static pressure distribution upstream. That said, the impacts of compressibility in reducing the inlet and passage scrubbing losses compounds to reduce the overall diffuser stagnation pressure loss coefficient. Thus, there is still a net benefit of compressibility for flow angles not near choke.

### 6.6.6 Effect of Secondary Flows

It has been shown in Section 6.5.7 that two categories of secondary flows are present at the diffuser throat in the form of counter-rotating vortex pairs. The background vortices originate in the nonuniform impeller exit flow, and are characterized by relatively weak vorticity distributed over large areas. The incidence vortices result from flow separation off the leading edge cusps at high or low incidence angles, and are characterized by local regions of relatively high vorticity. The positions and strength of these secondary flows vary with operating point. At low flow angles, the background vortices and pressure side incidence vortices are strongest at the diffuser throat. At high flow angles, the background vortices are weaker at the throat, and the incidence vortices are observed on the diffuser suction side throughout the inlet region.

This section establishes a link between these various secondary flows sources and the crossflow velocity field. It is then shown that this crossflow results in migration and accumulation of weak endwall flow between the vortices, reducing mixing effectiveness and influencing the position and extent of the diffuser passage separation. This mechanism is especially influential for the baseline diffuser, which experiences a larger separation than the truncated diffuser.

### 6.6.6.1 Relationship between Secondary Flows and Loss Accumulation

The distributions of stagnation pressure loss coefficient are shown in Figure 6.56 at 100% $N_{c25}$ on various crossflow planes throughout the baseline diffuser. Notice that a large region of high loss is observed on the diffuser pressure side at low flow angles, and on the diffuser suction side at high flow angles. This weak flow eventually separates further downstream in the diffuser passage. There are a number of mechanisms which could give rise to

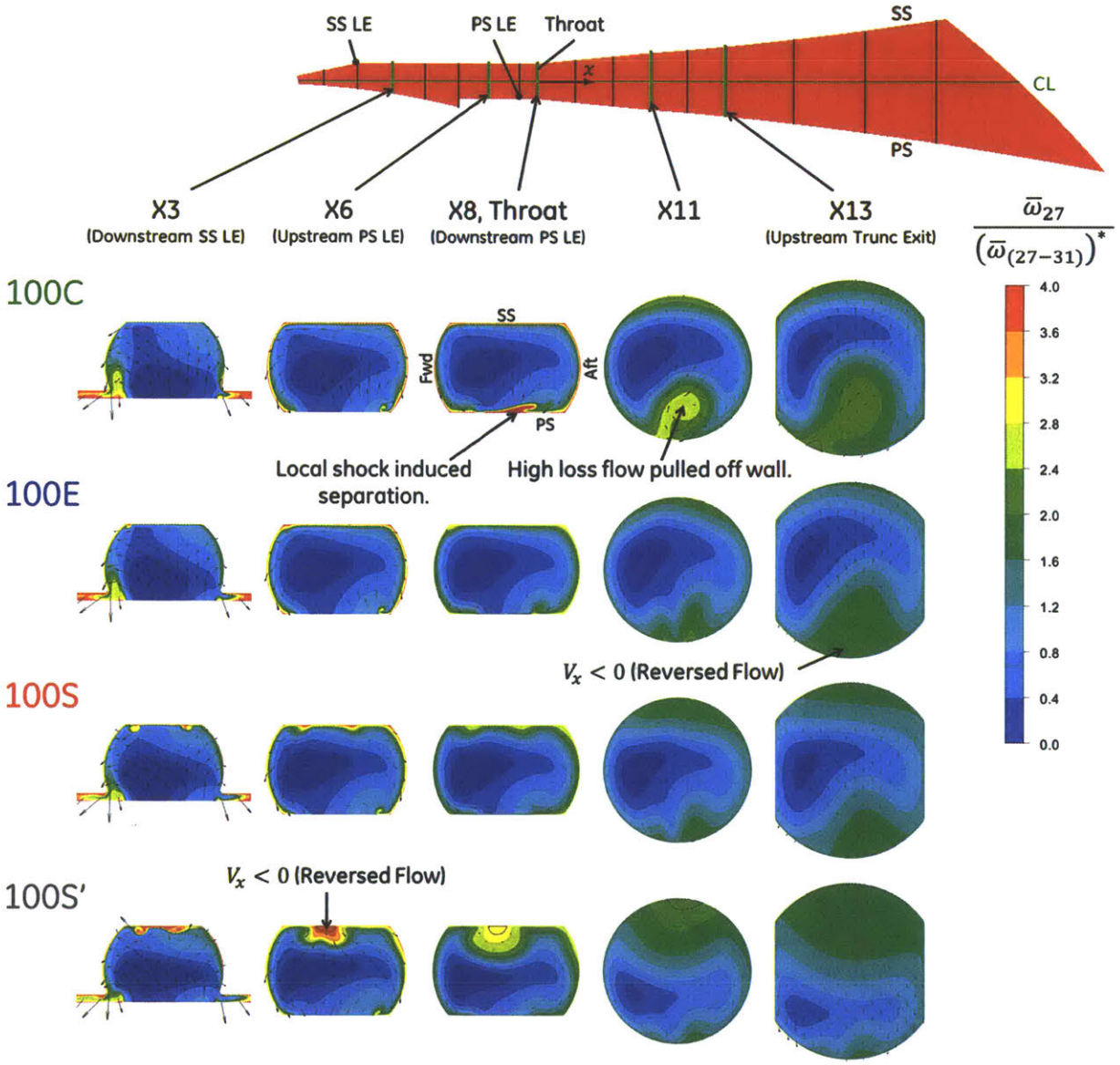


Figure 6.56: CFD calculated distributions of stagnation pressure loss coefficient at 100% $N_{c25}$ for baseline diffuser. Regions of high loss and resulting flow separation localized to area between vortices ($\boldsymbol{z} = \mathbf{0}$). As vortices switch from pressure to suction sides between 100S and 100S', so does high loss flow.

these loss distributions and resulting separation. It has already been shown that the loss incurred upstream of the diffuser leading edge is similarly dependent on flow angle. However, the localized pressure and suction side high loss regions are not present at the diffuser leading edge, and therefore must form downstream. This could be the result of loss generation, loss migration, or a combination of both within the diffuser.

Notice that the distribution of loss in the diffuser corresponds with the locations of the vortices shown in Figure 6.36. First, the regions of high loss are present on the same side of the diffuser passage as the incidence vortices. More significantly, the regions of high loss are localized precisely between the counter-rotating incidence vortices. That is, the boundary layer is thicker between the vortices than it is near the forward or aft endwalls. This is strong evidence that the vortices and loss distributions are related.

As discussed in Section 5.2, secondary flows influence the loss and nonuniformity through crossflow migration of high and low loss regions of flow. This can either diminish mixing via accumulation or clumping of the high loss fluid, or it can enhance mixing via stretching and increased surface area of the shear layer. One can interpret this shear layer stretching or compression in the transverse direction as a 3D extension of a traditional 2D boundary layer growth model. This is illustrated in Figure 6.57.

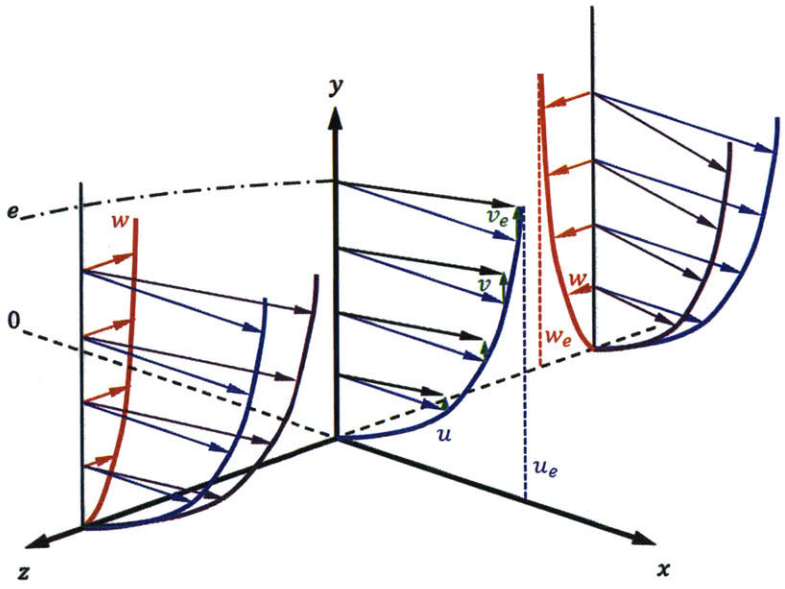


Figure 6.57: 3D effect of transverse velocity gradient, $\partial w/\partial z$, on boundary layer growth rate. Main flow velocity and direction represented by $u$ and $x$ respectively, wall normal velocity and direction represented by $v$ and $y$ respectively, and transverse velocity and direction represented by $w$ and $z$ respectively. Wall position represented by $0$, and boundary layer edge represented by $e$. Illustration shows $\partial w/\partial z<0$, which increases boundary layer growth rate relative to pure 2D boundary layer due to accumulation of high loss flow from sides.

Whereas the growth rate of a simplified 2D boundary layer is determined by its own thickness, shape, and edge velocity, this 3D boundary layer growth rate also depends on the rate at which nonuniformity enters or leaves the boundary layer control volume from the sides. This means there is a net 3D effect if the transverse velocity component has a non-zero gradient in the transverse direction, denoted $\partial w/\partial z$ in the local boundary layer coordinate system. If $\partial w/\partial z < 0$, the boundary layer grows at a faster rate than a 2D boundary layer, and mixing effectiveness is reduced. On the other hand, if $\partial w/\partial z > 0$, the boundary layer will not grow as fast as a 2D boundary layer, and mixing effectiveness is enhanced.

Both compression and stretching effects are present in the diffuser passage of interest. For a basic conical diffuser with no secondary flows, $\partial w/\partial z > 0$ everywhere in the boundary layer. The boundary layer is stretched in the transverse direction simply because the perimeter of the diffuser passage increases along its length (an analogous effect is found in external flow over a body of revolution). This effect is complicated by the more complex geometry of the diffusers of interest, but in general it is still present especially at the forward and aft endwalls. However, for this diffuser, the contribution of the vortices to the transverse velocity gradient is much stronger than the effect of the increasing perimeter. Figure 6.58 shows the velocity gradient in the z direction, $\partial V_z/\partial z$, which is transverse to the pressure and suction side boundary layers. The secondary flow field adds both positive and negative components to the shear layer transverse velocity gradient. This depends on the relative locations of each point in the shear layer to the vortices, and will be characterized in more detail in the following sections. In general, it is clear that the boundary layer is compressed in the transverse direction ($\partial V_z/\partial z < 0$) between the counter-rotating vortices. The largest transverse velocity gradients are near the vortices, and these correspond to the regions of the flow which separate first.

Another effect of the vortices is that the wall normal velocity gradient is large in between the vortices ($\partial V_y/\partial y$ in the diffuser coordinate system, or $\partial v/\partial y$ in the boundary layer local coordinate system). This is an additional 3D effect, which tends to stretch the shear layer in the wall normal direction. In other words, the secondary flows can pull weak flow off the wall into the main flow stream, enhancing mixing and reducing the extent of the separation. This effect is observed on the diffuser pressure side when the pressure side incidence vortices become strong. In fact, this effect is found to correspond to the piecewise shift between regions 1 and 2 of the diffuser pressure recovery trend shown in Figure 6.48.

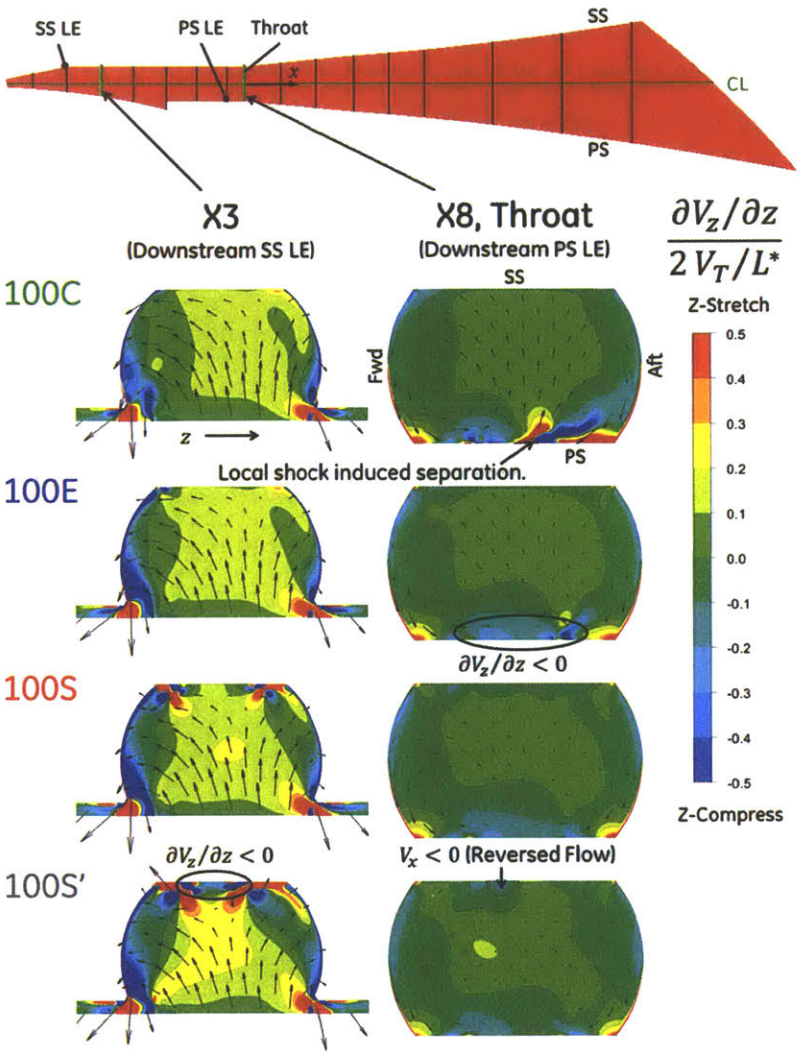


Figure 6.58: Transverse velocity gradient in z-direction ($\partial V_z/\partial z$). Applicable to diffuser pressure and suction side boundary layers. Boundary layer stretching indicated by $\partial V_z/\partial z>0$ and compression indicated by $\partial V_z/\partial z<0$. Boundary layer compression occurs between vortices

Figure 6.59 shows the entropy generation rates on various crossflow planes throughout the baseline diffuser. This indicates that the shear layers bounding the high loss regions are associated with higher loss generation rates. Of course, this loss generation also contributes to the observed loss distribution and resulting separation. However, the high loss generation is hypothesized to primarily be the result of the loss accumulation, not the initial cause of it. In other words, the region that has accumulated more weak flow must experience greater mixing losses. If the weak flow migrates differently as a result of the vortices moving between the pressure and suction sides, the regions of high loss generation will move as well. This hypothesis will be confirmed in the following sections.

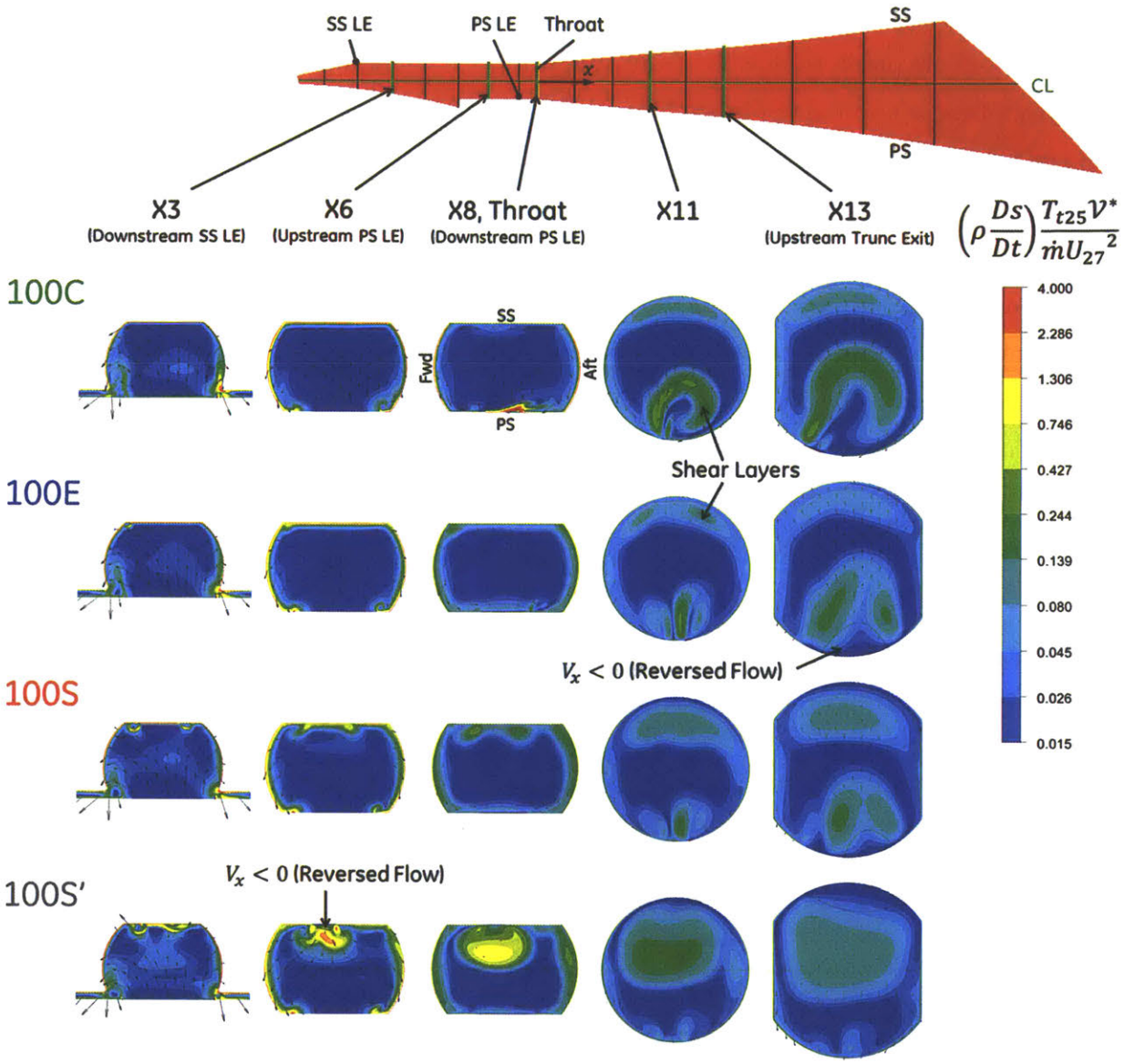


Figure 6.59: CFD calculated distributions of entropy generation rate at 100% $N_{c25}$ for baseline diffuser. High loss generation rates correspond to high loss regions. Hypothesize that this is result of loss accumulation; not cause of it.

### 6.6.6.2 Estimation of Transverse Velocity Gradient

To further understand the factors influencing the accumulation of weak flow between the counter-rotating vortices, and to evaluate the relative importance of the incidence and background vortices, a simplified model is implemented to estimate the strength of the transverse velocity gradient from the vorticity distribution.

For the purposes of this estimate, the secondary flow field is assumed to be two dimensional, such that the crossflow velocity distribution can be completely determined from the

vorticity distribution on that plane. This assumption introduces the least error when applied to a crossflow plane that is far from the diffuser leading edge. As a result, this estimation procedure is applied to planes X3 and X8, which are downstream of the leading edge on the suction and pressure sides respectively. The flow field associated with a point vortex is given by Equation 6.4, where Γ is the circulation of the vortex, $r$ is the distance to the vortex, and $V_\theta$ is the component of velocity circulating around the vortex as shown in Figure 6.60. Taking the velocity component in the $z$ direction and differentiating with respect to $z$ yields Equation 6.5. The velocity fields and gradients from multiple vortices can be superimposed. This is given by Equation 6.6 for a generalized vorticity distribution, where the circulation of each infinitesimal point is equal to $\omega_x dA$.

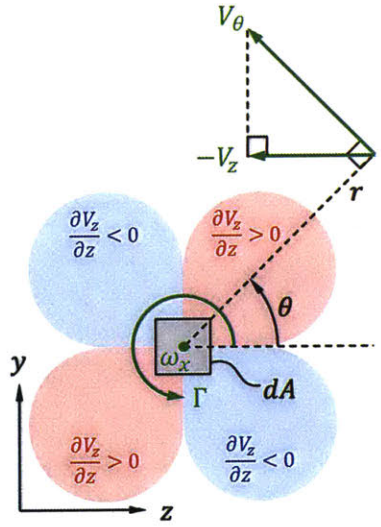


Figure 6.60: Velocity and velocity gradient fields associated with infinitesimal 2D vortex of strength $\Gamma=\omega_x dA$.

$$V_\theta = \frac{\Gamma}{2\pi r} \qquad \text{Equation 6.4}$$

$$\frac{\partial V_z}{\partial z} = \frac{\Gamma \sin(2\theta)}{2\pi r^2} \qquad \text{Equation 6.5}$$

$$\frac{\partial V_z}{\partial z} = \int \frac{\omega_x (y - y')(z - z')}{\pi[(y - y')^2 + (z - z')^2]^2} dy' dz' \qquad \text{Equation 6.6}$$

From Equation 6.5, one can see that there are three factors that determine the influence of a vortex on the crossflow velocity gradient: the strength of the vortex, the proximity of the vortex to the point of interest, and the angle of the vector between the vortex and the point of interest. The angles which maximize the impact of the vortex are located at 45 deg, 135 deg, 225 deg, and 315 deg relative to the $z$ axis, as indicated in Figure 6.60. Not sur-

prisingly, these are the approximate angles between the vortices and regions of weak flow on the diffuser pressure and suction sides.

To account for the zero velocity boundary condition at the diffuser wall, a few assumptions are made. First, the diffuser passage is approximated as a rectangle. It is then possible to devise a physical representation of the flow field with periodic boundary conditions by replacing the diffuser walls with planes of symmetry, as shown in Figure 6.61. This satisfies the original wall boundary condition since there can be no flow through a plane of symmetry. One can recognize that the flow field is impacted not only by the vortices observed in true diffuser flow, but also by the image vortices necessary to satisfy the boundary conditions. Since the impact of a vortex on the velocity gradient decays with $1/r^2$, and because only the diffuser pressure and suction sides are of interest, only the image vortices across the pressure and suction side symmetry planes are included respectively in these estimations. This essentially doubles the impact of each vortex. The induced boundary layer vorticity is neglected for this estimation, as this vorticity only exists to satisfy the no slip condition at the wall. While it certainly affects the flow field locally in the boundary layer, one can infer that the farfield impact is small since the induced vorticity is so near to its image.

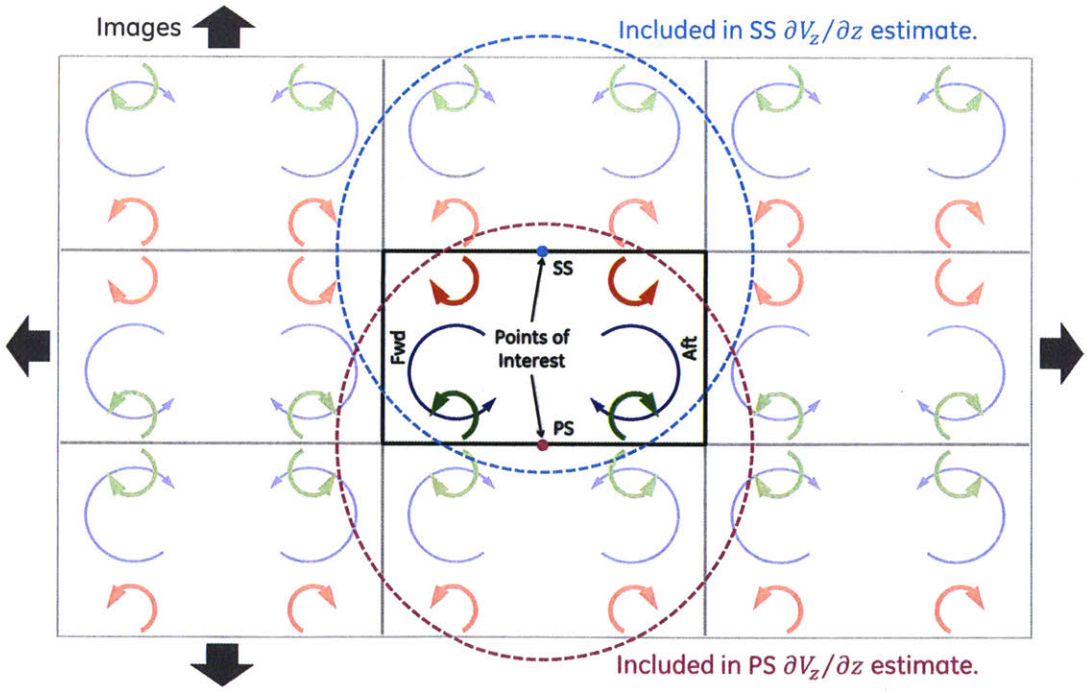


Figure 6.61: Representation of diffuser secondary flow field as superposition of vortex and image vortex 2D velocity fields. Transverse velocity gradients estimated using this approach.

By applying Equation 6.6 to the CFD calculated vortex regions (see Section 6.5.7.1) and corresponding image vortices, the contribution of each vortex to the transverse velocity gradient is estimated. Figure 6.62 shows these estimates for the diffuser suction side at the X3 cut plane and the diffuser pressure side at the X8 cut plane, both at the diffuser mid-plane ($z = 0$). The total estimated velocity gradient is also shown, as well as the maximum value that is sampled from the CFD solutions along the mid-plane. One can see that the total estimated velocity gradient closely matches the direct CFD measurements, both in terms of the trends and the magnitudes. This is an assurance that the estimation procedure is valid, and that it is predominantly the vortices—not the complex diffuser passage geometry—that gives rise to the large velocity gradients between the vortices.

The trends in the transverse velocity gradient generally follow the vortex circulation trends shown in Figure 6.40. There is a strong negative transverse velocity gradient just downstream of the leading edge at low flow angles on the diffuser pressure side, and at high flow angles on the diffuser suction side. This supports the hypothesis that the vortices contribute to the accumulation of high loss flow between them, and it establishes a causal link between the flow angle and the separation side and extent. Note that the significance of this effect relative to other boundary layer growth effects still has yet to be established in Section 6.6.6.3.

Figure 6.62 also yields insight about the relative importance of the different vortex sources. Although the incidence vortices and background vortices have comparable strength, the incidence vortices contribute more to the transverse velocity gradient because of their proximity to the pressure and suction side points of interest. By comparison, the influence of the background vortices varies little over the operating range. The background vortices actually contribute a positive component to the transverse velocity gradient on the diffuser suction side, improving mixing by stretching the boundary layer. However, this is overwhelmed by the opposite effect of the suction side incidence vortices at high flow angles. The trends observed at 80% $N_{c25}$ and 100% $N_{c25}$ are similar, as are the trends observed for the baseline and truncated diffusers.

Upon comparing Figure 6.40 with Figure 6.62, one can see that the impact of the incidence vortices on the transverse velocity gradient increases more rapidly than the vortex strength itself at extreme high and low flow angles. This is because the velocity field induced by the image vortices has the compounding effect of moving the two counter-rotating

vortices closer toward the diffuser mid plane as the flow progresses downstream of the diffuser leading edge. Note the differences in axis limits between the X3 and X8 cut planes, which suggest that the incidence vortices are more influential on the pressure side than the suction side. However, CFD simulations attempted at higher flow angles suggest this is not true, though these simulations did not converge due to stall.

Another observation which must be explained is the nonmonotonic trend in velocity gradient observed at low flow angles in Figure 6.62. At 80% $N_{c25}$ and a flow angle of -2.5 deg relative to the reference value, the pressure side mid plane velocity gradient vanishes at the X8 cut plane. This is due to a local shock induced pressure side separation which begins near the X8 cut plane (see Figure 6.8 and Figure 6.10). Because the flow must pass around the top and sides of the 3D separation bubble, the divergence of the velocity field on the crossflow plane must be positive at the start of the separation bubble (see Figure 6.58). Physically, this is enabled by a local increase in static pressure at the start of the separation bubble, or alternatively by the introduction of $y$ and $z$ vorticity components into the main flow which influence the velocity field in the crossflow plane. The same effect is observed at 100% $N_{c25}$, but at a higher flow angle of -2 deg, relative to the reference value (this is not obvious, since lower flow angles are not simulated at 100% $N_{c25}$). The increase in flow angle at which this shock induced separation occurs is due to the higher diffuser inlet Mach numbers associated with the higher corrected speed.

Note that the diffuser mid plane is not necessarily the location where the maximum boundary layer compression or resulting separation occurs for each operating point, and in fact the compression rate is quite sensitive to the $z$ position. However, this fixed plane is chosen for simplicity in sampling the CFD solution. The general conclusions from this study are not affected by this decision.

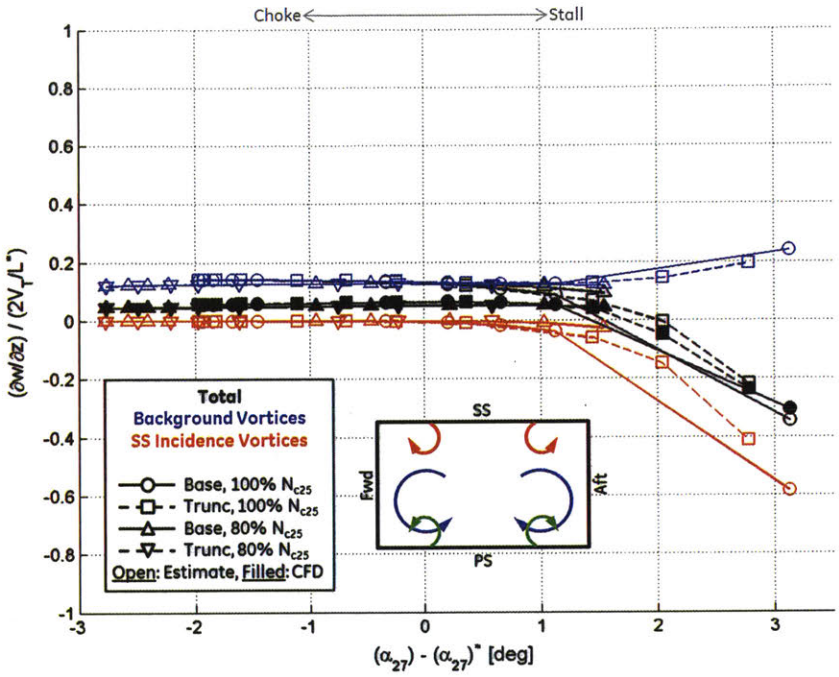


(a) X3 cut plane (downstream of suction side leading edge).

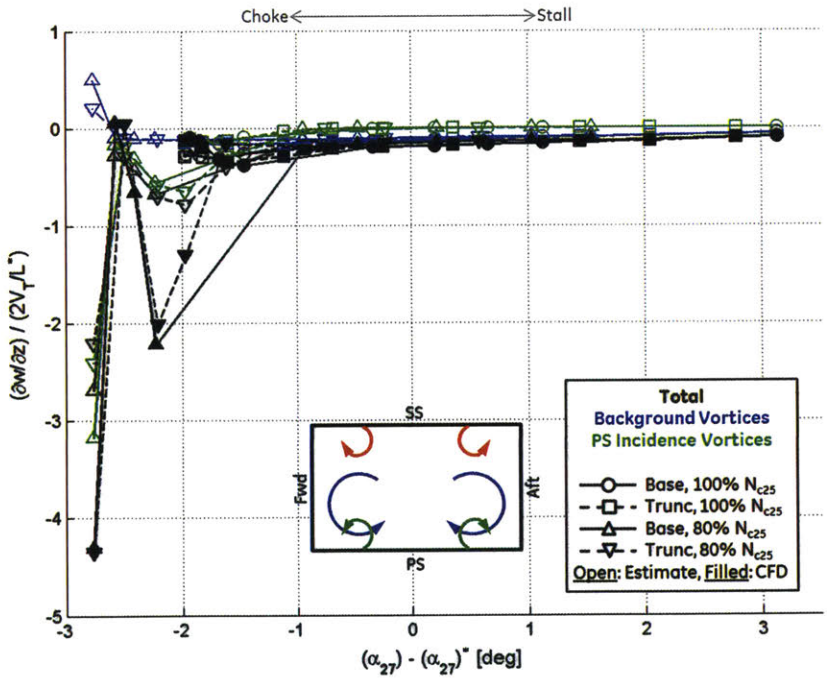


(b) X8 cut plane (downstream of pressure side leading edge).

Figure 6.62: Measured and estimated strength of transverse velocity gradient at diffuser mid plane versus impeller exit flow angle. Symbols and line styles denote diffuser configuration, compressor speed, and calculation assumptions, while colors denote different vortex sources. Suction side experiences negative transverse velocity gradient at high flow angles, pressure side at low flow angles. Dominant contribution due to incidence vortices.

#### 6.6.6.3 Effect of Loss Accumulation on Boundary Layer Growth and Pressure Recovery

To show that the counter-rotating vortices significantly influence the boundary layer growth rate and eventual separation observed between the vortices, it must be shown that the effect of loss accumulation, or transverse boundary layer compression, is significant relative to other boundary layer growth effects.

Wilkosz conducted a CFD study to evaluate the impact of the vortices on the boundary layer growth within the baseline diffuser [11]. In his simulations, Wilkosz directly imposed boundary conditions at the diffuser throat, including various pressure and suction side boundary layer thicknesses, as well as variations on the strength of the diffuser passage vortices. Wilkosz showed that the secondary flows contributed significantly to the diffuser pressure side passage separation. He hypothesized that this is due to the transport of the weak forward and aftward endwall flow onto the diffuser pressure side. Furthermore, Wilkosz showed that in the absence of these vortices, the separation instead transitions to the suction side due to the thicker suction side boundary layer that forms in the inlet.

An alternative approach is taken here to yield some additional insight into the particular effect of the vortices. A two equation 2D integral boundary layer model was proposed by Drela and Giles [20]. This model utilizes equations for the momentum thickness and kinetic energy thickness growth rates derived from integral mass, momentum, and energy conservation equations. Re-deriving these equations with incorporation of the 3D effect described in Section 6.6.6.2 yields Equation 6.7 and Equation 6.8. Subtracting Equation 6.7 from Equation 6.8 yields the kinetic energy shape factor growth rate, Equation 6.9. These equations are presented in the local boundary layer coordinate system. The terms that represent the flux of throughflow nonuniformity in the throughflow direction, denoted by subscript $x$, are captured in the conventional 2D integral boundary layer model described by Drela and Giles. The terms that represent the flux of throughflow nonuniformity in the boundary layer transverse direction, denoted by subscript $z$, are the result of the secondary flow field. The transverse gradients of terms will be nonzero if $\partial w/\partial z$ is nonzero, even if all other flow properties are uniform. Essentially, the 3D effect of the vortices can be treated as an additional source term in the 2D integral boundary layer equations. These terms are defined in the nomenclature portion of this thesis. Note that these equations neglect variations in the density and throughflow velocity in the $z$ direction.

$$\frac{x}{\theta_x}\frac{\partial \theta_x}{\partial x} = -\frac{x}{\theta_x}\frac{\partial \theta_z}{\partial z} - \frac{x}{u_e}\frac{\partial u_e}{\partial x}(2 + H_x - M_e^2) + \frac{x}{\theta_x}\frac{C_f}{2} \qquad \text{Equation 6.7}$$

$$\frac{x}{\theta_x^*}\frac{\partial \theta_x^*}{\partial x} = -\frac{x}{\theta_x^*}\frac{\partial \theta_z^*}{\partial z} - \frac{x}{u_e}\frac{\partial u_e}{\partial x}\left(3 + 2\frac{H_x^{**}}{H_x^*} - M_e^2\right) + \frac{x}{\theta_x^*}2C_D \qquad \text{Equation 6.8}$$

$$\frac{x}{H_x^*}\frac{\partial H_x^*}{\partial x} = \frac{x}{\theta_x}\frac{\partial \theta_z}{\partial z} - \frac{x}{\theta_x^*}\frac{\partial \theta_z^*}{\partial z} - \frac{x}{u_e}\frac{\partial u_e}{\partial x}\left(1 + 2\frac{H_x^{**}}{H_x^*} - H_x\right) + \frac{x}{\theta_x}\left(\frac{2C_D}{H_x^*} - \frac{C_f}{2}\right) \qquad \text{Equation 6.9}$$

To weigh the significance of the vortex source term relative to the other boundary layer growth terms, the momentum and kinetic energy thickness growth rates and vortex source terms are sampled from the 100E and 100S' CFD solutions for the baseline diffuser. The sampling is performed on the diffuser mid plane ($z = 0$) at various positions along the diffuser length shown in Figure 2.19. To calculate the integral boundary layer parameters, the boundary layer edge is defined as in Figure 6.63 for 100E and in Figure 6.64 for 100S'.

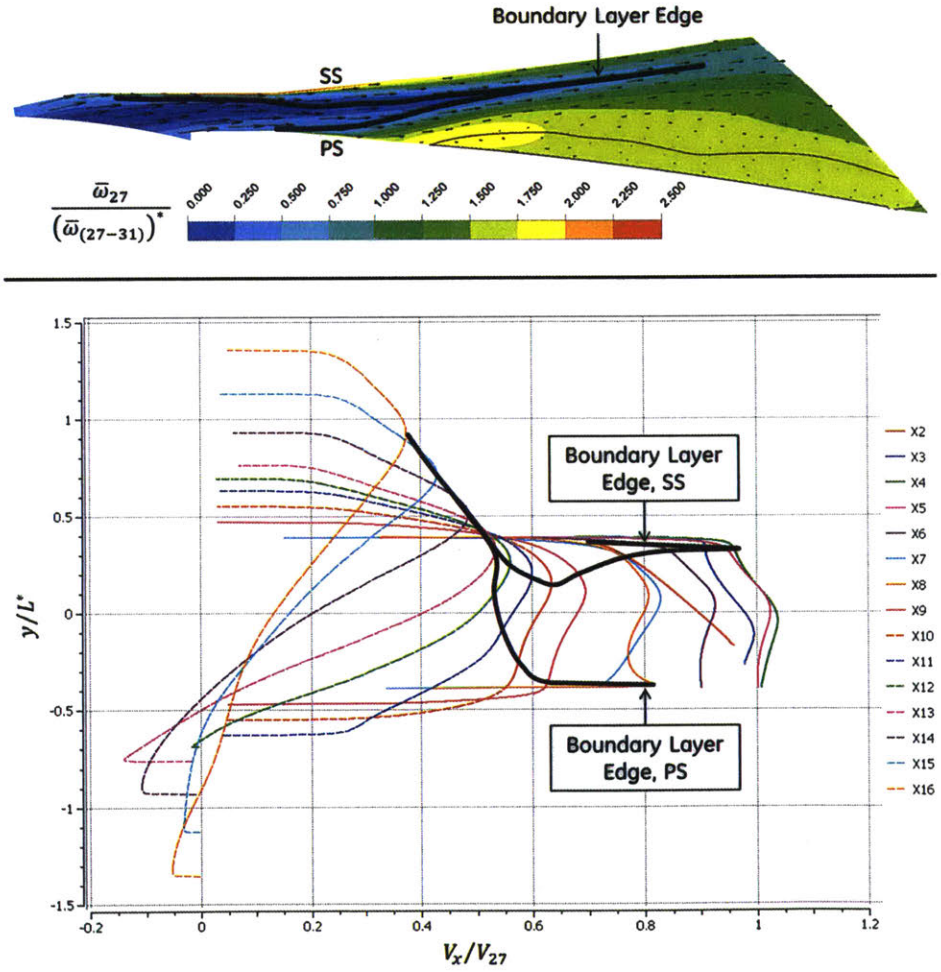


Figure 6.63: Definition of 100E boundary layer edge on baseline diffuser mid plane, showing relation with respect to diffuser geometry, stagnation pressure loss distribution, and velocity profiles. Definition used to extract boundary layer properties from CFD calculation.

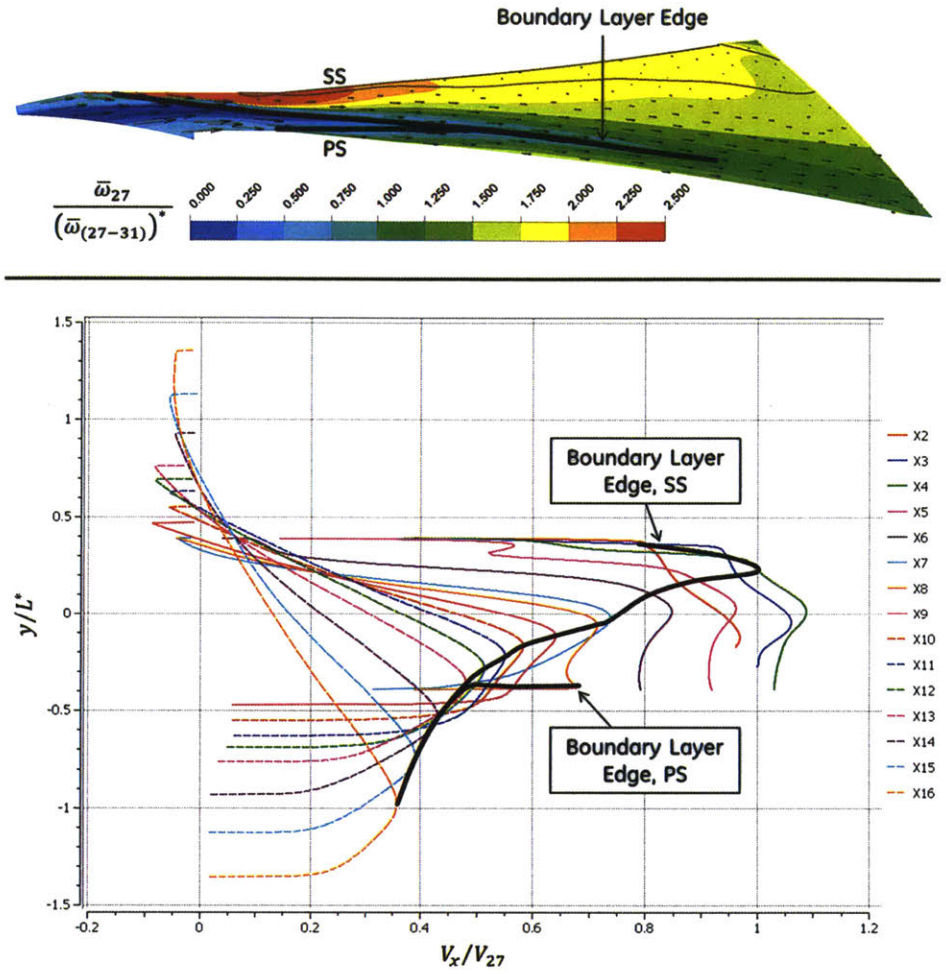


Figure 6.64: Definition of 100S' boundary layer edge on baseline diffuser mid plane, showing relation with respect to diffuser geometry, stagnation pressure loss distribution, and velocity profiles. Definition used to extract boundary layer properties from CFD calculation.

This boundary layer edge definition is not obvious for internal flows, since nonuniformities unrelated to the diffuser boundary layer already exist at the diffuser inlet. However, upon examining the pitchwise profiles of diffuser throughflow velocity, distinct boundary layer edges are observed to grow from the diffuser suction and pressure side leading edges.

The CFD calculated boundary layer growth rates and the contributions from the vortex source terms are plotted in Figure 6.65. One can see that the vortex source terms vary between positive and negative values. The negative values generally correspond to locations along the diffuser where flow separation begins or grows. As a result, the flow must diverge around the sides of the separation bubble, a 3D effect described in Section 6.6.6.2. On average, however, the diffuser pressure side boundary layer growth rate generally sees a positive contribution from the vortex source terms, with the source term being greater at

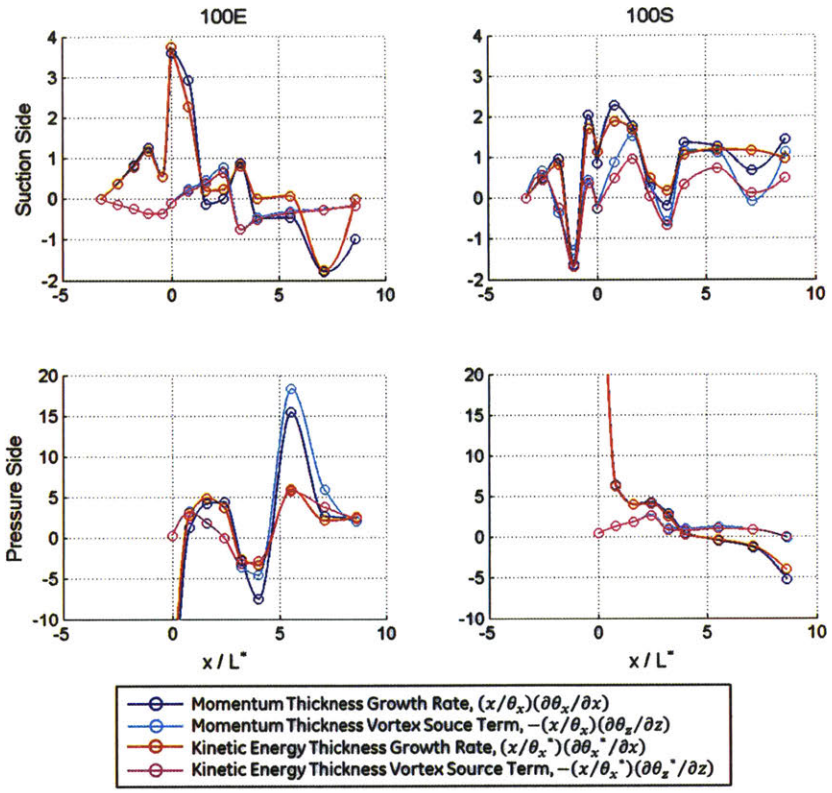


Figure 6.65: CFD calculated boundary layer growth rates and vortex source terms versus throughflow position for baseline diffuser. Growth rate closely correlates with vortex source terms on diffuser pressure side at 100E, and diffuser suction side at 100S'.

100E than at 100S'. On the suction side, the vortex source term is generally negative at 100E, due to the background vortices, and generally positive at 100S'. One can see that the overall boundary layer growth rates closely follows the trends and magnitudes of this vortex source terms on the pressure side at 100E and the suction side at 100S'. This confirms the hypothesis that the secondary flows contribute significantly to the boundary layer growth. Also notice from Equation 6.9 that the difference between the kinetic energy and momentum thickness vortex source terms is what influences the kinetic energy shape factor growth rate. In general, Figure 6.65 shows that these two source terms closely follow one another. However, the momentum thickness vortex source term is greater than the energy thickness vortex source term on the pressure side at 100E and the suction side at 100S'. This difference results in a reduction in kinetic energy shape factor, which tends to drive an attached boundary layer towards separation.

Another way to evaluate the importance of the secondary flows is to solve the integral boundary layer equations on the diffuser pressure and suction sides with and without the

vortex source term. To do this, Equation 6.7 and Equation 6.9 are numerically integrated along the length of the diffuser using a forward Euler integration scheme. Closure correlations proposed by Drela and Giles for the 2D integral boundary layer model are utilized for this modified model. These closure correlations define the kinetic energy shape factor, density shape factor, skin friction coefficient, and dissipation coefficient as functions of Mach number, Reynolds number, and shape factor [20]. The boundary layers are assumed to be fully turbulent and in equilibrium.

The diffuser inlet and passage components are each modeled separately. The diffuser inlet suction side boundary layer model begins at the X3 cut plane where the Reynolds number, Mach number, boundary layer thickness, and shape factor are specified. These are derived from the CFD calculations. The CFD calculated external velocity distribution is also specified along the length of the inlet. The disadvantage of specifying the velocity distribution is that the static pressure distribution is also specified; it cannot react to the boundary layer blockage. Another implication of specifying velocity is that the boundary layer cannot be modeled once it is separated.

Downstream of the throat, the external velocity distribution is not specified. Instead, the passage 1D area and width distributions are specified, and effective area is determined using blockages associated with the pressure and suction side boundary layer displacement thicknesses. In this way, the velocity distribution of the inviscid core is solved together with the pressure and suction side boundary layer parameters at each discrete location along the passage length. The boundary layers are assumed to uniformly span the entire width of the diffuser, and the forward and aftward endwall boundary layer thicknesses are neglected from the blockage calculation. To start the suction side boundary layer model, the results of the inlet suction side boundary layer model are utilized except where the inlet boundary layer separates. In this case, boundary layer displacement thicknesses and shape factors derived from the CFD results are specified. CFD derived starting conditions are also specified for the pressure side boundary layer.

This modified integral boundary layer model is used to simulate the 100E and 100S' operating points of the baseline diffuser. This is performed both with and without the CFD calculated vortex source terms shown in Figure 6.65. The resulting boundary layer displacement thicknesses and shape factors are shown in Figure 6.66 and Figure 6.67 respectively. The CFD calculated values are also shown for reference. With the vortex source

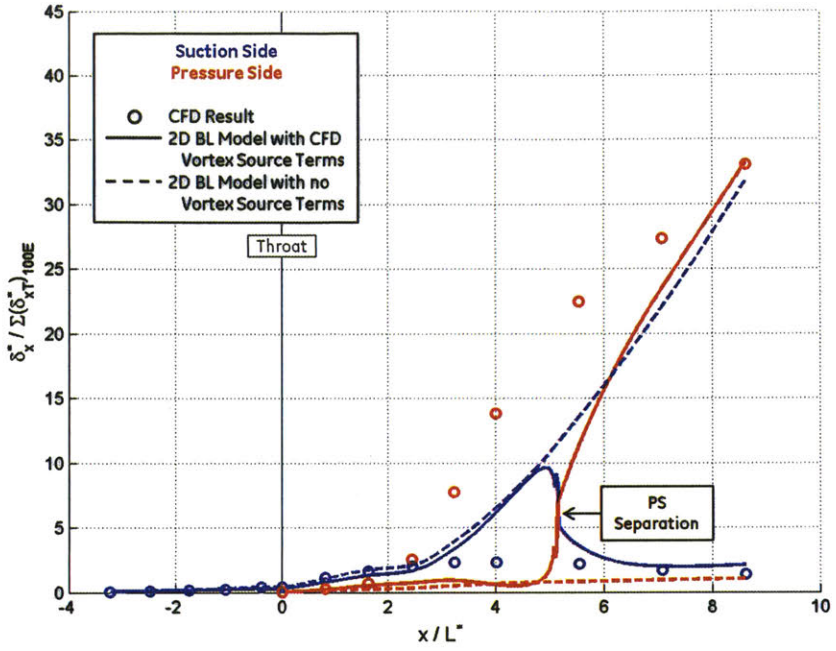


(a) 100E

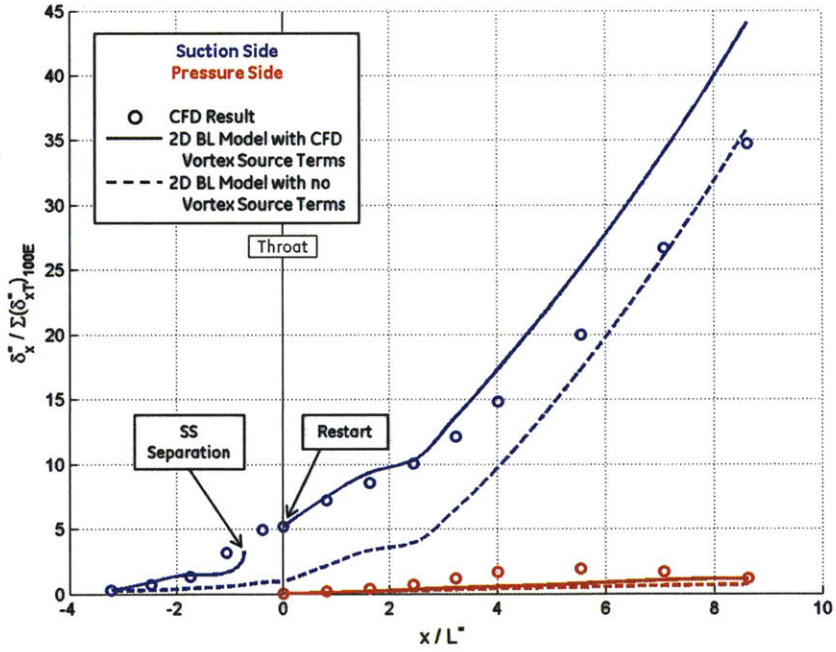


(b) 100S'

Figure 6.66: Boundary layer displacement thickness versus throughflow position for baseline diffuser. Includes CFD calculation as well as 2D boundary layer model calculations with and without vortex source terms. Excluding vortex source terms reduces displacement thicknesses. In addition, it causes the separation side to change at 100E, and it delays separation at 100S'.

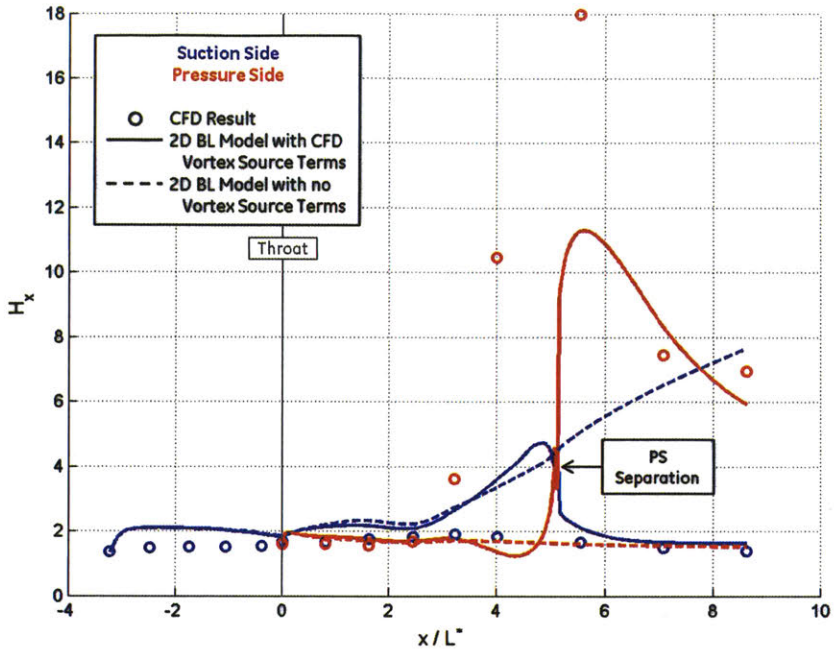


(a) 100E

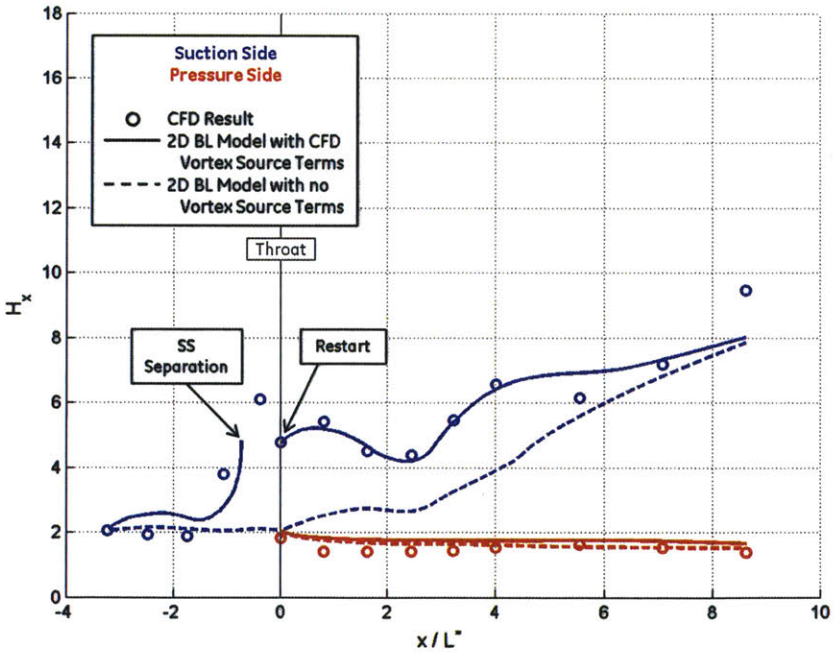


(b) 100S'

Figure 6.67: Boundary layer shape factor versus throughflow position for baseline diffuser. Includes CFD calculation as well as 2D boundary layer model calculations with and without vortex source terms. Excluding vortex source terms causes the separation side to change at 100E, and it delays separation at 100S'.

terms modeled, the simple boundary layer model correctly captures many of the boundary layer characteristics calculated by the CFD at both 100E and 100S'. Most notably, the separation side is captured. The approximate trends and magnitudes of the boundary layer thicknesses and shape factors are also captured. However, there are also some notable differences between the simple boundary layer model and the CFD. The pressure side separation location is delayed by the simple model at 100E, and in fact a small suction side separation and reattachment is observed immediately upstream. Also, the suction side boundary layer thickness is overestimated by the simple model at 100S'.

The differences between the CFD and integral boundary layer model calculations are small in comparison to the effect of the vortex source term. First, notice that at 100E with the vortices modeled, the boundary layer trends closely follow the trends in the vortex source term. This alone suggests that the vortices are important. Further evidence is provided upon removal of the vortex source term, as the diffuser separates on the suction side rather than the pressure side. At 100S', the boundary layer still separates on the suction side without the vortices modeled, but it is much thinner. These results are consistent with the study performed by Wilkosz [11].

The effects of the vortices on the diffuser mass blockage and static pressure recovery coefficient are shown in Figure 6.68 and Figure 6.69 respectively. Note that mass flow blockage is calculated using the potential core average flow properties rather than availability average properties as are used elsewhere in this thesis. Not surprisingly, the blockages throughout the diffuser passage are smaller without the vortices, significantly so for the 100S' operating point. As a result, the static pressure recovery coefficients are greater without vortices by 11% at 100E (23% relative to CFD) and 57% at 100S' (25% relative to CFD). Of course, there is much uncertainty associated with these numbers due to the simplicity of the integral boundary layer model and the clear differences in the results with respect to the CFD. Furthermore, the results are sensitive to changes in the vortex source terms and inlet conditions, which are measured from the CFD solutions with some subjectivity as previously explained. Nonetheless, the underlying physics captured by the modified integral boundary layer model give it enough credibility to assert that the vortices do have a significant impact on the boundary layer growth rate, the separation side (pressure vs. suction side), and ultimately the pressure rise capability. This is also consistent with the study performed by Wilkosz [11].

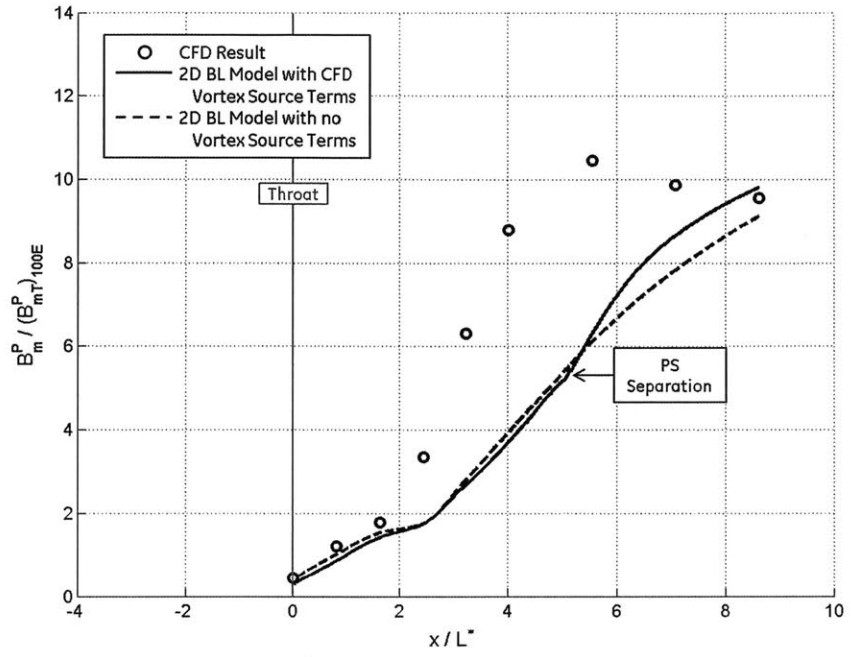


(a) 100E

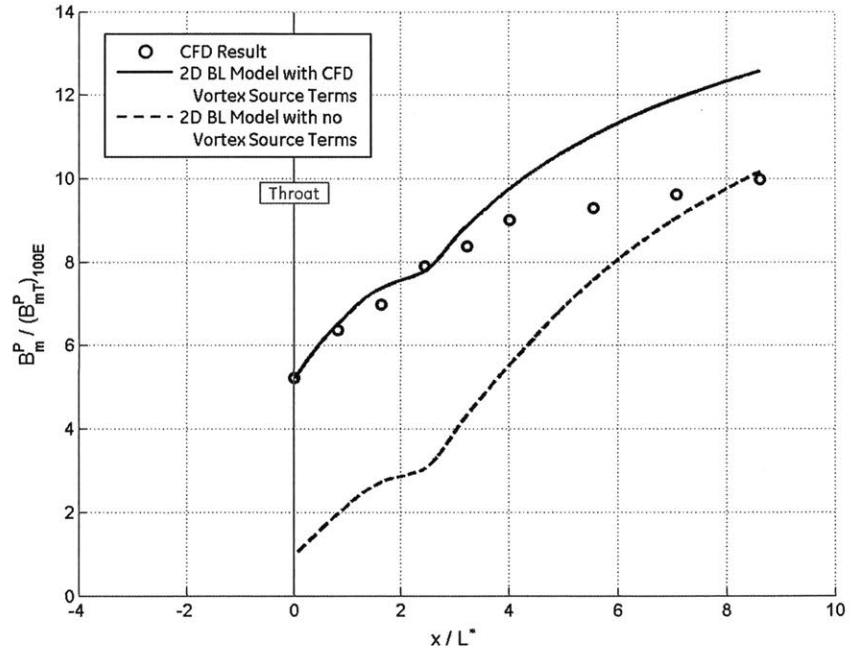


(b) 100S'

Figure 6.68: Mass blockage based on potential core average properties versus throughflow position for baseline diffuser passage. Includes CFD calculation as well as 2D boundary layer model calculations with and without vortex source terms. Excluding vortex source terms reduces blockage.

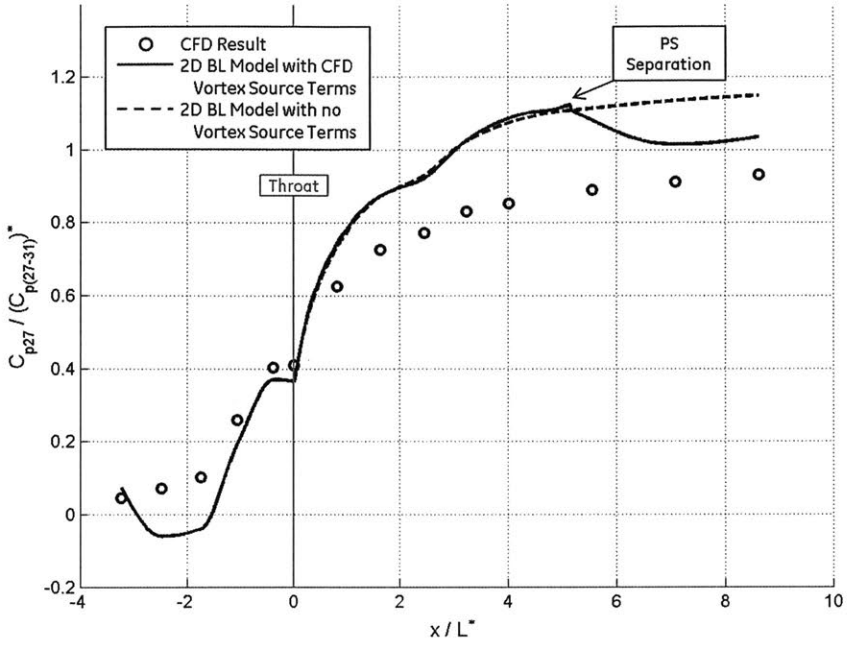


(a) 100E

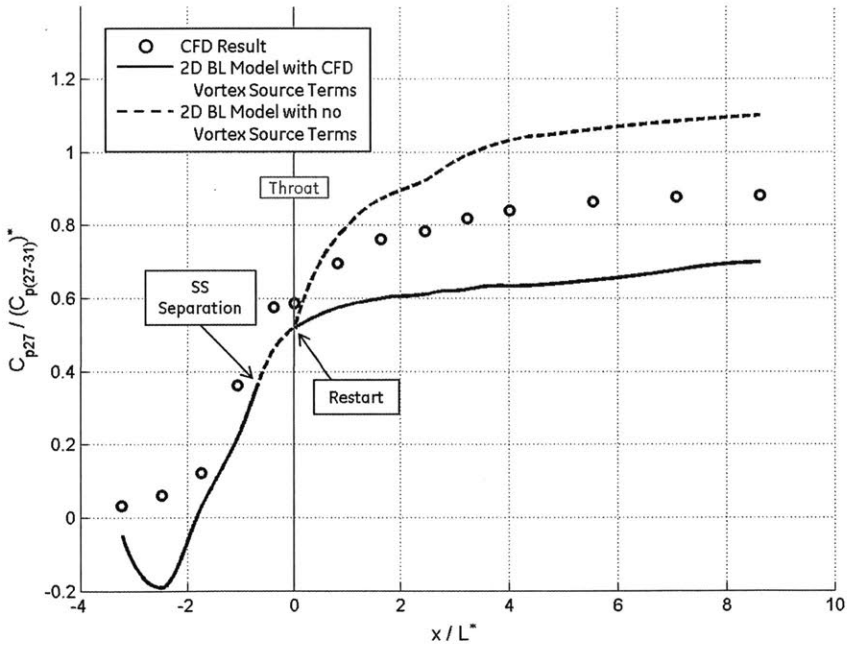


(b) 100S'

Figure 6.69: Static pressure recovery coefficient versus throughflow position for baseline diffuser. Includes CFD calculation as well as 2D boundary layer model calculations with and without vortex source terms. Excluding vortex source terms increases pressure recovery coefficient.

### 6.6.6.4 Scaling and Ordering for Boundary Layer Growth Mechanisms

The demonstrated impact of the vortices on the boundary layer raises interesting questions with respect to the truncated diffuser, or diffuser geometry in general. From Equation 6.7, one can infer that diffuser truncation has three effects: reducing the influences of the adverse pressure gradient, wall friction, and secondary flows. However, if one can better understand the effects of the diffuser geometry on each of these mechanisms, it might be possible to make design decisions that reduce the impact of one mechanism—the vortices for example—without sacrificing the diffuser's ideal pressure rise capability.

To weigh the importance of the vortices relative to the other mechanisms influencing the boundary layer growth, and to understand the effect of the diffuser geometry and inlet conditions, scales are estimated for the various terms in the integral boundary layer equations. For convenience, Equation 6.7 and Equation 6.9 are rewritten as Equation 6.10 and Equation 6.11 with the various terms labeled.

$$\frac{x}{\theta_x}\frac{\partial \theta_x}{\partial x} = \underbrace{\left[-\frac{x}{\theta_x}\frac{\partial \theta_z}{\partial z}\right]}_{Term\ 1} + \underbrace{\left[-\frac{x}{u_e}\frac{\partial u_e}{\partial x}(2 + H_x - M_e^2)\right]}_{Term\ 2} + \underbrace{\left[\frac{x}{\theta_x}\frac{C_f}{2}\right]}_{Term\ 3} \qquad \text{Equation 6.10}$$

$$\frac{x}{H_x^*}\frac{\partial H_x^*}{\partial x} = \underbrace{\left[\frac{x}{\theta_x}\frac{\partial \theta_z}{\partial z} - \frac{x}{\theta_x^*}\frac{\partial \theta_z^*}{\partial z}\right]}_{Term\ 4} + \underbrace{\left[-\frac{x}{u_e}\frac{\partial u_e}{\partial x}\left(1 + 2\frac{H_x^{**}}{H_x^*} - H_x\right)\right]}_{Term\ 5} + \underbrace{\left[\frac{x}{\theta_x}\left(\frac{2C_D}{H_x^*} - \frac{C_f}{2}\right)\right]}_{Term\ 6} \qquad \text{Equation 6.11}$$

Terms 1 and 4 of Equation 6.10 and Equation 6.11 are the vortex source terms, representing the compression or stretching of the boundary layer in the transverse direction. This $z$-flux momentum and kinetic energy thicknesses scale according to Equation 6.12 and Equation 6.13 respectively. In fact, if $w/u = w_e/u_e$ everywhere throughout the thickness of the boundary layer, these equations can be expressed as equalities. Using the scale $x \sim c$ and assuming the $x$-flux momentum thickness and throughflow velocity vary negligibly in the $z$ direction, Terms 1 and 4 scale according to Equation 6.14 and Equation 6.15 respectively. The familiar $\partial w/\partial z$ term from Sections 6.6.6.1 and 6.6.6.2 appears here. Note that Term 4 is the difference between two terms which scale similarly. Therefore, the difference must also scale in this manner. However, it must be recognized that if $w/u = w_e/u_e$ everywhere in the boundary layer, Term 4 will be identically equal to zero. In other words, the vortices can only contribute directly to a change in the shape factor if the profiles of transverse and throughflow velocity components differ from one another. This also means the sign of Term 4 cannot be known from these simplified scaling arguments.

$$\theta_z = \int_0^{y_e} \left(1 - \frac{u}{u_e}\right) \frac{\rho w}{(\rho u)_e} dy = \int_0^{y_e} \left(1 - \frac{u}{u_e}\right) \frac{\rho u}{(\rho u)_e} \frac{w}{u} dy \sim O\left[\frac{w_e}{u_e} \underbrace{\int_0^{y_e} \left(1 - \frac{u}{u_e}\right) \frac{\rho u}{(\rho u)_e} dy}_{\theta_x}\right] \quad \text{Equation 6.12}$$

$$= O\left[\frac{w_e}{u_e} \theta_x\right]$$

$$\theta_z^* = \int_0^{y_e} \left(1 - \frac{u^2}{u_e^2}\right) \frac{\rho w}{(\rho u)_e} dy$$

$$= \int_0^{y_e} \left(1 - \frac{u^2}{u_e^2}\right) \frac{\rho u}{(\rho u)_e} \frac{w}{u} dy \sim O\left[\frac{w_e}{u_e} \underbrace{\int_0^{y_e} \left(1 - \frac{u^2}{u_e^2}\right) \frac{\rho u}{(\rho u)_e} dy}_{\theta_x^*}\right] \quad \text{Equation 6.13}$$

$$= O\left[\frac{w_e}{u_e} \theta_x^*\right]$$

$$Term\ 1 = -\frac{x}{\theta_x} \frac{\partial \theta_z}{\partial z} \sim O\left[-\frac{c}{u_e} \frac{\partial w_e}{\partial z}\right] \quad \text{Equation 6.14}$$

$$|Term\ 4| = \left|\frac{x}{\theta_x} \frac{\partial \theta_z}{\partial z} - \frac{x}{\theta_x^*} \frac{\partial \theta_z^*}{\partial z}\right| \sim O\left[\frac{c}{u_e} \left|\frac{\partial w_e}{\partial z}\right|\right] \quad \text{Equation 6.15}$$

The scales for the vortex source terms can be further refined using the methodology provided in Section 6.6.6.2 for estimating the transverse velocity gradient, $\partial w_e / \partial z$. Equation 6.5 is rewritten below as Equation 6.16 with two small modifications. First, the velocity gradient attributable to a single vortex near the wall is doubled to account for the impact of its image vortex, which also contributes to the velocity field. Second, the number of vortices contributing the velocity gradient may be set by the factor $N_v$. For the diffusers of interest in this research, $N_v$ is equal to two since the counter-rotating vortices are close enough that the superposition of their transverse velocity gradients is significant in comparison to that of a single vortex. This happens when the distance between the vortices is on the order of twice the distance between the vortices and the wall. This is not the case immediately at the diffuser leading edge. However, as the vortices move downstream, the velocity field generated by the image vortices pushes them closer together. On the other hand, if the length or chord of the diffuser passage is much shorter relative to the vortex spacing, such as for an axial compressor stator, the vortices do not have the length to move within the regions of influence of one another and $N_v$ is equal to one.

$$\left|\frac{\partial w_e}{\partial z}\right| \approx \frac{N_v|\Gamma|\sin(2\theta)}{\pi r^2} \qquad \text{Equation 6.16}$$

The use of Equation 6.16 also requires additional estimates for the strengths and positions of the vortices. The strength of each vortex is assumed to scale according to Equation 6.17. This is based on circulation arguments similar to those employed in Section 6.5.7.3. To review, the origin of the vortices can be traced back to the boundary layer vorticity, and the circulation around a contour enclosing a portion of the boundary layer does not depend on the details of the boundary layer shape. Note that Equation 6.17 does not account for the diffuser incidence angle or the vortex source (background or incidence vortices), both of which are known to impact the vortex strength.

$$|\Gamma| \sim O\left[\frac{u_e A}{h}\right] \qquad \text{Equation 6.17}$$

As for the vortex positions, an angle of $\theta = -45$ deg is assumed between the vortices and the wall, capturing the approximate point along the wall where the vortices have the largest effect on transverse boundary layer compression as shown by Equation 6.18. This is also consistent with the relative positions of the vortices and the separation locations observed in the CFD results. The distance between the vortices and the diffuser wall is on the order of the boundary layer thickness. This is observed in the CFD results for both background and incidence vortices for the diffusers of interest, and it is explained by the fact that the vorticity originates in the boundary layer. The displacement thickness is selected as a measure of the boundary layer thickness, which can itself be further related to the mass blockage according to Equation 6.19.

$$\sin(2\theta) \sim O[1] \qquad \text{Equation 6.18}$$

$$r^2 \sim O[2\delta_x^{*2}] \sim O\left[\frac{1}{2}\left(\frac{B_m^P h}{(h^2/A' + 1)}\right)^2\right] \qquad \text{Equation 6.19}$$

Combining all of these effects, the scale governing the impact of the secondary flows on the boundary layer growth rate, terms 1 and 4, is given by Equation 6.20. Note that for an axial compressor blade row, the terms $h/c$ and $A/h^2$ can be related to the aspect ratio ($AR$), solidity ($\sigma$), and leading edge stagger angle ($\chi$) according to Equation 6.21 and Equation 6.22. Thus, the vortex source terms can also be written as Equation 6.23. Note that this scale is inversely proportional to the diffuser aspect ratio, such that the impact of the vortices can be great for low aspect ratios.

$$O[|Term\ 1|]\sim O[|Term\ 4|]\sim O\left[\frac{2N_v(h^2/A'+1)^2}{\pi(B_m^P)^2(h/c)(h^2/A')}\right] \quad \text{Equation 6.20}$$

$$AR=\frac{h}{c} \quad \text{Equation 6.21}$$

$$\lambda=\frac{h^2}{A'}=\frac{\sigma AR}{\cos\chi} \quad \text{Equation 6.22}$$

$$O[|Term\ 1|]\sim O[|Term\ 4|]\sim O\left[\frac{2N_v}{\pi}\frac{1}{(B_m^P)^2}\frac{1}{AR}\frac{(\lambda+1)^2}{\lambda}\right] \quad \text{Equation 6.23}$$

Terms 2 and 5 of Equation 6.10 and Equation 6.11 represent the effect of the pressure gradient on nonuniformity amplification. Assuming inviscid core flow and using the influence coefficients provided by Greitzer and Tan, the velocity variations can be related to area variations according to Equation 6.24 [17]. The scales $x\sim c$, $dx\sim c$, $A_e\sim A_{e2}$, and $dA_e\sim A_{e2}-A_{e1}$ are selected based on the diffuser geometry. Thus, the impacts of the pressure gradient on the boundary layer growth rates, terms 2 and 5, are governed according to the Equation 6.25 and Equation 6.26 scales respectively. Note that these scales are inversely related to the diffuser area ratio, though not proportionally. In this way, the effect of large area ratios is limited.

$$-\frac{du_e}{u_e}=\frac{dA_e}{A_e}\frac{1}{(1-M_e^2)} \quad \text{Equation 6.24}$$

$$Term\ 2=-\frac{x}{u_e}\frac{\partial u_e}{\partial x}(2+H_x-M_e^2)\sim O\left[\left(1-\frac{1}{A_{e2}/A_{e1}}\right)\left(\frac{2+H_x-M_e^2}{1-M_e^2}\right)\right] \quad \text{Equation 6.25}$$

$$Term\ 5=-\frac{x}{u_e}\frac{\partial u_e}{\partial x}\left(1+2\frac{H_x^{**}}{H_x^*}-H_x\right)\sim O\left[\left(1-\frac{1}{A_{e2}/A_{e1}}\right)\left(\frac{1+2\,H_x^{**}/H_x^*-H_x}{1-M_e^2}\right)\right] \quad \text{Equation 6.26}$$

Terms 3 and 6 of Equation 6.10 and Equation 6.11 represent the effects of wall friction and mixing within the boundary layer. These mechanisms will not be addressed here. For an aggressively diffusing flow, the wall friction contribution to the boundary layer growth rate is smaller than the pressure gradient contribution. In fact, for boundary layers that are nearly separated, the wall friction approaches zero. The effect of mixing or dissipation within the boundary layer has the effect of counteracting separation, or reducing the shape factor for an attached flow. This is an important consideration. However, the intention here is to investigate the mechanisms that contribute to separation.

The scales for the vortex and pressure gradient effects can now be compared to estimate the relative importance of these two mechanisms in contributing to the boundary layer growth. These are calculated for the baseline and truncated diffusers using $h=h_T$, $A=A_T$,

and $A_{e2}/A_{e1} = A^P_{e29}/A^P_{e28}$, and the results are tabulated in Table 6.1, normalized by the baseline diffuser values. These calculations are also performed for an axial compressor stator with geometry characterized by $AR = 2$, $\sigma = 1.5$, $\chi_{LE} = 45$, and $A_{e2}/A_{e1} = 1.2$. In addition, $N_v$ is assumed equal to one for the stator. The inlet conditions are assumed identical for each configuration. Therefore, because the scales are normalized to the baseline diffuser value, the quantities in Table 6.1 are purely functions of geometry. Only terms 1 and 2 are tabulated, since they have the same geometry dependence as terms 4 and 5 respectively.

| Physical Influence | Scale | Base Diffuser | Trunc Diffuser | Axial Stator |
|---|---|---|---|---|
| Secondary Flows | $O\left[\frac{Term\ 1}{(Term\ 1)_{Base}}\right]$ | 1 | 0.63 | 0.04 |
| Pressure Gradient | $O\left[\frac{Term\ 2}{(Term\ 2)_{Base}}\right]$ | 1 | 0.74 | 0.35 |
| $\frac{\text{Secondary Flows}}{\text{Pressure Gradient}}$ | $O\left[\left(\frac{Term\ 1}{(Term\ 1)_{Base}}\right)/\left(\frac{Term\ 2}{(Term\ 2)_{Base}}\right)\right]$ | 1 | 0.86 | 0.11 |

Table 6.1: Scales for vortex and pressure gradient impacts on boundary layer growth rate, normalized by baseline diffuser values. Relative influence of vortices decreases for truncated diffuser relative to baseline. Relative influence of vortices for axial compressor is order of magnitude lower than for diffusers.

The results of Table 6.1 may be used to compare the baseline diffuser, truncated diffuser, and axial compressor stator. Due to increased aspect ratio and reduced 1D area ratio, the impacts of the vortices (term 1) and pressure gradient (term 2) on the boundary layer growth both decrease for the truncated diffuser relative to the baseline diffuser, and they further decrease for the axial stator. Furthermore, the relative influences of the vortices (term 1/term 2) decrease for the truncated diffuser and the stator. This is because the vortex influence has an inversely proportional dependence on the diffuser length or chord (Equation 6.20), while the pressure gradient influence has a weak dependence on changes in 1D area ratio if the area ratio is already high (Equation 6.25 and Equation 6.26). This explains why the truncated diffuser separation switches from the pressure to the suction side at a lower flow angle than the baseline diffuser; the influence of the pressure side vortices is not as important as the adverse pressure gradient.

One of the most interesting insights from these scales is that for the axial stator, the relative impact of the secondary flows compared to the pressure gradient is an order of magnitude lower than it is for the baseline and truncated diffusers. The large influence of

the vortices on the boundary layer growth is unique to the low aspect ratios associated with centrifugal compressor diffusers.

It should be noted that when the diffuser leading edge boundary layer properties are used to calculate the scales without normalizing by the baseline diffuser quantities, the secondary flows scales (terms 1 and 4) are found to be two orders of magnitude larger than the pressure gradient scales (terms 2 and 5). Furthermore, the actual values of the vortex source terms shown in Figure 6.65 are much smaller than the term 1 scales. There are a few potential explanations for this. First, it is possible that some of the scaling assumptions are inaccurate. It is acknowledged that although the proposed scales should appropriately capture sensitivities to diffuser geometry and inlet conditions, the magnitudes may be incorrect. For example, the term 1 scale is sensitive to the distance between the vortex and the diffuser wall, which is somewhat arbitrarily characterized by the average boundary layer displacement thickness. Another possible explanation for the large term 1 scales is that they may be correct. Recall that the vortex source terms plotted in Figure 6.65 are sampled from the CFD results along the diffuser mid plane; they are not sampled immediately near the vortices where the transverse velocity gradients are larger. However, if the vortex source term scales really are much larger than the pressure gradient scales, the boundary layer growth would be almost entirely dependent on the vortices. This may be true local to the vortices even if it is not true on an average basis. Regardless of these concerns, the proposed scales are believed to appropriately capture sensitivities to the diffuser geometry shown in Table 6.1.

### 6.6.7 Reconciliation of Experimental and CFD Calculated Diffuser Performance Trends

As shown in Figure 6.48, the CFD calculated diffuser performance trends have been observed to follow a piecewise behavior that is not reflected in the experimental data, characterized by sudden changes in the slopes of the pressure rise and stagnation pressure loss coefficient characteristics with respect to diffuser inflow angle. As indicated in Figure 6.48, these regimes of behavior are broken into three parts: region 1 includes low flow angles near choke, region 2 encompasses the design flow angle, and region 3 includes high flow angles near or past compressor stall. The reason for this behavior has been identified in the previous sections as follows. At low flow angles, region 1 of the performance curve cor-

responds to the presence of strong pressure side incidence vortices. This results in greater stretching of the pressure side shear layer in the wall normal direction, increased mixing of the pressure side weak flow, and reduced extent of the pressure side flow separation relative to region 2. As a result the pressure recovery coefficients are higher in region 1 than they are in region 2. At high flow angles, region 3 corresponds to the shift in flow separation from the diffuser pressure side to the suction side. This is enabled by the presence of the suction side incidence vortices that correspond to higher incidence angles. Because the extent of a pressure side separation will decrease with flow angle whereas the extent of a suction side separation will increase with flow angle, a sudden change in the slope of the pressure recovery characteristic is observed between regions 2 and 3.

These differences are hypothesized to be related to unsteady effects, which are not modeled by RANS, and which may tend to smooth the time-averaged performance characteristics for the experimental measurements. As noted, the different regimes of the CFD calculated performance trends can be traced to changes in flow separation behavior (leading edge cusp separation influencing diffuser passage separation). However, flow separation is inherently unsteady. For example, during the transition between pressure and suction side separation regimes of operation (region 2 to region 3), it is likely that the diffuser passage separation actually oscillates between sides in an unsteady manner, or that different diffuser passages are separated on different sides at any given time. Additionally, the diffuser separation and associated performance strongly depends on the diffuser inlet flow angle, which is known to vary in an unsteady manner due to mechanisms such as the impeller rotation or rotating stall. Everitt proposed treating the unsteadiness in diffuser inflow angle in a quasi-steady manner [10]. That is, the unsteady compressor performance can be thought of as a time average of the steady performance results. This is a simplified understanding of what really happens, since the reduced frequency of the diffuser does not lend itself to quasi-steady treatment. However, the intuition that unsteadiness will smooth the steady performance trends is rational.

Regardless of these limitations, the flow mechanisms associated with the piecewise CFD regimes do make physical sense based on the arguments provided in the previous sections. The incidence vortices should be strongly influenced by the operating point, and the diffuser passage separation should be strongly influenced by the incidence vortices. Furthermore, the CFD calculations have been shown in Section 3.3.1 to closely capture time-averaged ex-

perimental measurements of the flow separation using stagnation pressure traverses and PIV. Therefore, the CFD results are still leveraged to gain valuable insights necessary for characterizing general performance trends and identifying the important flow mechanisms responsible for those trends.

### 6.6.8 Summary of Diffuser Passage Performance Assessment

The diffuser passage, representing the region of the diffuser downstream of the throat, contributes a significant fraction of the overall diffuser pressure rise. Despite the differences between the baseline and truncated diffuser geometry, the passage static pressure recovery and stagnation pressure loss coefficients are comparable. The static pressure recovery is determined primarily by three factors. The ideal pressure recovery coefficient is set by the diffuser 1D area ratio, which is greater for the baseline diffuser due to the lower exit flow angle. However, the larger exit blockage of the baseline diffuser, which is associated with additional wall friction, reduced mixing effectiveness, and consequent passage separation, reduces its pressure recovery capability down to the level of the truncated diffuser. Conversely, despite the additional nonuniformity associated with the thicker trailing edge of the truncated diffuser, the truncated diffuser exit flow is more uniform than the baseline diffuser due to the improved mixing that occurs in the vaneless space between the trailing edge and exit. This suggests that a deswirler design that is tailored to the greater exit flow angle of the truncated diffuser has the potential to increase the overall diffusion system static pressure recovery coefficient above that of the baseline configuration. The third factor influencing the static pressure rise of the diffuser is compressibility, which increases the pressure recovery coefficient and reduces the stagnation pressure rise coefficient at higher throat Mach numbers.

Together with the adverse pressure gradient, the secondary flows present in the diffuser passage are found to contribute significantly to the boundary layer growth and resulting flow separation. High loss boundary layer fluid is accumulated between the counter-rotating vortices. This redistribution of the weak flow reduces its ability to mix out, and as a result it is susceptible to nonuniformity amplification by the adverse pressure gradient. This mechanism can also be interpreted as the transverse compression of the boundary layer; an effect which is tied to the gradient of the transverse velocity component in the transverse direction ($\partial w/\partial z$ in the local boundary layer coordinate system). This transverse ve-

locity gradient is estimated based on the strengths and positions of the various vortices present in the CFD solutions, demonstrating that the incidence vortices are more influential than the background vortices despite their comparable strengths. A modified integral boundary layer model is implemented using additional vortex source terms to affect the boundary layer growth rate. This model demonstrates that the vortices have a large detrimental influence on the diffuser separation side, extent, and resulting static pressure recovery.

Using the integral boundary layer growth rate equations, scales are proposed to estimate the impacts of the vortices and the adverse pressure gradient for different diffuser geometries and inlet conditions. These are calculated for the baseline and truncated diffusers at the 100E operating point, demonstrating that the relative influence of the vortices is reduced for the truncated diffuser and explaining why its separation transitions to the suction side at a lower flow angle than the baseline diffuser. These scales are also used to show that the relative influence of the secondary flows is an order of magnitude higher for the diffusers of interest than it is for a representative axial compressor stator row. Thus, the large influence of the vortices on the boundary layer growth is unique to the low aspect ratios associated with centrifugal compressor diffusers.

## 6.7 Role of Diffuser Leading Edge Cusps

As discussed in Section 1.3, there is an observation in the literature that pipe diffusers generate more pressure recovery than vaned diffusers for the same inlet conditions. It is commonly hypothesized that this is due to an interaction between the leading edge cusps and secondary flows, which in turn reduces the diffuser throat blockage.

It has been shown in Section 6.5.7.2 that the leading edge cusps are partially responsible for the generation of incidence vortices in the diffuser inlet. Due to their concentrated proximity to the walls of the diffuser, it is further shown that in Section 6.6.6.2 that these incidence vortices have greater impact on the boundary layer than the background vortices, which form independent of the cusps. However, the effect of the vortices is to reduce local mixing effectiveness through transverse compression of the boundary layer and loss accumulation. This does not seem to be in line with the common hypothesis proposed in the literature.

Because the impact of the vortices on the forward and aftward endwall boundary layers is not quantified in this research, the overall impact of the vortices on the throat blockage cannot be directly assessed. However, it is plausible that the vortices could have the positive effect of stretching the endwall or corner boundary layers in the transverse direction, enhancing their mixing. Indeed for loss to accumulate in one place, it must be removed from somewhere else. Therefore, in the absence of a pressure side surface upstream of the throat, it is possible that the pressure side vortices could enhance mixing because the endwall boundary layers can be stretched without a loss accumulation penalty elsewhere. However, at high incidence angles when the suction side vortices are shown to induce a suction side boundary layer separation upstream of the throat, it is difficult to believe that the vortices would reduce the throat blockage.

One must also consider whether the throat blockage is a good metric by which to gauge the impact of the secondary flows or even the diffuser pressure recovery. If the throat blockage is assumed to correlate to the downstream mixing and nonuniformity amplification mechanisms, then this assumption is inaccurate if secondary flows significantly impact the mixing effectiveness between the throat and exit. In fact, this is the very argument employed in the literature to claim that the throat blockage is not correlated to the diffuser inlet blockage for a pipe diffuser. As demonstrated both in this research and by Wilkosz, the vortices increase the blockage at the diffuser exit [11]. Therefore, the vortices are detrimental to the pressure recovery of the tested diffusers at extreme flow angles, regardless of their impacts on throat blockage.

Wilkosz does show that for a high 1D area ratio radial pipe diffuser, the maximum pressure recovery potential can be achieved by employing a moderate level of secondary flows to stretch the thicker suction side boundary layer and balance the tendencies for the diffuser to want to separate on the pressure and suction sides [11]. Unfortunately, since the vortex strength is dependent on incidence, this cannot be achieved at all operating conditions. Furthermore, using strong vortices localized to the diffuser pressure side is not an effective way to achieve a benefit on the suction side.

Most of the evidence presented here suggests that the incidence vortices generated by the leading edge cusps do not benefit the pressure recovery potential of a transonic pipe diffuser. Therefore, more work must be done to understand why there is an observed pressure recovery advantage of pipe diffusers relative to vaned diffusers.

Even if the vortices do not increase the pressure recovery potential of a pipe diffuser, the degree to which the vortices are detrimental depends on the operating point. Therefore, by influencing the loss and pressure recovery characteristics, the vortices influence the compressor stability either beneficially or detrimentally depending on the incidence angle. This effect is discussed in Chapter 7.

## 6.8 Summary of Diffusion System Performance Assessment

The diffuser is found to be the primary contributor the performance of the overall diffusion system, defined as the diffuser and the deswirler together. The diffuser is further divided at the throat into inlet and passage subcomponents for detailed assessment. The performance of the inlet depends largely on the diffuser inlet flow angle. Secondary flows develop in the diffuser inlet dependent on the incidence angle, and these counter-rotating vortices act to accumulate flow between them and prevent nonuniformities from mixing out. This effect is more important for the longer baseline diffuser, contributing to the large separation, than it is for the shorter truncated diffuser.

# Chapter 7 Overall Compressor Stability Considerations

The most significant performance difference that has been experimentally demonstrated between the baseline and truncated diffuser configurations is that the stability line of the truncated diffuser is improved at high speed relative to the baseline diffuser configuration (see Figure 3.5). The purpose of this chapter is to explain the reason for this difference in terms of the performance limiting flow mechanisms that have been identified within the diffusers.

It is hypothesized that the onset of stall for the baseline diffuser configuration is initiated by a switch in diffuser passage separation side, which is itself initiated by the diminished strength of pressure side vortices and increased strength of the suction side vortices at high incidence angles. Because of the large separation extent of the baseline diffuser, this change in the diffuser stability dominates the overall compressor stability. Conversely, because the extent of the passage separation in the truncated diffuser is diminished, the switch in separation side does not have as drastic of an impact on the stability of the overall compressor. As the stability of the impeller is reduced with decreased speed and increased incidence, the stability advantage of the truncated diffuser configuration is gradually diminished for lower speeds.

## 7.1 Stability Fundamentals

A review of compressor stability fundamentals is provided to guide the stability discussion about the baseline and truncated diffuser configurations. Greitzer proposed a framework for thinking about the dynamic behavior of a compressor [21]. The 1D transient momentum equation for the compressor is given by Equation 7.1, where $\dot{m}$ is the physical mass flow rate of the compressor, $\Delta p_c$ can be thought of as the pressure rise generated by the compressor given its operating conditions, and $\Delta p$ is the instantaneous physical pressure differ-

ence across the compressor determined by the compressor backpressure. The ratio between the characteristic length and area of the compressor, $L/A$, is found from an integral along the compressor length defined according to Equation 7.2.

$$\frac{L}{A}\frac{d\dot{m}}{dt} = \Delta p_c - \Delta p \qquad \text{Equation 7.1}$$

$$\frac{L}{A} = \int \frac{ds}{A(s)} \qquad \text{Equation 7.2}$$

The compressor pressure rise depends on its operating point. In steady state operation, this is usually characterized in a compressor map by the compressor speed and mass flow, $\dot{m}$. On the other hand, the compressor backpressure depends not only on the compressor but on the downstream components as well (e.g. the combustor and turbine for a gas turbine engine). From Equation 7.1, one can see that in steady state ($d\dot{m}/dt = 0$) the compressor generates a pressure rise equal to the pressure difference across it ($\Delta p_c = \Delta p$). However, this is not so in transient operation.

To assess whether the compression system can operate stably, consider a small perturbation to the compressor mass flow at constant speed and back pressure. If the shape of the compressor speed line is such that $d(\Delta p_c)/d\dot{m} < 0$, then a reduction in mass flow will correspond to an increase in pressure rise, and by Equation 7.1 one can see that $d\dot{m}/dt > 0$. This acts to restoring the compressor back to its original mass flow. However, if $d(\Delta p_c)/d\dot{m} > 0$, then a reduction in mass flow will further result in $d\dot{m}/dt < 0$. This amplifies the mass flow perturbation, and the compressor operation becomes unstable.

In order to understand why a compressor stalls when it does, one needs to understand the effects that drive slope of the compressor pressure rise characteristic towards zero or greater as the mass flow is reduced. This could result from a single dominant stall initiating mechanism which rapidly changes the slope of the speed line with a small change in mass flow. Alternatively, this could result from a combination of multiple mechanisms which smoothly and gradually influence the slope of the speed line together.

It must also be understood that since stability is an engine system effect, the overall compressor speed line shape must be considered in a stability assessment. This means that even if the diffuser alone exhibits a $d(p_{31} - p_{t27})/d\dot{m} > 0$ characteristic, this could be stabilized by a $d(p_{t27} - p_{t25})/d\dot{m} < 0$ impeller characteristic. In a similar manner, the stability considerations of the compressor of interest may change if it is paired with an upstream axial compressor or a fan.

## 7.2 Hypothesized Stall Mechanisms

The results of the CFD simulations are interrogated near stall to hypothesize what mechanisms give rise to the observed compressor stability characteristics. Recall from Section 3.1 that the CFD simulations best representing the stall points are selected by comparing the diffuser inlet static pressure distributions with the experimental data measured near stall. In this way, the diffuser inlet flow angles are approximately matched between the experiments and CFD simulations. However, converged CFD solutions are also obtained at higher diffuser inflow angles than the experimental test rig. While the steady CFD simulations do not become unstable at the same operating point as the experimental rig, they are still interrogated to understand what flow mechanisms are present near the experimental stall operating point. In fact, the ability to obtain information about the diffuser at flow angles greater than the stalling flow angle is a luxury that only CFD can provide. The stalling mechanisms cannot be identified by looking at steady experimental measurements alone, since the state of the compressor changes too rapidly once these mechanisms appear.

A hypothesis is proposed to explain the difference between the baseline and truncated diffuser stall lines. Recall that the performance and flow mechanisms associated with the impeller and the diffuser inlet are identical between both diffuser configurations. Therefore, the stability differences must be attributable to mechanisms present in the diffuser passage. Recall from Figure 6.47 and Figure 6.48 that the CFD calculated diffuser passage loss and recovery trends have a piecewise appearance, with a sudden change in the slope of these characteristics occurring near stall, especially for the baseline diffuser (regions 2 to 3 indicated in Figure 6.48). This is the result of the incidence vortices and downstream separation transitioning between the pressure and suction sides of the diffuser with increased incidence angle, as explained in Section 6.2, 6.5.7, 6.6.6, and 6.6.8.

The effect on the compressor stability is explained by the illustration presented in Figure 7.1. The compressor mass flow is expressed as the impeller exit flow coefficient, and the pressure rise is expressed as the pressure rise coefficient. The overall compressor pressure rise characteristic is expressed as the sum of the impeller and diffusion system pressure rise characteristics. As the compressor is throttled toward stall, the extent of the diffuser pressure side separation diminishes due to the decreased strength of the pressure side incidence vortices. In this manner, the pressure side separation stabilizes the compressor op-

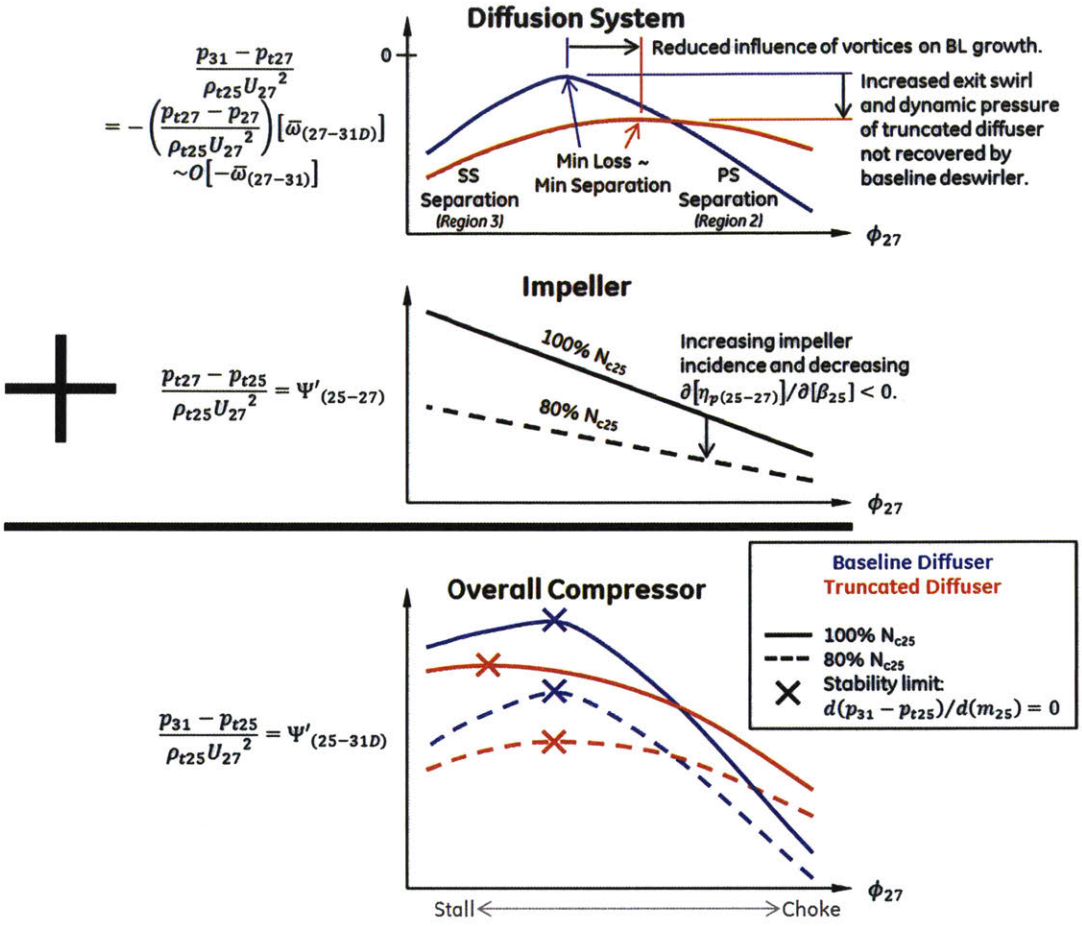


Figure 7.1: Illustration of diffusion system, impeller, and overall compressor pressure rise coefficients versus impeller exit flow coefficient, demonstrating combined effects of impeller and diffusion system on overall compressor stability. With baseline diffuser, compressor stability dominated by transition in diffuser separation side. With truncated diffuser, compressor stability determined by combination of impeller and diffuser pressure rise characteristics. Decreased slope of impeller characteristic with increased speed enables increased flow range with truncated diffuser, but not with baseline diffuser.

eration—not by improving the performance of the diffuser near stall, but by decreasing its pressure rise capability on reduced operating lines. However, the diffuser reaches its peak pressure recovery and minimum loss at some flow angle where the separation extent is minimized. Beyond this point, the suction side incidence vortices increase in strength while the pressure side vortices are diminished, the separation moves to the suction side, and its extent is increased as the compressor is throttled. This is a destabilizing effect. This hypothesis is supported by Wilkosz et. al. who identified a similar pressure recovery coefficient trend with respect to secondary flows strength, featuring regimes of pressure and suction side separation divided by the peak recovery coefficient [11].

The difference between the baseline and truncated diffusers is that the separation extent and its impact on the pressure rise characteristic are reduced for the truncated diffuser. While this means the truncated diffuser may not be as stabilizing on low operating lines, the change in slope of its pressure rise characteristic is less drastic as the separation transitions from the pressure to the suction side. Combined with the stabilizing effect of the impeller, the truncated diffuser can therefor operate stably at high speed with a suction side separation.

Because the stability of the compressor utilizing a truncated diffuser also depends on the slope of the impeller's pressure rise characteristic, the high speed benefit of the truncated diffuser is reduced at lower speeds, completely diminishing below 80% $N_{c25}$. This is because the impeller characteristics vary with compressor speed, even though the diffuser pressure rise characteristics do not. Recall from Section 4.2 that this is the result of an increase in impeller incidence angle with reduced speed. Near its design incidence angle (e.g. at high speed), the impeller loss is relatively insensitive to changes in incidence. However, at high incidence angles (e.g. at low speed), the impeller loss is more sensitive to changes in incidence angles as it is throttled. As a result, the stabilizing effect of the impeller pressure rise characteristic decreases with reduced speed, and the flow range of the truncated diffuser configuration reduces. On the other hand, the transition in separation side for the baseline diffuser dominates the slope of the overall compressor pressure rise characteristic so its stall line is not affected by impeller speed.

Based on these hypotheses about the mechanisms behind the compressor stability characteristics, one might infer that if the negative slope of the impeller pressure rise characteristic were further increased (i.e. made less negative) above what is observed at 80% $N_{c25}$, the truncated diffuser configuration would actually stall on a lower operating line than the baseline diffuser. However, this is not observed in the experimental data. There are two possible explanations for this. First, it is possible that stall measurements were not performed at low enough speeds to capture this effect. Based on Figure 3.5, the baseline diffuser configuration does in fact appear to have a small stall line advantage over the truncated diffuser configuration at 50% $N_{c25}$, but the significance of this small difference is uncertain. However, a more convincing explanation for the similar baseline and truncated diffuser stall lines below 80% $N_{c25}$ is that the slope of the impeller pressure rise characteristic actually doesn't change below this speed. Although the impeller incidence angle contin-

ues to increase at reduced speeds, the sensitivity of the impeller loss to marginal increases in flow angle is constant. Therefore, the slope of the impeller pressure rise characteristic is not changed between 50% $N_{c25}$ and 80% $N_{c25}$ as it is between 80% $N_{c25}$ and 100% $N_{c25}$.

The proposed hypothesis explaining the stability characteristics of this compressor is largely based on flow mechanisms observed in the CFD solutions: the transition of the diffuser passage separation from the pressure to the suction sides. However, this transition has not been confirmed experimentally. Furthermore, there are differences between the CFD and experimental performance trends, which are linked to this very mechanism (see Section 6.6.7). Therefore, more work must be done to assess these hypotheses. A few experiments are proposed for this purpose. First, high frequency pressure measurements could be recorded across the diffuser passage as the compressor is throttled into stall. Because the separation bubble is associated with streamline curvature around it, the static pressure distribution across the passage should change if the separation side changes near the onset of stall. It is actually likely that the separation side varies in an unsteady, periodic manner as the compressor is throttled, which could also be captured by high frequency pressure measurements. A second way to assess the stability hypotheses is to test the diffusers using different impellers with varying slopes of their pressure rise characteristics. This can be accomplished by using impellers with different degrees of backsweep. The stability hypothesis is supported if the impeller characteristics do not impact the overall compressor stall line with the baseline diffuser installed, but do impact the stall line with the truncated diffuser installed.

# Chapter 8 Summary

By leveraging the RWTH Aachen University experimental compressor measurements, CFD simulations, and low-order flow models, this research succeeds in addressing the questions.

While the baseline and truncated diffusers exhibit similar loss and pressure recovery characteristics, different mechanisms drive their performance levels. The baseline diffuser experiences greater wall friction and nonuniformity amplification effects than the truncated diffuser, resulting in a larger passage separation. While its 1D area ratio is high, the effective area ratio is reduced by the large exit blockage. The truncated diffuser, on the other hand, experiences much of its loss and some pressure rise during the mixing of the large trailing edge wakes. While the exit flow is more uniform than the baseline diffuser as a result of the long exit vaneless space, the effective area ratio is reduced by the higher exit flow angle, such that both diffuser configurations have comparable effective area ratios. However, in performing a mixed out analysis of the baseline and truncated diffuser exit flow, the truncated diffuser is found to have greater pressure recovery potential at its exit than the baseline diffuser due to the relative uniformity of the flow.

For both baseline and truncated diffusers, variations in the static pressure recovery and stagnation pressure loss coefficients between operating points are found to depend first on the diffuser inlet flow angle, and second on the inlet Mach number, corresponding closely with the compressor operating line and corrected speed respectively. The primary impact of compressibility is to choke the diffuser at low inlet flow angles. With increased diffuser inlet Mach number, the choking diffuser inlet 1D area ratio and thus flow angle must increase, as shown in Figure 8.1. In this way, the compressor flow range is reduced. Compressibility also increases the sensitivity of pressure and velocity changes to marginal area changes. This causes the static pressure to rise more rapidly throughout the diffuser, decreasing the average velocity relative to the inlet velocity and reducing the contribution of scrubbing losses to the stagnation pressure loss coefficient.

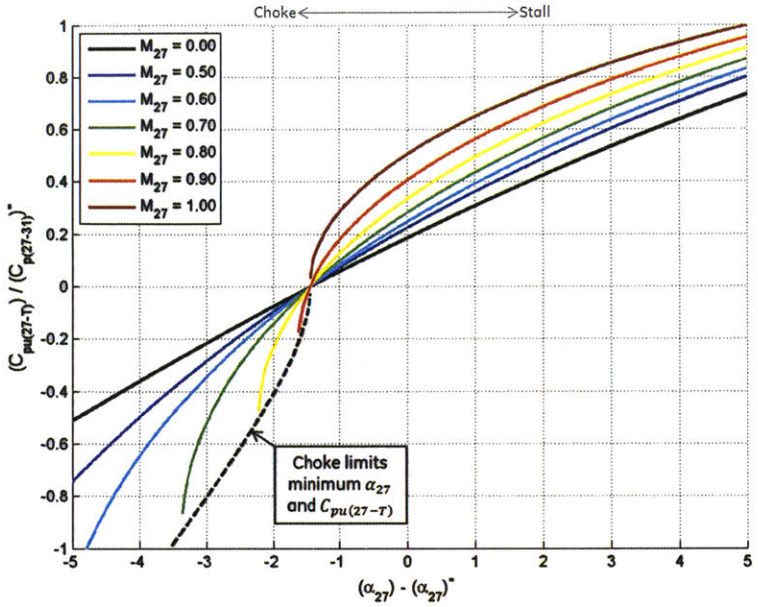


Figure 8.1: Ideal uniform diffuser inlet pressure recovery coefficient versus impeller exit flow angle. Choking limits minimum recovery and flow angle, thus limiting flow range.

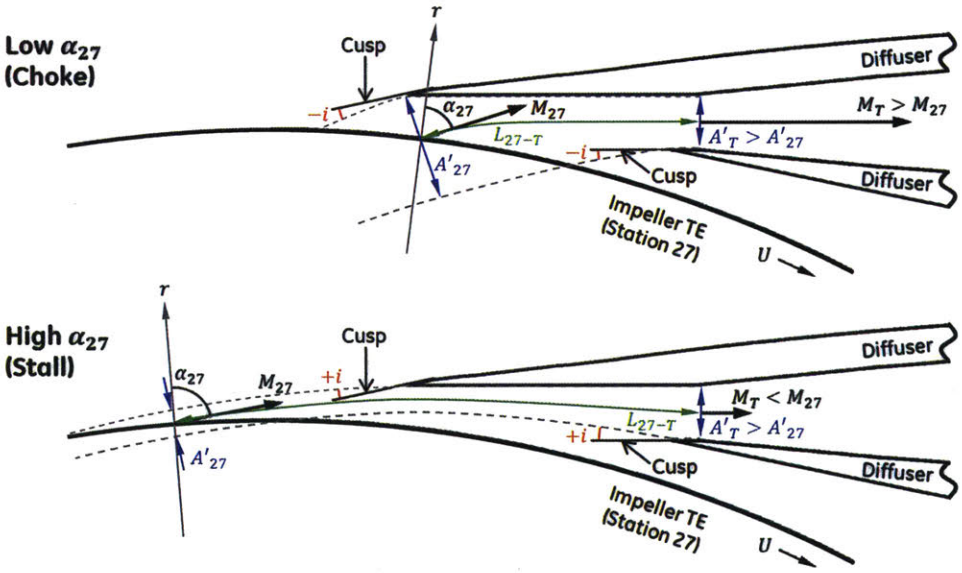


Figure 8.2: Illustration showing influence of diffuser inlet flow angle on 1D area ratio ($A'_T/A'_{27}$), path length ($L_{(1\text{-}2)}$), and incidence ($i$).

The flow angle has the primary effect of setting the 1D area ratio between the impeller exit and throat as shown in Figure 8.2, thus increasing inlet diffusion at high flow angles. The second most important effect of the flow angle is that it determines the diffuser leading edge and cusp incidence angle. This is hypothesized to result in incidence losses observed upstream of the diffuser throat, and it also influences the formation of secondary flows that persist throughout the diffuser passage. Increased flow angle also results in increased path

length and scrubbing losses between the impeller exit and the diffuser throat, but this effect is smaller than the others for this particular application where the two are close-coupled.

The aforementioned secondary flows consist of various pairs of counter-rotating vortices within the diffuser that can be grouped into two categories distinguished by their origin. The background vortices, which originate in the impeller exit nonuniformity and flow transition from impeller to diffuser, are predominantly concentrated near the endwalls and the diffuser pressure side. The incidence vortices, which result from boundary layer separation off the diffuser leading edge cusps, are localized near the diffuser pressure side at negative cusp incidence, and near the suction side at positive cusp incidence. Both background and incidence vortex types experience reorientation or amplification around the diffuser leading edge in a manner that is dependent on the incidence angle, as shown in Figure 8.3.

Contrary to the claim in the literature that the vortices improve the diffuser's pressure rise capability via enhanced mixing, they are shown to detrimentally impact the diffuser's pressure rise capability. This occurs through accumulation of high loss flow along the diffuser wall near the symmetry plane between the vortices, thereby reducing mixing effectiveness, increasing boundary layer growth rate, and contributing to the extent and location (pressure or suction side) of the aforementioned diffuser passage separation. Evidence for this is found by observing that the locations and strength of the vortices correspond to regions of high loss and flow separation downstream of the throat in the diffuser passage, as shown in Figure 8.4. To further assess this effect, a 2D integral boundary layer model is modified to accommodate CFD-measured source terms that represent the 3D transverse compression or stretching of the boundary layer by the secondary flow field, as shown in Figure 8.5. By adding and removing the vortex source terms from the model, the secondary flows are shown to dominate the boundary layer growth rate, as shown in Figure 8.6.

The modified integral boundary layer equations are further used to develop scales for the effects of the secondary flows and pressure gradient contributions to the boundary layer growth rate. The vortex source term is found to scale with the diffuser length, or inversely with aspect ratio. This reduction in secondary flows influence for the truncated diffuser explains why it experiences a reduced separation extent and a pressure-to-suction side separation transition at lower flow angles than the baseline diffuser. It also explains why the influence of secondary flows is less significant for an axial compressor blade row.

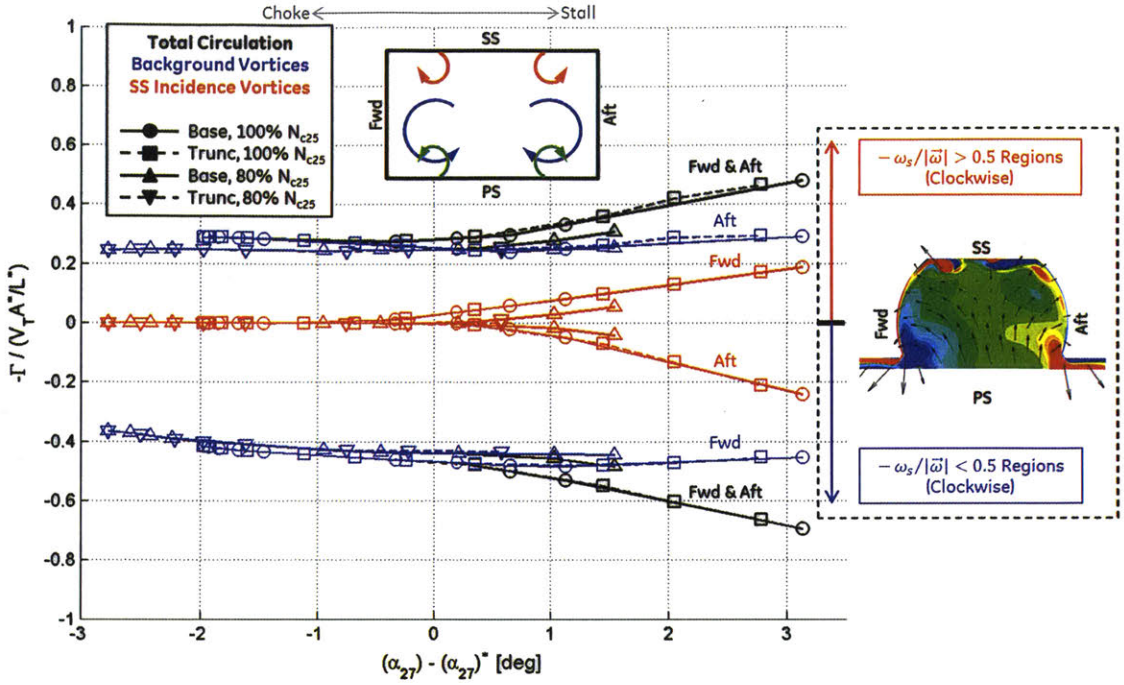


(a) X3 cut plane (downstream of suction side leading edge).

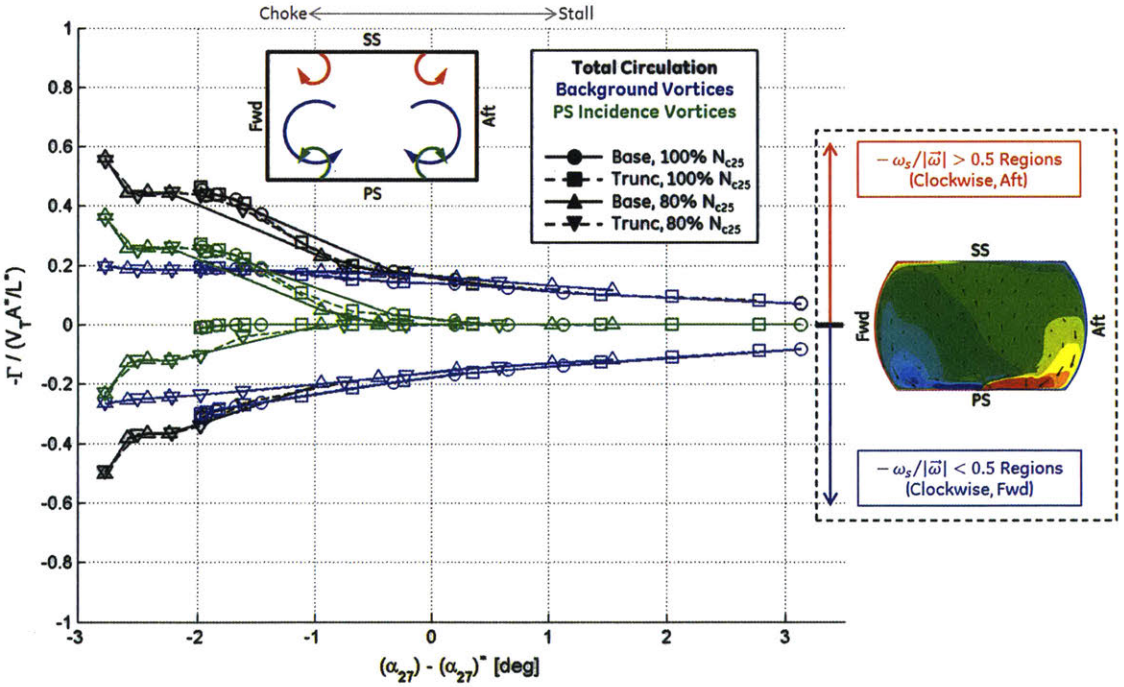


(b) X8 cut plane (downstream of pressure side leading edge).

Figure 8.3: Normalized circulation around vortex regions versus impeller exit flow angle. Symbols and line styles denote diffuser configuration and compressor speed, while colors denote different vortex sources. Pressure and suction side incidence vortices rapidly increase in strength below and above threshold flow angle. Background vortex strength unaffected by flow angle at X3, but increases with reduced flow angle at X8.

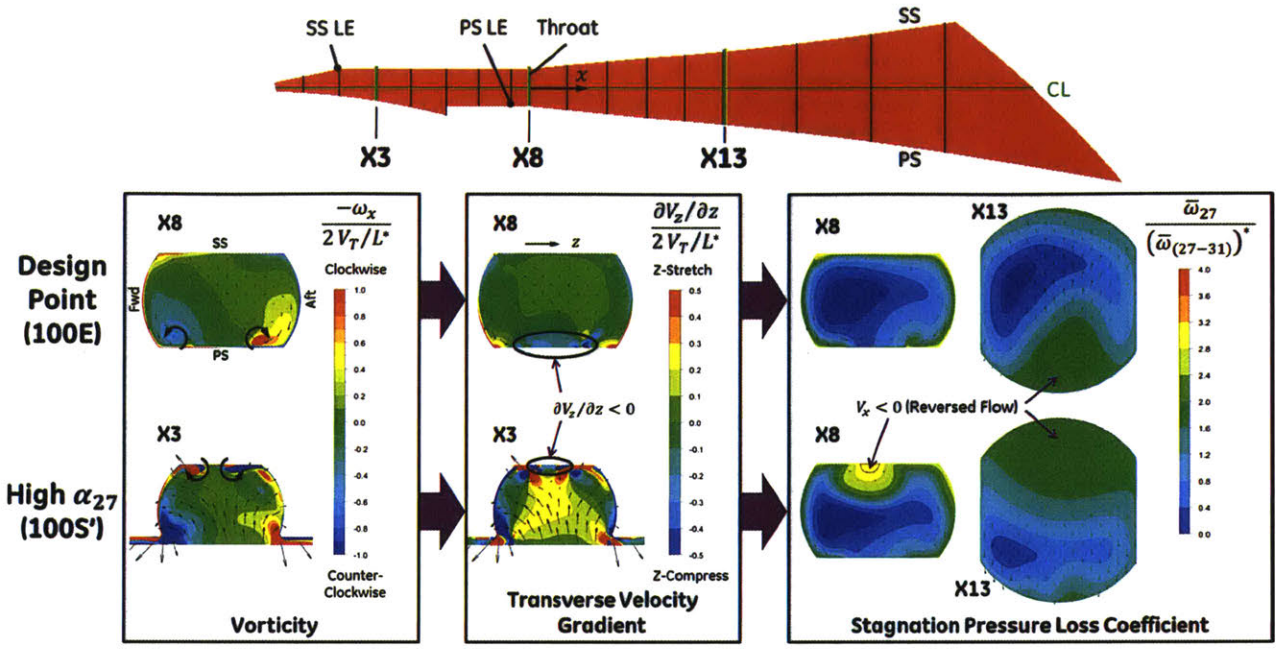


Figure 8.4: Relationship between secondary flows, transverse velocity gradient, and accumulation of high loss fluid. Streamwise vortices positioned near the diffuser wall cause weak flow to accumulate on the wall near the plane of symmetry between the vortices. As a result, mixing effectiveness is reduced, and mixing losses are localized to one side of the diffuser passage.

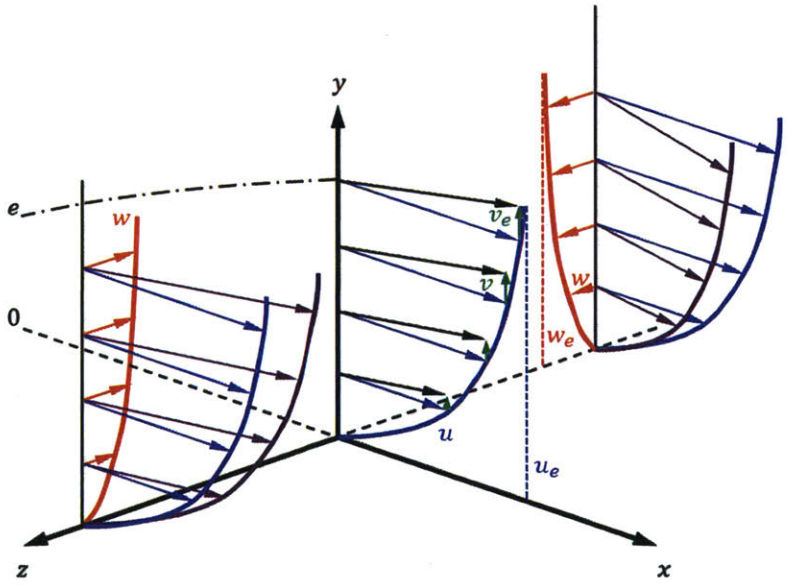


Figure 8.5: 3D effect of transverse velocity gradient, $\partial w/\partial z$, on boundary layer growth rate. Main flow velocity and direction represented by $u$ and $x$ respectively, wall normal velocity and direction represented by $v$ and $y$ respectively, and transverse velocity and direction represented by $w$ and $z$ respectively. Wall position represented by $0$, and boundary layer edge represented by $e$. Illustration shows $\partial w/\partial z<0$, which increases boundary layer growth rate relative to pure 2D boundary layer due to accumulation of high loss flow from sides.

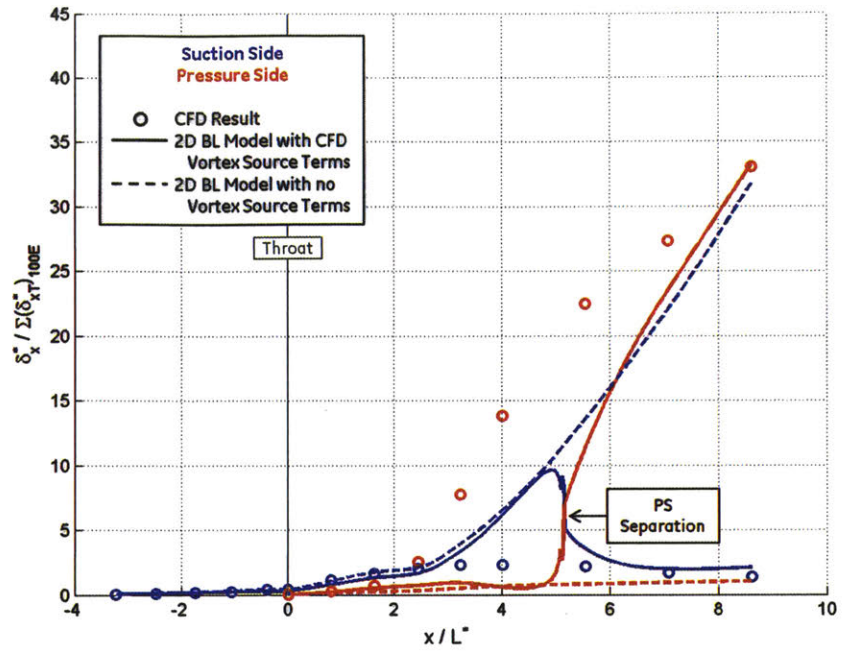


(a) 100E

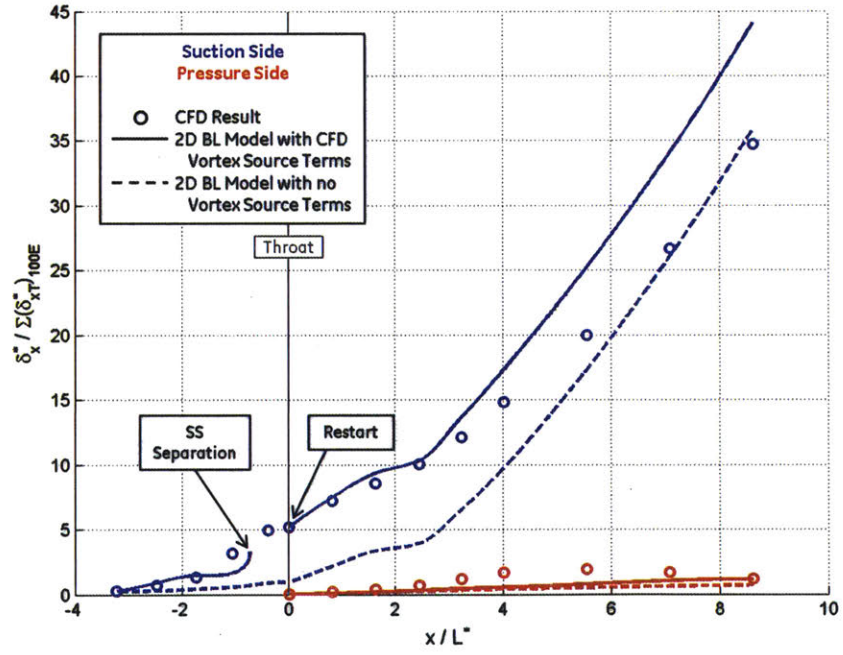


(b) 100S'

Figure 8.6: Boundary layer displacement thickness versus throughflow position for baseline diffuser. Includes CFD calculation as well as 2D boundary layer model calculations with and without vortex source terms. Excluding vortex source terms reduces displacement thicknesses. In addition, it causes the separation side to change at 100E, and it delays separation at 100S'.

While the baseline and truncated diffusers exhibit similar static pressure recovery and stagnation pressure loss coefficients, the stall line of the truncated diffuser configuration is improved over that of the baseline diffuser. Based on what has been learned about the factors driving the diffuser performance characteristics, a hypothesis is proposed to explain this difference. It is hypothesized that the onset of stall for the baseline diffuser configuration is initiated by the switch in diffuser passage separation side, which is itself initiated by the diminished strength of pressure side vortices and increased strength of the suction side vortices at high incidence angles. Because of the large separation extent of the baseline diffuser, this sudden change in slope of the diffuser pressure rise characteristic dominates the overall compressor stability as shown in Figure 8.7. Conversely, because the extent of the passage separation in the truncated diffuser is diminished, the switch in separation side does not have a drastic impact on the slope of the pressure rise characteristic or the overall compressor stability. As a result, the compressor can operate stably with a suction side separation on the truncated diffuser. However, as the stability of the impeller is reduced with decreased speed and increased incidence, the advantage of the truncated diffuser to the overall compressor stability is gradually diminished, also indicated in Figure 8.7.

The fact that secondary flows have a large influence on diffuser pressure rise capability and compressor stability is counter to conventional preliminary diffuser design approaches which neglect such 3D effects. The findings of this research may therefore be considered during preliminary design optimization to produce better-performing diffuser designs.

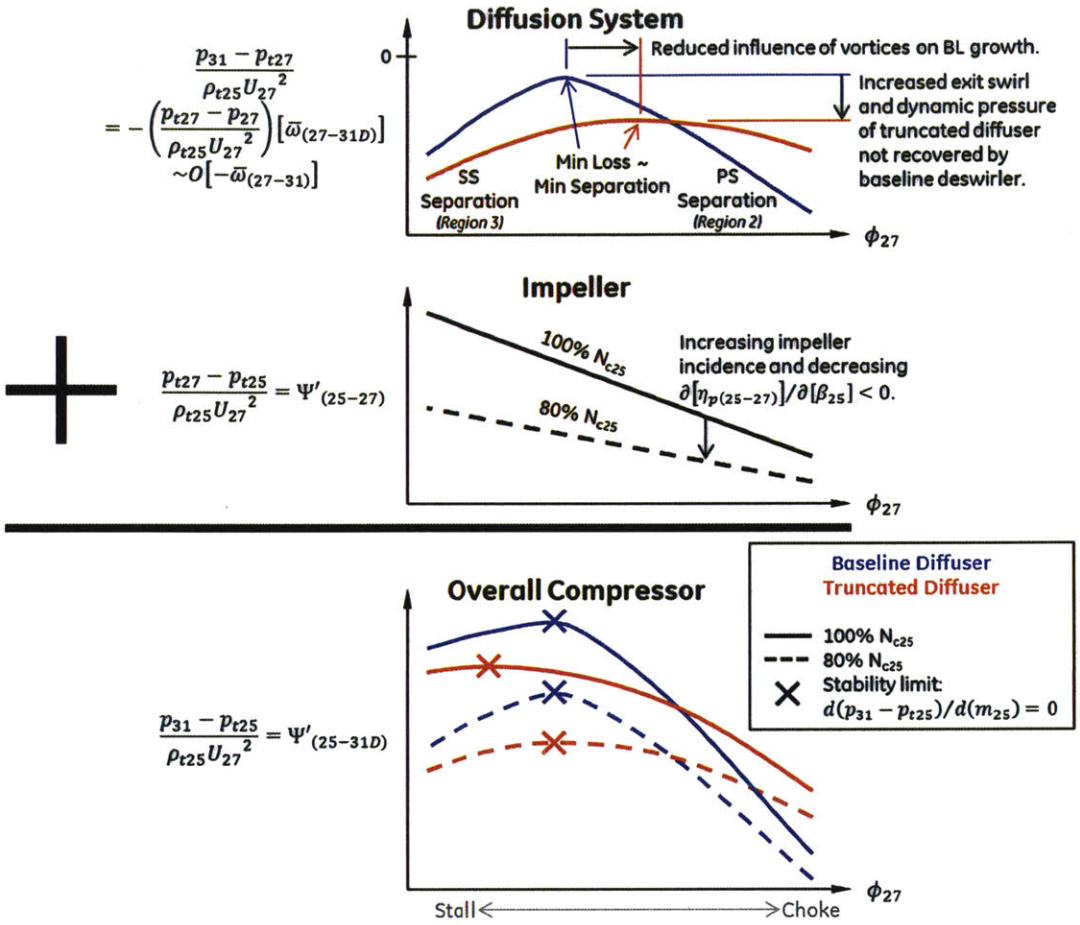


Figure 8.7: Illustration of diffusion system, impeller, and overall compressor pressure rise coefficients versus impeller exit flow coefficient, demonstrating combined effects of impeller and diffusion system on overall compressor stability. With baseline diffuser, compressor stability dominated by transition in diffuser separation side. With truncated diffuser, compressor stability determined by combination of impeller and diffuser pressure rise characteristics. Decreased slope of impeller characteristic with increased speed enables increased flow range with truncated diffuser, but not with baseline diffuser.

# Chapter 9 Conclusions

This research is successful at identifying a number of performance-limiting flow mechanisms within a centrifugal compressor stage, namely the diffuser. The relationships between these mechanisms and the diffuser geometry and operating conditions are established, and their corresponding impacts on diffuser pressure rise are quantified. Furthermore, an explanation for the compressor stability characteristics is hypothesized.

## 9.1 Objectives and Approach

This research sets out to characterize the pressure ratio, efficiency, and operable range of a centrifugal compressor stage, or more specifically the pressure recovery and loss coefficients of the diffusion system. This research was inspired by previous work performed at RWTH Aachen University utilizing a centrifugal compressor test rig with two different pipe diffuser configurations: a high 1D area ratio baseline diffuser and a truncated version of this same diffuser. Based on the findings from this work, the following research questions were posed:

- What flow mechanisms drive the observed performance trends in the tested centrifugal compressor across a range of speeds and throttle levels? What are the implications for other compressor designs?
- What are the differences in influential flow mechanisms between the baseline and truncated diffuser configurations? Why is the stall line of the centrifugal compressor improved with the truncated diffuser? What are the implications for other compressor designs?
- What impact do diffuser leading edge cusps and secondary flows have on the influential flow mechanisms within the diffuser?
- How do the impacts of the various flow mechanisms scale with different compressor geometries and operating conditions?

With the intention of moving beyond simply recognizing performance trends, a number of strategies are leveraged to describe and quantify the causal relationships between these trends and the fundamental performance limiting flow mechanisms. Experimental data acquired on a research compressor stage is interrogated along with a set of well-designed CFD computations. These are complemented by reduced order flow modeling to quantify the importance of specific flow mechanisms without confounding effects from other mechanisms, and to gain insight into the process by which these mechanisms influence performance. This includes utilization of the following strategies, which are unique to this research:

- A framework is established for evaluating the diffusion system in terms of interactions between subcomponents: the diffuser inlet, diffuser passage, and deswirler.
- A 2D integral boundary layer growth model is modified to include 3D secondary flows effects as source terms.

## 9.2 Key Findings

This research yields a number of significant findings. Performance variations between operating points are found to be primarily driven by changes in the impeller exit flow angle and secondarily by changes in impeller exit Mach number. The diffuser incidence angle greatly impacts the formation of secondary flows within the diffuser passage, which are found to have a detrimental effect on the diffuser pressure rise capability. The origin and performance impact of these secondary flows are summarized as follows:

- Secondary flows are made up of a superposition of two types of counter-rotating vortex pairs. "Background vortices" originate in the impeller exit nonuniformity and flow transition from impeller exit to diffuser inlet, while "incidence vortices" result from boundary layer separation off the diffuser leading edge cusps.
- Through accumulation of weak flow on the diffuser wall near the plane of symmetry between the vortices, secondary flows reduce mixing effectiveness in the diffuser passage and contribute to the passage separation extent and location (pressure side near choke, suction side near stall).
- The impact of the secondary flows on boundary layer growth is found to scale inversely with the diffuser aspect ratio.

The baseline and truncated diffuser pressure recovery and loss magnitudes and trends are comparable, though the responsible flow mechanisms differ. This is explained by the following:

- The two diffuser configurations have similar effective area ratios, with the baseline diffuser having a larger exit blockage but lower exit flow angle than the truncated diffuser.
- The truncated diffuser experiences greater loss due to the thicker trailing edge, while the baseline diffuser experiences greater inefficiency due to wall friction and nonuniformity amplification.

The truncated diffuser improves the compressor's high-speed stall line relative to the baseline diffuser. Based on insights gained from the experimental and CFD results, the following hypothesis is developed to explain this observation:

- With the baseline diffuser, the compressor stalls when diffuser separation switches from the pressure side (stabilizing) to the suction side (destabilizing).
- With the truncated diffuser, the compressor stalls due to gradual reduction in diffuser stability as suction side loss worsens. Instability is not immediately initiated when separation side switches for the truncated diffuser, since the separation extent is reduced relative to the baseline diffuser. Compressor stability is also dependent on the impeller characteristics.

The fact that secondary flows have a large influence on diffuser pressure rise capability and compressor stability is counter to conventional preliminary diffuser design approaches which neglect such 3D effects. The findings of this research may therefore be considered during preliminary design optimization to produce better-performing diffuser designs.

## 9.3 Future Work

This research has generated a number of other questions that could be pursued in future work. These are proposed below:

- Are the hypotheses regarding the stall behavior of this compressor supported by further experimentation? A number of experimental studies are proposed in Section 7.2 to verify the hypotheses.
- Do the scales proposed to gauge the impacts of the vortices and pressure gradient on the boundary layer growth rate accurately capture the effects of diffuser geometry

and inlet conditions for other experimental compressor stages? Can the vortex source term scale be modified to include the effects of incidence, vortex source (background vs. incidence vortices), and migration of the vortices toward one another along the passage length?

- Are there scenarios or areas where the incidence and background vortices could be beneficial for the diffuser pressure recovery coefficient? For example, what are the effects of the vortices on the endwall or corner boundary layers within the diffuser passage?
- What is the source of the so-named incidence losses that are observed upstream of the diffuser leading edge? Are these the result of cusp incidence, an interaction with the impeller tip bleed slots, or something else?
- What are the performance-limiting flow mechanisms in the impeller and deswirler?
- Why are there differences between the CFD and experimental results? Specifically, why do CFD simulations calculate an overall compressor work input, pressure rise, and efficiency that are higher than experimentally measured? Also, why do the CFD calculated diffuser loss and pressure recovery characteristics exhibit a piecewise appearance not observed in the experimental results?
- What effects do the various CFD simplifications have on the conclusions of this research and the additional research questions above? Specifically, what are the effects of unsteadiness or impeller-diffuser interaction, grid refinement in the diffuser vortex and separation shear layers, and various turbulence modeling assumptions?
- Can the mixed out average be defined in such a way that it is useful for reversed flows or flows with high crossflow static pressure gradients? Alternatively, can a metric be derived to determine the usefulness of the mixed out average for a given application?

# Appendix A Problems with the Mixed Out Average

Everitt proposed that the mixed out average was a better choice of averaging schemes for interpreting diffuser performance results than the availability average used by Filipenco [10]. Everitt found that the impeller exit mixed out average flow angle collapsed his diffuser performance data better than the momentum averaged flow angle, where the mixed out average effectiveness was used as the performance criteria. He argued that because the momentum averaged flow angle is calculated from mass averaged velocity components, too much weight may be placed on the meridional component of velocity, resulting in low average flow angles for highly nonuniform flows. Conversely, Everitt proposed that using the mixed out average flow angle resulted in an appropriate higher average flow angle since the meridional velocity component is reduced through the mixing process and resulting static pressure rise.

While both availability and mixed out averaged 1D flow properties may be useful, more weight is placed on the availability average here. Regarding the flow angle, the momentum average is thought to appropriately weight the meridional velocity component, while the mixed out average underweights it. To demonstrate this, one can imagine the limiting case of a swirling flow in the radial-circumferential plane, such as at the diffuser inlet, where there is only flow through half of the annulus, as shown in Figure A.1. The diffuser only truly experiences incoming flow through half of the annulus at an angle $\alpha_1$. The availability averaged set of 1D flow properties captures this, with the momentum averaged flow angle being equal to $\alpha_1$, and a mass flow blockage being used to represent the nonuniformity. Conversely, the mixed out average set of 1D flow properties does not represent the nonuniformity as a blockage, and instead it artificially increases the flow angle above what is truly experienced by the diffuser. If one wishes to characterize a mechanism that is incidence driven, it is the author's claim that the availability average flow angle is a better choice.

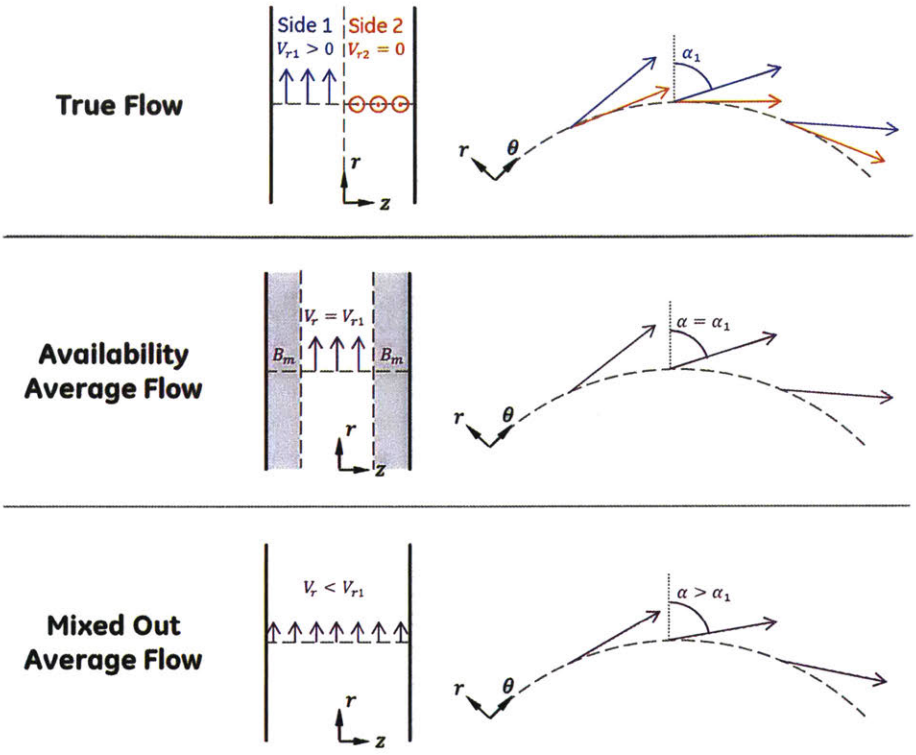


Figure A.1: Averaging of a nonuniform swirling flow in a radial vaneless diffuser. Availability average only considers flow moving radially through diffuser, while mixed out average considers flow not moving through diffuser.

Another issue with the mixed out average is that it can yield unrealistic results if the constant area assumption breaks down, and wall forces or pressure gradient heavily influence the true flow. In fact, it can actually violate the second law of thermodynamics if flow reversal is present, such as in the diffuser vaneless space and passage for the test compressor, or if the static pressure is highly nonuniform over the averaging plane, such as near the diffuser leading edge where there is streamline curvature. Figure A.2 shows the availability and mixed out average loss coefficients throughout the baseline diffuser based on the 100S' CFD results, calculated at the averaging planes shown in Figure 2.18. As you can see, the mixed out average loss is actually lower than the availability average loss in the inlet region where there is flow reversal across the averaging plane and circumferential static pressure nonuniformity. Because the availability average uses the true entropy flow per unit area to calculate stagnation pressure, a lower mixed out average loss represents a nonphysical reduction in entropy. The mixed out average near the diffuser exit is also questionable due to flow reversal that is present there.

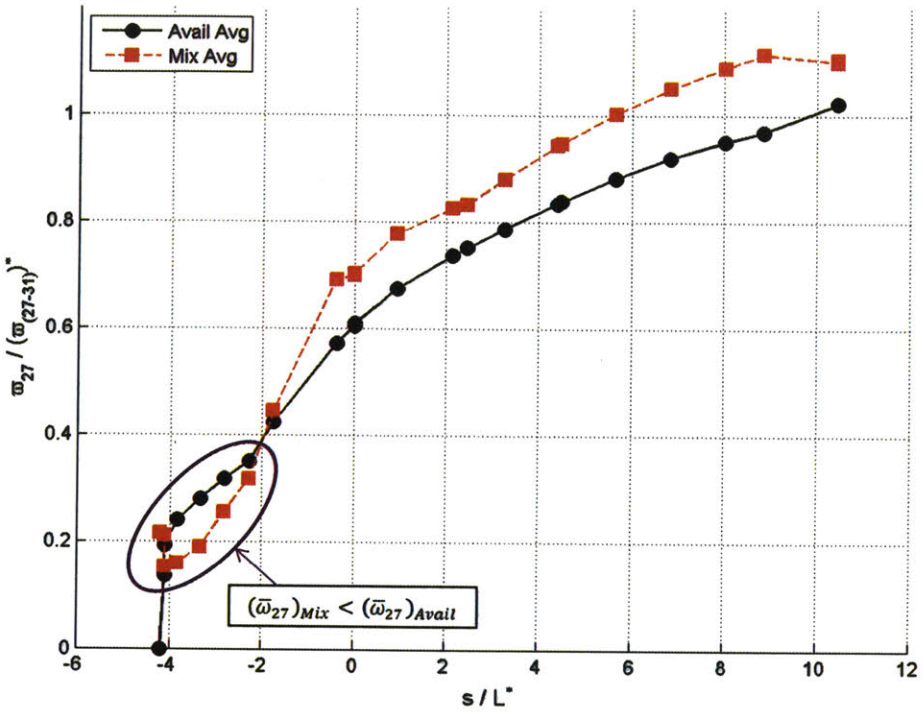


Figure A.2: Availability and mixed out average 1D stagnation pressure loss coefficient throughout baseline diffuser at 100S'. Mixed out entropy is lower than true entropy in diffuser inlet, a nonphysical artifact of mixed out average assumptions.

This violation of the second law of thermodynamics can be explained by applying the mixed out average to the incompressible flow shown in Figure A.3. In the presence of reversed flow, the mixed out average not only represents a mixing process, but also a flow splitting process, whereby some fraction of the inflow becomes reversed within the confines of the mixed out average control volume and the other fraction mixes out and exits the control volume uniformly. However, wall forces and pressure gradients must be present in some form to give rise to this type of flow in reality. Because the assumptions of the mixed out average analysis do not allow for these physical mechanisms to split and reverse the flow, the average can yield a set of 1D flow properties with lower entropy than the inflow.

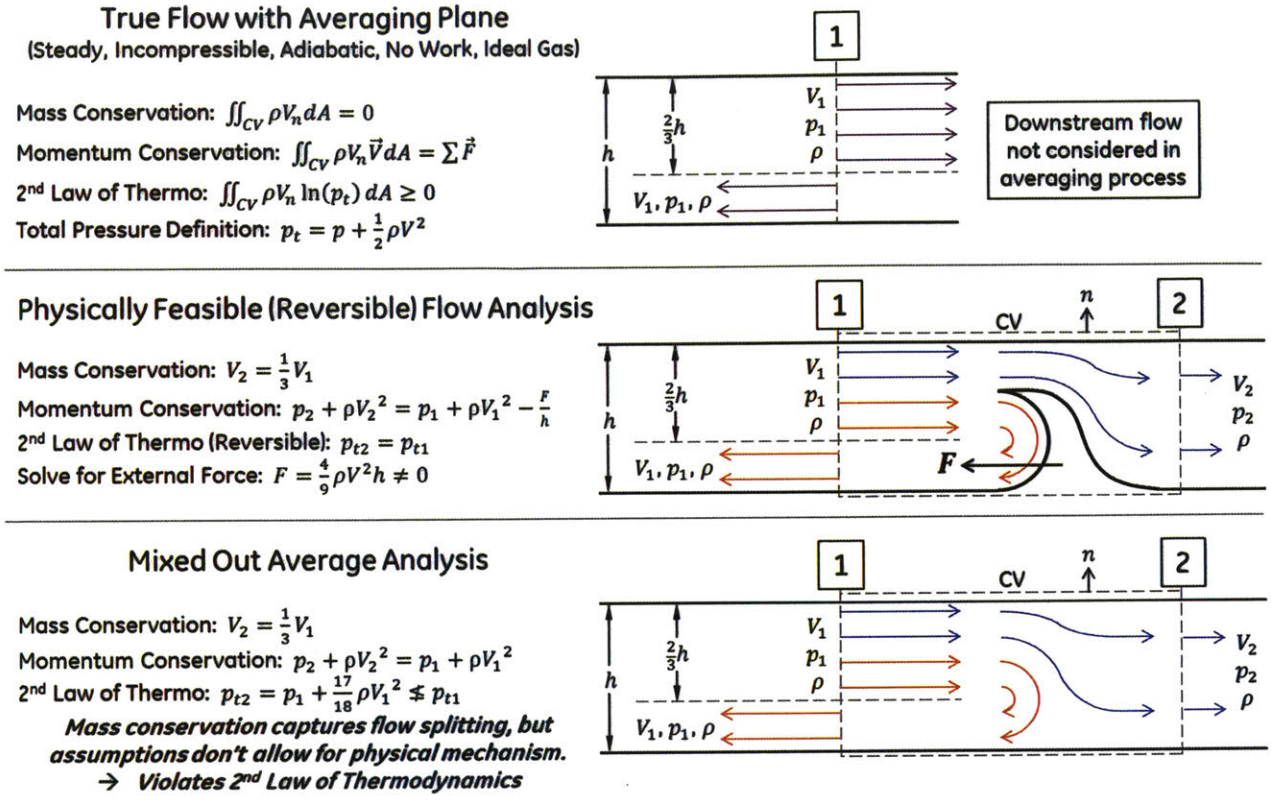


Figure A.3: Example of flow field where mixed out average analysis yields nonphysical entropy reduction. Flow reversal cannot occur in constant area channel. Therefore, mixed out average does not account for physical mechanism that can give rise to flow reversal.

# Bibliography


[1] U. Zachau, "Experimental Investigation on the Diffuser Flow of a Centrifugal Compressor Stage with Pipe Diffuser," *PhD Thesis, RWTH Aachen University,* 2007.

[2] U. Zachau, C. Buescher, R. Niehuis, H. Hoenen, D. C. Wisler and Z. M. Moussa, "Experimental Investigation of a Centrifugal Compressor Stage with Focus on the Flow in the Pipe Diffuser Supported by Particle Image Velocimetry (PIV) Measurements," in *Proceedings of ASME Turbo Expo 2008: Power for Land, Sea, and Air,* Berlin, Germany, 2008.

[3] R. Kunte, P. Schwarz, B. Wilkosz, P. Jeschke and C. Smythe, "Experimental and Numerical Investigation of Tip Clearance and Bleed Effects in a Centrifugal Compressor Stage with Pipe Diffuser," in *Proceedings of ASME Turbo Expo 2011,* Vancouver, Canada, 2011.

[4] R. Kunte, P. Jeschke and C. Smythe, "Experimental Investigation of a Truncated Pipe Diffuser with a Tandem Deswirler in a Centrifugal Compressor Stage," *Journal of Turbomachinery, Vol. 135,* p. 031019, 2013.

[5] D. J. Cockrell and E. Markland, "A Review of Incompressible Diffuser Flow," *Aircraft Engineering and Aerospace Technology,* pp. 286-292, 1963.

[6] L. R. Reneau, J. P. Johnston and S. J. Kline, "Performance and Design of Straight, Two-Dimensional Diffusers," *Journal of Basic Engineering,* pp. 141-150, March 1967.

[7] G. Sovran and E. D. Klomp, "Experimentally Determined Optimum Geometries for Rectilinear Diffusers with Rectangular, Conical, or Annular Cross-Section," *Fluid Mechanics of Internal Flow,* 1967.

[8] N. A. Cumpsty, Compressor Aerodynamics, New York, NY: John Wiley & Sones, Inc., 1989.

[9] V. G. Filipenco, "Experimental Investigation of Flow Distortion Effects on the Performance of Radial Discrete-Passage Diffusers," *GTL Report 206, Massachusetts Institute of Technology,* 1991.

[10] J. Everitt, "The Role of Impeller Outflow Conditions on the Performance and Stability of Airfoil Vaned Radial Diffusers," *PhD Thesis, Massachusetts Institute of Technology,* 2014.

[11] B. Wilkosz, P. Schwarz, N. Chen, P. Jeschke and C. Smythe, "Numerical Investigation of the Steady Separation Inducing Mechanisms in a Passage Diffuser with Application of the Two-Equation Turbulence Models," in *Conference on Modelling Fluid Flow,* Budapest, Hungary, 2012.

[12] D. P. Kenny, "The History and Future of the Centrifugal Compressor in Aviation Gas Turbines," *SAE Technical Paper 841635,* October, 1984.

[13] D. P. Kenny, "A Comparison of the Predicted and Measured Performance of High Pressure Ratio Centrifugal Compressor Diffusers," in *ASME International Gas Turbine and Fluids Engineering Conference and Products Show*, San Francisco, CA, 1972.

[14] Y. K. P. Shum, "Impeller-Diffuser Interaction in Centrifugal Compressors," *PhD Thesis, Massachusetts Institute of Technology,* 2000.

[15] B. Wilkosz, M. Zimmermann, P. Schwarz, P. Jeschke and C. Smythe, "Numerical Investigation of the Unsteady Interaction within a Close-Coupled Centrifugal Compressor Used in an Aero Engine," in *Proceedings of ASME Turbo Expo*, San Antonio, 2013.

[16] N. A. Cumpsty and J. H. Horlock, "Averaging Nonuniform Flow for a Purpose," *Journal of Turbomachinery,* pp. 120-129, 2005.

[17] E. M. Greitzer, C. S. Tan and M. B. Graf, Internal Flow: Concepts and Applications, Cambridge, UK: Cambridge University Press, 2004.

[18] B. Wilkosz, "Aerodynamic Losses in an Aero Engine Centrifugal Compressor with a Close-Coupled Pipe-Diffuser and a Radial-Axial Deswirler," *PhD Thesis, RWTH Aachen University,* 2014.

[19] I. ANSYS, ANSYS Help, Canonsburg, PA, Version 16.1.

[20] M. Drela and M. B. Giles, "Viscous-Inviscid Analysis of Transonic and Low Reynolds Number Airfoils," *AIAA Journal,* pp. 1347-1355, 1987.

[21] E. M. Greitzer, "Surge and Rotating Stall in Axial Flow Compressors," *Journal of Engineering for Power,* pp. 190-198, April 1976.